Pharmacological characterisation of small molecule RGD-mimetics targeting αvβ6-mediated activation of TGFβ in idiopathic pulmonary fibrosis

Thesis submitted for the degree of

Doctor of Philosophy

at the University of Strathclyde

by

Robert J. Slack

Strathclyde Institute of Pharmacy and Biomedical Sciences

University of Strathclyde

December 2015

‘This thesis is the result of the author’s original research. It has been composed by the author and has not been previously submitted for examination which has led to the award of a degree.’

Signed: Date:

Pharmacological characterisation of small molecule RGD-mimetics targeting αvβ6-mediated activation of TGFβ in idiopathic pulmonary fibrosis

Robert J. Slack

Fibrosis and Lung Injury Discovery Performance Unit, GlaxoSmithKline Medicines Research Centre, Stevenage, Hertfordshire, UK, SG1 2NY.

Abstract

Fibrosis is the formation of scar tissue due to injury or long-term inflammation and is a leading cause of morbidity and mortality in disorders that include idiopathic pulmonary fibrosis (IPF). The alpha-v beta-6 (αvβ6) integrin has been identified as playing a key role in the activation of transforming growth factor-β (TGFβ) that is hypothesized to be pivotal in the development of IPF. Therefore, the αvβ6 integrin was identified as an attractive therapeutic target for this debilitating disease and a drug discovery programme to identify inhaled small molecule αvβ6 selective arginyl-glycinyl-aspartic acid (RGD)-mimetics was initiated within GlaxoSmithKline. The primary aim of this study was to pharmacologically characterise the small molecule αvβ6 RGD-mimetics generated in a range of test systems. RGD ligands including peptides, antibodies and small molecule RGD-mimetics were characterised *in vitro* using methods that included radioligand binding, cell adhesion, flow cytometry, co-culture TGFβ bioassays, confocal microscopy and immunohistochemistry. This included the use of soluble recombinant integrin protein, stable and primary cells expressing integrins recombinantly or endogenously and human lung tissue from normal and IPF donors. Compound **3** generated from an internal medicinal chemistry programme was shown to bind to the αvβ6 with high affinity (pM) and displayed fast association with the integrin followed by slow dissociation kinetics in all systems investigated. Using [^{3}H]compound **3** the quantification of the upregulation of αvβ6 from normal to IPF human lung tissue has been determined for the first time with data suggesting αvβ6 exists in a highly activated state within diseased tissue. In human lung primary epithelial cells co-cultured with a TGFβ reporter cell system, compound **3** was shown to inhibit with high potency the activation of TGFβ with a prolonged duration of action. In the same primary lung epithelial cells compound **3** caused a rapid internalisation of αvβ6 (minutes) followed by a slow return of the integrin to the cell surface (hours). It was shown that αvβ6 is degraded in lysosomes post-internalisation by compound **3** that would suggest the slow return of integrin to the surface and sustained duration of action is a consequence of new αvβ6 synthesis. From the chemical series of small molecule RGD-mimetic compounds identified, compound **3** has been shown to display the desirable pharmacological characteristics required for targeting a prolonged inhibition of TGFβ activation in the IPF lung via blockade of the αvβ6 integrin.

Acknowledgments

I would like to thank my academic supervisors Prof. Susan Pyne and Prof. David Flint and industrial supervisor Dr. Jane Denyer for their help, guidance and support during the course of my project. I would also like to thank Dr. Steve Ludbrook for his advice and expertise on all things integrins, Prof. Simon Macdonald and the rest of the αvβ6 medicinal chemist team (especially Dr. John Pritchard and Dr. Niall Anderson) for the supply of tool and test molecules and my industrial placement students Rebecca Rogers, Maryam Hafeji and Lloyd Bibby for laboratory support. I would like to thank Prof. Andrew Fisher for supply of human IPF lung tissue and tissue sections.

I would also like to thank Dr. David Budd, Sylvia Fung, Becky Graves, Dr. David Hall, Emma Koppe, Dr. Pauline Lukey, Dr. Sally-Anne Rumley and Giovanni Vitulli for their input into scientific discussions and general support of this project. For help in setting up this collaboration with the University of Strathclyde I would like to thank Prof. Harry Kelly, Prof. Billy Kerr and Vikki Barrett as well as Prof. Richard Marshall for having the foresight to back this initiative.

I would like to thank my family for all their love and support, especially my parents John and Carol Slack and my in-laws Ray and Joyce Pamment for the countless cups of tea/coffee and childcare. Finally, I would like to thank and dedicate this work to my wife Lynsey and sons Rhys and Tomos who deserve all my gratitude for allowing me the time to complete this endeavour and who act as a constant source of inspiration and motivation on a daily basis. This is as much yours as it is mine.

Abbreviations

3D, three dimensional

AEC, alveolar epithelial cell

ALAT, Latin America Thoracic Association

ALK, activin receptor-like kinase

ANOVA, one-way analysis of variance

APC, allophycocyanin

ATS, American Thoracic Society

BAL, bronchoalveolar lavage

BCECF-AM, 2',7'-bis-(2-carboxyethyl)-5-(and-6)-carboxyfluorescein, acetoxymethyl ester)

B_{max}, total number of binding sites

BRAD, Biological Reagents and Assay Development

BSA, bovine serum albumin

CHAPS, 3-[(3-cholamidopropyl)dimethylammonio]-1-propanesulfonate

coSMAD, common mediator SMAD

CRC, concentration-response curve

CTGF, connective tissue growth factor

dH_2O, distilled water

DMEM, Dulbecco's Modified Eagle Medium

DMSO, dimethyl sulphoxide

DPM, disintegrations per minute

EC_{50}, molar concentration that produces 50% of maximum activation

ECM, extracellular matrix

EDTA, ethylenediaminetetraacetic acid

ELISA, enzyme-linked immunosorbent assay

EMT, epithelial-mesenchymal transition

ERK, extracellular signal-regulated kinase

ERS, European Respiratory Society

FAC, final assay concentration

FACS, fluorescence activated cell sorting

FCS, fetal calf serum

$fLAP_1$, full length LAP_1

FP, fluorescence polarisation

FVC, forced vital capacity

GPCR, G-protein receptor coupled receptor

GSK, GlaxoSmithKline

GST-LAP_1, glutathione S-transferase fusion LAP-TGFβ-1

H&E, haematoxylin and eosin

HBSS, Hank's balanced salt solution

HEPES, 4-(2-hydroxyethyl)-1-piperazineethanesulfonic acid

hHERG, human Ether-à-go-go-Related Gene

HRCT, high resolution computed tomography

hTGFβRII-APC, APC-conjugated polyclonal human anti-human TGFβ receptor II

HTS, high throughput screening

hα5-APC, APC-conjugated mouse monoclonal anti-human integrin alpha-5

hα8-PE, PE-conjugated mouse monoclonal anti-human integrin alpha-8

hαv-PE, PE-conjugated mouse monoclonal anti-human integrin alpha-v

hαvβ3-PE, PE-conjugated mouse monoclonal anti-human integrin αvβ3

hαvβ5-APC, APC-conjugated mouse monoclonal anti-human integrin αvβ5

hβ1-APC, APC-conjugated mouse monoclonal anti-human integrin beta-1

hβ6-PE, PE-conjugated mouse monoclonal anti-human integrin beta-6

hβ8-APC, APC-conjugated mouse monoclonal anti-human integrin beta-8

IC_{50}, molar concentration that produces 50% of maximum inhibition

ICC, immunocytochemistry

IgG, immunoglobulin

IgG2B-PE, PE-conjugated mouse IgG2B isotype control

IHC, immunohistochemistry

IL-13, interleukin-13

IMS, industrial methylated spirits

IPF, idiopathic pulmonary fibrosis

JNK, c-Jun NH2-terminal kinase

JPS, Japanese Respiratory Society

K_D, equilibrium dissociation constant

K_I, equilibrium inhibition constant

k_{off}, dissociation rate constant

k_{on}, association rate constant

LAP, latency-associated peptide

LLC, large latent complex

LPA, lysophosphatidic acid

LPAR2, lysophosphatidic acid receptor 2

LS, liquid scintillation

LTBP, latent TGFβ-binding protein

MAPK, mitogen-activated protein kinase

MFI, mean fluorescence intensity

MIDAS, metal ion-dependent adhesion site

MMP, matrix metalloproteinases

n_H, Hill slope

NHBE cells, normal human bronchial epithelial cells

NSB, non-specific binding

PAI-1, plasminogen inhibitor-1

PAR1, protease-activated receptor 1

PBS, phosphate buffered saline

PE, phycoerythrin

pEC_{50}, negative $\log_{10} EC_{50}$

PEI, poly-ethylenimine

pIC_{50}, negative $\log_{10} IC_{50}$

pK_D, negative $\log_{10} K_D$

pK_I, negative $\log_{10} K_I$

RGD, arginyl-glycinyl-aspartic acid

RLU, relative luciferase units

RPMI, Roswell Park Memorial Institute

R-SMAD, receptor-specific SMAD

SAR, structure activity relationship

SBE, SMAD-binding element

SCP, Screening and Compound Profiling

SD, standard deviation

SEM, standard error of the mean

SLF, simulated lung fluid

SMAD, Sma and Mad related protein

SPR, surface plasmon resonance

TBS, Tris-buffered saline

TGFβ receptor I, TGFβRI

TGFβ receptor II, TGFβRII

TGFβ, transforming growth factor-β

$tLAP_1$, truncated LAP_1

$tLAP_3$, truncated LAP_3

TMLC, transformed mink lung cell

UIP, usual interstitial pneumonia

α5β1, alpha-5 beta-1

αSMA, alpha-smooth muscle actin

α-SMA, alpha-smooth muscle actin

αvβ1, alpha-v beta-1

αvβ3, alpha-v beta-3

αvβ5, alpha-v beta-5

αvβ6, alpha-v beta-6

αvβ8, alpha-v beta-8

TABLE OF CONTENTS

Figures

Tables

CHAPTER 1: INTRODUCTION

1.1 Idiopathic pulmonary fibrosis

Fibrosis is the formation of scar tissue due to injury or long-term inflammation and is a leading cause of morbidity and mortality (Wynn, 2007). Fibrotic disorders include idiopathic pulmonary fibrosis (IPF), hepatic fibrosis and renal fibrosis and there are currently limited pharmacological therapeutic options for patients suffering from these diseases (O'Connell *et al.*, 2011; Gossard and Lindor, 2011). IPF is the most common of the idiopathic interstitial pneumonias (inflammatory condition of the interstitium, the tissue and space around the air sacs of the lungs, arising spontaneously or from an unknown cause) that has been classified by the American Thoracic Society (ATS), European Respiratory Society (ERS), Japanese Respiratory Society (JPS) and the Latin American Thoracic Association (ALAT) consensus statement (Raghu *et al.*, 2011) as "chronic, progressive fibrosing interstitial pneumonia of unknown cause, occurring primarily in older adults,... limited to the lungs... characterised by progressive worsening of dyspnea and lung function... associated with a poor prognosis". In the UK the incidence of IPF is 4.6 people per 100,000 per year with a similar value in the US of 6.8 people per 100,000 per year (O'Connell *et al.*, 2011), with 5,000 new cases diagnosed annually in the UK (Navaratnam *et al.*, 2011). In addition, 5,000 people in the UK with IPF die each year, which equates to more than the patients dying from ovarian cancer, lymphoma, leukaemia or kidney cancer (Navaratnam *et al.*, 2011) and this puts into perspective the need for further research into the disease and identification of new therapies.

Although research into this disease area has grown during the last decade, the exact cause remains unclear. The current hypothesis attributes the cause to an abnormal and dysfunctional interaction between the lung epithelium and mesenchyme whereby

injury of the alveolar epithelial cell population gives rise to an irregular wound healing process (Selman *et al.*, 2001). In a normal wound healing response a return to an intact epithelium post-injury is critical. Injury results in the release of a number of epidermal and fibroblast growth factors (transforming growth factor-β (TGFβ), hepatocyte growth factor, keratinocyte growth factor) as well as chemokines, interleukins and prostaglandins that contribute to a normal repair process. These serve to coordinate cell migration (of mesenchymal stem cells that proliferate and differentiate to aid restoration of epithelial function) via matrix materials (collagen, fibronectin), integrins and matrix metalloproteinases (MMP) (Crosby and Waters, 2010).

The abnormal wound healing associated with IPF (as depicted in Figure 1.1.1) is typified by atypical activation of epithelial cells via deregulation of embryological pathways such as the Wnt/wingless (Königshoff *et al.*, 2009) and sonic hedgehog pathways (Coon *et al.*, 2006). This leads to excessive extracellular matrix (ECM) deposition, wounding and fibroblast-myofibroblast foci formation (see Figure 1.1.2) that is followed by loss of lung architecture and normal respiratory function. However, the initiating stimulus for this injury and then subsequent abnormal repair still remains a mystery. It has been hypothesised that it is the result of an unidentified environmental stimulus affecting individuals genetically predisposed to the disease (Noth and Martinez, 2007). Conversely, although factors associated with IPF have been determined e.g. smokers are deemed to be at higher risk of the disease (Baumgartner *et al.*, 1997), a causal link between the disease and any environmental exposure has not been shown. Correspondingly, conclusive evidence from studies investigating genetic predisposition to IPF is yet to be obtained and is unaided by the

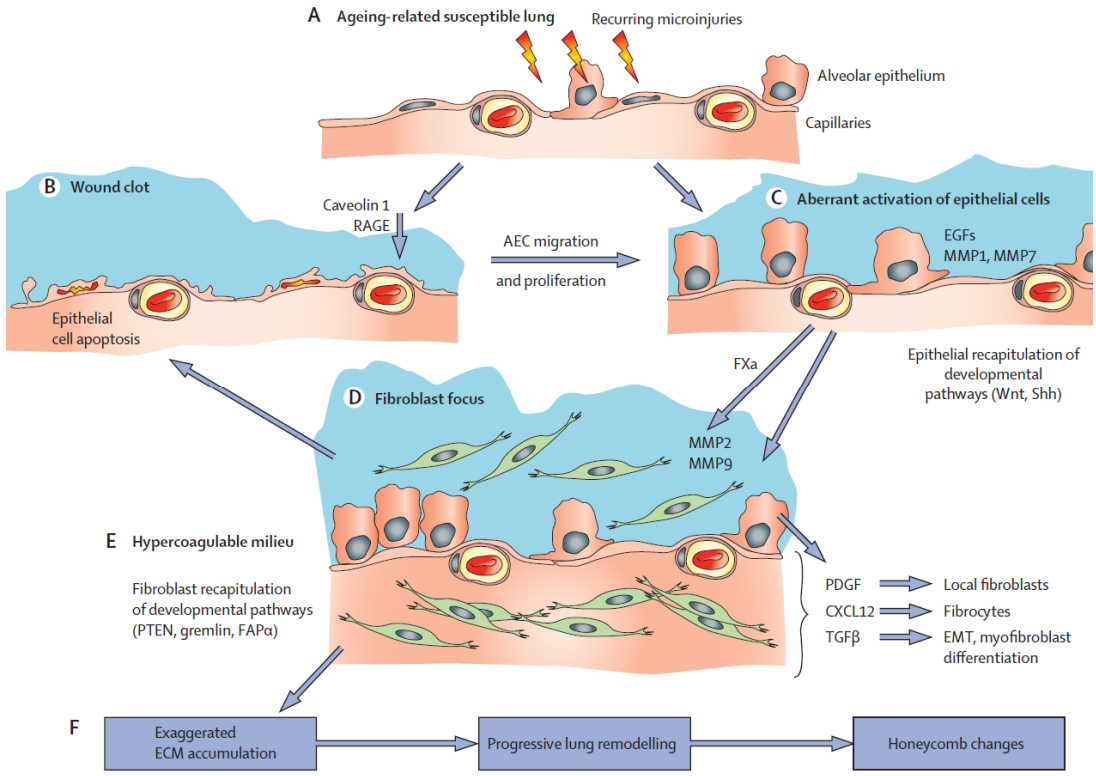

Figure 1.1.1 The current mechanisms proposed for the origin and development of IPF. Abnormal wound healing associated with IPF in an age-related susceptible lung (A) is typified by atypical activation of epithelial cells via deregulation of embryological pathways such as the Wnt/wingless and sonic hedgehog pathways (C). This leads to excessive extracellular matrix (ECM) deposition, wounding (B) and fibroblast-myofibroblast foci formation (D) that is followed by loss of lung architecture (B) and normal respiratory function (E and F). AEC, alveolar epithelial cell; CXCL12, CXC chemokine ligand 12; ECM, extracellular matrix; EGF, epidermal growth factor; EMT, epithelial-mesenchymal transition; FVIIa, Factor VIIa; FX, Factor X; FXa, Factor X activated; FAPα, fibroblast activation protein α; MMP, matrix metalloproteinase; PDGF, platelet-derived growth factor; PTEN, phosphatase and tensin homologue; RAGE, receptor for advanced glycation end products; Shh, sonic hedgehog; TF, tissue factor; TGFβ, transforming growth factor β (taken from King *et al.*, 2011).

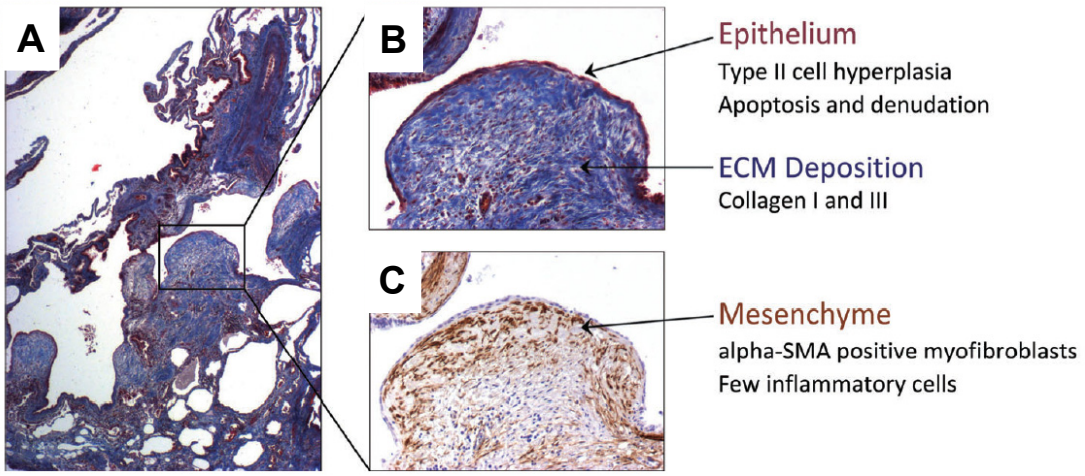

Figure 1.1.2 The fibroblast-myofibroblast fibrotic foci observed in histological lung samples obtained from IPF patients. Epithelial type II cells undergo hyperplasia and apoptosis resulting in denudation of the epithelial layer (A) and (B), accompanied by increased extracellular matrix (ECM) deposition of collagen I and III (B – blue stain). The mesenchyme is flooded with myofibroblasts positive for alpha-smooth muscle actin (α-SMA) (C – brown stain) but with limited inflammatory cells infiltrate (taken from Datta *et al.*, 2011).

difficulties in recruiting a sufficient patient population (Molina-Molina *et al.*, 2008). It has also been hypothesised that IPF is caused by an inflammatory cascade initiated following injury of the alveolar epithelium, however this now appears unlikely due the lack of activity displayed by anti-inflammatory and immunosuppressive therapy (O'Connell *et al.*, 2011).

From the time of diagnosis the median survival rate for an IPF patient is 2 to 5 years with the mean age of presentation being 66 years (Meltzer and Noble, 2008). A final diagnosis of IPF requires a number of criteria to be met (Molina-Molina *et al.*, 2010) depending on whether a surgical lung biopsy is completed demonstrating usual interstitial pneumonia (UIP). If a biopsy is taken then a diagnosis of IPF can be reached if other known causes of a UIP histological pattern can be excluded. This is required to be combined with suggestive high resolution computed tomography (HRCT) (see Figure 1.1.3) and abnormal restrictive pulmonary function studies (decreased forced vital capacity (FVC) or forced expiratory volume in 1 second). If no biopsy is obtained then the criteria for diagnosis are much greater in number and separated into major and minor criteria, of which all the major plus at least 3 minor criteria are required to be present in order to conclude a final diagnosis. The major criteria are: exclusion of other known causes of interstitial lung disease; abnormal restrictive pulmonary function studies; typical HRCT images demonstrating abnormalities of IPF; and no evidence to support an alternative diagnosis from either bronchoalveolar lavage (BAL) or transbronchial lung biopsy. All these need to be present including 3 of the following minor criteria: patient older than 50 years old; greater than 3 month duration of illness; inspiratory crackles (persistent rattling or crackling noises originating in or near the base of both lungs); and onset of

A

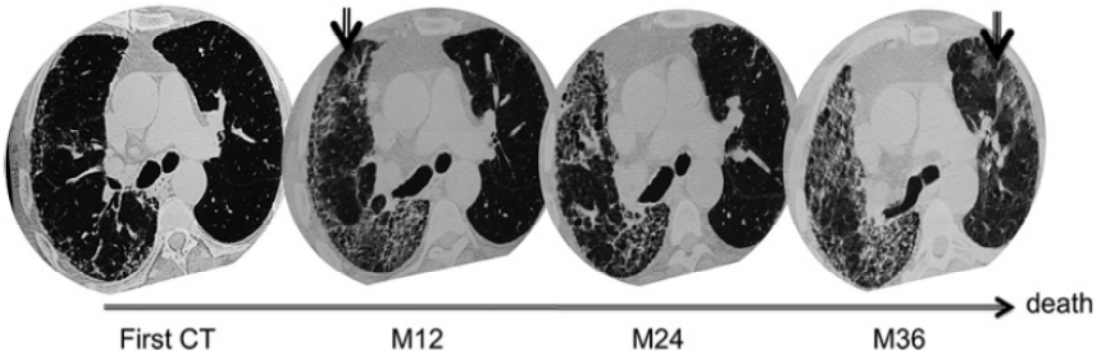

B

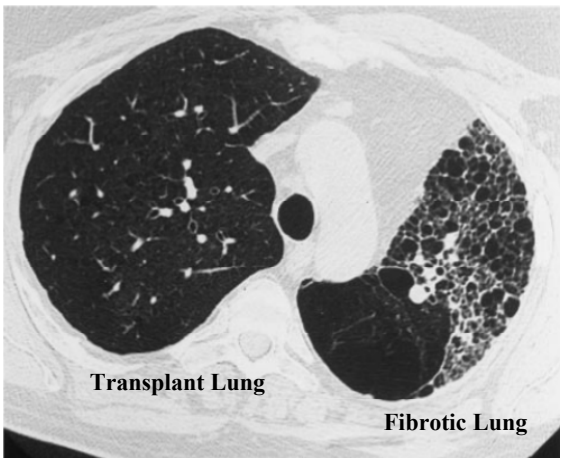

Figure 1.1.3 High resolution computed tomography images demonstrating the progression of IPF. (A) Arrows highlighting ground glass opacities (HRCT term describing a hazy area of increased attenuation in the lung that have preservation of bronchial and vascular markings) and honeycomb lesions, both suggestive of IPF. For distinction, a normal (transplant) compared with an IPF (fibrotic) lung is demonstrated on the HRCT image in (B) where a patient has undergone a single lung transplantation (Figure 2A and 2B taken from Tcherakian *et al.*, 2011 and Wahidi *et al.*, 2002 respectively). HRCT, high resolution computed tomography; M, months.

unexplained breathlessness following exertion, in order for IPF diagnosis to be confirmed.

The therapeutic options for IPF were limited up until the recent global approvals of pirfenidone and nintedanib (as detailed below), and lung transplantation offered the only treatment with a survival benefit to patients. Even with the emergence of promising therapies transplantation still remains the only option for the more severe patient populations who are unable to access the more recent efficacious pharmacological treatments (Costabel, 2015). However, the success of transplantation is dependent on numerous factors including the experience of surgeons and physicians at transplant centres as well as the risk of organ rejection. Transplant is also only reserved for a small population of patients who are deemed to be most appropriate for the procedure (criteria includes being less than 65 years old, absence of other major organ dysfunction and good nutritional state). The lack of availability of transplant lungs also contributes to it not being an option for the majority of IPF patients. In addition, the risk of organ rejection with a lung transplant results in patients being treated with immune-suppressants for the remainder of their lives making this a less than optimal treatment solution. In terms of historical pharmacological therapy for the treatment of IPF there has been no significant evidence from clinical trials completed on potential drugs to persuade the ATS/ERS/JPS/ALAT consensus statement (Raghu *et al.*, 2011) to give a clear and overwhelming recommendation. The design and implementation of clinical studies in IPF are still in their infancy and as detailed below the trials that have been completed for the most part have been on established drugs already licensed for non-fibrotic diseases. End points for measuring the success of an IPF clinical trial remain in the

majority of studies the mortality rate combined with pulmonary function studies (FVC, diffusing capacity of carbon monoxide) and quality of life scoring (Raghu *et al.*, 2011). However, as the understanding of the heterogeneous progression of IPF in the different clinical phenotypes improves and the data from historical clinical trials builds, the recruitment, design and execution of clinical trials going forward will be greatly enhanced. Due to the lack of clear evidence, the ATS/ERS/JPS/ALAT concensus statement strongly recommends that certain therapies are not used at all in the treatment of IPF. These include corticosteroid mono-therapy (anti-inflammatory via activation of glucocorticoid receptors and suppression of anti-inflammatory proteins that include annexin-1, interleukin-10, mitogen-activated protein kinase phosphatase-1 and I-κBα (Adcock and Lane, 2003)) and colchicines (anti-inflammatory via inhibition of neutrophils motility and activity by inhibiting the polymerisation of tubulin into microtubes and disrupting the cellular cytoskeleton (Ben-Chetrit *et al.*, 2005)) and cyclosporin A (immunosuppression via inhibition of T-cell activity by blocking the phosphatase activity of calcineurin (Ho *et al.*, 1996). Other contraindications include combined corticosteroid and immune-modulator therapy, interferon-γ 1b (recombinant interferon-γ that is an anti-inflammatory via numerous mechanisms including effects on leukocyte trafficking and T-cell activation following activation of the interferon-γ receptor (Schroder *et al.*, 2004)), bosentan (endothelin-1 receptor antagonist inhibiting the pro-fibrotic effects of endothelin-1 receptor A and B (Clozel and Salloukh, 2005)) and etanercept (anti-inflammatory via inhibition of tumor necrosis factor-α that mediates immune responses (Goffe and Cather, 2003)). In addition, where pharmacological therapies are advocated they are weakly backed and only for a minority of patients. These

include acetylcysteine mono-therapy (a mucolytic with antioxidant effects that were hypothesised to offer a potential therapeutic benefit in fibrosis (Zafarullah *et al.*, 2002)), combined acetylcysteine, azathioprine (immunosuppressive drug via anti-metabolic and pro-apoptotic mechanisms (Cara *et al.*, 2004)) and prednisone (corticosteroid). A significant proportion of the therapies trialled in IPF prior to 2011 have been either anti-inflammatory or immunosuppressant. This was based on the original theory that IPF is caused by an inflammatory cascade initiated following injury of the alveolar epithelium. The poor or lack of efficacy observed with agents such as corticosteroids and azathioprine suggest this theory was incorrect (or at least targeting this mechanism alone is insufficient) and it resulted in the field searching for new and more relevant therapeutic targets for IPF. This coupled with growing interest in IPF by many of the large pharmaceutical companies resulted in major breakthroughs in the treatment of IPF between 2011 and 2015 that are still yet to be captured in an updated ATS/ERS/JPS/ALAT concensus statement for the treatment of the disease.

The first of the major drug breakthroughs for IPF was the small molecule pirfenidone that historically had been shown to display analgesic, anti-pyretic and anti-inflammatory activity (Gan *et al.*, 2011). Again, as a result of its anti-inflammatory effects it was investigated in a range of *in vivo* models of fibrosis and these demonstrated a consistent anti-fibrotic activity related to reduction in TGFβ and collagen production (Schaefer *et al.*, 2011). However, pirfenidone's exact mechanism of action is still yet to be determined (Gan *et al.*, 2011). The US and European patent rights to pirfenidone were purchased by InterMune Inc. (acquired by Roche (UK) in August 2014) in 2007 who over the subsequent 7 years funded

numerous IPF clinical studies culminating in the phase III studies CAPACITY (Clinical Studies Assessing Pirfenidone in Idiopathic Pulmonary Fibrosis: Research of Efficacy and Safety Outcomes) and ASCEND (Assessment of Pirfenidone to Confirm Efficacy and Safety in Idiopathic Pulmonary Fibrosis). It was shown in these studies that in IPF patients pirfenidone reduced the progression of disease compared with placebo (King *et al.*, 2014). This was demonstrated by the measurement of lung function (FVC), exercise tolerance (6 minute walk distance) and progression-free survival. However, over combined studies the adverse events profile observed for pirfenidone has been observed to be poor with gastrointestinal (GI) (gastrointestinal upset, nausea, vomoting, dyspepsia and diarrhoea) and dermatological related (photosensitivity, rash and pruritus) side effects shown to be the most common (Jiang *et al.*, 2012; King *et al.*, 2014).

At a similar time to the phase III studies for pirfenidone, nintedanib (a small molecule tyrosine kinase inhibitor formerly known as BIBF 1120) was also at a comparable stage of clinical development. Nintedanib had originally been developed by Boehringer Ingelheim Inc. (Germany) for the treatment of various solid tumours by inhibiting the pro-angiogenic pathways of the vascular endothelial growth factor, fibroblast growth factor receptor and platelet-derived growth factor receptor families as well as the Src and Flt-3 kinases (Roth *et al.*, 2015). Following the implication of these growth factors in fibrosis (Chaudhary *et al.*, 2007), nintedanib was re-positioned as a potential therapeutic in IPF that culminated in the INPULSIS™ phase III clinical trials. These studies demonstrated that nintedanib slowed the progression of IPF as measured by reduction in the FVC of patients compared with placebo groups, however with a high rate (61.5 %) of diarrhoea being observed (Richeldi *et*

al., 2014). The side effect profiles demonstrated by pirfenidone and nintedanib in clinical trials (Taniguchi *et al.*, 2010; Richeldi *et al.*, 2011; King *et al.*, 2014; Richeldi *et al.*, 2014) combined with these therapeutics not being available to all patient populations (Costabel, 2015), makes them less than optimal stand-alone treatments suggesting there is still room for therapeutic improvement within this disease area. As such, there is still the requirement for improved treatments that have reduced side effects and improved efficacy that could be taken in addition to or as a replacement to the current standard of care provided for some IPF patients by pirfenidone and nintenanib.

One of the primary candidates as a drug target for IPF is TGFβ1 due to the overwhelming evidence showing it to be a key player in fibrotic disease both *in vitro* and *in vivo* (reviewed in more detail in section 1.2). Direct TGFβ1 inhibition aside, there are also a number of other targets currently under investigation either at the bench or in clinical experiments. These include but are not limited to connective tissue growth factor (CTGF), interleukin-13 (IL-13) and lysophosphatidic acid (LPA). CTGF is a chemoattractant and fibroblast mitogen and its expression has been shown to be increased in the BAL fluid from IPF patients (Allen *et al.*, 1999) and to cause tissue fibrosis when selectively expressed in fibroblasts *in vivo* (Sonnylal *et al.*, 2010). Although its receptor and signalling pathway is yet to be fully elucidated, there is currently a CTGF-neutralising antibody (FG-3019, Fibrogen, USA) in Phase II trials for IPF. BAL samples from IPF patients have also been shown to contain increased levels of the Th2 cytokine IL-13 (Hancock *et al.*, 1998) and, *in vitro* IL-13 promotes the apoptosis of epithelial cells (Borowski *et al.*, 2008). As such an antibody approach targeting IL-13 was chosen by AstraZeneca (UK) with

the anti-IL-13 antibody tralokinumab in Phase II clinical trials for IPF. LPA is a phospholipid derivative and an endogenous agonist for the eight G-protein coupled receptor (GPCR) subtypes LPA1-8. The target validation generated for LPA includes increased levels of LPA in BAL fluid in patients with IPF (Tager *et al.*, 2008). In addition, the LPA1 and 2 receptors have both been identified as potentially playing a role in lung fibrosis with LPA1 activation resulting in fibroblast recruitment in a mouse model of induced lung injury (Tager *et al.*, 2008) and increased LPA2 immunoreactivity observed in IPF lung samples (Xu *et al.*, 2009). As a consequence Bristol-Myers Squibb (USA) are currently developing an LPA1 antagonist (AM152) that has successfully completed Phase I trials and is currently heading into Phase II. In addition, there are also potential therapies being developed to target the ECM and the regulation of its structure and function in fibrotic disorders (Bonnans *et al.*, 2014). This includes the antibody simtuzumab that targets the matrix enzyme lysyl oxidase-like 2 (LOXL2) (Barry-Hamilton *et al.*, 2010) that is being investigated clinically in a Phase II IPF trial.

1.2. Transforming growth factor-β and its role in IPF

One of the leading drug targets currently being investigated for IPF, both clinically and pre-clinically is the cytokine TGFβ. TGFβ exists in three highly homologous (70-80 %) isoforms TGFβ1, TGFβ2 and TGFβ3 with differences only observed in a limited number of amino acid regions (Kubiczkova *et al.*, 2010). They have been shown to all exert their functional effects via the same receptor and signalling pathways (Cheifetz *et al.*, 1987; Mittl *et al.*, 1996). All the TGFβ isoforms are

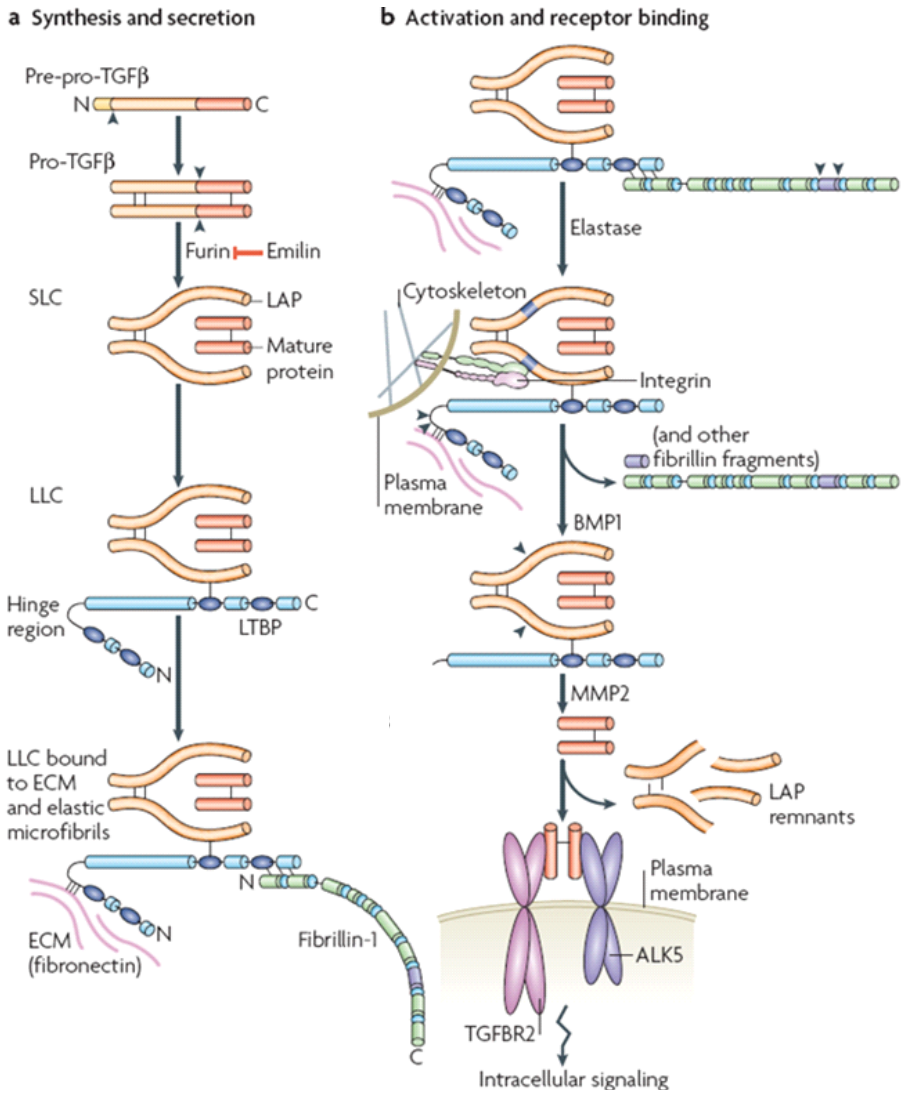

Figure 1.2.1 The synthesis, secretion, activation and receptor binding of transforming growth factor-β. TGFβ exists in three highly homologous isoforms TGFβ1, TGFβ2 and TGFβ3 that are all synthesised as precursors. A larger complex, referred to as the large latent complex (LLC), is formed between a TGFβ isoform homodimer, a latency-associated peptide (LAP) and a latent TGFβ-binding protein (LTBP). The TGFβ isoform homodimer is bound to LAP via a non-covalent association and the LTBP is bound to LAP via a disulphide bond. LTBP is able to associate with the ECM via an interaction between its N-terminal and hinge region. The activation of TGFβ from its inactive form within the LLC can occur either via proteolysis, extreme pH changes or mechanical stretch following binding of the LAP component of the large complex to plasma membrane-bound integrin receptors. The enzymes MMP2 and MMP9 as well as thrombospondin 1 have been shown to activate TGFβ via proteolytic cleavage whilst integrins play a role in activation following mechanical stretch. ALK5, Activin-like kinase-5 (also referred to as TGFβ receptor I); BMP1, Bone morphogenetic protein-1; ECM, Extracellular matrix; LAP, Latency associated peptide; LLC, Large latent TGFβ complex; LTBP, Latent TGFβ binding peptide; MMP2, Matrix metalloprotease-2 (MMP2); SLC, Small latent TGFβ complex; TGFβ, Transforming growth factor β; TGFβR2, TGFβ receptor II (adapted from ten Dijke and Arthur, 2007).

synthesised as precursors in a larger complex referred to as the large latent complex (LLC). The LLC is formed between a TGFβ isoform homodimer, a latency-associated peptide (LAP) and a latent TGFβ-binding protein (LTBP) (as depicted in Figure 1.2.1) (ten Dijke and Arthur, 2007). The TGFβ isoform homodimer is bound to LAP (that is individual to each TGFβ isoform – LAP_1 for TGFβ1, LAP_2 for TGFβ2 and LAP_3 for TGFβ3) via a non-covalent association and the LTBP is bound to LAP via a disulphide bond. LTBP is able to associate with the ECM via binding of the LTBP hinge region with matrix molecules and it has been shown that fibronectin binds to LTBP during TGFβ1 activation (Fontana *et al.*, 2005). The activation of TGFβ from its inactive form within the LLC can occur either via proteolysis, extreme pH changes (Lyons *et al.*, 1988) or mechanical stretch following binding of the LAP component of the large complex to plasma membrane-bound integrin receptors. The enzymes MMP2 and MMP9 (Wang *et al.*, 2006; Yu and Stamenkovic, 2000) as well as thrombospondin 1 (Schultz-Cherry *et al.*, 1994) have been shown to activate TGFβ via proteolytic cleavage whilst both the alpha-v beta-5 (αvβ5) and alpha-v beta-6 (αvβ6) integrins play a role in activation following mechanical stretch (Margadant and Sonnenberg, 2010).

Subsequent to activation, free TGFβ is released from the LLC and can bind the transmembrane TGFβ receptor II (TGFβRII) (a member of the type II serine/threonine receptor family). This in turn results in the recruitment of and heterodimerisation with the TGFβ receptor I (TGFβRI) (a member of the type I serine/threonine receptor family also known as activin receptor-like kinases (ALKs)). This heterodimerisation initiates signalling by transphosphorylation of the TGFβRI by the TGFβRII that can be subsequently transmitted into the cell via either a

canonical (Sma and Mad related protein (SMAD)-dependent) or non-canonical TGFβ pathway. The SMAD-dependent pathway is depicted in Figure 1.2.2 where the phosphorylation of TGFβ receptor-specific SMADs takes place.

Post-phosphorylation the receptor-specific SMADs (or R-SMADs), SMAD2 and SMAD3, form a heterodimeric complex and translocate into to the nucleus with the common mediator SMAD (coSMAD), SMAD4. Upon entry into the nucleus the R-SMAD/co-SMAD complex binds with high affinity and specificity to the genomic SMAD-binding element (SBE) sequence, requiring additional DNA binding transcription factors that associate with specific sequences flanking the SBE (Shi and Massague, 2003). Although the R-SMADs primary function is the regulation of transcription they have also been shown to control the biogenesis of microRNA (Figure 1.2.2) (Davis-Dusenbery and Hata, 2011). The SBE sequence has been shown to be located in the promoter regions of a number of pro-fibrotic genes that include alpha-smooth muscle actin (αSMA), fibronectin and type I collagen (Castelino and Varga, 2010). In addition, mice deficient in SMAD3 are protected from bleomycin-induced lung fibrosis that demonstrates the pro-fibrotic effects as a consequence of canonical TGFβ pathway activation (Zhao *et al.*, 2002).

The non-canonical TGFβ pathways activated following binding of TGFβ to its receptors include mitogen-activated protein kinases (family includes p38, c-Jun NH_2-terminal kinase (JNK) and extracellular signal-regulated kinase (ERK)), phosphoinositide 3-kinase and nuclear factor-κB (Figure 1.2.3). In lung fibroblasts the mitogen-activated protein kinase (MAPK) family members JNK and ERK have been shown to induce αSMA and collagen production (Hu *et al.*, 2006; Caraci *et al.*,

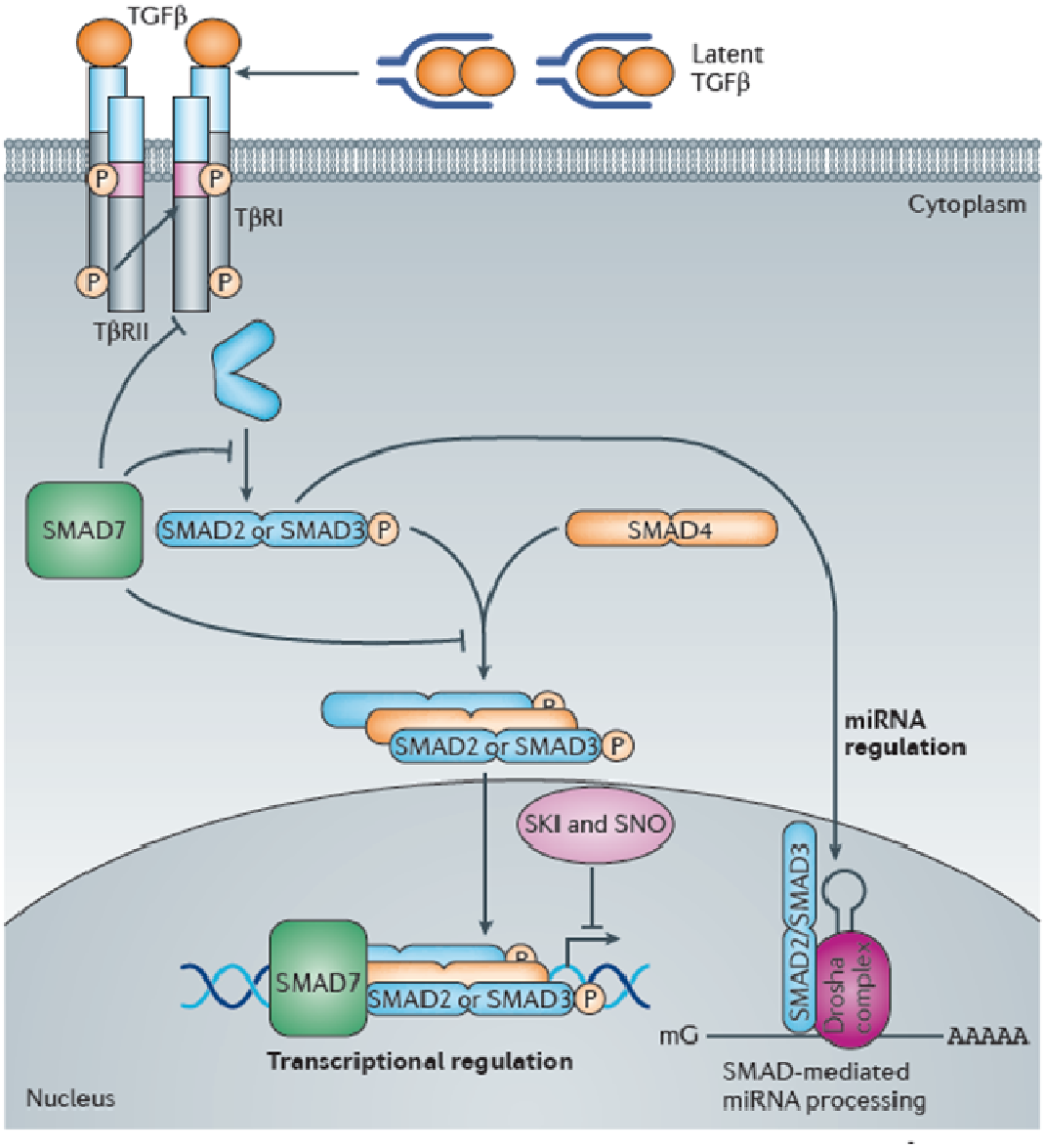

Figure 1.2.2 Schematic depicting the core canonical TGFβ-SMAD signalling pathway. Free TGFβ is released from the large latent TGFβ complex and can bind the transmembrane TGFβ receptor II (TGFβRII). This in turn results in the recruitment of and heterodimerisation with the TGFβ receptor I (TGFβRI). This heterodimerisation initiates signalling by transphosphorylation of the TGFβRI by the TGFβRII that can be subsequently transmitted into the cell via phosphorylation of TGFβ receptor-specific SMADs. Post-phosphorylation the receptor-specific SMADs (or R-SMADs), SMAD2 and SMAD3, form a heterodimeric complex and translocate into to the nucleus with the common mediator SMAD (coSMAD), SMAD4. Upon entry into the nucleus the R-SMAD/co-SMAD complex binds with high affinity and specificity to the genomic SMAD-binding element (SBE) sequence, requiring additional DNA binding transcription factors that associate with specific sequences flanking the SBE. Inhibitors of the different stages of the pathway are also shown (SMAD7 and the nuclear proteins SKI and SNO). AAAAA, represents 3' polyadeylation of mRNA; mG, represents 5' capping of mRNA; miRNA, microRNA; SMAD, Sma and Mad protein; TGFβ, Transforming growth factor β; TβRI, TGFβ receptor I; TβRII, TGFβ receptor II (taken from Akhurst and Hata, 2012).

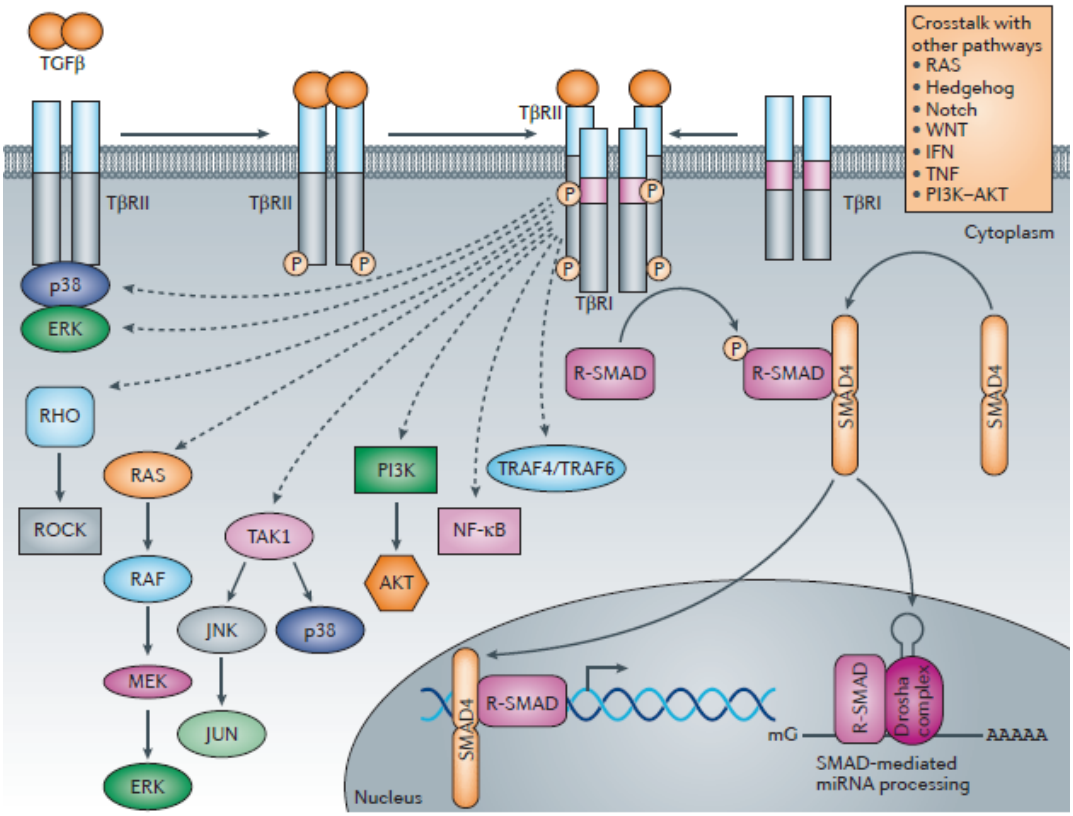

Figure 1.2.3 Schematic depicting the non-canonical TGFβ signalling pathways. Free TGFβ is released from the large latent TGFβ complex and can bind the transmembrane TGFβ receptor II (TGFβRII). This in turn results in the recruitment of and heterodimerisation with the TGFβ receptor I (TGFβRI). This heterodimerisation initiates signalling by transphosphorylation of the TGFβRI by the TGFβRII that can be subsequently transmitted into the cell through the non-canonical TGFβ signalling pathways. These include signalling via activation of p38, ERK, RHO, RAS, TAK1, PI3K, NF-κB and TRAF4/TRAF6. The canonical TGFβ-SMAD pathway is also shown (bottom right) as well as the other crosstalk pathways capable of influencing the canonical and non-canonical TGFβ pathways (box top right). AAAAA, represents 3' polyadeylation of mRNA; AKT, protein kinase B; ERK, extracellular signal-regulated kinase; IFN, interferon; JNK, JUN N-terminal kinase; MEK, mitogen-activated protein kinase kinase; mG, represents 5' capping of mRNA; miRNA, microRNA; NF-κB, nuclear factor-κB; p38, p38 mitogen-activated protein kinase; PI3K, phosphoinositide 3-kinase; RAF, rapidly accelerated fibrosarcoma; RAS, rat sarcoma; ROCK, RHO-associated protein kinase; R-SMAD, receptor-specific SMAD; SMAD, Sma and Mad protein; TAK1, TGFβ-activated kinase 1; TGFβ, Transforming growth factor β; TNF, tumour necrosis factor; TRAF4, TNF receptor associated factor 4; TRAF6, TNF receptor associated factor 6; TβRI, TGFβ receptor I; TβRII, TGFβ receptor II (taken from Akhurst and Hata, 2012).

2008) whilst p38 has been demonstrated to provide resistance to apoptosis (Horowitz *et al.*, 2004). In addition to this, other signalling pathways (including the Ras and Wnt) have been shown to crosstalk with both the canonical and non-canonical TGFβ pathways (Guo and Wang, 2009).

It is clear that the complexity of TGFβ signalling, in addition to the crosstalk with other pathways, can result in modulation of gene expression that will result in a wide range of spatially and temporally specific biological effects (Akhurst and Hata, 2012). These are known to include inhibition of cell proliferation, epithelial-mesenchymal transition (EMT) induction, fibroblast phenotypic differentiation into myofibroblasts, ECM regulation, immune-suppression and inflammation (Khalil *et al.*, 1996; Koli *et al.*, 2008; Fernandez and Eickelberg, 2012). Consequently, any loss in the normal regulation of TGFβ has the potential to result in a disease state that will be cell/tissue specific within the body. The biological effects of the three TGFβ isoforms are varied and this is best demonstrated by the studies on knockout mice that show very different phenotypes. Although no significant abnormal development was evident in the TGFβ1 knockout mice, approximately 20 days post-birth organ failure and death was observed attributed to generation of a wasting syndrome coupled with an inflammatory cell response and tissue necrosis (Shull *et al.*, 1992). In contrast, TGFβ2 knockout mice display perinatal mortality shortly before, during or within minutes of birth due to a wide range of defects (Sanford *et al.*, 1997), whilst in the TGFβ3 knockout mortality is observed within 20 hours of birth due to an immature pulmonary phenotype (Kaartinen *et al.*, 1995). In addition, expression of the isoforms is also distinct and dependent on tissue (Millan *et al.*, 1991). Although the TGFβ isoforms share signalling pathways it is clear that the difference

in tissue expression and the complexity of signalling pathways that exists, may explain the very different phenotypes displayed in knockout mice and the extrapolations that have been made into predicting specific roles in human disorders.

The TGFβ1 isoform has been shown to be a major contributor in the fibrogenesis of IPF, as well as many other fibrotic disorders. One of the key pieces of evidence in the human disease setting is the high levels of TGFβ1 (compared with TGFβ2 and 3) present in the lungs of IPF patients (Khalil *et al.*, 1996) and these findings are also observed in animal models of lung fibrosis (Hoyt and Lazo, 1988; Coker *et al.*, 1997). In addition, pulmonary fibrosis induced by bleomycin in rodent *in vivo* models has been shown to be attentuated by ALK5 (TGFβRI) inhibitors (Bonniaud *et al.*, 2005; Higashiyama *et al.*, 2006). The key cell types involved in the pathogenesis of IPF have been shown to be epithelial cells and fibroblasts (see section 1.1), and there is a significant body of evidence that TGFβ1 has a substantial effect upon these. Epithelial cells have been shown to undergo migration (Yu *et al.*, 2008), EMT (Kim *et al.*, 2006) and apoptosis (Hagimoto *et al.*, 2002) due to TGFβ1, whilst effects on fibroblasts include increased collagen synthesis and ECM production, proliferation and transformation into myofibroblasts (Chambers *et al.*, 2003; Raghow *et al.*, 1987). In addition, TGFβ has also been shown to reduce the expression of tissue inhibitor of metalloproteinase and induce the production of MMP2, MMP9 and plasminogen inhibitor-1 (PAI-1) (Derynck *et al.*, 2001) that have all been implicated in IPF (Ramos *et al.*, 2001; Senoo *et al.*, 2010). All these data strongly suggest a key role of TGFβ1 in the pathogenesis of IPF and therefore it is an obvious cytokine to target with therapeutic agents for the disease. Numerous therapeutic approaches have been taken to target TGFβ for a number of fibrotic and non-fibrotic disorders. These

include generating antibodies to bind and reduce the available TGFβ, decreasing its activation, inhibiting its signalling pathway or direct blockade of the TGFβRI or II (Ackhurst and Hata, 2012). However, the majority of these approaches are accompanied with the potential negative side effects of globally blocking TGFβ due to the many key roles it plays in the body. It is clear from knockout mice studies and the wealth of literature generated on TGFβ that global inhibition could result in auto-immune responses and an inability to effectively control inflammation. In addition, a number of on-target toxicology effects have been observed with ALK5 inhibitors that include the formation of heart valve lesions (Anderton *et al.*, 2011). Therefore, in order to negate these risks in IPF treatment, one strategy would be to endeavour to only block the TGFβ1 effects in the local environment of the fibrotic foci.

1.3. The alpha-v beta-6 integrin receptor as a therapeutic target in IPF

Integrins are heterodimeric, transmembrane glycoprotein receptors that have a primary function to act as signalling proteins in mammals (Hynes, 1987). They are made up of an α and β-subunit, of which in mammals there are 18 and 8 variants respectively (see Figure 1.3.1) that can make up to 24 heterodimers (Hynes, 2002). The α and β-subunits are bound in a noncovalent complex that forms the ligand binding site and their primary role is to act as adhesion receptors. In order to fulfil this role they have the ability to signal in both directions across the plasma membrane so called ‘inside-out’ signalling (Faull and Ginsberg, 1996), by either binding extracellular ligands or interacting with the cytoskeleton via their intracellular domains.

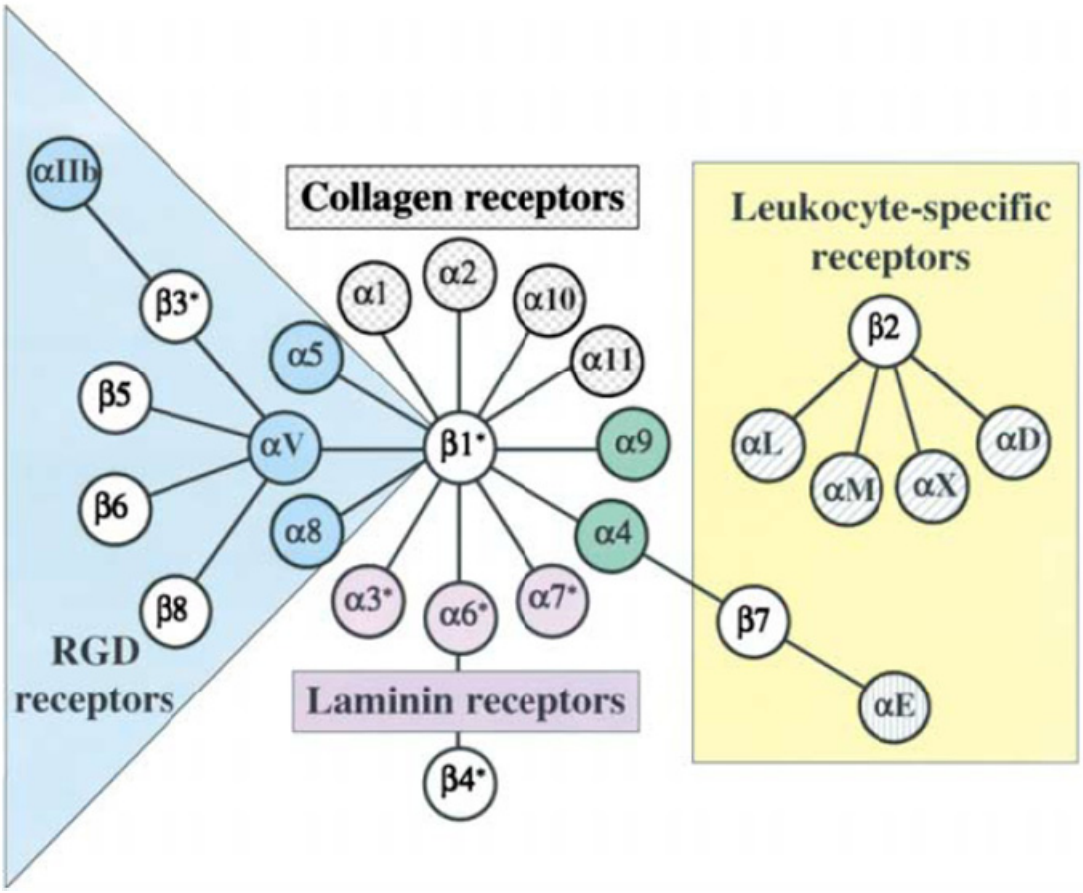

Figure 1.3.1 The integrin receptor family. The RGD or arginyl-glycinyl-aspartic acid represents the single letter amino acid code for arginine (R), glycine (G) and aspartic acid (D), the amino acid sequence binding motif shared by the endogenous ligands for this integrin sub-family (taken from Hynes, 2002).

The heterodimer structure comprising of one α- and one β-subunit is depicted in cartoon form in Figure 1.3.2 and is based upon the crystal structures that have been solved for a number of integrins (Lau *et al.*, 2009; Dong *et al.*, 2012). Both subunits are characterised by a large extracellular ectodomain (made up of a number of different components), a single transmembrane helix and a short intracellular cytoplasmic domain. Integrins can exist in both activated (upright conformation) and inactivated (bent conformation) states where they demonstrate a high and low affinity for ligands respectively (Figure 1.3.2). Activation can occur via a number of mechanisms that include extracellular ligand binding (referred to as 'outside-in' signalling), intracellular β-integrin tail activation (referred to as 'inside-out' signalling) and divalent cation occupancy of the ligand-binding pocket. The bi-directional signalling displayed by integrins makes them an essential receptor family to enable human cells to respond to changes in the extracellular environment ('outside-in' signalling) but also able to influence the extracellular environment ('inside-out' signalling). Information from the extracellular environment is communicated into cells via ligand binding to integrins resulting in changes in cell polarity, cytoskeletal structure, gene expression and cell survival and proliferation (Shattil *et al.*, 2010). In addition, ligand binding shifts the integrin affinity state from low (inactive) to high (active). In the opposite direction, intracellular activators such as talin are able to bind to the cytoplasmic tail of the β-subunit evoking a conformational change that shifts the integrin to a high affinity state more readily able to bind extracellular ligands enabling cell migration and ECM assembly and remodelling (Calderwood *et al.*, 2013). In addition to these activation mechanisms, divalent metal cations (Ca^{2+}, Mg^{2+} and Mn^{2+}) are not only a pre-requisite of binding

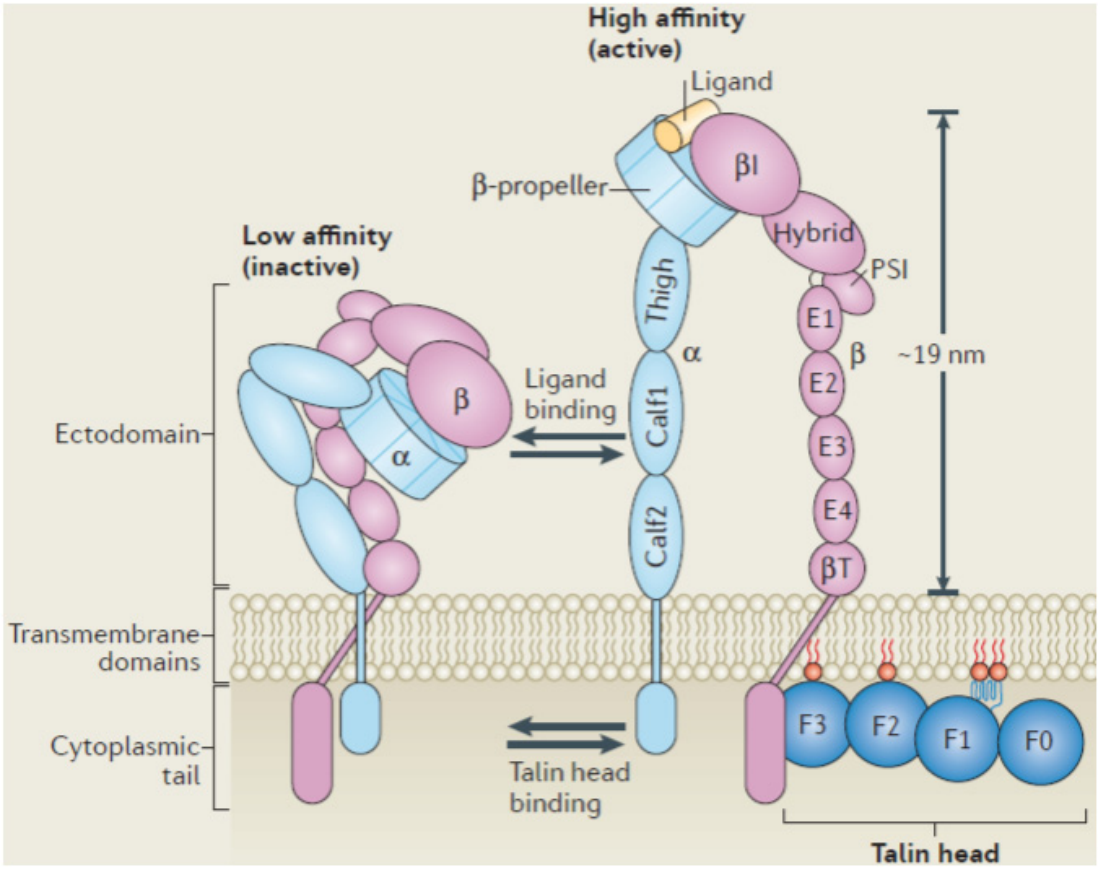

Figure 1.3.2 Structure and activation states of integrin receptors. Integrins can exist in both activated and inactivated states where they demonstrate a high and low affinity for ligands respectively (taken from Calderwood *et al.*, 2013). Activation can occur via a number of mechanisms that include extracellular ligand binding (referred to as 'outside-in' signalling), intracellular β-integrin tail activation (referred to as 'inside-out' signalling) and divalent cation occupancy of the ligand-binding pocket (Tiwari *et al.*, 2011). βI, βI domain; E1, ectodomain-1; E2, ectodomain-2; E3, ectodomain-3; E4, ectodomain-4; F0, FERM (F for 4.1 protein and E for ezrin) domain 0; F1, FERM domain-1; F2, FERM domain-2; F3, FERM domain-3; PSI, plexin-semaphorin-integrin domain.

of integrin ligands (Luo *et al.*, 2007), but can also influence the activation state (Tiwari *et al.*, 2011). Multiple binding sites for divalent metal cations within the βI domain of the integrin β-subunit have been identified including the metal ion-dependent adhesion site (MIDAS), adjacent to metal ion-dependent adhesion site (ADMIDAS) and ligand-induced metal ion-binding site (LIMBS) (Luo *et al.*, 2007). MIDAS physiologically binds Mg^{2+} that is required for ligand binding whilst LIMBS functions as a positive regulatory site (Chen *et al.*, 2003) and ADMIDAS as a negative regulatory site (Mould *et al.*, 2003). Mn^{2+} for the majority of integrins increases ligand binding affinity whilst Ca^{2+} can increase or decrease depending on the concentration and which of the LIMBS or ADMIDAS it engages (Luo *et al.*, 2007).

The integrin family is split into sub-families that consist of receptors with related properties. The arginyl-glycinyl-aspartic acid (RGD) sub-family of integrins (Figure 1.3.1) share an amino acid binding motif (arginine (R), glycine (G) and aspartic acid (D)) in their endogenous ligands, with selectivity for these ligands determined by their surrounding amino acid sequences (Ruoslahti, 1996). These endogenous RGD ligands include fibronectin, vitronectin, fibrinogen, von Willebrand factor, thrombospondin, laminin, tenascin, osteopontin and LAP.

Within the RGD family of integrins, αvβ6 has been identified as playing a role in the activation of TGFβ1 from the constitutively expressed latent TGFβ1 (Figure 1.3.3), and with this having such a pivotal role in IPF (see section 1.2), this integrin is a potential therapeutic target for this disease. αvβ6 activation of TGFβ1 from the constitutively expressed latent TGFβ1 occurs post-binding of the RGD sequence,

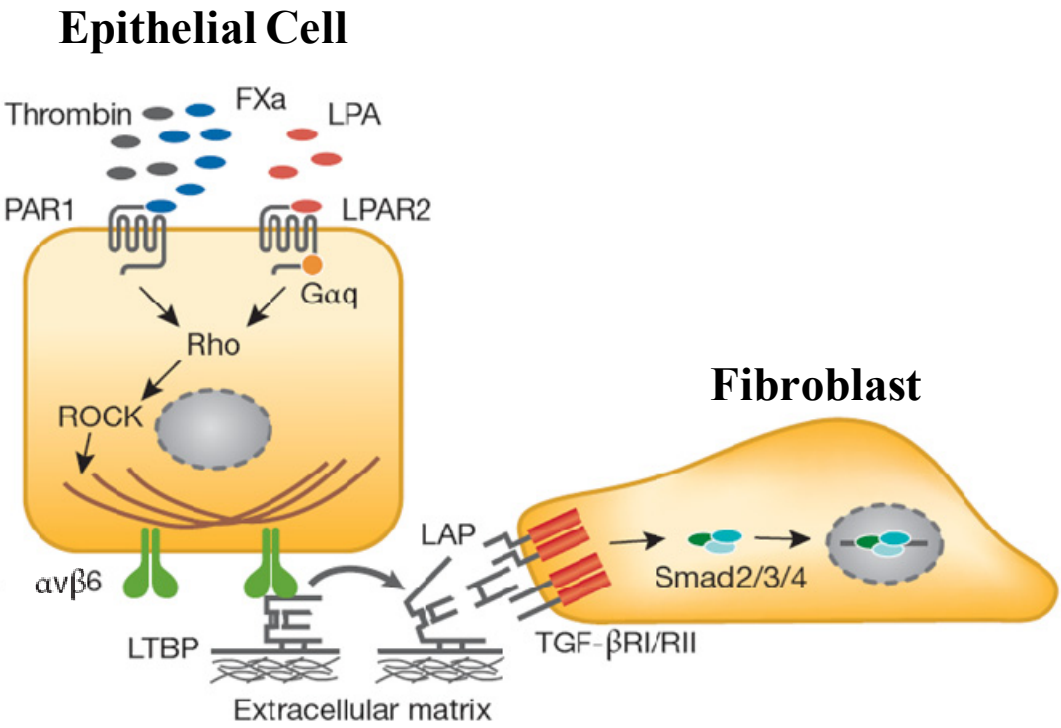

Figure 1.3.3 The activation of TGFβ by the αvβ6 RGD integrin. αvβ6 activation of TGFβ1 from the constitutively expressed latent TGFβ1 occurs post-binding of the RGD sequence, located in the LAP_1 component of the LLC, to the RGD binding site located in the interface between the αv and β6 integrin subunit. This interaction results in the β6 cytoplasmic domain binding to intracellular actin cytoskeleton that, when activated by mechanical stretch induced by cell contraction, induces a conformational change of the LLC and presentation of active TGFβ1 to its receptors evoking canonical TGFβ signalling. FXa, Coagulation factor X; Gαq, G-protein αq; LAP, Latency associated peptide; LPA, Lysophosphatidic acid; LPAR2, Lysophosphatidic acid receptor 2; LTBP, Latent TGFβ binding protein; PAR1, protease-activated receptor 1; ROCK, Rho-associated kinase; SMAD, Sma and Mad protein; TGFβ, Transforming growth factor β; TGFβRI/II, TGFβ receptor I/II complex (adapted from Margadant and Sonnerberg, 2010).

located in the LAP_1 component of the LLC, to the RGD binding site located in the interface between the αv and β6 integrin subunits (Goodwin and Jenkins, 2009). This interaction results in the β6 cytoplasmic domain binding to intracellular actin cytoskeleton that, when activated by mechanical stretch, induces a conformational change in the LLC and presentation of active TGFβ1 to its receptors evoking canonical TGFβ signalling (Munger *et al.*, 1999; Xu *et al,*. 2009; Tatler and Jenkins, 2012). Recently, the crystal structure for αvβ6 has been resolved by Dong and co-workers in the absence and presence of a TGFβ3 peptide (Dong *et al.*, 2014). This showed for the first time via crystallography the engagement of the αvβ6 integrin with an endogenous ligand (Figure 1.3.4) in addition to revealing the key βI-domain loops (designated specificity-determining loops 1, 2 and 3) that contributed to the specificity of ligand binding.

αvβ6 is an epithelial-restricted integrin that was first identified in the early 1990s (Busk *et al.*, 1992) and demonstrates a high affinity for fibronectin, tenascin, LAP_1 and LAP_3 (LAP_2 does not contain an RGD binding motif (Sheppard, 2008)). In the epithelia of healthy adults the global expression of αvβ6 is relatively low with the exception of the GI tract (Sipos *et al.*, 2004), the endometrium during the menstrual cycle (Huang *et al.*, 1996), and diffuse expression associated with subclinical inflammation in the lung and kidney (Breuss *et al.*, 1995). Upon injury or inflammation the expression of αvβ6 is observed to be upregulated significantly on epithelial cells. This has been shown in a range of diseases and organs that include acute lung injury and IPF (Breuss *et al.*, 1995; Horan *et al.*, 2008), fibrosis of the liver and kidney (Popov *et al.*, 2008; Sheppard, 2004), carcinomas of the breast,

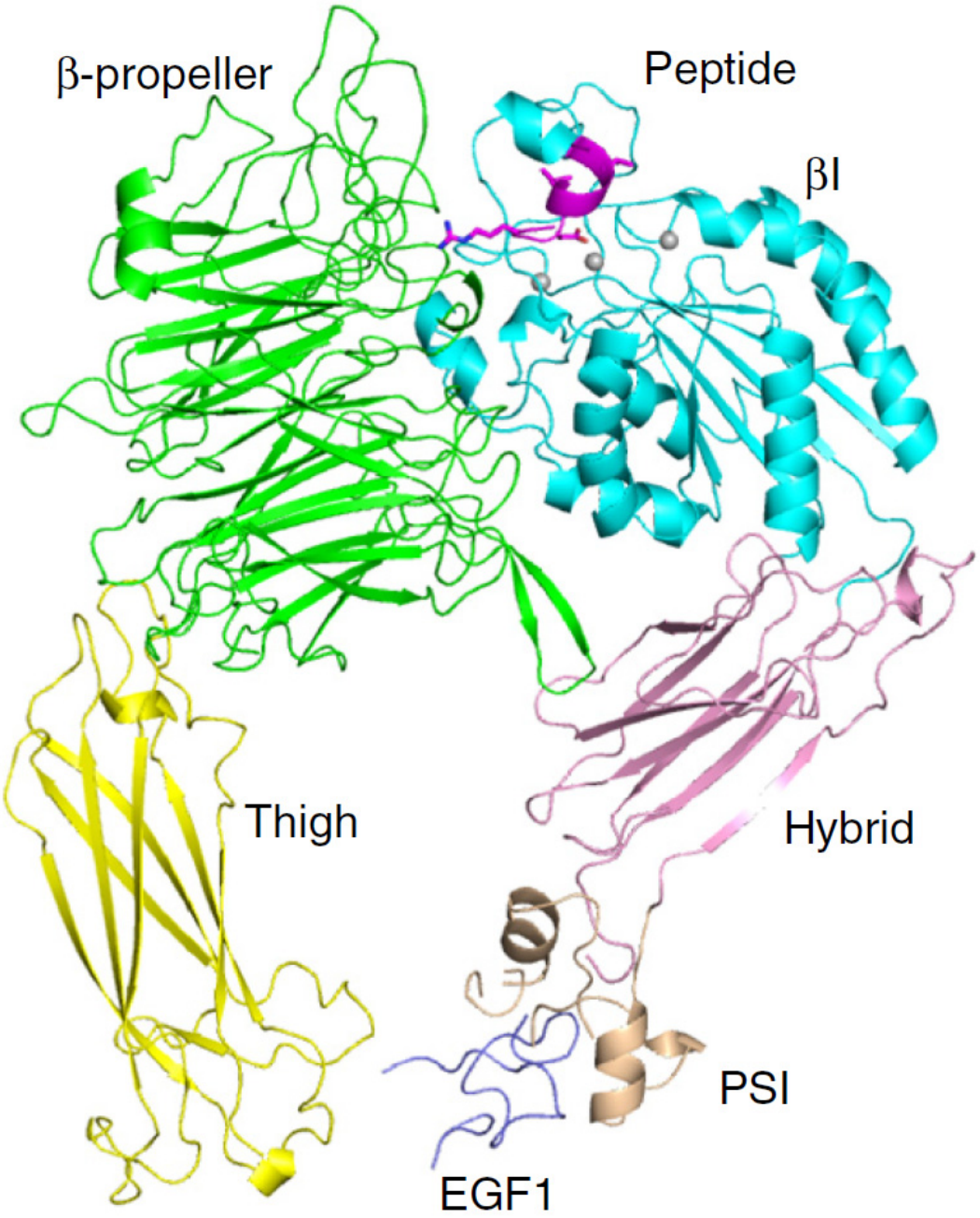

Figure 1.3.4 Ribbon diagram of the αvβ6 integrin headpiece in the presence of pro-TGFβ3 peptide as determined via crystallography. The integrin domains within the αvβ6 integrin headpiece are shown in different colours with the pro-TGFβ3 peptide shown in magenta (adapted from Dong *et al.*, 2014). βI, βI domain; EGF1, epidermal growth factor-like domain-1; PSI, plexin-semaphorin-integrin domain.

lung, mouth, skin, colon, stomach and endometrium among others (Bandyopadhyay and Raghavan, 2009). The low global expression of αvβ6 in the healthy human adult would suggest that knockout β6 mice may be relatively unaffected by its genetic mutation, if the mouse is predictive of human. As such, in the knockout β6 mouse model demonstrated by Huang and co-workers (Huang *et al.*, 1996) no embryonic or post-natal lethality was observed, in contrast to the TGFβ1-3 knockouts. The primary observations in this phenotype were shown to be juvenile baldness (as a result of macrophage infiltration in response to low-level injury), lymphocyte activation and accumulation in the lungs as well as hyperesponsiveness to acetylcholine in the airways (Huang *et al.*, 1996). This implicated αvβ6 as playing a role in the regulation of inflammation in the lung and skin, with low level injury shown not to be resolved normally. However, none of the effects observed resulted in significant abnormalities or a lethal outcome with a healthy phenotype observed up to 6 months with mice gaining weight normally and shown to be fertile. Although not conclusive in terms of cross-over into human subjects, the β6 knockout mouse suggests that if αvβ6 was targeted as a therapeutic in IPF the potential for side effects by blocking a basal level of the receptor outside of the lung would be negligible. The only concern would be the function of αvβ6 suppressing alveolar macrophage activation as there is the potential that via uncontrolled MMP12 production (and subsequent macrophage activation), inhibition of αvβ6 could result in emphysema (Morris *et al.*, 2003). However, it has been demonstrated with a proposed selective αvβ6 therapeutic antibody (Horan *et al.*, 2008) that there is a clear therapeutic window achievable between doses that result in MMP12 production and macrophage activation and attenuation of fibrosis, as determined in a bleomycin-induced fibrosis lung model.

The landmark studies implicating αvβ6 and its role in TGFβ1 activation within pulmonary inflammation and fibrosis were carried out by Munger and co-workers (Munger *et al.*, 1999). One of the key pieces of evidence generated in these studies was with the β6 knockout mouse, where it was shown that this mouse phenotype was protected from bleomycin-induced lung fibrosis. This in turn led to further studies specifically hypothesising a key role for αvβ6 in IPF. A large amount of the evidence generated for targeting inhibition of the αvβ6 integrin in IPF has been produced as part of the development of a selective non-RGD mimetic αvβ6 therapeutic antibody, STX-100, by Stromedix Inc. (USA) (acquired by Biogen Idec (USA) in March 2012). The key data generated for STX-100 during its pre-clinical phase was completed *in vivo* in the bleomycin-induced lung fibrosis model. Although widely accepted not to be a true representative model of IPF (Scotton and Chambers, 2010), due to the lack of certain characteristic histological features of the disease, like fibroblastic foci and hyperplastic type II alveolar epithelial cells, this is the primary pre-clinical model adopted for testing the majority of potential IPF therapeutics. However, the bleomycin-induced fibrosis in this model is associated with an increased level of αvβ6 integrin as the fibrosis in the lung develops (Munger *et al.*, 1999) making the model relevant for testing anti-αvβ6 therapeutics. STX-100 has been shown to attenuate the fibrosis in the bleomycin-induced mouse model in both a prophylactic and therapeutic mode of administration with significant reductions in hydroxyproline (measure of collagen) and blockade of TGFβ signalling (nuclear SMAD2/3 phosphorylation) observed (Horan *et al.*, 2008). In addition to these studies a mouse strain with a luciferase reporter gene (linked to colIα2 gene promoter) (Inagaki *et al.*, 1998) was used to quantitatively measure collagen gene

expression post-bleomycin challenge. Although hydroxyproline is the "gold standard" method for measuring the efficacy of therapeutics in the bleomycin-induced lung fibrosis model (Kliment *et al.*, 2011), the sensitivity offered by this measurement of collagen as a surrogate for fibrosis is poor, with consistently low signal to background and high variability observed. The bleomycin-induced lung fibrosis model generated in luciferase reporter gene transgenic mice by Horan and co-workers (Horan *et al.*, 2008), displayed a more sensitive method for determining drug efficacy and attenuation of collagen deposition. This allowed the demonstration of a clear dose-dependent effect of STX-100 as well as showing a therapeutic window between the positive anti-fibrotic nature of αvβ6 inhibition and the potential negative effect of inflammatory cell and macrophage activation via raised MMP12 levels.

This pre-clinical package generated with STX-100 provided significant validation of the αvβ6 integrin as a potential therapeutic target in IPF. It also provided sufficient data to warrant the further development of STX-100 and it is currently scheduled for Phase II clinical trials in IPF patients (patients being recruited as of May 2012 http://clinicaltrial.gov/ct2/show/NCT01371305). One clear benefit of the strategy to inhibit TGFβ1 via αvβ6, further demonstrated in the development of STX-100, is that this would limit TGFβ1 blockade to the local environment of the fibrosis and negate the risks of global TGFβ1 inhibition. The key evidence for this, as previously highlighted, is that αvβ6 is highly up regulated in human pulmonary fibrosis but shows limited expression in the lungs of healthy individuals (Figure 1.3.5). Further evidence for a key role in IPF has also recently been highlighted where the integrin

A

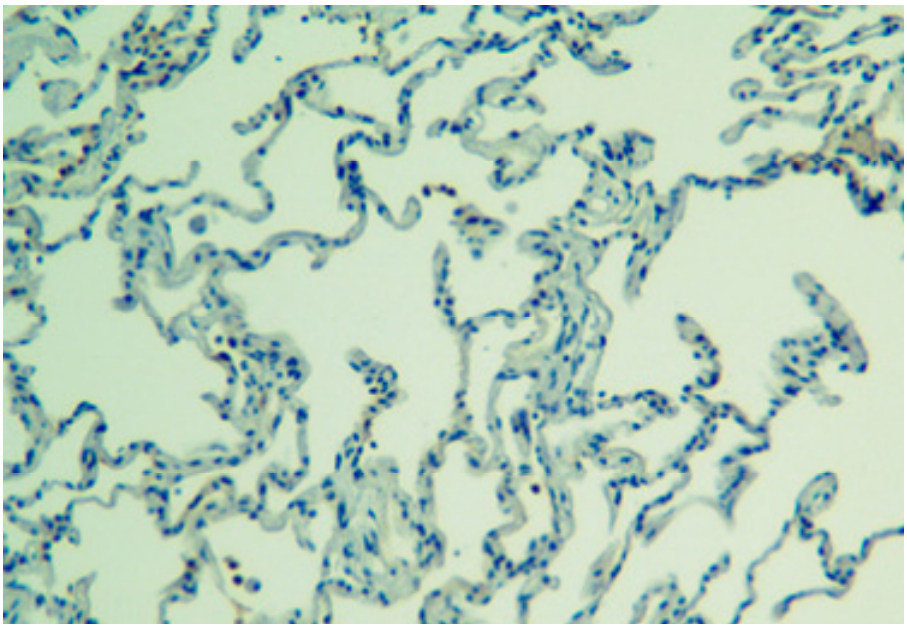

B

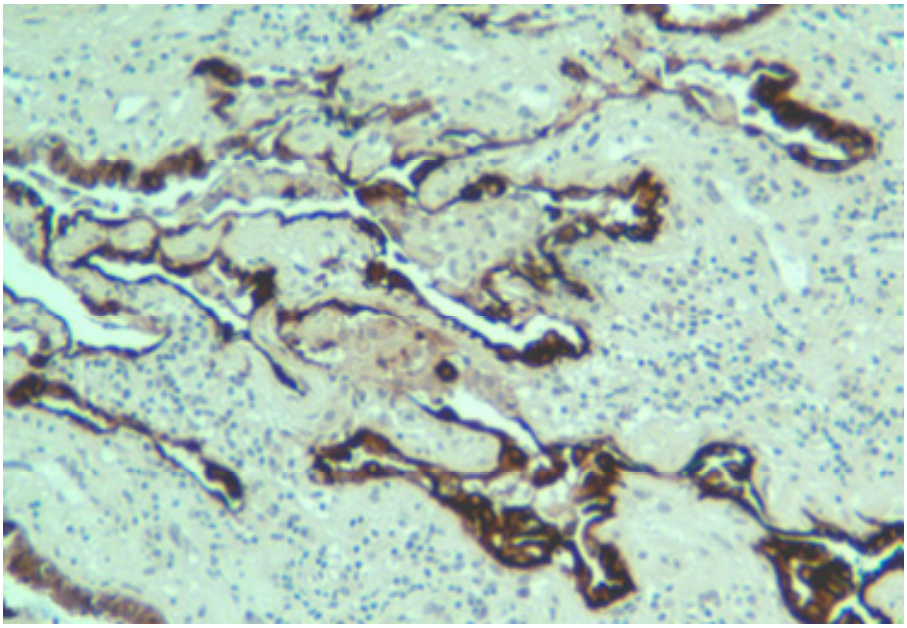

Figure 1.3.5 Expression of the αvβ6 integrin in healthy and IPF human pulmonary tissue. The expression of αvβ6 integrin was measured by immunohistological staining in healthy (A) and IPF (B) lung tissue (adapted from Horan *et al.*, 2008). The cells expressing the αvβ6 integrin are shown by the brown staining.

was suggested as a potential prognostic biomarker for general interstitial lung diseases (Saini *et al.*, 2015). In addition, there is the added potential that αvβ6 may also be relevant in other fibrotic disease states in the liver and kidneys (Popov *et al.*, 2008; Sheppard, 2004) as well as cancer (Bandyopadhyay and Raghavan, 2009). As such STX-100 and 264RAD (αvβ6/alpha-v beta-8 (αvβ8) therapeutic antibody (Eberlain *et al.*, 2012)) have been positioned as potential therapies for fibrosis and/or cancer in multiple organs. Although αvβ5 has also been implicated in IPF (Margadant and Sonnerberg, 2012), the current weight of literature providing evidence of target validation in the disease remains firmly behind αvβ6 (Tatler and Jenkins, 2012). However, it remains a possiblilty that the remaining αv RGD integrins (alpha-v beta-1 (αvβ1), alpha-v beta-3 (αvβ3) and αvβ8) could also play a role in fibrotic disease within and beyond the lung, with recent literature implicating a role for αvβ1 (Henderson *et al.*, 2013; Reed *et al.*, 2015). Although it is worth highlighting that these recent studies investigating the role of αvβ1 in fibrosis are limited to mouse models, with no significant data in human diseased tissue. Recent data has suggested that the roles of αvβ3 and αvβ5 in fibrosis are more relevant in the heart (Sarrazy *et al.*, 2014) but these are limited to *in vitro* systems. In IPF lung the expression of αvβ5 has been shown to be upregulated (Scotton *et al.*, 2009) but no functional data has been generated to show that this is a major contributor to TGFβ generation in disease models. However, as the αv integrins have been shown to be transcriptionally under the control of TGFβ (Zambruno *et al.*, 1995), an upregulation in disease alone driven by this growth factor is not evidence of a contribution to its activation. The potential of αvβ8 as an anti-fibrotic target in chronic obstructive pulmonary disease has been demonstrated using a selective antibody (Minagawa *et*

al., 2014), but the expression and functional role of this integrin in IPF has not been established.

As with all drug discovery initiatives, the potential advantages associated with engaging a target have to be weighed up against the potential disadvantages, as has been highlighted above for αvβ6. It is predicted pre-clinically that for the other αv integrins there might be a greater risk in engagement in terms of safety from long-term exposure of inhibitors. For αvβ1 the risks are difficult to assess for this heterodimer due to the general lack of information available that in part is due to the inability to generate a β1 knockout mouse phenotype, as homozygous β1 null mice do not survive through to birth (Stephens *et al.*, 1995). Although this highlights the key role of the β1 subunit in development and the potential risk of blockade, it provides limited information related to αvβ1 specifically. In addition, the β1 subunit pairs with an additional 11 α-subunits other than αv (Figure 1.3.1); therefore, the β1 knockout mouse phenotype highlights the requirement for a therapeutic to be extremely selective for αvβ1, which could be a challenge with so many integrin heterodimers sharing the same β-subunit. The main liabilities for αvβ3 and αvβ5 are based around their roles in the maintenance of a normal vasculature. Both have been shown to be key in angiogenesis (Friedlander *et al.*, 1995; Eliceiri and Cheresh, 1998) in addition to increased vascular permeability observed when αvβ3 is inhibited (Su *et al.*, 2012). For αvβ8, it has been demonstrated that the loss of this integrin on dendritic cells of mice results in autoimmunity and a colitis phenotype (Travis *et al.*, 2007). In addition, it has also been shown to be critical for regulation of neurovascular physiology (Mobley *et al.*, 2009). Therefore, the current literature on the αv RGD integrins would suggest the conservative approach would be to

selectively target αvβ6 in the lung for IPF, due to either predicted or unknown safety liability of inhibiting αvβ1, αvβ3, αvβ5 and αvβ8, balanced with the likelihood of a benefit in terms of an anti-fibrotic effect via inhibition of TGFβ activation.

In terms of chemical tractability (the degree of complexitiy involved in the chemical modification of a hit compound) of integrins as drug targets, from the perspective of historical drug discovery initiatives and clinical studies, this is a challenging field. Integrins have been identified to play major roles in a number of diseases, prior to the more recent findings in fibrosis, that have included autoimmune disorders, cancer, infections and thrombosis (Cox *et al.*, 2010). As a result of the pre-clinical target validation of a number of integrins in these diseases, as of early 2012, ~260 anti-integrin drugs had been entered into clinical trials (Figure 1.3.6) over the preceding 15 years that had resulted in only 5 approved therapeutics on the market (Goodman and Picard, 2012). In addition, the majority of these approved drugs have targeted a single integrin, the αIIbβ3 RGD integrin, for thrombosis that demonstrates only a very small proportion of the integrin family have been shown to be tractable drug targets. This highlights the challenge of discovering new drugs against this target class that is likely a result of their highly complex functional roles in both normal and disease biology.

1.4. Summary of study aims

The αvβ6 integrin has been implicated in playing a key role in IPF and therefore is an attractive therapeutic target for this disease. To identify a small molecule αvβ6 RGD-mimetic that could be used to test this hypothesis clinically, a drug discovery programme was initiated within GlaxoSmithKline (GSK) focussing on the discovery

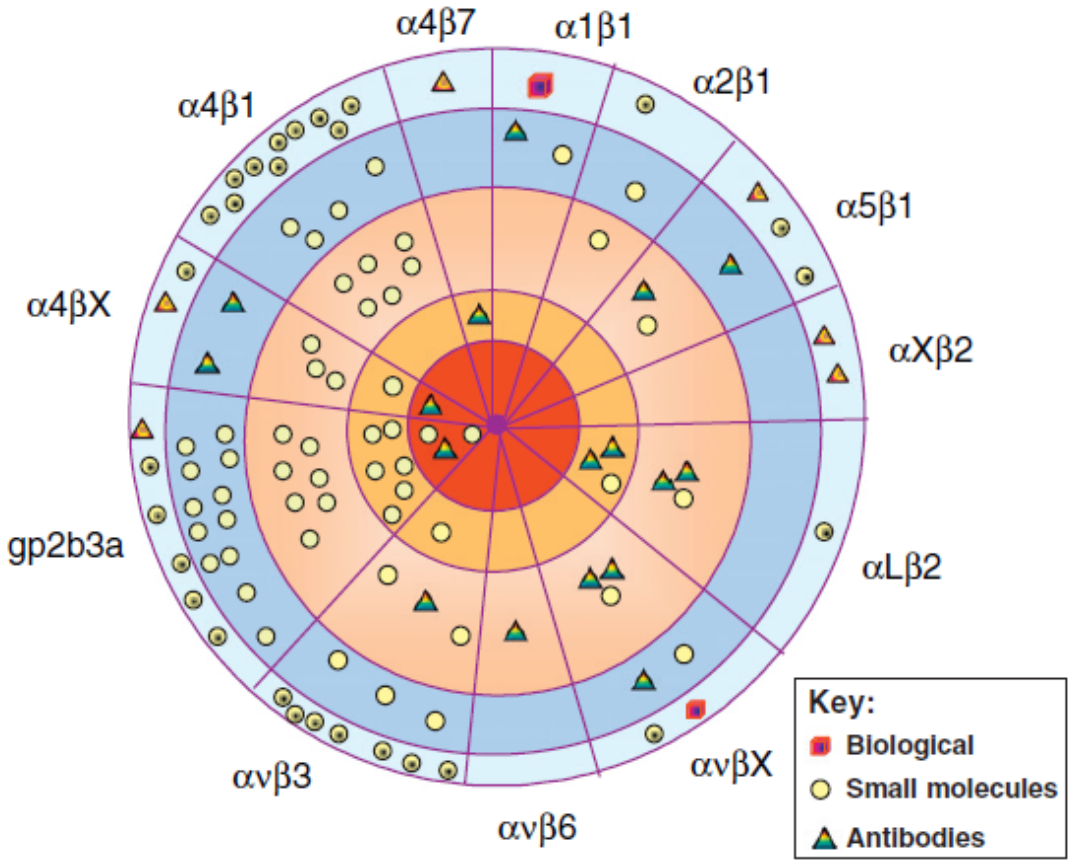

Figure 1.3.6 The distribution and clinical stage of drugs targeting integrins. The different types of therapeutics are shown by symbol with red squares indicating a biological e.g. medicinal product from biological source, yellow circles indicating small molecules or peptides and green triangles indicating antibodies. The stage of clinical development is also shown with those in the light blue area from discontinued trials through to dark blue showing Phase I, then Phase II in pale orange, Phase III in dark orange and approved drugs in the central red circle (taken from Goodman and Picard, 2012).

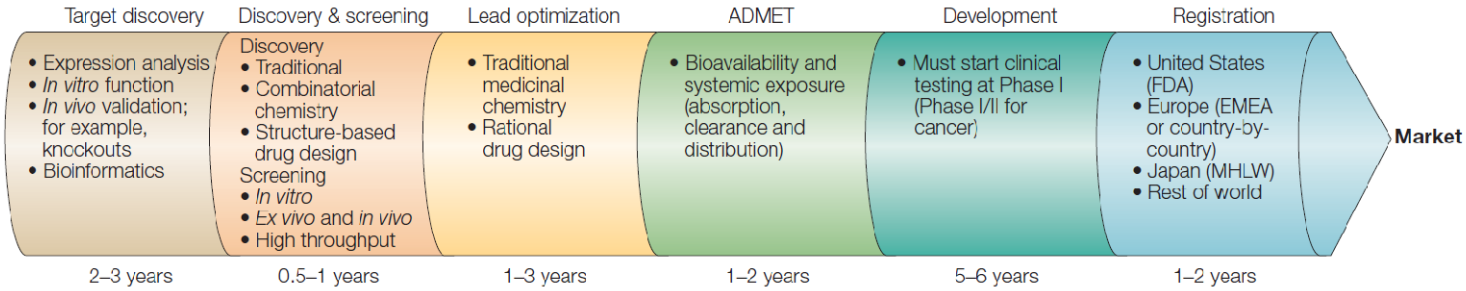

Figure 1.4.1 Flow chart depicting a simplified version of the drug discovery process. The discovery/screening and lead optimisation phases are shown in orange and yellow, respectively (adapted from Ashburn and Thor, 2004). ADMET, adsorption, distribution, metabolism, excretion and toxicity; EMEA, European Medicines Agency; FDA, Food and Drug Administration; MHLW, Ministry of Health, Labour and Welfare.

of a drug candidate that could be dosed via an inhaled nebulised administration directly into the lung. The primary aim of this study was to pharmacologically characterise the small molecule αvβ6 RGD-mimetics that were generated from this drug discovery initiative by developing, designing and implementing key assays and experiments to aid in the selection and development of a lead chemical series. The aim was to identify and address the key scientific questions that require answering during the passage of this programme through the early stages of drug discovery (as shown in Figure 1.4.1). This encompasses post-selection of αvβ6 as a potential target in IPF and screening initiatives to identify novel chemical molecules (high throughput screening (HTS) of focussed compound sets and chemistry based structure activity relationship (SAR) assays). This would then be followed by lead optimisation (ligand/integrin interaction studies encapsulating affinity, selectivity, kinetics and functional effects in basic protein based assays through to cellular (recombinant and primary cells) and disease tissue) and candidate selection for progression into clinical studies. This thesis will focus on the pharmacological characterisation of novel αvβ6 small molecule RGD-mimetics proposed as potential therapeutic agents for IPF by targeting the inhibition of the TGFβ pathway. In addition, both selective and non-selective αvβ6 peptide and small molecule tools will be investigated to aid the progress of both *in vitro* assay development and for potential use in *in vivo* studies.

CHAPTER 2: MATERIALS AND METHODS

2.1 Materials

All the small molecule RGD-mimetics, cilengitide and SB-525334 ((Figure 2.1) TGFβRI inhibitor (Grygielko *et al.*, 2005)) used in this study were synthesised by the Fibrosis and Lung Injury Discovery Performance Unit Medicinal Chemistry group at GSK Medicines Research Centre (Stevenage, UK). Full length LAPβ_1 (fLAP$_1$) (Figure 2.2) was purchased from Sigma-Aldrich Co. Ltd. (Gillingham, UK). Truncated LAPβ_1 (tLAP$_1$), truncated LAPβ_3 (tLAP$_3$) and the αvβ6 selective peptide NAVPNLRGDLQVLAQKVART (A20FMDV2 derived from the foot-and-mouth disease virus (Logan *et al.*, 1993)) were synthesized by Cambridge Research Biochemicals (Cleveland, UK) (Figure 2.2). A20FMDV2 and compound **3** were radiolabelled with [^{3}H] by Quotient Bioresearch (Radiochemicals) Ltd. (Cardiff, UK) and had a specific activities of 20 and 196 Ci/mmol respectively (Figure 2.3). Compound **1** (pan-αv small molecule RGD-mimetic) was radiolabelled with [^{3}H] by RC TRITEC Ltd. (Teufen, Switzerland) and had a specific activity of 16.1 Ci/mmol (Figure 2.3). All other chemicals and reagents were purchased from Sigma-Aldrich Co. Ltd. (Gillingham, UK) unless otherwise stated.

Normal human bronchial epithelial (NHBE) cells, growth medium and supplements were purchased from Lonza (Lonza Group Ltd, Basel, Switzerland). All other cell culture media and reagents were obtained from Invitrogen (Invitrogen Ltd., Paisley, UK). All tissue culture flasks and plates were purchased from Greiner Bio-One (Firckenhausen, Germany) unless otherwise stated.

All antibodies used were commercially available and obtained from R&D Systems (Minneapolis, MN, USA) unless otherwise stated and at a stock concentration of 10

µg/ml. These included antibodies for flow cytometry: phycoerythrin (PE) conjugated mouse immunoglobulin (IgG) 1 isotype control, PE-conjugated mouse IgG2B isotype control (IgG2B-PE), PE-conjugated mouse monoclonal anti-human integrin alpha-v (hαv-PE) (Abcam, Cambridge, MA, USA), PE-conjugated mouse monoclonal anti-human integrin alpha-8 (hα8-PE), PE-conjugated mouse monoclonal anti-human integrin alpha-v beta 3 (hαvβ3-PE), PE-conjugated mouse monoclonal anti-human integrin beta-6 (hβ6-PE), allophycocyanin (APC) conjugated goat IgG isotype control, APC-conjugated mouse IgG1 isotype control, APC-conjugated mouse IgG2B isotype control, APC-conjugated polyclonal human anti-human TGFβ receptor II (hTGFβRII-APC), APC-conjugated mouse monoclonal anti-human integrin alpha-5 (hα5-APC), APC-conjugated mouse monoclonal anti-human integrin beta-1 (hβ1-APC), APC-conjugated mouse monoclonal anti-human integrin alpha-v beta-5 (hαvβ5-APC) and APC-conjugated mouse monoclonal anti-human integrin beta-8 (hβ8-APC).

These included antibodies for immunocytochemistry (ICC) and immunohistochemistry (IHC): mouse IgG1 isotype control (Dako Denmark A/S, Glostrup, Denmark), sheep IgG isotype control (Abcam, Cambridge, MA, USA), sheep polyclonal anti-human integrin β6, biotinylated rabbit anti-mouse IgG (Dako Denmark A/S, Glostrup, Denmark), biotinylated rabbit anti-sheep IgG (Vector Laboratories Inc., Burlingame, CA, USA) and donkey anti-sheep IgG Alexa Fluor® 488 (Invitrogen Ltd., Paisley, UK). These included for functional integrin blocking studies: mouse IgG1 isotype control, mouse IgG2A isotype control (generated by BioPharm Research and Development department at GSK Medicines Research Centre (Stevenage, UK)), monoclonal anti-human integrin αv clone 17E6 (Merck

Millipore, Billerica, MA, USA), monoclonal anti-human integrin β1 clone 4B4 (Beckman Coulter Inc., Brea, CA, USA), monoclonal anti-human integrin αvβ5 clone 5H9, monoclonal anti-human integrin αvβ6 clone 10D5 (Merck Millipore, Billerica, MA, USA) and monoclonal anti-human TGFβ1, 2 and 3 clone 1D11 (neutralising antibody).

All small molecule test compounds, A20FMDV2, $tLAP_1$ and $tLAP_3$ were made up in 100 % DMSO at a stock concentration of 10 mM. $fLAP_1$ was made up to 2 μM in PBS containing 0.1% w/v bovine serum albumin (BSA). Chloroquine, chlorpromazine and filipin were made up in distilled water (dH_2O) at a stock concentration of 1 mM (chloroquine) or 1 mg/ml (chlorpromazine and filipin). All ligands tested in functional cell assays and radioligand binding assays were completed in a final dimethyl sulphoxide (DMSO) concentration of 0.1 % and 1 % respectively, unless otherwise stated.

2.2 Cell culture

2.2.1. K562 cell culture, freezing and recovery

The myelogenous leukemia K562 cell line (Lozzio and Lozzio, 1975) stably expressing the αvβ6 integrin (K562-αvβ6) was generated by the Biological Sciences Department at GSK Medicines Research Centre (Stevenage, UK) using previously described methods (Ludbrook *et al.*, 2003). K562-αvβ6 cells were cultured as a suspension in T175 tissue culture flasks using aseptic techniques in equal volumes of Roswell Park Memorial Institute (RPMI) 1640 and Dulbecco's Modified Eagle's Medium (DMEM) containing 10 % heat inactivated fetal calf serum (FCS), 2 mM glutamine and 1 mg/ml geneticin in 95 %:5 % air:CO_2 at 37ºC. Cells were then

frozen in 90 % FCS (dialysed):10 % DMSO in 5 ml aliquots (~1.5 x 10^8 cells/ml) and stored at –140ºC until required for use in cell adhesion assays. Cells in 5 ml aliquots were recovered by defrosting in a 37ºC water bath before transferring into 20 ml of Hank's balanced salt solution (HBSS; Ca^{2+} and Mg^{2+} free) containing 25 mM 4-(2-hydroxyethyl)-1-piperazineethanesulfonic acid (HEPES) maintained at 37ºC. The cell suspension was then centrifuged at 300 *g* for 5 min, the supernatant removed and the cell pellet re-suspended in HBSS containing 25 mM HEPES. Cells were then counted on a NucleoCounter NC-3000 (ChemoMetec, Allerød, Denmark) and re-suspended to the required cell density for use in cell adhesion assays.

2.2.2. SW480-αvβ6 cell culture

The colon cancer SW480 cell line (Agrez *et al.*, 1996) stably expressing the αvβ6 integrin (SW480-αvβ6) was generated by the Biological Sciences Department at GSK Medicines Research Centre (Stevenage, UK) using the protocol described for the K562-αvβ6 cell line (Ludbrook *et al.*, 2003). Frozen aliquots (in 90 % dialysed FCS:10 % DMSO) of SW480-αvβ6 cells were placed into culture as a monolayer adhered in T175 tissue culture flasks using aseptic techniques. Cells were maintained in SW480-αvβ6 cell medium (DMEM containing 10 % heat inactivated FCS, 4 mM glutamine, 1 mg/ml geneticin) in 95 %:5 % air:CO_2 at 37ºC and were harvested when ~80 % confluent using TrypLE™ Express. Cells were then re-suspended in phosphate buffered saline (PBS), centrifuged at 300 *g* for 5 min prior to re-suspension in SW480-αvβ6 co-culture medium (DMEM with phenol red containing 0.1 % heat inactivated FCS and 2 mM $MgCl_2$). Cells were then counted on a

NucleoCounter NC-3000 (ChemoMetec, Allerød, Denmark) and re-suspended to the required cell density.

2.2.3. Transformed mink lung cell (TMLC) culture

The epithelial transformed mink lung cell (TMLC) line which expresses firefly luciferase under the control of a TGFβ-sensitive portion of the PAI-1 promoter (Abe *et al.*, 1994) was obtained from Professor Daniel Rifkin (New York University, NY, USA). Frozen aliquots (in 90 % dialysed FCS:10 % DMSO) of TMLCs were placed into culture as a monolayer adhered in T175 tissue culture flasks using aseptic techniques. Cells were maintained in TMLC cell medium (DMEM containing 10 % heat inactivated FCS, 2 mM glutamine, 0.25 mg/ml geneticin) in 95 %:5 % air:CO_2 at 37ºC and were harvested when ~80 % confluent using Accutase®. Cells were then re-suspended in PBS, centrifuged at 300 *g* for 5 min prior to re-suspension in TMLC co-culture medium (DMEM with phenol red containing 0.1 % heat inactivated FCS). Cells were then counted on a NucleoCounter NC-3000 (ChemoMetec, Allerød, Denmark) and re-suspended to the required cell density. For co-culture experiments with NHBE cells 20 μM LPA was added to the TMLC co-culture medium.

2.2.4. NHBE cell culture

Frozen aliquots of NHBE cells obtained from a single donor were placed into culture (defined as passage 0 (P0)) as a monolayer adhered to type I collagen coated T75 or T175 tissue culture flasks using aseptic techniques. Cells were maintained in NHBE cell medium (bronchial epithelial growth medium (BEGM™) containing 0.6 mM $MgCl_2$) supplemented with BEGM™ Clonetics™ SingleQuots (containing bovine pituitary extract, insulin, hydrocortisone, GA-1000 (consisting of 30 mg/ml

gentamicin and 15 μg/ml amphotericin), retinoic acid, transferrin, triiodothyronine, epinephrine and human epidermal growth factor) in 95 %:5 % air:CO_2 at 37ºC and were harvested when ~80 % confluent using Accutase®. Cells were then re-suspended in PBS, centrifuged at 300 *g* for 5 min prior to re-suspension in either NHBE cell medium, NHBE/TMLC co-culture medium (DMEM containing 0.1 % heat inactivated FCS) or flow cytometry buffer (RPMI 1640 (without L-glutamine and phenol red) containing 10 mM HEPES, 1 % w/v BSA and 2 mM $MgCl_2$). Cells were then counted on a NucleoCounter NC-3000 (ChemoMetec, Allerød, Denmark) and re-suspended to the required cell density.

2.3 Recombinant soluble integrin proteins

Purified soluble protein preparations (recombinantly derived from Chinese Hamster Ovary cells) for the human (αvβ1, αvβ3, αvβ5, αvβ6 and αvβ8) integrin proteins profiled were all purchased from R&D Systems Inc. (Minneapolis, MN, USA). Protein preparations were reconstituted in sterile PBS to a stock concentration of 100 μg/ml (except for human αvβ5 (50 μg/ml)) as per manufacturer's recommendation and aliquots stored at -80ºC until use.

2.4 Human lung parenchyma membrane preparation

Normal (non-fibrotic) human lungs (designated by medical history with a mean donor age of 42 (range 23-58)) from organ donors were obtained from the National Disease Research Interchange (Philadelphia, PA, USA) in accordance with local human biological sample management procedures. Post-transplant lung tissue samples from IPF patients (disease state defined by medical history and post-transplant pathology confirmed by a board-certified pathologist experienced in

evaluating pulmonary fibrosis) with a mean donor age of 54 (range 44-62)) were obtained from Newcastle University (Newcastle upon Tyne, Tyne and Wear, UK) in accordance with local human biological sample management procedures. Human biological samples were sourced ethically and their research use was in accord with the terms of the informed consent. Human lung parenchyma tissue (between 2 and 15 g) obtained from 6 normal and 6 IPF donors was dissected and cleaned of adherent connective and fatty tissue. Tissue samples were suspended in ice-cold assay buffer (50 mM Tris, 154 mM NaCl, 10 mM $MgCl_2$ and 2 mM ethylenediaminetetraacetic acid (EDTA), pH 7.4 (HCl)) and homogenised with an Ultra-Turrax homogeniser (IKA, Staufen, Germany) for 20 s followed by 4 x 4 strokes in a glass-teflon homogeniser. Homogenised tissue was washed in assay buffer and centrifuged at 500 *g* for 10 min at 4ºC. The supernatant was then harvested and centrifuged at 40,000 *g* for 15 min at 4ºC with the resulting pellet resuspended in assay buffer and centrifuged a second time at 40,000 *g* for 15 min at 4ºC. Membrane pellets were then passed 10 x through a 0.22 mm needle, resuspended in assay buffer (without EDTA) and protein concentration determined using the bicinchoninic acid method (Smith *et al.*, 1985) using bovine serum albumin as a standard. The membrane suspensions were frozen in aliquots at -80°C until required.

2.5 K562-αvβ6 and NHBE cell adhesion assay

Glutathione S-transferase fusion LAP-TGFβ-1 (GST-LAP_1) protein, corresponding to the RGD integrin-binding domain of LAP_1 (amino acids 242-252 – GRRGDLATIHG), was available within GSK (Biological Sciences Department, GSK Stevenage, Hertfordshire, UK) and generated as previously described

(Ludbrook *et al.*, 2003). GST-LAP_1 was coated (100 µl/well) onto 96-well MaxiSorp® flat-bottom plates (Thermo Fisher Scientific, MA, USA) at a concentration of 100 µg/ml and incubated for 2 h at 37ºC. Plates were then washed twice with 200 µl/well PBS after which blocked with 3 % w/v BSA in PBS (100 µl/well) for 1 h. Plates were then washed twice with 200 µl/well PBS and 25 µl/well of cell adhesion assay buffer (Hank's balanced salt solution (HBSS) containing 25 mM HEPES) containing 8 mM $MgCl_2$ was added. Test compounds (small molecule RGD-mimetics, antibodies or peptides) were made up in cell adhesion assay buffer (0.4 % DMSO to give a final DMSO concentration of 0.1 %) and added to plates (25 µl/well). NHBE or K562-αvβ6 cells were re-suspended to 0.25 or 3 x 10^6 cells/ml respectively, and 2',7'-bis-(2-carboxyethyl)-5-(and-6)-carboxyfluorescein, acetoxymethyl ester (BCECF-AM) added to give a final concentration of 5 µM prior to a 10 min incubation at 37ºC. 12,500 cells/well (50 µl/well) NHBE cells or 0.15 x 10^6 cells/well (50 µl/well) K562-αvβ6 cells were then added to plates (giving a final $MgCl_2$ concentration of 2 mM) prior to a 30 min incubation at 37ºC. Plates were then washed twice with 200 µl/well PBS and 50 µl/well 0.5 % Triton X-100 detection solution added. Following a 5 min incubation at ambient temperature (20-22ºC) fluorescence (relative light units) was measured (excitation wavelength 485 nm and emission wavelength 535 nm) using an EnVision® multilabel plate reader (PerkinElmer LAS UK Ltd., Beaconsfield, UK) or Tecan Safire (Tecan Group Ltd., Männedorf, Switzerland). Full concentration-response curves (CRCs) were generated for test compounds in the K562-αvβ6 assay format to allow determination of the molar concentration that produced 50 % of maximal inhibition (IC_{50}) (as described under section 2.12 Data analysis). In order to average data between separate

experimental determinations in the K562-αvβ6 assay format, data were normalised within experiments using a positive (10 mM EDTA) and negative control (0.1 % DMSO).

2.6 Radioligand binding studies

2.6.1. General protocols for radioligand binding assays

All radioligand binding experiments were performed in 96-well (2 ml deep-well) plates at 37ºC in either binding buffer (25 mM HEPES, 100 mM NaCl, 2 mM $MgCl_2$ (unless otherwise stated) and 1 mM 3-[(3-cholamidopropyl)dimethylammonio]-1-propanesulfonate (CHAPS) at pH 7.4 (NaOH) unless otherwise stated) or simulated lung fluid (SLF) (0.5 mM $MgCl_2$, 103 mM NaCl, 4 mM KCl, 0.9 mM Na_2HPO_4, 0.4 mM Na_2SO_4, 2.5 mM $CaCl_2.2H_2O$, 7 mM $C_2H_3NaO_3$, 31 mM $NaHCO_3$ and 0.3 mM $C_6H_6O_7.2H_2O.3Na$, 1 mM CHAPS at pH 7.4) (Marques *et al.*, 2011). Radioligand binding studies completed with recombinant soluble integrin proteins were in a total volume of either 0.5 ml ([^{3}H]compound **1** and [^{3}H]A20FMDV2) or 1.5 ml ([^{3}H]compound **3**) consisting of 50 µl/well of either unlabelled compound at varying concentrations or vehicle (1 % DMSO), 50 µl of radioligand ([^{3}H]compound **1,** [^{3}H]compound **3** or [^{3}H]A20FMDV2) and either 0.4 or 1.4 ml/well of purified integrin. [^{3}H]compound **1** was tested against the following human integrins with the final assay concentration (FAC) of protein shown in parentheses:- αvβ1 (1.5 nM), αvβ3 (0.1 nM), αvβ5 (1 nM), αvβ6 (0.075 nM and 0.3 nM for low and high protein assay format respectively), αvβ8 (2 nM) and α5β1 (0.3 nM). [^{3}H]compound **3** was tested against human αvβ6 at 30 pM and also in cell based assays with NHBE cells at 30,000 cells/well. Radioligand binding studies completed with human lung

parenchyma membranes were in a total volume of either 0.5 ml (association and dissociation binding studies) or 1.5 ml (saturation binding studies) consisting of 50 µl/well of either unlabelled compound or vehicle (1 % DMSO), 50 µl of radioligand ([^{3}H]compound **3**) and 0.4 or 1.4 ml/well of membranes (µg/well dependent on the number of binding sites (B_{max}) of individual membrane fragment preparations and ranged between 12 to 50 µg/well).

Non-specific binding (NSB) was determined with either 10 µM SC-68448 (pan-αv small molecule RGD-mimetic (Carron *et al.*, 1998) (Figure 2.3)), 1 or 10 µM A20FMDV2 (selective αvβ6 peptide) or 10 mM EDTA (chelating agent). Specific binding was measured by subtracting the NSB from the total radioligand binding in the presence of vehicle (1 % DMSO). Plates were incubated with gentle agitation for the time periods indicated and binding terminated by rapid vacuum filtration through a 48-well Brandel harvester (Brandel Inc. Gaithersburg, MD, USA) onto GF/B (for [^{3}H]compound **1** and [^{3}H]compound **3**) or GF/C (for [^{3}H]A20FMDV2) filter papers pre-soaked in 0.3 % v/v poly-ethylenimine (PEI). Samples were washed rapidly three times with ice cold dH_2O and filters transferred into liquid scintillation (LS) vials containing 4 ml LS fluid (Ultima-Flo™ M, PerkinElmer LAS UK Ltd., Beaconsfield, UK). The amount of radioligand bound to integrin protein was measured by LS spectroscopy using a TriCarb 2900 TR LS counter (PerkinElmer LAS UK Ltd., Beaconsfield, UK). By the same method the concentration of total radioligand added to each well was calculated for data analysis and also to determine the percentage of radioligand bound, thus allowing the investigation of the amount of free radioligand in the system to determine if ligand depletion was occurring (Hulme and Birdsall, 1992).

2.6.2. Radioligand characterisation

Association, dissociation and saturation binding studies were performed with [^{3}H]compound **1**, [^{3}H]compound **3** and [^{3}H]A20FMDV2 to determine radioligand binding kinetics at the αvβ6 in human recombinant soluble protein as well as in human lung parenchyma membranes generated from healthy and IPF lung tissue (association rate constant (k_{on}), dissociation rate constant (k_{off}), equilibrium dissociation constant (K_D) and B_{max} were calculated as described under section 2.12 Data analysis). For association binding, human αvβ6 integrin protein or membranes were incubated with varying concentrations of either [^{3}H]compound **1** (~1 to 5 nM), [^{3}H]compound **3** (~0.02 to 0.1 nM) or [^{3}H]A20FMDV2 (~0.3 to 2 nM) for varying times up to 4 h prior to filtration. For dissociation binding, human αvβ6 integrin protein or membranes were pre-incubated for 1 h with a fixed concentration of radioligand (~1 to 2 nM for [^{3}H]compound **1** or [^{3}H]A20FMDV2 and ~0.04 to 0.24 nM for [^{3}H]compound **3**) before dissociation was initiated by either the addition of an excess of unlabelled compound or 10 mM EDTA then incubation for varying times up to 72 h prior to filtration. For saturation binding, human αvβ6 integrin protein was incubated with increasing concentrations of radioligand ([^{3}H]compound **1** ~0.01 to 44 nM, [^{3}H]compound **3** ~0.001 to 1.2 nM or [^{3}H]A20FMDV2 ~0.01 to 6 nM) for either 6 or 24 h prior to filtration. Saturation binding was also completed with NHBE cells with increasing concentrations of [^{3}H]compound **3** (~0.01 to 3.3 nM) following a 6 h incubation. For saturation binding in human lung parenchyma membranes were incubated with increasing concentrations of [^{3}H]compound **3** (~0.0002 to 1.2 nM) for 72 h prior to filtration. Saturation binding was also completed for [^{3}H]compound **1** (~0.07 to 138 nM) against the αvβ1, αvβ3, αvβ5 and

αvβ8 integrins following either a 2 h (αvβ5 and αvβ8) or 6 h (αvβ1 and αvβ3) incubation. All saturation studies allowed the determination of K_D (allowing equilibrium dissociation constant (K_I) values to be calculated in competition binding studies as described under section 2.12 Data analysis) and B_{max} values. To demonstrate the divalent cation dependency of integrin binding and allow comparison between the small molecule RGD-mimetic and peptide radioligands, the specific binding window of [^{3}H]compound **1**, [^{3}H]compound **3** and [^{3}H]A20FMDV2 was measured against αvβ6 in the presence of a range of concentrations of Ca^{2+}, Mg^{2+} and Mn^{2+}.

2.6.3. Determination of αvβ6 integrin ligand affinity and selectivity

In order to determine the affinity and selectivity of integrin ligands, competition binding displacement studies were completed where integrin protein was incubated with a fixed concentration of either [^{3}H]compound **1** or [^{3}H]A20FMDV2 (~1 to 10 nM dependent on integrin), and single or increasing concentrations of unlabelled test ligand (small molecule RGD-mimetics and peptides) for either 2 h (αvβ5 and αvβ8), 6 h (αvβ1, αvβ3, αvβ6) or 24 h (αvβ6) prior to filtration.

2.6.4. Determining the αvβ6 receptor dissociation rates of unlabelled integrin ligands

To determine the receptor dissociation rates of unlabelled integrin ligands, 2 x K_I concentrations of unlabelled test ligand (small molecule RGD-mimetics and peptides) were incubated with αvβ6 protein for 1 h prior to addition of excess [^{3}H]compound **1** (50 x K_D = ~50 nM) and then incubated at 37°C for varying times up to 48 h prior to filtration.

2.7 Flow cytometry

2.7.1. General flow cytometry protocols

All flow cytometry assays were performed in 96-well polypropylene microplates with SW480-αvβ6 and NHBE cells suspended in flow cytometry buffer (45 µl/well with cell density dependent on experimental type) in the absence or presence of 5 µl/well compound or vehicle (0.1 % DMSO). If required, cells were permeabilised by incubating with 0.2 % w/v saponin for 5 min at ambient temperature (20-22ºC) prior to compound/vehicle addition. Inhibition of clathrin or lipid raft mediated-endocytosis was investigated by pre-incubating NHBE cells with either 2 µg/ml chlorpromazine or 10 µg/ml filipin (Imanov, 2008) respectively (both made up in flow cytometry buffer), for 5 min prior to addition of compound or vehicle (0.1 % DMSO). Plates were incubated for varying time points under different conditions dependent on experiment type. Experiments were stopped by addition of 10 µl/well isotype control or flow antibody and transferring plates to 4^{o}C for 1 h. Plates were washed twice by centrifuging at 300 *g* for 5 min, removing supernatant and adding flow cytometry buffer (150 µl/well). After the second wash cells were resuspended in flow cytometry buffer (200 µl/well) and cell suspensions transferred into a 96 well round bottom polypropylene plate (Corning Inc. Life Sciences, Tewksbury, MA, USA). Cell samples were then acquired on a fluorescence activated cell sorting (FACS) Canto II (BD Biosciences, San Jose, CA, USA) using a high throughput sampler system and BD FACS Diva™ version 6.1.3 software. Cells were identified by their forward and side-scatter characteristics and the mean fluorescence intensity of antibody conjugated cells measured. The fluorescence was quantified on at least

5,000 cells and following acquisition all data was exported as flow cytometry standard format 3.0 files with raw data values captured as mean fluorescence intensity (MFI). Fluorescence-activated cell analyses histograms were plotted using FlowJo software (Tree Star Inc. Ashland, OR, USA).

2.7.2. Surface expression of αv, α5, α8, β1, αvβ3, αvβ5, β6 and β8 integrins and TGFβRII on SW480-αvβ6 and NHBE cells

Cultured NHBE cells were harvested at passage 1 (P1), 2 (P2), 3 (P3) and 4 (P4) and re-suspended in flow cytometry buffer. 50,000 NHBE cells (50 µl/well) were added to 96-well polypropylene microplates and 10 µl/well antibody isotype control/hαv-PE, hα5-APC, hα8-PE, hβ1-APC, hαvβ3-PE, hαvβ5-APC, hβ6-PE, hβ8-APC or hTGFβRII-APC antibody added. Samples were then processed and read on the FACS Canto II as detailed in section 2.7.1. The protocol was identical for SW480-αvβ6 cells.

2.7.3. Ligand-induced αvβ6 internalisation and recycling in NHBE cells

For internalisation CRCs, cultured NHBE cells were harvested and re-suspended in flow cytometry buffer and 70,000 NHBE cells (45 µl/well) added to 96 well polypropylene microplates containing 5 µl/well compound at varying concentrations or vehicle (0.1 % DMSO). Plates were incubated for 2 h in 95 %:5 % air:CO_2 at 37ºC prior to addition of 10 µl antibody isotype control or hβ6-PE. Samples were then processed and read on the FACS Canto II as detailed in section 2.7.1. For determining the rate of ligand-induced αvβ6 internalisation, cultured NHBE cells were harvested and re-suspended in flow cytometry buffer and 70,000 NHBE cells (45 µl/well) added to 96 well polypropylene microplates containing 5 µl/well

compound (at a concentration that caused maximal internalisation) or vehicle (0.1 % DMSO). Plates were incubated in 95 %:5 % air:CO_2 at 37°C for varying times up to 1 h and then transferred immediately on to ice to stop any further internalisation. Antibody isotype control or hβ6-PE (10 µl/well) were then added to plates. Samples were then processed and read on the FACS Canto II as detailed in section 2.7.1. For determining the rate of αvβ6 recycling (reversal of ligand-induced αvβ6 internalisation), cultured NHBE cells were harvested and re-suspended in flow cytometry buffer and 70,000 NHBE cells (45 µl/well) added to 96 well polypropylene microplates containing 5 µl/well compound (at a concentration that caused maximal internalisation) or vehicle (0.1 % DMSO). Plates were incubated in 95 %:5 % air:CO_2 at 37°C for 1 h then centrifuged at 500 *g* for 5 min, supernatant removed and cell pellets re-suspended in PBS (150 µl/well). This process was repeated prior to re-suspension of cells in cell medium (150 µl/well) and incubation for varying times up to 48 h. Plates were then transferred on to ice and 10 µl/well antibody isotype control or hβ6-PE added. Samples were then processed and read on the FACS Canto II as detailed in section 2.7.1.

2.8 Immunocytochemistry (ICC) and immunohistochemistry (IHC) staining

2.8.1 β6 integrin ICC staining and confocal microscopy

Cultured NHBE cells were harvested, re-suspended in NHBE cell medium and 25,000 cells (300 µl//well) seeded on to 8 well Lab-Tek® chamber slides (Corning Inc. Life Sciences, Tewksbury, MA, USA) then left for 24 h to adhere in 95 %:5 % air:CO_2 at 37ºC. Cell medium was then removed and replaced with fresh cell medium (300 µl/well) containing compound **3** (at a concentration that caused

maximal internalisation (250 nM)) or vehicle (0.1 % DMSO) and incubated for 1 or 24 h at 4°C or 37°C in the absence or presence of 10 μM of the lysosomal inhibitor chloroquine.

Chamber slides were then washed three times with PBS (300 μl/well) followed by addition of ice-cold fixative (PBS/4 % paraformaldehyde (PFA)) for 15 min on ice. PFA solution was removed and chamber slides were then washed three times with PBS (300 μl/well). Chamber slides were blocked with PBS/15 mM glycine (200 μl/well) for 20 min, then Image-iT™ FX Signal Enhancer (Invitrogen Ltd., Paisley, UK) (120 μl/well) and then PBS/1 % gelatine or PBS/1 % gelatine/0.2 % w/v saponin (200 μl/well) for 20 min with wells washed twice with PBS (500 μl/well) between additions of blocking solutions. Isotype control or sheep polyclonal anti-human integrin β6 antibody (1/100 in PBS) (120 μl/well) were then added to chamber slides for 4 h at ambient temperature (20-22ºC) followed by washing with either PBS/1 % gelatine or PBS/1 % gelatine/0.2 % w/v saponin (200 μl/well) for 5 min. Secondary antibody, donkey anti-sheep Alexa Fluor® 488 (1/200 in PBS) (120 μl/well) was added to chamber slides for 1 h at ambient temperature (20-22ºC) followed by washing with PBS/1 % gelatine or PBS/1 % gelatine/0.2 % w/v saponin (200 μl/well) for 5 min then PBS (500 μl/well). Hoechst 33342 (Invitrogen Ltd., Paisley, UK) at 5 μM in PBS (120 μl/well) was added to chamber slides for 10 min to stain cell nuclei and wells were then washed twice with PBS (500 μl/well) and viewed on a Leica TCS SP5 (Leica Microsystems Inc., Milton Keynes, UK) confocal microscope to generate a three dimensional (3D) z-stack. Quantitative analysis of the intensity of β6 staining (cytoplasmic Alexa Fluor® 488) by immunofluorescence

confocal microscopy was completed using Columbus™ Image Data Storage and Analysis System (PerkinElmer LAS UK Ltd., Beaconsfield, UK).

2.8.2 IHC staining of human lung tissue

2.8.2.1. Tissue section sourcing and preparation

Paraffin tissue sections (5 μm thick) from the human lungs used for generation of parenchyma membrane preparations in section 2.4 were provided by either the Target and Pathway Validation department at GSK Medicines Research Centre (Stevenage, UK) or Newcastle University (Newcastle upon Tyne, Tyne and Wear, UK) with 3 serial tissue sections provided from a single tissue block per donor. Individual staining protocols for the proteins of interest were completed as detailed in the sections below (section 2.8.2.2 and 2.8.2.3), with all incubations carried out at ambient temperature (20-22ºC) unless otherwise stated.

2.8.2.2. Haematoxylin and eosin (H&E) IHC staining

Haematoxylin and eosin (H&E) staining was completed by the Laboratory Animal Sciences department at GSK Medicines Research Centre (Stevenage, UK) using a standard protocol (as detailed in Appendix section 8.2.4) on the Leica ST5020 Multistainer (Leica Microsystems Inc., Milton Keynes, UK).

2.8.2.3. β6 integrin IHC staining

Tissue sections were immersed in citric acid-based antigen-unmasking solution (Vector Laboratories Inc., Burlingame, CA, USA) and microwaved for 15 min prior to being washed in dH_2O. Tissues sections were then incubated for 15 min in 1 % v/v H_2O_2 in methanol, washed in dH_2O and then in Tris-buffered saline (TBS) (Dako

Denmark A/S, Glostrup, Denmark). Tissue sections were then blocked with avidin followed by biotin for 15 min, with samples washed in TBS following each block. Tissue sections were further blocked in whole rabbit serum (Dako Denmark A/S, Glostrup, Denmark) for 20 min prior to incubation with sheep polyclonal anti-human integrin β6 antibody (1/100 in PBS) for 4 h. Tissue sections were then washed in TBS and incubated with biotinylated rabbit anti-sheep IgG antibody (1/200 in PBS) for 30 min prior to a further TBS wash. Streptavidin-horseradish peroxidase (Dako Denmark A/S, Glostrup, Denmark) 1/500 in PBS was applied to sections for 30 min before being washed with TBS followed by dH_2O. Tissue sections were then incubated with 3,3'-diaminobenzidine in chromogen solution (Dako Denmark A/S, Glostrup, Denmark) for 5 min, washed in dH_2O, placed in Mayer's Haematoxylin (Pioneer Research Chemicals Ltd., Colchester, Essex, UK) for 20 s and finally washed in dH_2O. Tissue sections were then dehydrated by passing through ascending concentrations of alcohol (70 % v/v industrial methylated spirits (IMS) followed by 90 % v/v IMS and 100 % IMS).

2.9 TGFβ activation bioassay

2.9.1. SW480-αvβ6 cell/TMLC co-culture assay

Cultured TMLCs were harvested, re-suspended in TMLC co-culture medium and 10,000 cells (100 µl/well) seeded in 96-well clear collagen I coated plates Invitrogen (Invitrogen Ltd., Paisley, UK) then left for 2 h to adhere in 95 %:5 % air:CO_2 at 37ºC. Cultured SW480-αvβ6 cells were harvested, re-suspended in SW480-αvβ6 co-culture medium (0.4 x 10^6 cells/ml) and placed on ice for 2 h. SW480-αvβ6 cells were then seeded at 40,000 cells/well (100 µl/well) in 96-well clear tissue culture

plates (Corning Inc. Life Sciences, Tewksbury, MA, USA) containing 10 µl/well vehicle (0.1 % DMSO) or test compounds (small molecule RGD-mimetics, antibodies, TGFβ1 or peptides) and incubated at ambient temperature (20-22ºC) for 30 min. TMLCs were washed by removal of supernatant, addition and then removal of 100 µl/well TMLC co-culture medium. SW480-αvβ6 cells (including vehicle/test compounds) were then transferred (110 µl) onto the TMLCs and incubated for 20 h incubation in 95 %:5 % air:CO_2 at 37ºC. Supernatants were then removed from the SW480-αvβ6 cell/TMLC co-culture and 100 µl/well PBS (containing 1 mM $CaCl_2$ and 1 mM $MgCl_2$) and 100 µl/well Steady-Glo® Reagent (Promega Corporation, Madison, WI, USA) added. Plates were then incubated at ambient temperature (20-22ºC) for 5 min before supernatants were transferred to 96-well white, solid bottom plates and luminescence (relative luciferase units (RLU)) read on a MicroBeta® TriLux (PerkinElmer LAS UK Ltd., Beaconsfield, UK). In order to quantify the active TGFβ being released from the SW480-αvβ6 cells, TGFβ1 standard curves were also completed in the absence of test compound.

2.9.2. NHBE cell/TMLC co-culture assay

Cultured NHBE cells were harvested, re-suspended in NHBE cell medium and 25,000 cells (100 µl/well) seeded in 96-well clear collagen I coated plates then left for 24 h to adhere in 95 %:5 % air:CO_2 at 37ºC before removal of medium. Cultured TMLCs were harvested, re-suspended in TMLC co-culture medium containing 20 µM LPA and 25,000 cells (100 µl/well) seeded onto the NHBE cells. Vehicle (0.1 % DMSO) or test compounds (small molecule RGD-mimetics, TGFβ1 or peptides) were then added (10 µl/well) and plates incubated for 24 h in 95 %:5 % air:CO_2 at

37ºC. Supernatants were then removed from the NHBE cell/TMLC co-culture and 100 µl/well PBS (containing 1 mM $CaCl_2$ and 1 mM $MgCl_2$) and 100 µl/well Steady-Glo® Reagent (Promega Corporation, Madison, WI, USA) added. Plates were then incubated at ambient temperature (20-22ºC) for 5 min before supernatants were transferred to 96-well white, solid bottom plates and luminescence (RLUs) read on a MicroBeta® TriLux (PerkinElmer LAS UK Ltd., Beaconsfield, UK). For washout studies test compounds were incubated with NHBE cell/TMLC co-culture for 1 h. Cells were then washed three times by removing supernatant and replacing with PBS (250 µl/well) prior to addition of TMLC co-culture medium (250 µl/well) and plates were then incubated for a further 24 h in 95 %:5 % air:CO_2 at 37ºC prior to addition of read reagents (as described above). Washout studies were also completed in the presence of the lysosomal inhibitor chloroquine (10 µM made up in TMLC co-culture medium). In order to quantify the active TGFβ being released from the NHBE cells, TGFβ1 standard curves were also completed in the absence of test compound.

To measure direct inhibition of the TGFβRI/II complex by test compounds, cultured TMLCs were harvested, re-suspended in TMLC co-culture medium and 50,000 cells (100 µl/well) seeded in 96-well clear collagen I coated plates Invitrogen (Invitrogen Ltd., Paisley, UK) then left for 1 h to adhere in 95 %:5 % air:CO_2 at 37ºC. Prior to addition of 10 µl/well TGFβ1 (FAC 10 ng/ml), 10 µl/well vehicle (0.1 % DMSO) or test compounds were added to TMLCs and incubated at ambient temperature (20-22ºC) for 1 h. Plates were incubated for 20 h incubation in 95 %:5 % air:CO_2 at 37ºC then supernatants were removed and 100 µl/well PBS (containing 1 mM $CaCl_2$ and 1 mM $MgCl_2$) and 100 µl/well Steady-Glo® Reagent (Promega Corporation, Madison,

WI, USA) added. Plates were then incubated at ambient temperature (20-22ºC) for 5 min before supernatants were transferred to 96-well white, solid bottom plates and luminescence (RLUs) read on a MicroBeta® TriLux (PerkinElmer LAS UK Ltd., Beaconsfield, UK).

2.10 Quantification of β6 and PAI-1 messenger ribonucleic acid (mRNA) expression in NHBE cells

Cultured NHBE cells were harvested, re-suspended in cell medium and 50,000 cells (500 µl/well) seeded on to type I collagen-coated 24-well plates then left for 24 h to adhere in 95 %:5 % air:CO_2 at 37ºC. Compound or vehicle (0.1 % DMSO) (5 µl/well) were added and plates were incubated for a further 24 h in 95 %:5 % air:CO_2 at 37ºC. Cells were then washed 3 times with ice-cold PBS (500 µl//well) and stored at -80ºC for preparation and expression profiling of β6 and PAI-1 messenger ribonucleic acid (mRNA) by the Biological Sciences Department at GSK Medicines Research Centre (Stevenage, UK) (as detailed in Appendix section 8.2.5) by quantitative polymerase chain reaction (qPCR).

2.11 Data analysis

Analysis of all experiments was completed using Prism 5.0 (GraphPad Software, San Diego, CA, USA). In order to allow the results between binding experiments to be combined, where appropriate, disintegrations per minute (DPM) values were normalised to give the amount (in femtomoles as calculated by the methods described in Motulsky and Christopoulos, 2004) of radioligand bound per amount (ng) of purified protein (fmol/ng).

Specific binding data from association binding experiments were fitted to a one-phase association model (Equation 1 where *Binding* is the level of binding observed in test well and k_{ob} is the observed rate constant in inverse units of time (min^{-1})).

$$Binding = Binding_{t=0} + \left(Binding\ plateau - Binding_{t=0}\right).1 - exp^{(-K_{ob}.min)} \quad (1)$$

To calculate the association rate constant k_{on} (in units of inverse molar inverse time ($M^{-1}.min^{-1}$)) from K_{ob}, Equation 2 was used (where k_{off} is the dissociation rate constant in inverse units of time (min^{-1})). From Equation 2 k_{on} values were subsequently used to calculate association half-life ($t_{1/2}$) values at fixed radioligand concentrations using the equation $t_{1/2} = 0.693/k_{on}$.

$$K_{ob} = [radioligand] \cdot k_{on} + k_{off} \quad (2)$$

To calculate the percentage of radioligand bound in dissociation binding studies at each time point Equation 3 was used (where *TB* is total binding of radioligand determined in the presence of vehicle (1 % DMSO) and *NSB* is non-specific binding determined in the presence of 10 μM SC-68448, all measured at the same time point in DPM).

$$\%\ Radioligand\ Bound = \left[\frac{\left(Binding - NSB\right)}{\left(TB - NSB\right)}\right] \times 100 \quad (3)$$

Dissociation binding data for radioligands and unlabelled integrin ligands were fitted to either a one-phase dissociation model (Equation 4 where $NSB_{t=\infty}$ is non-specific binding determined at infinite time) or a two-phase dissociation model (Equations 5a, b and c where *FP* is the span of the fast dissociation phase, *SP* is the span of the slow dissociation phase, $k_{off(FAST)}$ is the fast phase dissociation rate constant and $k_{off(SLOW)}$ is the slow phase dissociation rate constant (both in inverse units of time (min^{-1})) and *%F* is the fraction of the fast dissociation phase.

$$Binding = \left(Binding_{t=0} - Binding\ \ plateau\right).exp^{(-k_{off}.min)} + NSB_{t=\infty} \quad (4)$$

From Equation 4 and 5c k_{off} values were subsequently used to calculate dissociation $t_{1/2}$ values using the equation $t_{1/2} = 0.693/k_{off}$.

$$FP = \left(Binding_{t=0} - Binding\ plateau\right)\left(\%F \times 0.01\right) \quad (5a)$$

$$SP = \left(Binding_{t=0} - Bindingplateau\right)\left((100 - \%F) \times 0.01\right) \quad (5b)$$

$$Binding = Binding\,plateau + FP.exp^{(-k_{off}(FAST).min)} + SP.exp^{(-k_{off}(SLOW).min)} \quad (5c)$$

Specific binding data from saturation experiments were fitted to a one affinity site model with Hill slope (Equation 6 where n_H = Hill slope coefficient) where appropriate to determine K_D and B_{max} values. For visualisation only, specific binding data from saturation experiments was also analysed via Scatchard transformation (Scatchard, 1949) using the method described in Motulsky and Christopoulos, 2004.

$$Binding = \frac{B_{max}\left[radioligan\,d\right]^{n_H}}{K_D^{n_H} + \left[radioligan\,d\right]^{n_H}} \quad (6)$$

All CRCs and competition binding displacement curves were fitted using non-linear regression analysis (four-parameter logistic equation with variable slope (Hill, 1909)) with EC_{50} or IC_{50} values calculated from the fits.

To calculate the percentage inhibition of radioligand binding or cell adhesion Equation 7 was used (where *TB* is total binding of radioligand (DPM) or total cell adhesion (fluorescence intensity) determined in the presence of vehicle (1 % DMSO), *Binding* is the level of binding observed in DPM (radioligand binding) or fluorescence intensity (cell adhesion) at a particular concentration of unlabelled integrin ligand and *NSB* is non-specific binding determined in the presence of 10 µM

SC-68448 (radioligand binding in DPM) or 10 mM EDTA (cell adhesion in fluorescence intensity)).

$$\%\ Inhibition\ Binding/Cell\ Adhesion = \left[\frac{(TB - Binding)}{(TB - NSB)}\right] \times 100 \qquad (7)$$

IC_{50} values generated from competition binding curves against [^{3}H]compound **1**, [^{3}H]compound **3** and [^{3}H]A20FMDV2 (where [^{3}H]compound **1**, [^{3}H]compound **3** and [^{3}H]A20FMDV2 saturation binding curve $n_H = 1$) were converted to equilibrium dissociation constant (K_I) values using the Cheng-Prusoff equation (Cheng and Prusoff, 1973) (Equation 8 where L^* is the radioligand concentration).

$$K_I = \frac{IC_{50}}{1 + \frac{[L^*]}{K_D}} \qquad (8)$$

In studies designed to determine the αvβ6 receptor dissociation rates of unlabelled integrin ligands, the percentage inhibition of radioligand binding was calculated at each time point using Equation 7 (where *TB* is total binding of radioligand (DPM) determined in the presence of vehicle (1 % DMSO), *Binding* is the level of binding observed in DPM at a 2 x K_I concentration of unlabelled integrin ligand and *NSB* is non-specific binding (DPM) determined in the presence of 10 μM SC-68448). This data was an indicator of the amount of unlabelled ligand remaining bound at the integrin at a given time point.

In flow cytometric experiments, isotype controls for each of the specific antibodies were used to determine the background fluorescence (MFI) of non-specific antibody binding and therefore were subtracted from the antibody MFI to give the specific window. Measurement of the β6 integrin subunit in flow cytometric assays was used

as a surrogate for the αvβ6 heterodimer and for ligand-induced internalisation CRCs data were expressed as % internalised αvβ6 using Equation 9 (where *x* represents the MFI of hβ6-PE staining in the absence of test compound, *y* represents the MFI of hβ6-PE staining in the presence of compound and *z* represents the MFI of IgG2B-PE staining).

$$\%\ Internalised\ \alpha v\beta 6 = \frac{(x-y)}{(x-z)} \times 100 \quad (9)$$

For rates of ligand-induced internalisation and subsequent recycling of β6, data were expressed as % αvβ6 surface expression using Equation 10 (where *% αvβ6 SE* is the % αvβ6 surface expression, *x* represents the MFI of hβ6-PE staining in the absence of compound, *y* represents the MFI of hβ6-PE staining in the presence of compound and *z* represents the MFI of IgG2B-PE staining).

$$\%\ \alpha v\beta 6\ SE\ = 100 - \left(\frac{(x-y)}{(x-z)} \times 100 \right) \quad (10)$$

The ligand-induced β6 internalisation data for compounds were fitted to a one-phase decay model (Equation 11 where *% αvβ6 SE* is the % αvβ6 surface expression, k_{in} is the internalisation rate constant in inverse units of time (min^{-1}) and *% αvβ6* $SE_{t=\infty}$ is % αvβ6 surface expression determined at infinite time). Internalisation $t_{1/2}$ values were calculated using the equation $t_{1/2} = 0.693/k_{in}$.

$$\%\ \alpha v\beta 6\ SE = \left(\%\alpha v\beta 6 SE_{t=0} - \%\alpha v\beta 6 SE_{plateau}\right).exp^{(-k_{in}.\,min)} + \%\alpha v\beta 6 SE_{t=\infty} \quad (11)$$

The recycling data for β6 post-ligand-induced internalisation with compounds were fitted to a one-phase association model (Equation 12 where *% αvβ6 SE* is the % αvβ6 surface expression, k_{out} is the recycling rate constant in inverse units of time (h^{-1})). Recycling $t_{1/2}$ values were calculated using the equation $t_{1/2} = 0.693/k_{out}$.

$$\%\ \alpha v\beta 6\ SE\ = \left(\%\,\alpha v\beta 6\,SE_{\ plateau}\ - \%\,\alpha v\beta 6\,SE_{\ t=0}\right)\left(1 - exp^{\left(-k_{out}.h\right)}\right) \qquad (12)$$

To calculate the percentage inhibition of TGFβ activation production from SW480-αvβ6 and NHBE cells, Equation 13 was used (where *max [RLU]* is the maximum RLU measured in the presence of vehicle (0.1 % DMSO), *test [RLU]* is the RLU measured at a particular concentration of compound and *min [RLU]* is RLU measured in the presence of 0.1 μM compound **3**).

$$\%\ Inhibition\ TGF\beta\ Activation = \left[\frac{\left(max[\,RLU\,] - test[\,RLU\,]\right)}{\left(max[\,RLU\,] - min[\,RLU\,]\right)}\right] \times 100 \qquad (13)$$

To calculate the percentage release of TGFβ from SW480-αvβ6 and NHBE cells, Equation 14 was used (where *max [RLU]* is the maximum RLU measured in the presence of vehicle (0.1 % DMSO), *test [RLU]* is the RLU measured at a particular concentration of compound and *min [RLU]* is RLU measured in the presence of 0.1 μM compound **3**).

$$\%\,TGF\beta\ Release = 100 - \left[\left[\frac{\left(max[\,RLU\,] - test[\,RLU\,]\right)}{\left(max[\,RLU\,] - min[\,RLU\,]\right)}\right] \times 100\right] \qquad (14)$$

Quantitative analysis of the intensity of β6 staining by immunofluorescence confocal microscopy was completed using Columbus™ Image Data Storage and Analysis System (PerkinElmer LAS UK Ltd., Beaconsfield, UK) analysis algorithms. Cell nuclei were detected using the 'Find Nuclei' algorithm (method A) as blue (Hoechst 33342 dye) fluorescent regions > 30 pixel^2, with a split factor of 7.0, an individual threshold of 0.40 and a contrast > 0.10. Cytoplasmic and membrane regions of cells were detected using 'Find Cytoplasm' algorithm (method A) as green (Alexa Fluor® 488) fluorescent regions with an individual threshold of 0.15. Using these alogorithms cells were identified and counted by their nuclei (Hoechst 33342 dye

staining) and whole cell mean β6 marker intensity (Alexa Fluor® 488 fluorescence) calculated.

Where applicable for fitting data with a line of best fit, the equation $y = mx + c$ was used (where m is the gradient and c is the intercept the linear regression fit) and a r^2 value reported. All statistical analyses were completed using Prism 5.0 (GraphPad Software, San Diego, CA, USA) and differences of $p < 0.05$ were considered to be statistically significant. Statistical significance between two data sets was tested using a Student's unpaired *t*-test. One-way analysis of variance (ANOVA) was used for comparison of more than two datasets and, where significance was observed, an appropriate post-test completed. For determination of statistical difference between a single data set and a hypothetical value a one-sample *t*-test was carried out. For comparison of model fitting the extra sum-of-squares F test was used with a threshold $p < 0.05$. Unless otherwise indicated, data shown graphically and in the text are either mean ± standard deviation (SD) or, where three or more data points/individual experiments have been completed, mean ± standard error of the mean (SEM).

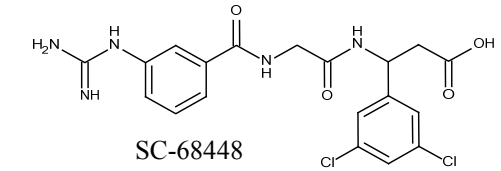

SC-68448

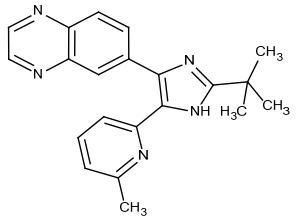

SB-525334

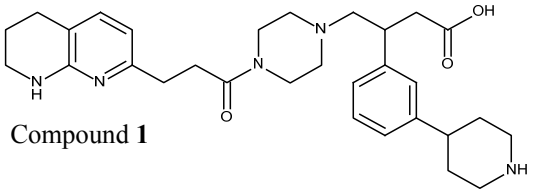

Compound **1**

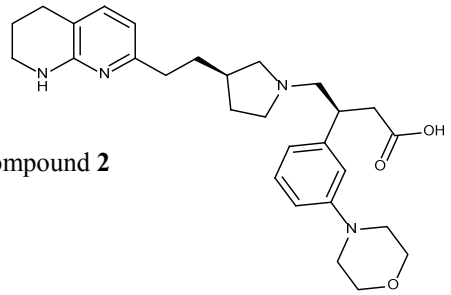

Compound **2**

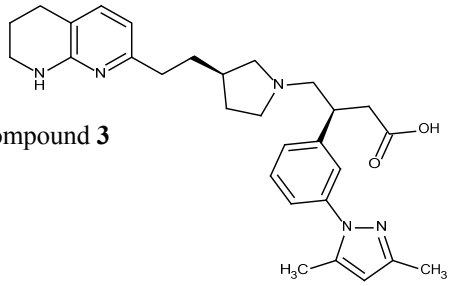

Compound **3**

Figure 2.1 Chemical structures of the small molecules used in this study.

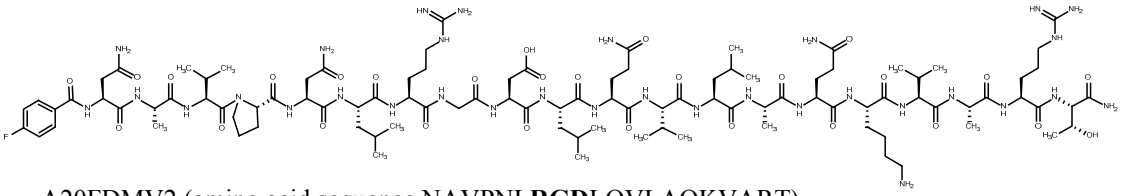

A20FDMV2 (amino acid sequence NAVPNL**RGD**LQVLAQKVART)

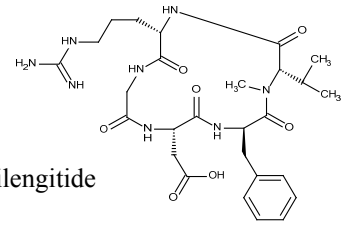

Cilengitide

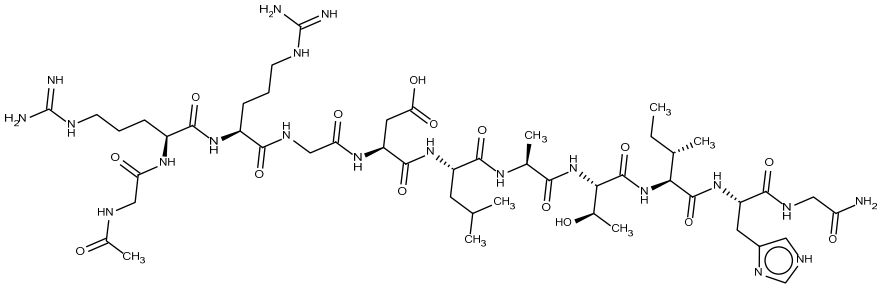

Truncated LAP_1 ($tLAP_1$)
(amino acid sequence GR**RGD**LATIHG)

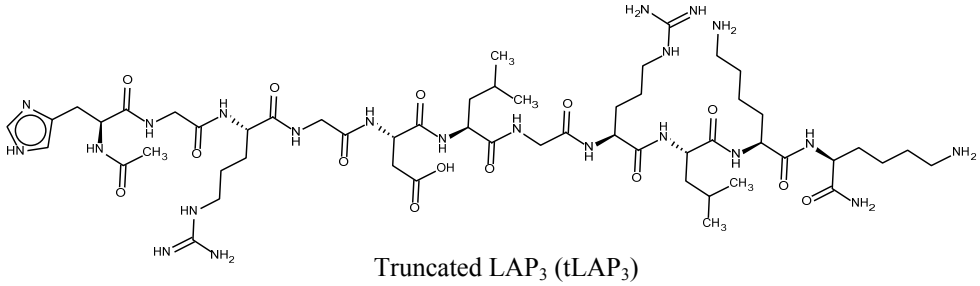

Truncated LAP_3 ($tLAP_3$)
(amino acid sequence HG**RGD**LGALKK)

LSTCKTIDMELVKRKRIEAIRGQILSKLRLASPPSQGEVPPGPLPEAVLALYNSTRDRV
AGESAEPEPEPEADYYAKEVTRVLMVETHNEIYDKFKQSTHSIYMFFNTSELREAVP
EPVLLSRAELRLLRLKLKVEQHVELYQKYSNNSWRYLSNRLLAPSDSPEWLSFDVT
GVVRQWLSRGGEIEGFRLSAHCSCDSRDNTLQVDINGFTTGR**RGD**LATIHGMNRPF
LLLMATPLERAQHLQSSRHRR

Full length LAP_1 ($fLAP_1$) amino acid sequence (RGD integrin binding sequence in bold)

Figure 2.2 Chemical structure and/or amino acid sequence of peptides used in this study.

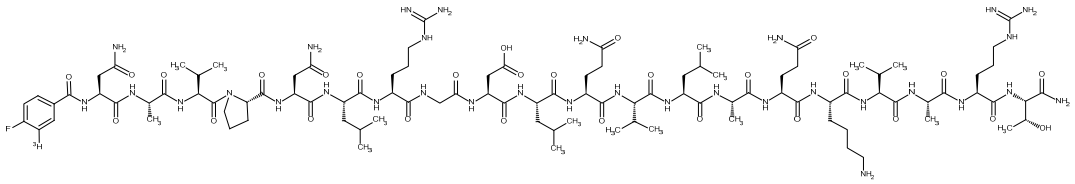

[^{3}H]A20FDMV2 (amino acid sequence NAVPNL**RGD**LQVLAQKVART)

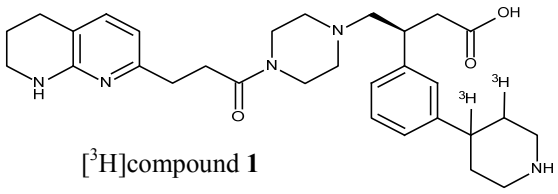

[^{3}H]compound **1**

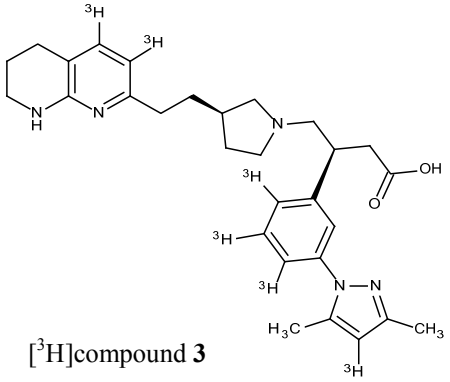

[^{3}H]compound **3**

Figure 2.3 Chemical structure and/or amino acid sequence of the radioligands used in this study.

CHAPTER 3: DETERMINING THE AFFINITY, SELECTIVITY AND KINETICS OF NOVEL, SMALL MOLECULE αVβ6 RGD-MIMETICS

3.1. Introduction

In order to achieve inhibition of TGFβ activation via αvβ6, a small molecule RGD-mimetic would be required to bind to the RGD binding site of the integrin and thereby compete with the endogenous large latent complex (consisting of the TGFβ1 or 3 isoform homodimer, LAP_1 or LAP_3 and the LTBP), or specifically the LAP_1 or LAP_3 component as it is this that contains the RGD amino acid binding motif. It is hypothesised that this would then result in a reduction in formation of active TGFβ and an inhibition of its pro-fibrotic effects. In order to effectively compete with the LLCs of either TGFβ1 or 3 from αvβ6, it would be hypothesised that a high affinity small molecule RGD-mimetic would be desirable to allow the delivery of a smaller dose of drug that would reduce the risk of off-target side effects. This could be dependent on both its selectivity compared with the other αv integrins as well as non-integrin off-target engagements.

Historically, the determination of the ability of an integrin ligand to compete with an endogenous ligand has been measured in either a cell adhesion assay (Barry *et al.*, 2000; Ludbrook *et al.*, 2003) or competitive binding enzyme-linked immunosorbent assay (ELISA) (Hausner *et al.*, 2007). The IC_{50} values generated via these techniques measure the ability of the integrin ligand to inhibit the binding of an endogenous peptide ligand to the integrin that is either recombinantly expressed in a cell line (cell adhesion) or a soluble integrin preparation (ELISA). Although efficient in being able to differentiate the rank order of IC_{50} values of a set of ligands against a particular integrin and also being high throughput (allowing hundreds of compounds to be screened every week in a full CRC format), one of the limitations of both these assay types is that a true affinity (K_I) value cannot be calculated. In order to measure a true

affinity or K_I of a ligand the Cheng-Prusoff equation (Cheng and Prusoff, 1973) is required (see section 2.11 Data analysis) that allows the binding affinity (K_D) and the amount of competing ligand to be taken into consideration. This equation corrects for these parameters and allows a true affinity estimate for a ligand in the absence of a competing ligand. In the assay system mentioned above, the parameters required for the Cheng-Prussoff can either not be determined or are a crude estimate. In addition, these assay types do not allow a full characterisation of the type of binding of the ligands in terms of being competitive and reversible (or not), and the kinetics of the ligand-integrin interaction cannot be ascertained.

As alternatives to the classical methods of determining integrin ligand affinity there are a number of options that include both new technologies (surface plasmon resonance (SPR), fluorescence polarisation (FP) binding (Copeland *et al.*, 2006)) and more established methodology (radioligand binding (Hulme and Trevethick, 2010)). Again there are advantages and disadvantages with all of these: SPR allows the determination of k_{on} and k_{off} of unlabelled ligands but analysis of small molecules is challenging due to the small changes in the resonance observed with low molecular weight ligands; FP binding assays are high throughput but suffer the same limitations as those described for the cell adhesion and ELISA formats; radioligand binding assays allow accurate binding characterisation including kinetics but are low throughput, higher cost and not as safe relative to non-radioactive alternatives. However, despite its limitations the radioligand binding assay still remains one of the most informative methods for characterising the interactions between a ligand and its protein/receptor binding partner. Interestingly, the method has not been used in characterisation of the binding of ligands with the αvβ6 integrin and has only been

used sparingly in the integrin field (Wong *et al.*, 1996; Egger *et al.*, 2003). Therefore, initial experimental studies described in this chapter were aimed at the characterisation of the radioligand binding profiles of a tritiated ([^{3}H]) pan-αv small molecule RGD-mimetic ([^{3}H]compound **1**) and a [^{3}H] αvβ6 selective peptide ([^{3}H]A20FMDV2). This would provide informative data on the similarities and differences between a small molecule RGD-mimetic and an RGD peptide binding interaction with the αvβ6 integrin. It will also provide tools and information for further studies exploring the binding of ligands to αvβ6 and other integrins in more complex physiological systems *in vitro* and *in vivo*.

Over the last 10 years there has been a significant body of literature implicating αvβ6 as a key player in IPF. As such, a drug discovery programme to identify small molecule αvβ6 inhibitors was set-up within GSK. Once a small molecule drug target has been selected the initial focus is upon generation of novel chemical entities that investigate the unexplored chemical space for the interaction with the biological target. The source of these new chemical templates can be generated from a number of different methods that can include HTS of millions of small molecule libraries or focussed screening sets containing chemical starting points, re-designing existing templates from the scientific literature and/or modelling from an endogenous ligand (if a structure for this is available). Regardless of the source of the small molecule, biological assays are required to test the activity as well as characterise and define the desired properties of a potential drug candidate. The early biological assays required for screening significant numbers of molecules on a regular basis e.g. hundreds of compounds every week, have to be robust and high throughput. Therefore, generally they are basic systems that have limitations in terms of the

information provided. Usually they will give an early measure of the binding affinity of a compound for the target protein (for example an enzyme, receptor or ion channel) or a functional potency measurement, that will allow molecules to be ranked and chemists to complete SAR analysis. The process then becomes more complex as other physico-chemical properties of these molecules are optimised whilst aiming to maintain the same activity at the target protein. Further complexity is added again when selectivity for the target protein is important whether within a sub-group of proteins (e.g. RGD integrins) or compared to a potential detrimental interaction with a known toxic mechanism (human Ether-à-go-go-Related Gene ion channel (Fermini and Fossa, 2003)).

There exists a fine balance between the throughput of an individual or panel of assays and their limitations in terms of physiological relevance and inter-assay comparisons. In the case of αvβ6 as a potential therapeutic target for IPF, in addition to the usual requirements for a small molecules physico-chemical properties to give it the best chance of progression as a drug (Walters, 2012), there is the selectivity over the other RGD integrins (specifically the αv integrins). The literature gives its weight to a selective αvβ6 small molecule being the most desired profile for IPF (Tatler and Jenkins, 2012) and therefore determination of an accurate selectivity profile early in the drug discovery process is critical. Historically this selectivity question has been answered in cell adhesion assays defining an IC_{50} value for inhibition of cells (recombinantly expressing an integrin) binding to an endogenous ligand coated on the plastic of a microtitre plate. The determination of selectivity of small molecules in these assay types is flawed due to the inability to correct for the concentration of competing endogenous ligand present as well as its affinity for the

integrin, as described previously. This issue is further exacerbated with the use of different competing endogenous ligands between different integrins.

Therefore, the later experimental studies described in this chapter were aimed at the identification and profiling of high affinity and αvβ6 selective small molecule RGD-mimetics by validation of the most appropriate test systems to investigate these characteristics within the constraints of throughput. In addition, to determine the dissociation profiles of small molecule RGD-mimetics from the αvβ6 integrin, the design and implementation of a novel radioligand binding assay is described. This has allowed the opportunity to compare the kinetics of potential drug candidates at a much earlier stage of the optimisation process and thus increase the chance of discovery and development of a drug with a long duration of action. This would only allow molecules with the most desirable profiles, in terms of affinity, selectivity and kinetics, to be taken forward for further analysis in more complex physiological systems *in vitro* and *in vivo*, and aid in the characterisation and development of a novel αvβ6 small molecule RGD-mimetic inhibitor as a potential therapeutic agent for IPF.

3.2. Results

3.2.1. General radioligand binding assay optimisation

In order to develop accurate and robust radioligand binding assays for [^{3}H]compound **1** (against αvβ1, αvβ3, αvβ5, αvβ6 and αvβ8 integrins) and for [^{3}H]A20FMDV2 (against the αvβ6 integrin), a number of conditions were optimised. These included integrin protein concentration, number of filtration washes, filter mat soak solution,

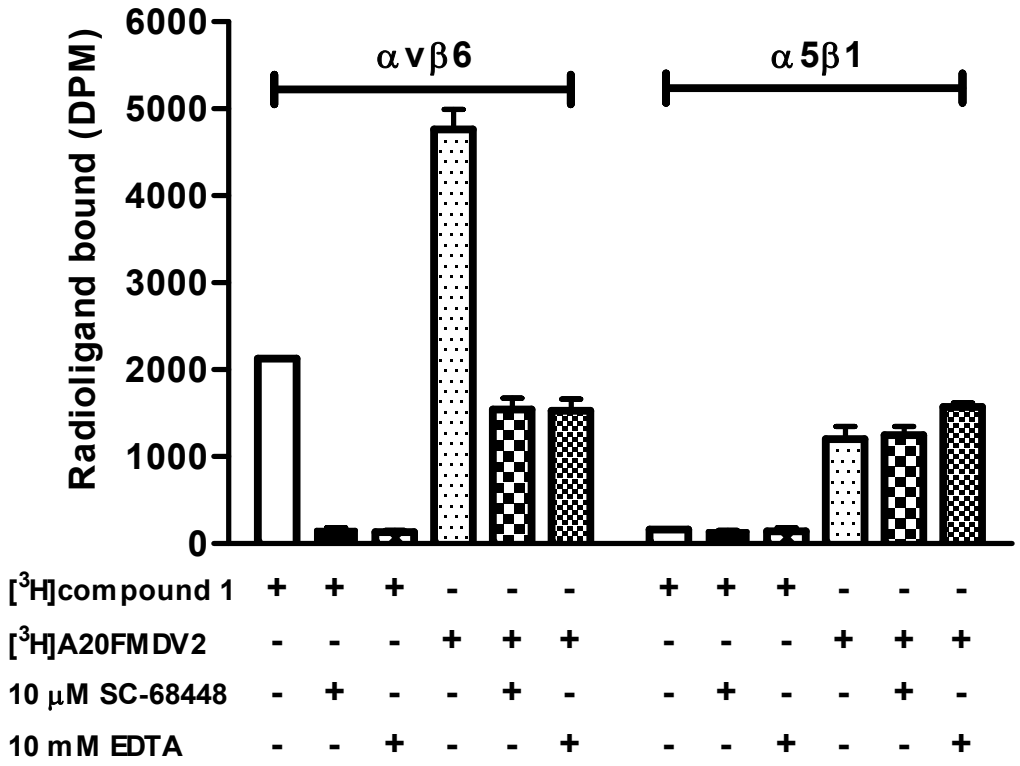

Figure 3.2.1 [^{3}H]compound 1 and [^{3}H]A20FMDV2 specifically bind in a divalent metal cation-dependent manner to αvβ6 but do not bind to α5β1. Total and non-specific binding of radioligands were measured by incubation of [^{3}H]compound **1** or [^{3}H]A20FMDV2 with soluble integrin protein in the presence of either vehicle (1 % DMSO), 10 μM SC-68448 or 10 mM EDTA (chelating agent). Plates were then filtered after a 6 h incubation and the amount of radioligand bound to integrin measured by liquid scintillation spectroscopy. Experiments were carried out using ~1 nM concentrations of radioligand with the same concentration of each integrin type per well (0.3 nM). Data shown are the mean ± SD of duplicate points and are representative of four individual experiments with similar results.

wash buffer and incubation time. The concentration of integrin used in each radioligand binding assay was optimised to ensure < 30 % of radioligand was bound under all conditions. This would negate the issues associated with ligand depletion and deviation from the law of mass action (Hulme and Birdsall, 1992) that could result in the underestimation of affinity values within an assay. However, during saturation studies with [^{3}H]A20FMDV2 it was observed that at some of the lower radioligand concentrations tested >30 % radioligand was bound. The experimental analyses to investigate if ligand depletion was occurring within these datasets are detailed in Results 3.2.5. The average % radioligand bound observed was 8.9 ± 0.4 % for [^{3}H]compound **1** and 27.0 ± 2.5 % for [^{3}H]A20FMDV2 (mean ± SEM, n=25-46) in the αvβ6 integrin assays. However, for competition binding with [^{3}H]A20FMDV2 the average % radioligand bound observed was 10.7 ± 1.4 % (mean ± SEM, n=4). The average % radioligand bound observed within αvβ1, αvβ3, αvβ5 and αvβ8 binding experiments was 2.3 ± 0.4, 5.2 ± 0.5, 2.7 ± 0.4 and 1.4 ± 0.1 %, respectively (mean ± SEM, n=8-20).

A high level of NSB (as defined by 10 μM SC-68448) was observed in experiments where no washes were included post-filtration of binding plates (data not shown). As the number of washes was increased a reduction in NSB and a stabilisation of the specific binding window (measured by subtracting the NSB from the total radioligand binding in the presence of vehicle (1 % DMSO)) was observed, with three washes resulting in an optimum specific binding window and low NSB (data not shown). In addition, soaking of filter mats pre-filtration in water resulted in a high level of radioligand bound to the filter mat and this was overcome by soaking in 0.3 % v/v PEI (data not shown). This method is routinely used in radioligand

filtration binding assays to coat NSB sites on filters prior to filtration and also aid in capture of soluble receptors (Hulme and Birdsall, 1992).

Another condition that can affect affinity measurements in radioligand filtration binding assays is the buffer used to wash filters. In some cases a change in the composition of buffer from that used in the dilution of reagents (binding buffer) to that used for washing filters (wash buffer) e.g. in these studies a HEPES based binding buffer washed with dH_2O, can result in a decrease in the affinity of a radioligand for its receptor. Therefore, to ensure this was not occurring, saturation binding was completed using binding buffer and dH_2O. No difference in affinity was observed between conditions ([^{3}H]compound **1** $\log_{10} K_D$ (pK_D) values of 8.94 ± 0.07 and 8.85 ± 0.18 for dH_2O and binding buffer respectively, and [^{3}H]A20FMDV2 pK_D values of 9.75 ± 0.10 and 9.89 ± 0.04 for dH_2O and binding buffer respectively (mean ± SEM, n=4-8)).

To test if saturation and competition binding experiments were being completed at equilibrium i.e. that binding was at steady state in the system (Hulme and Trevethick, 2010), extended incubation times were required. As all experiments were undertaken at physiological temperature (37ºC) a robust and stable specific binding window was required, in some cases, up to 24 h. Both αvβ3 ([^{3}H]compound **1**) and αvβ6 ([^{3}H]compound **1** and [^{3}H]A20FMDV2) were shown to exhibit a stable specific window up to 6 h (48 h for [^{3}H]compound **1** binding to αvβ6) (data not shown). The specific windows observed for [^{3}H]compound **1** binding to αvβ5 and αvβ8 were only stable for 2 h at 37ºC, potentially due to protein degradation with these integrin protein preparations (data not shown). However, due to the low affinity [^{3}H]compound **1** exhibited for αvβ5 and αvβ8 (Table 3.2.3) and therefore the

predicted fast kinetics, an incubation time of 2 h would be predicted to be sufficient for equilibrium to be achieved with this radioligand binding to αvβ5 and αvβ8.

No specific binding was observed for [^{3}H]compound **1** and [^{3}H]A20FMDV2 against the alpha-5 beta-1 (α5β1) integrin (Figure 3.2.1) showing that these radioligands did not bind to this integrin. Therefore, α5β1 acted as a control recombinant protein preparation generated via the same method as the other integrins tested and thus supported a conclusion that the observations in the individual αvβ1, αvβ3, αvβ5, αvβ6 and αvβ8 integrin assays were due to binding to these integrins alone.

3.2.2. [^{3}H]compound 1 and [^{3}H]A20FMDV2 αvβ6 integrin binding divalent cation dependency

The regulation of ligand binding to integrins has been shown to be dependent on divalent cations due to the presence of allosteric cation binding sites within their protein structure (Plow *et al.*, 2000; Hynes, 2002). Binding of [^{3}H]compound **1** and [^{3}H]A20FMDV2 to αvβ6 also required the presence of divalent cations with Ca^{2+}, Mg^{2+} and Mn^{2+} able to support the binding of [^{3}H]compound **1** and [^{3}H]A20FMDV2 (Figure 3.2.2). The propensity to support the binding of [^{3}H]A20FMDV2 is comparable between all the cations tested and all enabled maximal binding of [^{3}H]A20FMDV2 to αvβ6. However, Mn^{2+} (EC_{50} 2.3 ± 0.5 μM) was able to support this at much lower concentrations compared with Mg^{2+} (EC_{50} 59.9 ± 4.0 μM) and Ca^{2+} (EC_{50} 79.7 ± 26.2 μM) (mean ± SEM, n=4). This trend was also observed with [^{3}H]compound **1** (EC_{50}'s of 3.2 ± 0.9 μM, 235.7 ± 55.3 μM and 211.7 ± 42.7 μM for Mn^{2+}, Mg^{2+} and Ca^{2+}, respectively). There was a significant difference between the EC_{50} observed for Mg^{2+} between radioligands (ANOVA, Bonferroni post-test, $p <$

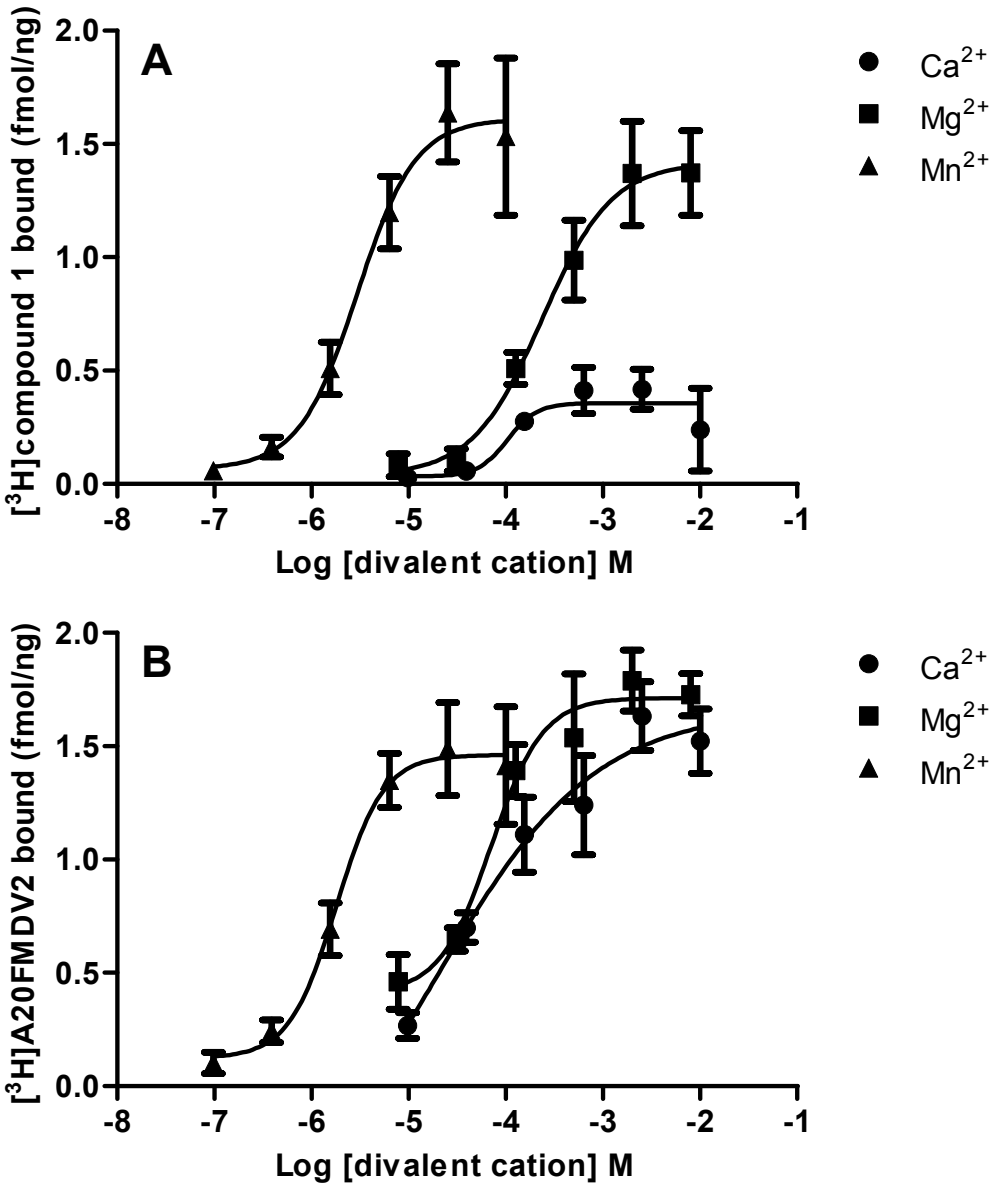

Figure 3.2.2 [^{3}H]compound 1 and [^{3}H]A20FMDV2 display different αvβ6 binding profiles in the presence of different divalent metal cations. Specific binding of radioligands were measured by incubation of [^{3}H]compound **1** (A) or [^{3}H]A20FMDV2 (B) with soluble αvβ6 integrin protein (0.3 nM) in the presence of either vehicle (1 % DMSO) or 10 μM SC-68448 in the presence of increasing concentrations of Ca^{2+}, Mg^{2+} or Mn^{2+}. Plates were then filtered after a 6 h incubation and the amount of radioligand bound to αvβ6 measured by liquid scintillation spectroscopy. Specific binding was measured by subtracting the non-specific binding (10 μM SC-68448) from the total radioligand binding in the presence of vehicle (1 % DMSO) with disintegration per minute values converted to fmol/ng (as detailed in 2.11 Data analysis section). Experiments were carried out using between 2 and 4 x K_D concentrations of radioligand. Data shown are the mean ± SEM of four individual experiments carried out in quadruplicate.

0.05) and Ca^{2+} was unable to produce maximal binding of the small molecule RGD-mimetic radioligand (up to a concentration of 10 mM) compared with Mn^{2+} and Mg^{2+}.

3.2.3. [^{3}H]compound 1 and [^{3}H]A20FMDV2 αvβ6 integrin kinetic binding studies

In kinetic binding studies the association of [^{3}H]compound **1** and [^{3}H]A20FMDV2 to the αvβ6 integrin was measured at ~K_D and 5 x K_D concentrations of radioligand. Global fitting of the association kinetic model to specific association binding data resulted in k_{on} values of 9.7 ± 1.1 x 10^7 and 5.7 ± 0.2 x 10^7 $M^{-1}.min^{-1}$ for [^{3}H]compound **1** and [^{3}H]A20FMDV2 respectively (mean ± SEM, n=4). The association with the αvβ6 observed for [^{3}H]compound **1** was ~1.7 fold faster than that of [^{3}H]A20FMDV2. In addition to determining accurate k_{on} values for [^{3}H]compound **1** and [^{3}H]A20FMDV2, the time it took to reach plateau at these concentrations of radioligand was required to determine the optimum radioligand/integrin pre-incubation period in dissociation binding studies. For [^{3}H]compound **1** the plateau (i.e. when equilibrium or steady state) was achieved at 15 and 15 min and for [^{3}H]A20FMDV2 at 45 and 60 min, for the K_D and 5 x K_D concentrations of radioligand respectively (Figure 3.2.3). Therefore, the pre-incubation time used in dissociation studies for both radioligands was 1 h to ensure equilibrium binding with the αvβ6 integrin had been achieved in the system at radioligand concentrations > K_D.

In order to measure dissociation k_{off} and $t_{1/2}$ values and gain insight into any mechanistic differences between [^{3}H]compound **1** and [^{3}H]A20FMDV2, dissociation

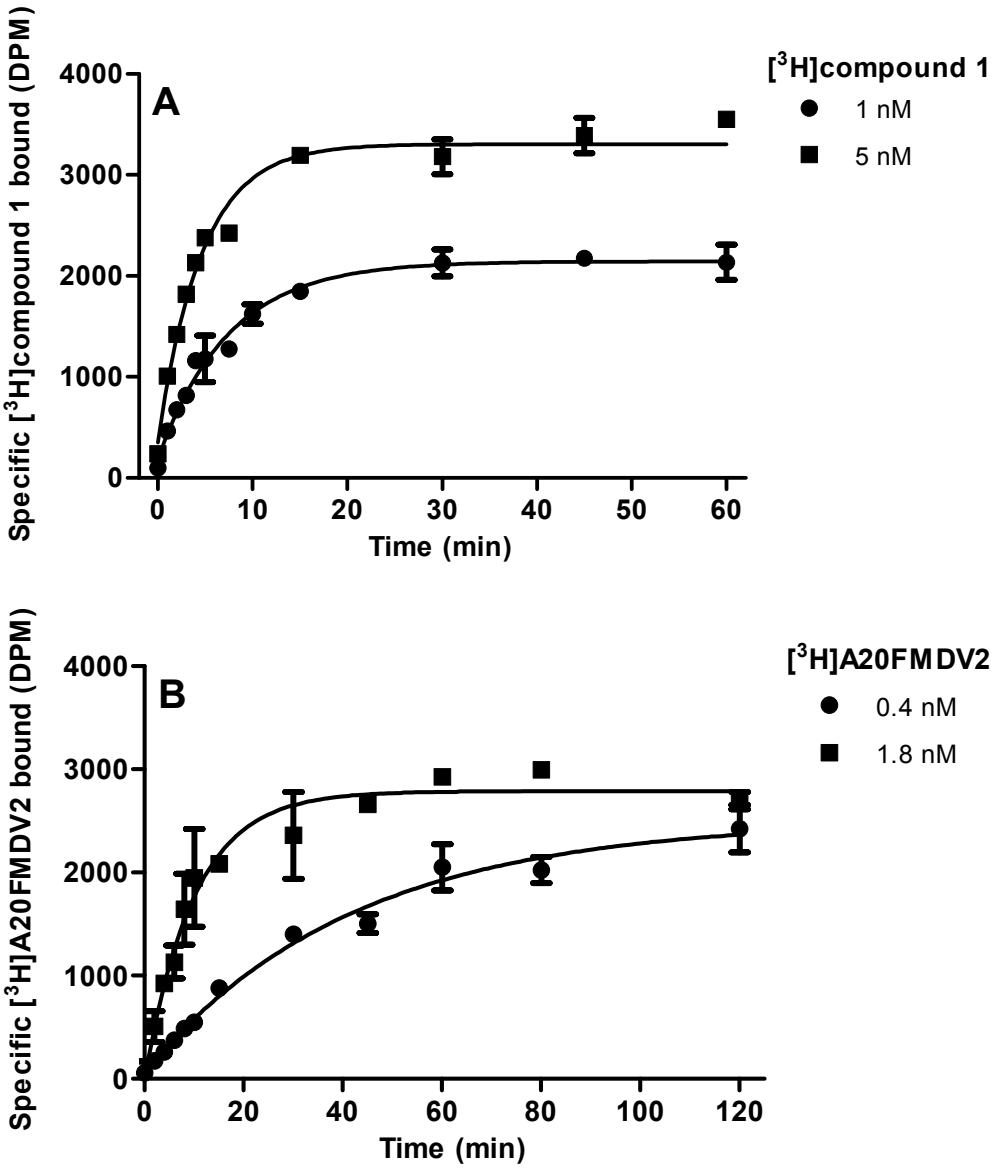

Figure 3.2.3 Association binding kinetics of [^{3}H]compound 1 (A) and [^{3}H]A20FMDV2 (B) to the αvβ6 integrin. Specific binding of radioligands were measured by incubation of [^{3}H]compound **1** or [^{3}H]A20FMDV2 with soluble αvβ6 integrin protein (0.3 nM) in the presence of either vehicle (1 % DMSO) or 10 μM SC-68448. Plates were then filtered after the time indicated and the amount of radioligand bound to αvβ6 was measured by liquid scintillation spectroscopy. Specific binding was measured by subtracting the non-specific binding (10 μM SC-68448) from the total radioligand binding in the presence of vehicle (1 % DMSO). Association binding data were generated at the radioligand concentrations indicated (~ K_D and 5 x K_D) and globally fitted to the association kinetic model (see 2.11 Data analysis section). Data shown are the mean ± SD of duplicate points and are representative of four individual experiments with similar results.

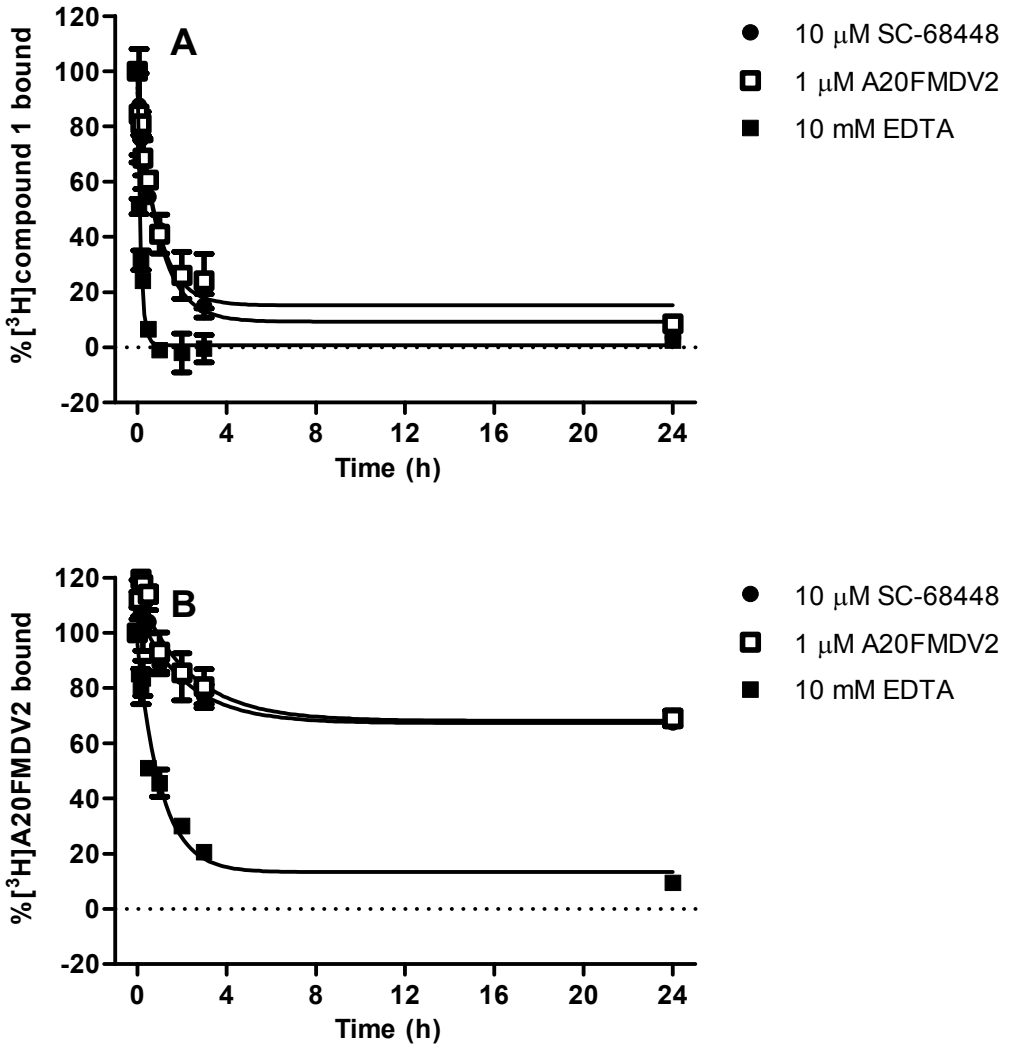

Figure 3.2.4 Dissociation αvβ6 binding kinetic profiles of [^{3}H]compound 1 (A) are different to [^{3}H]A20FMDV2 (B). Soluble αvβ6 integrin protein was pre-incubated for 1 h with a fixed concentration of radioligand (~1 nM) before dissociation was initiated by either addition of 10 μM SC-68448, 1 μM A20FMDV2 or 10 mM EDTA. Plates were then filtered after the time indicated and the amount of radioligand bound to αvβ6 was measured by liquid scintillation spectroscopy. Total and non-specific binding values were measured at each time point in the presence of vehicle (1 % DMSO) and 10 μM SC-68448 respectively, and were used to calculate the % inhibition of radioligand bound to the αvβ6 integrin (see 2.11 Data analysis section). Dissociation binding data were fitted to a one-phase dissociation model (see 2.11 Data analysis section), where appropriate, to generate k_{off} values. Data shown are the mean ± SD of duplicate points and are representative of at least four experiments with similar results.

	Radioligand Dissociation $t_{1/2}$ (min)		
Dissociating Condition	*10 μM SC-68448*	*1 μM A20FMDV2*	*10 mM EDTA*
[^{3}H]compound 1	15.9 ± 5.0	17.1 ± 4.8	5.1 ± 1.9
[^{3}H]A20FMDV2	*94.6 ± 20.1	*101.2 ± 19.3	119.7 ± 13.9

Table 3.2.1 Dissociation binding kinetics of [^{3}H]compound 1 and [^{3}H]A20FMDV2 from the αvβ6 integrin. Dissociation of [^{3}H]compound **1** and [^{3}H]A20FMDV2 from the soluble αvβ6 integrin protein was initiated (following a 1 h pre-incubation with integrin) by either addition of 10 μM SC-68448, 1 μM A20FMDV2 or 10 mM EDTA. Dissociation binding data from each of these methods of dissociation were fitted to a one-phase dissociation model (see 2.11 Data analysis section) to generate k_{off} values. k_{off} values were subsequently used to calculate dissociation half-life ($t_{1/2}$) values using the equation $t_{1/2} = 0.693/k_{off}$. Data shown are mean values ± SEM for at least four individual determinations. *$t_{1/2}$ for the dissociation observed (dissociation plateaued with ~68-70 % [^{3}H]A20FMDV2 remaining bound) over time course tested (24 h). $t_{1/2}$, half-life.

was initiated via a number of different methods post-radioligand association to integrin. These included the addition of either 10 μM SC-68448, 1 μM A20FMDV2 or 10 mM EDTA. For all methods of dissociation, a single phase dissociation of [^{3}H]compound **1** binding from the αvβ6 integrin was observed with complete dissociation achieved at 24 h (Figure 3.2.4A). For [^{3}H]compound **1** the dissociation profiles initiated by 10 μM SC-68448 and 1 μM A20FMDV2 were comparable (Figure 3.2.4A) and the $t_{1/2}$ values (shown in Table 3.2.1) were not significantly different (ANOVA, Bonferroni post-test, $p > 0.05$ completed on $\log_{10}$ $t_{1/2}$ values). The $t_{1/2}$ observed when 10 mM EDTA was used to initiate dissociation was faster (~3-fold) compared with the other methods although the difference was not significant (ANOVA, Bonferroni post-test, $p > 0.05$). For [^{3}H]A20FMDV2 the dissociation profiles initiated by 10 μM SC-68448 and 1 μM A20FMDV2 were comparable and only a partial dissociation of the radioligand was observed (Figure 3.2.4B). At 24 h, 70 ± 2 % and 68 ± 2 % (mean ± SEM, n=4) of the radioligand was still bound following the initiation of dissociation using 10 μM SC-68448 and 1 μM A20FMDV2 respectively. However, with 10 mM EDTA a single phase dissociation of [^{3}H]A20FMDV2 binding from the αvβ6 integrin was observed with complete dissociation achieved by 24 h (Figure 3.2.4B). Although full dissociation was not observed for [^{3}H]A20FMDV2 with 10 μM SC-68448 and 1 μM A20FMDV2 the $t_{1/2}$ values for both these conditions were calculated as a plateau between 3 and 24 h was achieved. These rates were not significantly different from that observed with 10 mM EDTA (ANOVA, Bonferroni post-test, $p > 0.05$ completed on $\log_{10}$ $t_{1/2}$ values). There was a trend for increased $t_{1/2}$ values between [^{3}H]A20FMDV2 and [^{3}H]compound **1** for all dissociating conditions tested. Nonetheless, only a significant

difference was observed when comparing EDTA induced dissociation where the $t_{1/2}$ for [^{3}H]A20FMDV2 was observed to be ~24-fold slower than that of [^{3}H]compound **1** (ANOVA, Bonferroni post-test, $p < 0.01$).

3.2.4. [^{3}H]compound 1 and [^{3}H]A20FMDV2 integrin saturation binding studies

[^{3}H]compound **1** and [^{3}H]A20FMDV2 saturation binding studies were carried out with the αvβ6 integrin to characterise the mode of binding, determine the affinity and compare the number of binding sites labelled for each radioligand. Specific binding data from saturation experiments with [^{3}H]compound **1** were fitted to a one affinity site model (with Hill slope (n_H)) and analysis resulted in the pK_D, B_{max} and n_H values shown in Table 3.2.2. The binding to αvβ6 was saturable and high affinity (Figure 3.2.5A) with the n_H not significantly different from unity (one-sample *t*-test completed on $\log_{10} n_H$ vs. 0, $p > 0.05$) suggesting the binding of [^{3}H]compound **1** to αvβ6 followed the law of mass action at a single site. Saturation binding studies with [^{3}H]compound **1** against αvβ1, αvβ3, αvβ5 and αvβ8 were also completed (Table 3.2.3). Saturable binding of [^{3}H]compound **1** with these integrins was also observed with n_H values not significantly different from unity (one-sample *t*-test completed on $\log_{10} n_H$ vs. 0, $p > 0.05$), suggesting the binding of [^{3}H]compound **1** to these integrins also followed the law of mass action at a single site. The affinity of [^{3}H]compound **1** for αvβ3 and αvβ6 was comparable, as was its affinity for αvβ1, αvβ5 and αvβ8. [^{3}H]compound **1** exhibited an ~9 to 20-fold higher affinity for αvβ3 and αvβ6 compared with αvβ1, αvβ5 and αvβ8 (Table 3.2.3).

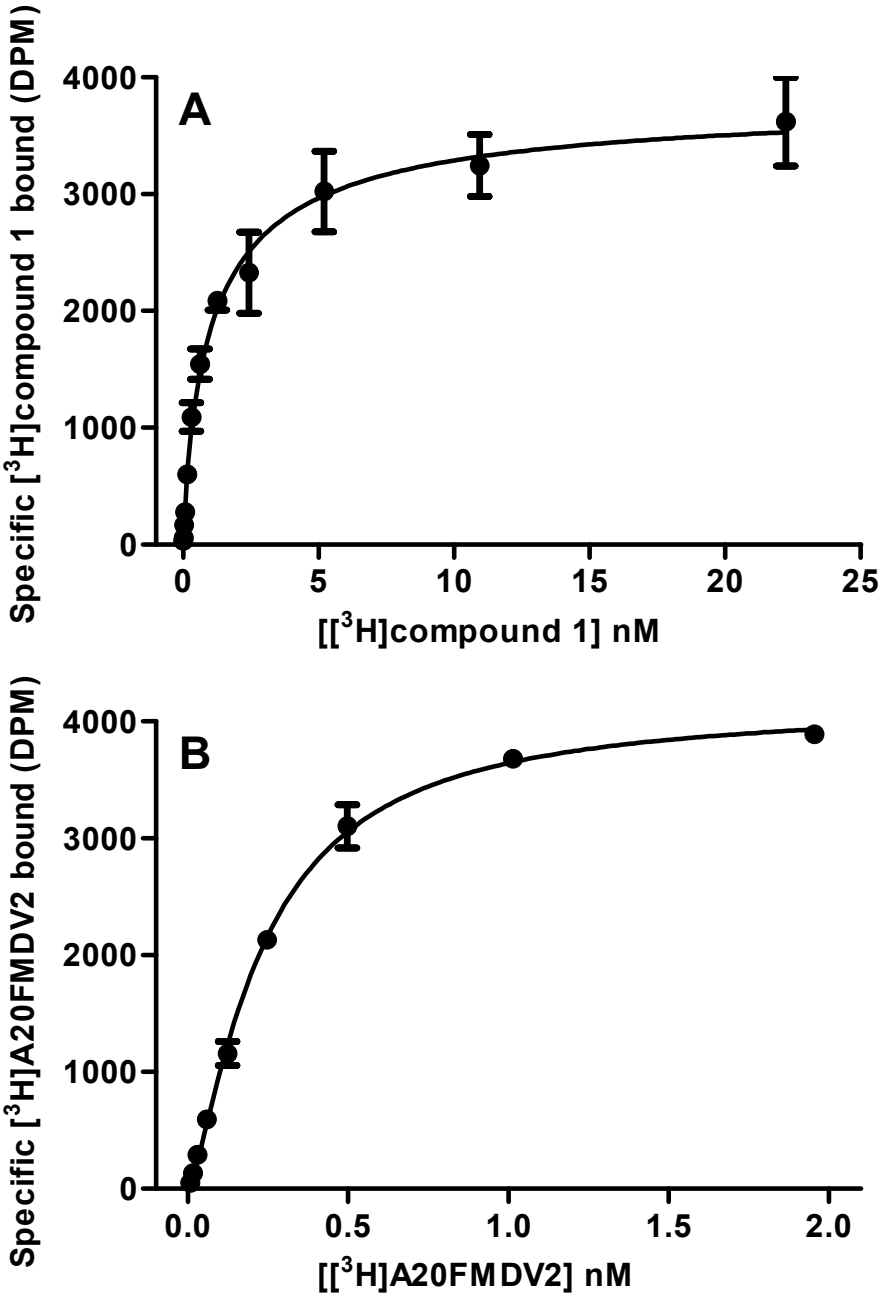

Figure 3.2.5 Saturation binding of [^{3}H]compound 1 and [^{3}H]A20FMDV2 to αvβ6. Specific binding of [^{3}H]compound **1** (A) and [^{3}H]A20FMDV2 (B) were measured by incubation of increasing concentrations of radioligand with soluble αvβ6 integrin protein (0.3 nM) in the presence of either vehicle (1 % DMSO) or 10 μM SC-68448. Plates were then filtered after a 6 h incubation and the amount of radioligand bound to αvβ6 was measured by liquid scintillation spectroscopy. Specific binding was measured by subtracting the non-specific binding (10 μM SC-68448) from the total radioligand binding in the presence of vehicle (1 % DMSO). Specific saturation binding data were fitted to a one affinity site model with Hill slope (see 2.11 Data analysis section). Data shown are the mean ± SD of duplicate points and are representative of eight individual experiments with similar results.

Radioligand	K_D (nM)	pK_D	Hill slope (n_H)	B_{max} (fmol/ng)
[^{3}H]compound 1	1.27 ± 0.26	8.94 ± 0.07	1.00 (0.73, 1.26)	2.73 ± 0.34
[^{3}H]A20FMDV2	0.22 ± 0.07	9.75 ± 0.10	1.20 (0.96, 1.44)	3.60 ± 0.41

Table 3.2.2 Saturation binding parameters for the binding of [^{3}H]compound 1 and [^{3}H]A20FMDV2 at the αvβ6 integrin. Specific saturation binding data were fitted to a one affinity site model with Hill slope (see 2.11 Data analysis section). Data shown are mean values ± SEM or 95 % confidence limits (shown in parentheses) for eight individual determinations. pK_D, negative $\log_{10}$ of K_D.

αv Integrin	*[^{3}H]compound **1** pK_D*	*[^{3}H]compound **1** Hill slope (n_H)*
αvβ1	7.98 ± 0.12	1.59 (0.86, 2.32)
αvβ3	9.17 ± 0.15	1.09 (0.25, 1.92)
αvβ5	7.88 ± 0.15	1.00 (0.41, 1.58)
αvβ6	8.94 ± 0.07	1.00 (0.73, 1.26)
αvβ8	7.96 ± 0.13	1.26 (0.79, 1.72)

Table 3.2.3 Saturation binding parameters for the binding of [^{3}H]compound 1 at the αv integrins. [^{3}H]compound **1** specific saturation binding data were fitted to a one affinity site model with Hill slope to determine K_D and n_H values (see 2.11 Data analysis section). Data shown are mean values ± SEM or 95 % confidence limits (shown in parentheses) for at least four individual determinations. pK_D, negative $\log_{10}$ of K_D.

Specific binding data from saturation experiments with [^{3}H]A20FMDV2 were fitted to a one affinity site model (with Hill slope (n_H)) and analysis resulted in the pK_D, B_{max} and n_H values shown in Table 3.2.2. The binding to αvβ6 was saturable and high affinity (Figure 3.2.5B) with the n_H not significantly different from unity (one-sample *t*-test completed on $\log_{10}$ n_H vs. 0, $p > 0.05$) suggesting the binding of [^{3}H]A20FMDV2 to αvβ6, as observed with [^{3}H]compound **1**, followed the law of mass action at a single site. Saturation binding for [^{3}H]A20FMDV2 to αvβ6 was also completed following a 24 h incubation time to ensure equilibrium had been achieved during the 6 h incubation time. The pK_D value calculated at 24 h was 9.69 ± 0.07 and this was not significantly different to the values determined at 6 h (Table 3.2.2) (ANOVA, Bonferroni post-test, $p > 0.05$). The affinity of [^{3}H]A20FMDV2 for αvβ6 was ~6-fold higher than that of [^{3}H]compound **1** and there was no significant difference observed between B_{max} values (Table 3.2.2) (Student's unpaired *t*-test, $p > 0.05$). These values were also comparable to literature B_{max} values using a solid-phase receptor binding assay with a purified protein preparation of αvβ3 (1.05 fmol/ng – Huang *et al.*, 2010), suggesting the B_{max} values determined in this study were typical when using soluble integrin protein preparations. As mentioned previously, during saturation studies with [^{3}H]A20FMDV2 it was observed that at some of the lower radioligand concentrations tested >30 % of the radioligand was bound to the αvβ6 integrin. Therefore in these studies there is likely ligand depletion at the lower concentrations of radioligand that could result in an under estimation of the affinity of the radioligand (Hulme and Birdsall, 1992). However, due to there being no significant difference (ANOVA, Bonferroni post-test, $p > 0.05$) between the pK_D values determined by saturation binding studies for [^{3}H]A20FMDV2 and

negative $\log_{10}$ K_I (pK_I) values determined by competition binding studies (Table 3.2.4) for A20FMDV2 against [^{3}H]compound **1**, this showed that ligand depletion in saturation binding studies was not an issue.

3.2.5. [^{3}H]compound 1 and [^{3}H]A20FMDV2 competition binding studies

In order to determine the affinity of unlabelled integrin ligands at the αvβ6 integrin under equilibrium conditions, competition displacement binding curves were measured against [^{3}H]compound **1** and [^{3}H]A20FMDV2 following a 6 h incubation period. The pK_I values determined for a range of unlabelled integrin ligands are summarised in Table 3.2.4. All unlabelled ligands inhibited the binding of [^{3}H]compound **1** and [^{3}H]A20FMDV2 except the αvβ3/5 selective molecule cilengitide (based on the cyclic peptide cyclo(-RGDfV-) (Goodman *et al.*, 2002)) when tested up to a top concentration of 1 μM. All ligands that did inhibit binding (except $fLAP_1$ against [^{3}H]A20FMDV2 due to the inability to test at concentrations above 50 nM) caused inhibition of radioligand binding to NSB levels (Figure 3.2.6) when tested against both radioligands. The pK_I values determined against [^{3}H]compound **1** correlated well with those determined against [^{3}H]A20FMDV2 (Figure 3.2.7). Unlabelled A20FMDV2 competition binding curves against [^{3}H]compound **1** at αvβ6 resulted in a pK_I that was not significantly different to the pK_D values determined for [^{3}H]A20FMDV2 in saturation binding studies (ANOVA, Bonferroni post-test, $p > 0.05$) (Tables 3.2.2 and 3.2.4). Unlabelled A20FMDV2 competition binding curves up to 1 μM against [^{3}H]compound **1** at αvβ1, αvβ3, αvβ5 and αvβ8 resulted in no inhibition of radioligand binding. The pK_I values determined for unlabelled compound **1** against [^{3}H]compound **1** at αvβ1, αvβ3, αvβ5, αvβ6 and αvβ8 were not significantly different to the values determined by saturation binding

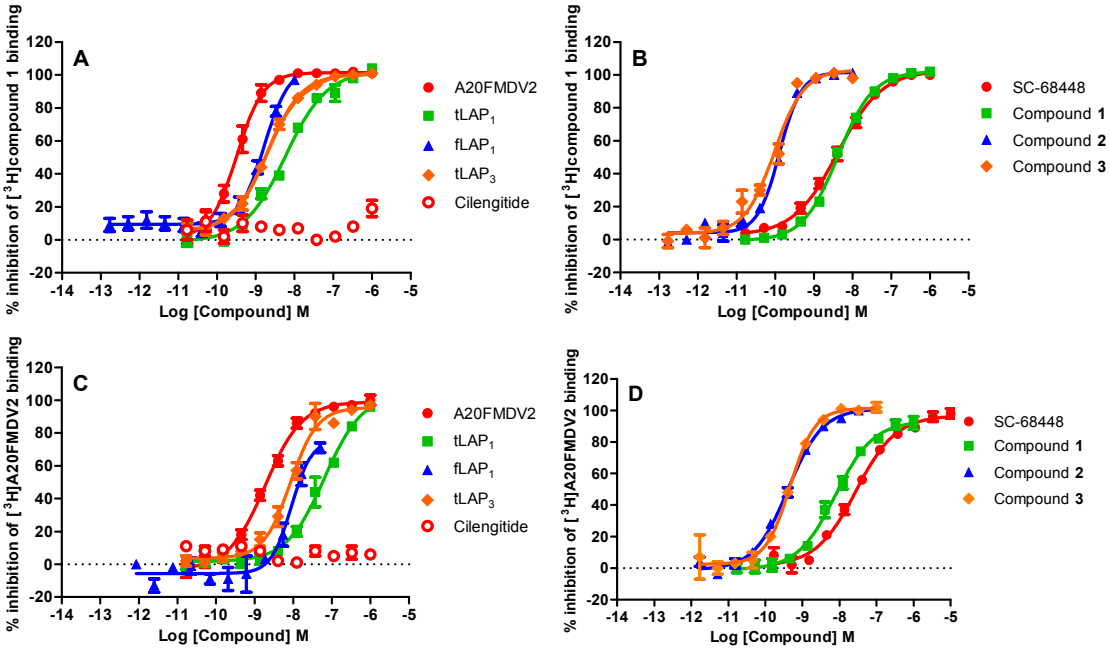

Figure 3.2.6 Competition displacement binding curves for integrin ligands against [^{3}H]compound 1 and [^{3}H]A20FMDV2 with the αvβ6 integrin. Full competition binding curves were generated by incubating unlabelled integrin ligand at a range of concentrations with soluble αvβ6 integrin protein (0.3 nM) and [^{3}H]compound **1** (~1 nM) or [^{3}H]A20FMDV2 (~2 nM). Plates were then filtered after a 6 h incubation and the amount of radioligand bound to αvβ6 was measured by liquid scintillation spectroscopy. Total and non-specific binding values were measured in the presence of vehicle (1 % DMSO) and 10 μM SC-68448 respectively, and were used to calculate the % inhibition of radioligand bound to the αvβ6 integrin (see 2.11 Data analysis section). Competition binding data were fitted using non-linear regression analysis (four-parameter logistic equation with variable slope (Hill, 1909)) (see 2.11 Data analysis section). Competition binding displacement curve data are the mean ± SEM of at least four individual experiments carried out in singlicate.

Integrin Ligand	pK_I ([^{3}H]compound ***1***)	Hill slope (n_H) ([^{3}H]compound ***1***)	pK_I ([^{3}H]A20FMDV2)	Hill slope (n_H) ([^{3}H]A20FMDV2)
SC-68448	8.56 ± 0.05	0.91 (0.85, 0.97)	8.34 ± 0.28	1.00 (0.87, 1.14)
A20FMDV2	9.82 ± 0.04	1.39 (0.89, 1.87)	9.62 ± 0.05	0.89 (0.67, 1.12)
tLAP$_1$	8.70 ± 0.07	0.87 (0.78, 0.96)	8.54 ± 0.12	1.01 (0.81, 1.22)
fLAP$_1$	9.19 ± 0.10	*1.31 (1.03, 1.59)	9.00 ± 0.08	1.84 (0.56, 3.11)
tLAP$_3$	8.91 ± 0.08	1.05 (0.93, 1.16)	8.95 ± 0.12	0.97 (0.70, 1.23)
Cilengitide	<6.35	N/A	<6.92	N/A
Compound 1	8.62 ± 0.03	0.97 (0.81, 1.14)	9.10 ± 0.07	0.89 (0.57, 1.21)
Compound 2	10.2 ± 0.02	*1.51 (1.39, 1.64)	10.3 ± 0.03	0.96 (0.66, 1.27)
Compound 3	10.4 ± 0.09	*1.64 (1.21, 2.08)	10.4 ± 0.02	1.18 (0.79, 1.56)

Table 3.2.4 The pK_I and Hill slope values at the αvβ6 integrin from competition binding between [^{3}H]compound 1 or [^{3}H]A20FMDV2 and a range of integrin ligands. Competition binding data were fitted using non-linear regression analysis (four-parameter logistic equation with variable slope (Hill, 1909)) (see 2.11 Data analysis section) to generate n_H and IC_{50} values. IC_{50} values generated were converted to K_I values using the Cheng-Prusoff equation (Cheng and Prusoff, 1973) (see 2.11 Data analysis section). Data shown are mean values ± SEM or 95 % confidence limits (shown in parentheses) for at least four individual determinations. *denotes n_H significantly greater than unity (one-sample *t*-test completed on $\log_{10} n_H$ vs. 0, $p < 0.05$). pK_I, negative $\log_{10}$ of K_I.

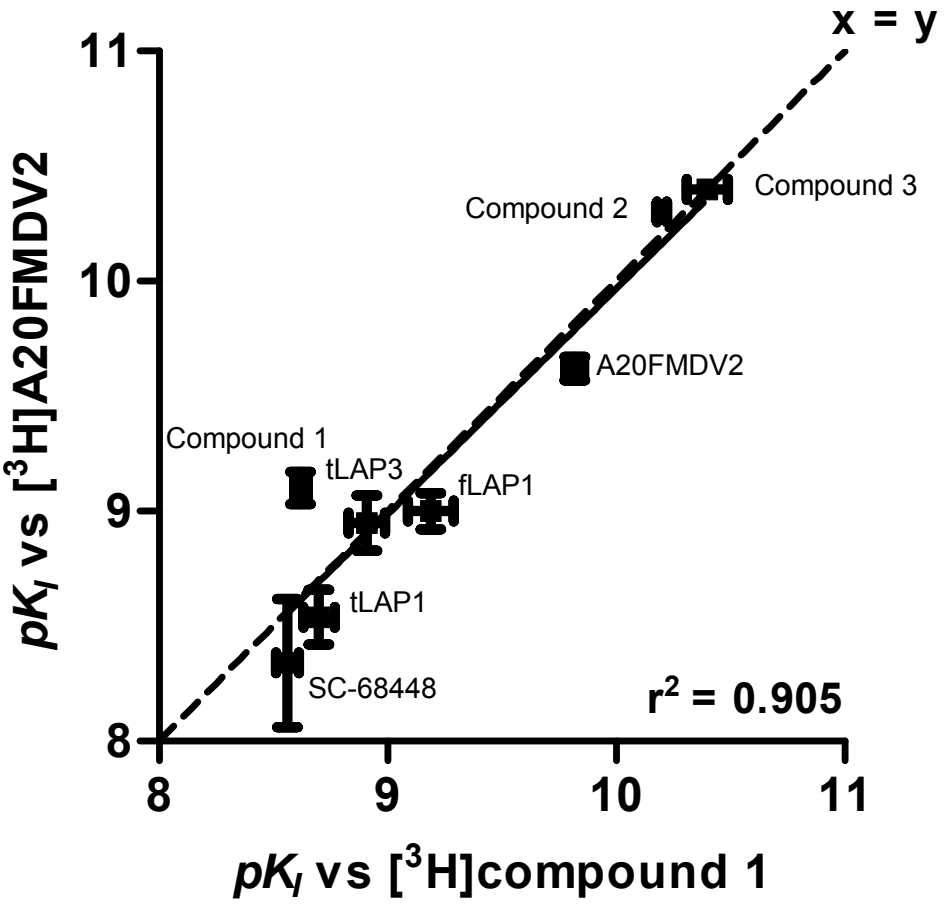

Figure 3.2.7 ***pK_I*** **values generated for integrin ligands from αvβ6 competition displacement binding curves against [^{3}H]compound 1 and [^{3}H]A20FMDV2 show a good correlation.** Full competition binding curves were generated by incubating unlabelled integrin ligand at a range of concentrations with soluble αvβ6 integrin protein (0.3 nM) and either [^{3}H]compound **1** (~1 nM) or [^{3}H]A20FMDV2 (~2 nM). Plates were then filtered after a 6 h incubation and the amount of radioligand bound to αvβ6 was measured by liquid scintillation spectroscopy. Total and non-specific binding values were measured in the presence of vehicle (1 % DMSO) and 10 μM SC-68448 respectively, and were used to calculate the % inhibition of radioligand bound to the αvβ6 integrin (see 2.11 Data analysis section). Competition binding data were fitted using non-linear regression analysis (four-parameter logistic equation with variable slope (Hill, 1909)) (see 2.11 Data analysis section) to generate n_H and IC_{50} values. K_I values were calculated from IC_{50} values (see 2.11 Data analysis section) and the pK_I (negative $\log_{10}$ of K_I) values generated for each unlabelled integrin ligand against [^{3}H]compound **1** and [^{3}H]A20FMDV2 are correlated (dotted line shows the straight line x = y and the solid line shows the linear regression fit with the r^2 value shown inset (see 2.11 Data analysis section). pK_I shown are the mean ± SEM of at least four individual experiments carried out in singlicate.

	pK_I				
αv Integrin	*αvβ1*	*αvβ3*	*αvβ5*	*αvβ6*	*αvβ8*
Compound 1	7.14 ± 0.02	8.75 ± 0.04	7.64 ± 0.03	8.62 ± 0.03	7.81 ± 0.04
A20FMDV2	<6.22	<6.45	<6.13	9.82 ± 0.04	<6.13

Table 3.2.5 Selectivity profile of compound 1 and A20FMDV2 against the αvβ1, αvβ3, αvβ5, αvβ6 and αvβ8 integrins determined by competition binding studies. Compound **1** and A20FMDV2 competition binding data were fitted using non-linear regression analysis (four-parameter logistic equation with variable slope (Hill, 1909)) (see 2.11 Data analysis section). IC_{50} values generated from competition binding curves against [^{3}H]compound **1** were converted to K_I values using the Cheng-Prusoff equation (Cheng and Prusoff, 1973) (see 2.11 Data analysis section). Data shown are mean values ± SEM for at least four individual determinations. pK_I, negative $\log_{10}$ of K_I.

studies completed with [^{3}H]compound **1** at these integrins, except for αvβ1 where a ~7-fold lower affinity was observed for compound **1** (ANOVA, Bonferroni post-test, $p > 0.05$) (Tables 3.2.3 and 3.2.5). In addition, the affinity observed for $fLAP_1$ under all conditions was comparable to that of the $tLAP_1$ (Table 3.2.4).

3.2.6. Comparison of cell adhesion and radioligand binding assays for profiling integrin small molecule RGD-mimetics

In order to compare the rank order of activity of a range of novel small molecule RGD-mimetics between cell adhesion and radioligand binding assays for the αvβ3, αvβ5, αvβ6 and αvβ8 integrins, negative $\log_{10}$ IC_{50} (pIC_{50}) values generated in cell adhesion (as an empirical measure of competitor potency) were correlated with pK_I values (true affinity measure) (Figure 3.2.8). In addition, the average fold shift between pIC_{50} and pK_I values within each integrin comparison were also calculated (fold shift = pK_I - pIC_{50}). The average fold shifts observed for αvβ3, αvβ5, αvβ6 and αvβ8 were 1.6 (1.3 to 1.8), 1.0 (0.5 to 1.8), 2.0 (1.4 to 2.8) and 0.5 (-0.3 to 1.2), respectively (mean with minimum and maximum values shown in parentheses, n=16-47). The straight lines that corresponded to the average fold shifts for each integrin are shown as the solid lines on the individual correlations in Figure 3.2.8. The largest average fold shift difference was shown with αvβ6 followed by αvβ3 then αvβ5 and finally αvβ8. αvβ8 displayed the closest agreement between cell adhesion and radioligand binding and this was the only integrin that had any values on or to the left of the x = y line (shown as dotted line Figure 3.2.8D). A set of small molecule RGD-mimetics and peptides were further investigated to compare the cell adhesion and radioligand binding assays for αvβ6 (Table 3.2.6). A similar trend was observed with a shift observed for all test ligands except cilengitide, that did not

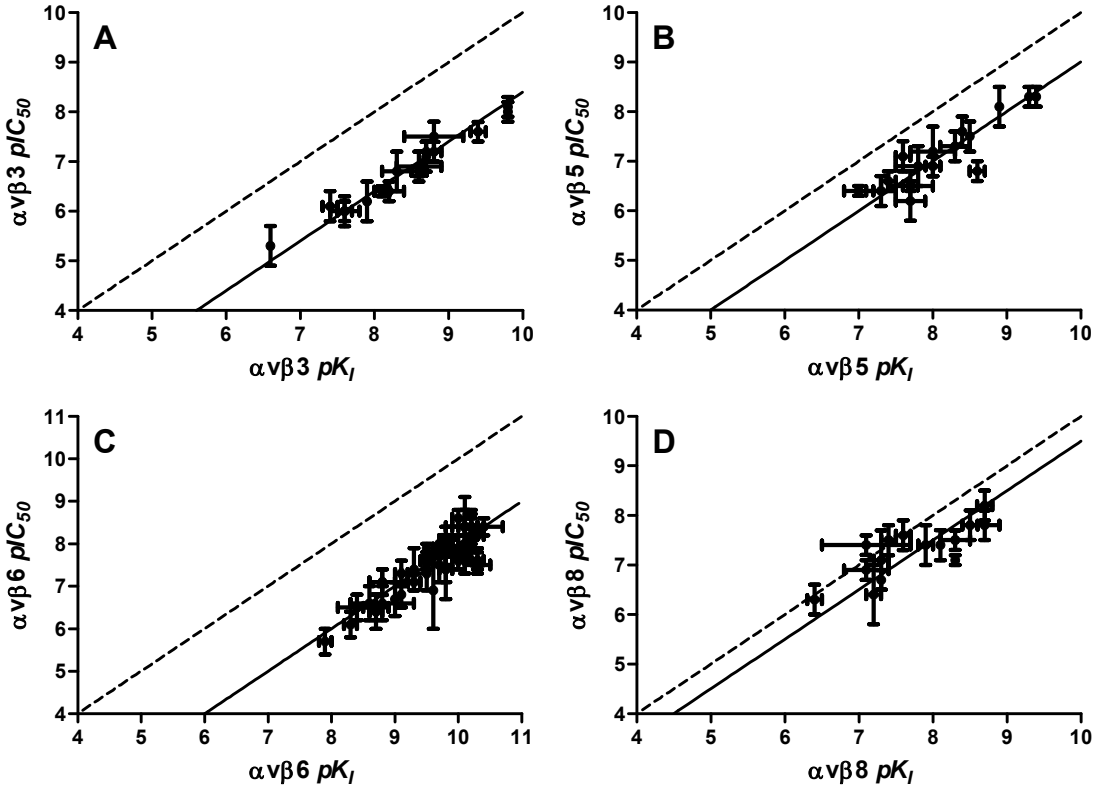

Figure 3.2.8 Correlation of pIC_{50} and pK_I values generated with small molecule RGD-mimetics from cell adhesion or radioligand competition binding (against [^{3}H]compound 1) studies, respectively, with either the αvβ3 (A), αvβ5 (B), αvβ6 (C) or αvβ8 (D) integrin. Full concentration response curves in cell adhesion assays were generated by incubating small molecule RGD-mimetics at a range of concentrations with K562 cells recombinantly expressing either the αvβ3, αvβ5, αvβ6 or αvβ8 integrin in plates coated with endogenous integrin ligand (for full details see 2. Materials and Methods and 8. Appendix sections). Plates were incubated for 30 min prior to removal of non-adherent cell populations and the remaining adherent cells were then quantified by fluorescence using BCECF-AM. Total and non-specific binding values were measured in the presence of vehicle (1 % DMSO) and 10 mM EDTA respectively, and were used to calculate the % inhibition of cell adhesion and IC_{50} values (see 2.11 Data analysis section). Full competition binding curves were generated by incubating small molecule RGD-mimetics at a range of concentrations with either the αvβ3, αvβ5, αvβ6 or αvβ8 soluble integrin protein (for integrin concentration see 2. Materials and Methods section) and [^{3}H]compound **1** (~1 to 7 nM dependent on integrin). Plates were then filtered after either a 2 h (αvβ5 and αvβ8) or 6 h (αvβ3 and αvβ6) incubation and the amount of radioligand bound to integrin was measured by liquid scintillation spectroscopy. Total and non-specific binding values were measured in the presence of vehicle (1 % DMSO) and 10 µM SC-68448 respectively, and were used to calculate the % inhibition of radioligand bound to each integrin tested (see 2.11 Data analysis section). Cell adhesion concentration response curves and competition binding data were fitted using non-linear regression analysis (four-parameter logistic equation with variable slope (Hill, 1909)) (see 2.11 Data analysis section) to generate n^H and IC_{50} values. K_I values were calculated from IC_{50} values (see 2.11 Data analysis section) and the pK_I (negative $\log_{10}$ of K_I) value generated for each unlabelled integrin ligand against [^{3}H]compound **1** are correlated for each integrin with the corresponding pIC_{50} (negative $\log_{10}$ of IC_{50}) value generated from cell adhesion (dotted line shows the straight line x = y, solid line shows the average fold-shift of pIC_{50} to pK_I for each integrin). pIC_{50} and pK_I shown are the mean ± SD of at least two individual experiments carried out in singlicate.

Integrin Ligand	*pK_I* *([^{3}H]compound **1**)*	*Hill slope (n_H)* *([^{3}H]compound **1**)*	*pIC_{50}* *(Cell adhesion)*	*Hill slope (n_H)* *(Cell adhesion)*
SC-68448	8.56 ± 0.05	0.91 (0.85, 0.97)	6.52 ± 0.02	0.85 (0.83, 0.88)
A20FMDV2	9.82 ± 0.04	1.39 (0.89, 1.87)	7.26 ± 0.21	*2.18 (1.39, 2.97)
tLAP$_1$	8.70 ± 0.07	0.87 (0.78, 0.96)	6.53 ± 0.06	0.96 (0.75, 1.18)
fLAP$_1$	9.19 ± 0.10	*1.31 (1.03, 1.59)	7.46 ± 0.32	*1.41 (1.07, 1.75)
tLAP$_3$	8.91 ± 0.08	1.05 (0.93, 1.16)	7.08 ± 0.14	1.07 (0.70, 1.44)
Cilengitide	<6.35	N/A	<5.00	N/A
Compound 1	8.62 ± 0.03	0.97 (0.81, 1.14)	7.48 ± 0.25	*0.78 (0.57, 0.99)
Compound 2	10.2 ± 0.02	*1.51 (1.39, 1.64)	8.34 ± 0.05	*1.31 (1.19, 1.42)
Compound 3	10.4 ± 0.09	*1.64 (1.21, 2.08)	8.50 ± 0.08	*1.67 (1.48, 1.87)

Table 3.2.6 The *pK_I* and *pIC_{50}* values, with associated Hill slope values, at the αvβ6 integrin from competition binding with [^{3}H]compound 1 or cell adhesion to glutathione S-transferase fusion-LAP$_1$ for a range of small molecule RGD-mimetics and peptides. Radioligand competition binding and cell adhesion concentration response curve data were fitted using non-linear regression analysis (four-parameter logistic equation with variable slope (Hill, 1909)) (see 2.11 Data analysis section) to generate IC_{50} and n_H values. IC_{50} values generated in radioligand competition binding studies were converted to K_I values using the Cheng-Prusoff equation (Cheng and Prusoff, 1973) (see 2.11 Data analysis section). Data shown are mean values ± SEM or 95 % confidence limits (shown in parentheses) for at least four individual determinations. Radioligand binding data shown taken from Table 3.2.4. *denotes n_H significantly greater than unity (one-sample *t*-test completed on $\log_{10}$ n_H vs. 0, $p < 0.05$). pIC_{50}, negative $\log_{10}$ of IC_{50}; pK_I, negative $\log_{10}$ of K_I.

cause any inhibition of cell adhesion or radioligand binding at the concentrations tested against αvβ6. All test ligands had a n_H significantly greater than unity except SC-68448 and $tLAP_1$ in the cell adhesion assay (one-sample *t*-test completed on $\log_{10}$ n_H vs. 0, $p < 0.05$). In radioligand binding studies compound **2**, compound **3** and $fLAP_1$ had a n_H significantly greater than unity (one sample *t*-test completed on $\log_{10}$ n_H vs. 0, $p < 0.05$).

For note, the pIC_{50} data presented in Figure 3.2.8 for αvβ3, αvβ5, αvβ6 and αvβ8 cell adhesion assays were generated in the Biological Sciences Department at GSK Stevenage (Hertfordshire, UK) with full methods detailed in the Appendix section 8.2. The pIC_{50} and n_H data presented in Table 3.2.6 for the αvβ6 cell adhesion assay are combined data from the author's experiments and routine assay screening also generated in the Biological Sciences Department at GSK Stevenage.

3.2.7. Selectivity of small molecule RGD-mimetics and peptides for the αvβ1, αvβ3, αvβ5, αvβ6 and αvβ8 integrins

In order to determine the selectivity prolife of a range of integrin ligands, competition binding curves were completed with [^{3}H]compound **1** against αvβ1, αvβ3, αvβ5, αvβ6 and αvβ8 (Figure 3.2.9). The control small molecule RGD-mimetics SC-68448 and compound **1** were shown to be the least selective ligands (Figure 3.2.9 and Table 3.2.7). The ligand with the greatest selectivity was the $tLAP_1$ peptide for the αvβ6 integrin, with a minimum of ~3,000 fold selectivity observed over αvβ1, αvβ3, αvβ5 and αvβ8. $tLAP_1$ pK_I values generated for αvβ1, αvβ3, αvβ5 and αvβ8 were comparable (Table 3.2.7). Cilengitide was selective for the αvβ1, αvβ3 and αvβ5 integrins compared with αvβ6 and αvβ8 (up to 1 μM). Cilengitide

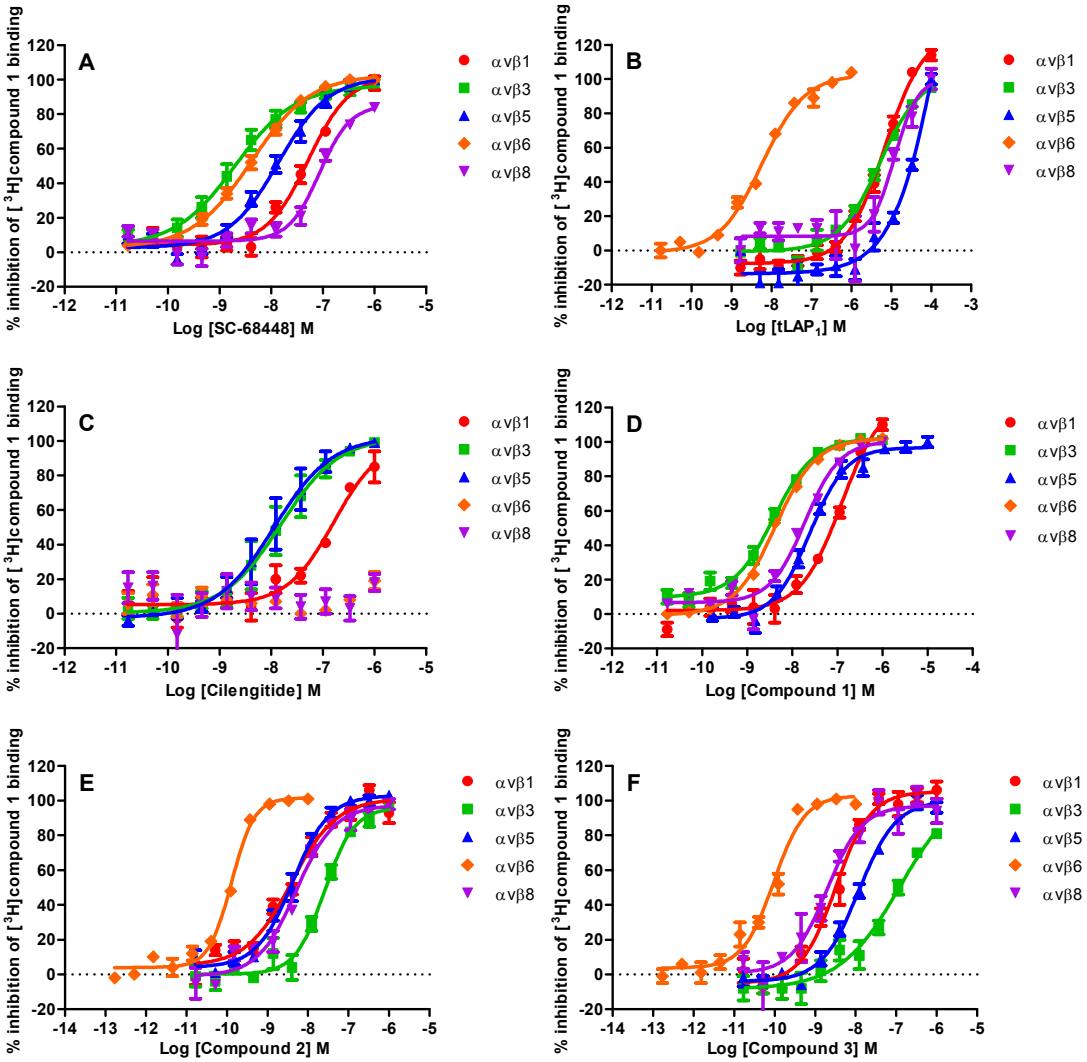

Figure 3.2.9 The selectivity profiles of integrin ligands for the αvβ1, αvβ3, αvβ5, αvβ6 and αvβ8 integrins determined by competition binding studies. Full competition binding curves were generated by incubating unlabelled integrin ligand at a range of concentrations with either the αvβ1, αvβ3, αvβ5, αvβ6 or αvβ8 soluble integrin protein (for integrin concentration see 2. Materials and Methods section) and [^{3}H]compound **1** (~1 to 7 nM dependent on integrin). Plates were then filtered after either a 2 h (αvβ5 and αvβ8) or 6 h (αvβ1, αvβ3 and αvβ6) incubation and the amount of radioligand bound to integrin was measured by liquid scintillation spectroscopy. Total and non-specific binding values were measured in the presence of vehicle (1 % DMSO) and 10 µM SC-68448 respectively, and were used to calculate the % inhibition of radioligand bound to each integrin tested (see 2.11 Data analysis section). Competition binding data were fitted using non-linear regression analysis (four-parameter logistic equation with variable slope (Hill, 1909)) (see 2.11 Data analysis section). Competition binding curves are shown for SC-68448 (A), tLAP$_1$ (B), cilengitide (C), compound **1** (D), compound **2** (E) and compound **3** (F) against αvβ1, αvβ3, αvβ5, αvβ6 and αvβ8. Competition binding displacement curve data are the mean ± SEM of at least four individual experiments carried out in singlicate.

	pK_I				
αv Integrin	*αvβ1*	*αvβ3*	*αvβ5*	*αvβ6*	*αvβ8*
SC-68448	7.51 ± 0.09	8.89 ± 0.09	8.07 ± 0.08	8.56 ± 0.05	6.98 ± 0.04
tLAP$_1$	5.40 ± 0.05	5.62 ± 0.09	4.77 ± 0.01	8.70 ± 0.07	5.07 ± 0.06
Cilengitide	7.10 ± 0.16	8.39 ± 0.24	8.04 ± 0.30	<6.35	<6.15
Compound 1	7.14 ± 0.02	8.75 ± 0.04	7.64 ± 0.03	8.62 ± 0.03	7.81 ± 0.04
Compound 2	8.61 ± 0.09	8.03 ± 0.05	8.48 ± 0.09	10.2 ± 0.02	8.45 ± 0.05
Compound 3	8.68 ± 0.17	7.43 ± 0.05	7.95 ± 0.07	10.4 ± 0.09	8.70 ± 0.10

Table 3.2.7 Selectivity profiles of a range of integrin small molecule RGD-mimetics and peptides against the αvβ1, αvβ3, αvβ5, αvβ6 and αvβ8 integrins determined by competition binding studies. Competition binding data were fitted using non-linear regression analysis (four-parameter logistic equation with variable slope (Hill, 1909)) (see 2.11 Data analysis section). IC_{50} values generated from competition binding curves against [^{3}H]compound **1** were converted to K_I values using the Cheng-Prusoff equation (Cheng and Prusoff, 1973) (see 2.11 Data analysis section). Data shown are mean values ± SEM for at least four individual determinations. pK_I, negative $\log_{10}$ of K_I.

demonstrated a comparable affinity for αvβ3 and αvβ5 with αvβ1 affinity ~9- and 19-fold less than αvβ5 and αvβ3 respectively. The novel small molecule RGD-mimetics compound **2** and **3** exhibited selectivity for αvβ6 over the other integrins tested by at least 93-fold. Overall, compound **3** displayed a greater selectivity for αvβ6 compared with compound **2**.

3.2.8. Effect of αvβ6 protein concentration and incubation time on affinity estimates

To investigate the sensitivity of the [^{3}H]compound **1** competition binding experiments completed with 0.3 nM αvβ6 integrin (defined as 'high protein' assay format), a selection of small molecule RGD-mimetics were investigated with a lower concentration of αvβ6 integrin protein (0.075 nM – defined as 'low protein' assay format). SC-68448 (low affinity, control ligand) was compared with compound **2** and **3** (high affinity, novel ligands). No significant change in affinity was observed for SC-68448 and compound **2** between the high and low protein formats (SC-68448 pK_I 8.56 ± 0.05 high vs. 8.72 ± 0.06 low protein; compound **2** pK_I 10.2 ± 0.02 high vs. 10.6 ± 0.04 low protein) (ANOVA, Bonferroni post-test, $p > 0.05$, mean ± SEM, n=5-38). A significant shift was observed for compound **3** (pK_I 10.4 ± 0.09 high vs. 11.0 ± 0.09 low protein) (ANOVA, Bonferroni post-test, $p < 0.05$, mean ± SEM, n=6-8). No significant difference was observed in pK_I values between compound **2** in the high and low protein format (ANOVA, Bonferroni post-test, $p > 0.05$, mean ± SEM, n=5-9). To further test the sensitivity of the affinity estimates in the low protein format, and to determine if equilibrium between radioligand, unlabelled ligand and integrin had been achieved, pK_I values for compound **2** and **3** were also measured following a 24 h incubation (compound **2** pK_I 10.5 ± 0.14 and compound **3**

pK_I 10.7 ± 0.08 (mean ± SEM, n=4)). No significant difference was observed in pK_I values for compound **2** and **3** determined following a 6 vs. 24 h incubations in the low protein format (ANOVA, Bonferroni post-test, $p > 0.05$, mean ± SEM, n=4-6). Conversely, the n_H values (compound **2** n_H = 1.44 (0.88, 2.01) at 6 h vs. 0.98 (0.45, 1.52) at 24 h; compound **3** n_H = 1.55 (1.31, 1.78) at 6 h vs. 1.08 (0.49, 1.68) at 24 h, mean n_H with 95 % confidence limits shown in parentheses, n=4-6) were closer to unity when measured at 24 h and for compound **3** it was no longer significantly greater than unity (one-sample *t*-test completed on $\log_{10} n_H$ vs. 0, $p > 0.05$). In contrast, the n_H for compound **2** following a 6 h incubation was not significantly greater than unity (one-sample *t*-test completed on $\log_{10} n_H$ vs. 0, $p > 0.05$).

3.2.9. Dissociation binding kinetics of unlabelled ligands from the αvβ6 integrin

To allow the ranking of unlabelled ligands in terms of rate of dissociation from the αvβ6 integrin, a novel methodology was developed where the association of [^{3}H]compound **1** was used as surrogate for the dissociation of an unlabelled ligand from a pre-formed unlabelled ligand/integrin complex. Using this method the dissociation profiles observed and k_{off} and $t_{1/2}$ values calculated for compound **1** (fast and full dissociation) and A20FMDV2 (slow and partial dissociation) closely matched those observed for the radiolabelled forms of these ligands (Figure 3.2.4 compared with Figure 3.2.10). SC-68448, compound **1** and $fLAP_1$ all had similar dissociation profiles (relatively fast) whilst the profile of compound **2** was slower in comparison. The dissociation profile of compound **3** was even slower than that observed for compound **2**. Although this assay format was primarily used to rank ligands dissociation profiles, pooled data from individual experiments were fitted to

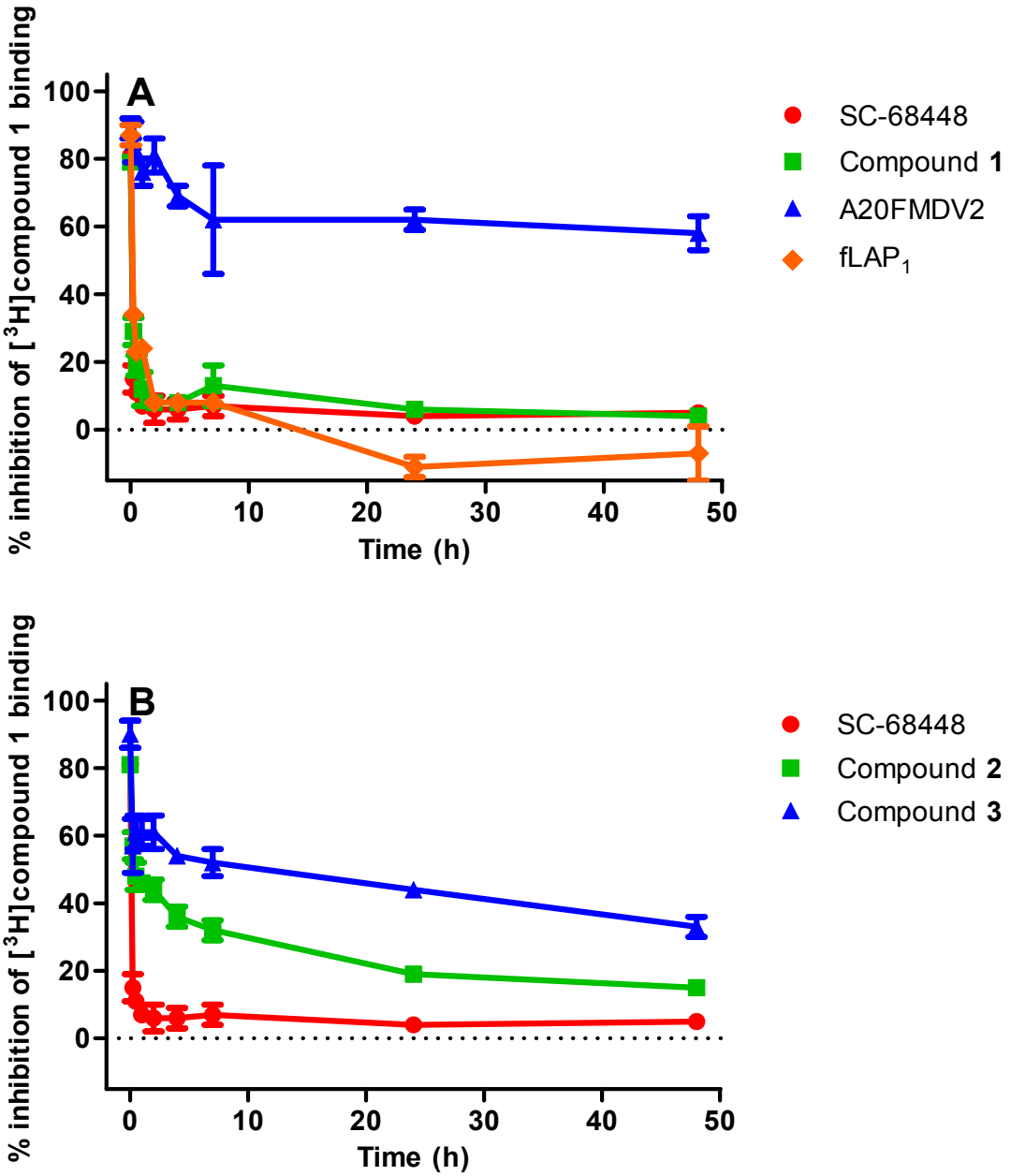

Figure 3.2.10 Unlabelled small molecule RGD-mimetics and peptides demonstrate different dissociation binding kinetics from αvβ6. Dissociation of unlabelled ligands from the soluble αvβ6 integrin protein was initiated (following a 1 h pre-incubation with integrin) by addition of 50 x K_D (~50 nM) [^{3}H]compound **1** in the presence of 2 mM Mg^{2+}. Plates were then filtered after the time indicated and the amount of radioligand bound to αvβ6 was measured by liquid scintillation spectroscopy. Total and non-specific binding values were measured at each time point in the presence of vehicle (1 % DMSO) and 10 μM SC-68448 respectively, and were used to calculate the % inhibition of radioligand bound to the αvβ6 integrin (see 2.11 Data analysis section). Data shown are the mean ± SEM of at least four individual experiments carried out in quadruplicate.

Integrin Ligand	k_{off} (min^{-1})	$t_{1/2}$ (min)
SC-68448	0.137 ± 0.014	5.1
A20FMDV2	*0.004 ± 0.001	*157.2
fLAP$_1$	0.049 ± 0.016	14.2
Compound 1	0.075 ± 0.010	9.3
Compound 2	0.006 ± 0.003	121.3
Compound 3	*POOR FIT	*POOR FIT

Table 3.2.8 Dissociation binding kinetics of unlabelled small molecule RGD-mimetics and peptides from αvβ6. Dissociation of unlabelled ligands from the soluble αvβ6 integrin protein was initiated (following a 1 h pre-incubation with integrin) by addition of 50 x K_D (~50 nM) [^{3}H]compound **1**. Dissociation binding data were fitted to a one-phase dissociation model (see 2.11 Data analysis section) to generate k_{off} values. k_{off} values were subsequently used to calculate half-life ($t_{1/2}$) values using the equation $t_{1/2} = 0.693/k_{off}$. Data shown are mean values ± SEM for at least four individual determinations. *denotes incomplete dissociation over time course tested (48 h). POOR FIT, full dissociation curve poorly defined therefore no $k_{off}/t_{1/2}$ calculated; k_{off}, dissociation rate constant; $t_{1/2}$, dissociation half-life.

a one-phase dissociation model (see 2.11 Data analysis section) to generate the k_{off} and $t_{1/2}$ values in Table 3.2.8. The low affinity ligands SC-68448, $fLAP_1$ and compound **1** all dissociated with a comparable rate that was faster than that observed for the high affinity ligand, compound **2**. For compound **3** a one-phase dissociation model did not best describe the data and the fit was poor (r^2 value of 0.66 vs. ≥ 0.84 for all other fits) due to lack of a well defined plateau at the longer time points. Although it appeared the dissociation of compound **3** from the αvβ6 integrin was bi-phasic no fit could be achieved when a two-phase dissociation model was applied to the data (see 2.11 Data analysis section).

3.3. Discussion

[^{3}H]compound 1 binds with high affinity to the αvβ6 RGD binding site in a competitive and reversible manner

Compound **1** is a small molecule compound that was identified as part of a drug discovery screening campaign to identify αvβ6 integrin RGD-mimetics. Historical data on compound **1** completed in cell adhesion assays (see Appendix 8.3.4, Table 8.3.1) had shown it to be a pan-αv molecule that inhibited the binding of αvβ3, αvβ5, αvβ6 and αvβ8 with comparable IC_{50} values (all comparisons made between IC_{50} values at these integrins resulted in 1.0 to 2.5-fold differences). Compound **1** was chosen to be radiolabelled with [^{3}H] to allow an in-depth characterisation of the binding profile of a small molecule RGD-mimetic with αvβ6 and other RGD directed integrins. Data presented in this chapter have shown that [^{3}H]compound **1** binds to the αvβ6 RGD binding site with high affinity (nanomolar). Binding to the RGD site has been confirmed by the lack of binding to αvβ6 in the absence of divalent cations

(either by addition of a chelating agent (EDTA) or titration of divalent cations) or the presence of high concentrations of RGD peptides ($fLAP_1$, $tLAP_1$, $tLAP_3$ and A20FMDV2). The propensity for supporting binding between the different divalent cations tested in this study has shown Mn^{2+} to be the most efficient, followed by Mg^{2+} and then Ca^{2+}, the latter only able to support partial binding when tested at maximal concentrations (Figure 3.2.2A). The higher potency observed with Mn^{2+} suggested that there was a mixed αvβ6 integrin population in the soluble protein preparation either in the low or high affinity state that could be activated with greater efficiency by this divalent cation (Plow *et al.*, 2000).

It has also been shown that [^{3}H]compound **1** binds with high affinity to the αvβ3 integrin and with moderate affinity to αvβ1, αvβ5 and αvβ8. The interesting observation from the binding studies is that the selectivity profile for compound **1** is much different compared with that defined in the cell adhesion studies. In cell adhesion, compound **1** has a comparable potency between integrins whereas in binding studies with [^{3}H]compound **1** there is a clear difference between αvβ3 and αvβ6 compared with αvβ5 and αvβ8. This highlights the pitfalls of using a panel of cell adhesion assays to define selectivity profiles of unlabelled integrin ligands.

The mode of binding of [^{3}H]compound **1** with the αvβ6 RGD binding site has been shown to be a simple, competitive and reversible interaction (Figures 3.2.4A and 3.2.5). Association with the αvβ6 RGD binding site (Figure 3.2.3A) is relatively fast in terms of an association rate constant for a ligand-protein/receptor interaction. Following a pre-incubation with integrin, to allow the radioligand-integrin complex to form, the radioligand can be fully competed off the integrin by either a small molecule RGD-mimetic (SC-68448) or an RGD peptide (A20FMDV2) (Figure

3.2.4A). However, the rate of dissociation was faster with the addition of 10 mM EDTA compared with the addition of a competitive integrin ligand. EDTA is sequestering any metal ions from the system, which will include the removal of Mg^{2+} in the binding buffer that is required to be bound to the allosteric cation binding site on the integrin to enable RGD ligand binding (Plow *et al.*, 2000; Hynes, 2002). Therefore, EDTA is affecting an allosteric, non-competitive mechanism and in radioligand dissociation binding studies a faster k_{off} can be indicative of this mechanism of action compared with a direct competitive interaction (Christopoulos and Kenakin, 2008).

[^{3}H]A20FMDV2 binds with high affinity to the αvβ6 RGD binding site with reversibility dependent on experimental conditions

With the FMDV derived peptide A20FMDV2 demonstrating such a high affinity and selectivity for αvβ6, it has been used to great effect as a tool in the cancer field, especially as a radiotracer for *in vivo* imaging studies investigating αvβ6 expression in tumours (Hausner *et al.*, 2007; Hausner *et al.*, 2009). A20FMDV2 was chosen to be radiolabelled with [^{3}H] to allow an in-depth characterisation of an RGD peptide's binding profile with αvβ6 to compare to that of a small molecule RGD-mimetic. As was the case with [^{3}H]compound **1**, [^{3}H]A20FMDV2 binds to the αvβ6 RGD binding site with high affinity confirmed via the same observations for [^{3}H]compound **1** i.e. lack of binding to αvβ6 in the presence of EDTA, low concentrations of divalent cations or the presence of high concentrations of RGD peptides. However, the interaction between [^{3}H]A20FMDV2 and the αvβ6 integrin appears to be much more complicated and differs significantly from that of [^{3}H]compound **1**. [^{3}H]A20FMDV2's association (Figure 3.2.3B) with αvβ6 integrin is slower than that

of [^{3}H]compound **1** (~1.7-fold), although this is the more comparable piece of data between the two radioligands. It is in dissociation studies where the key differences were observed. In dissociation studies, addition of EDTA was the only method capable of causing full dissociation of [^{3}H]A20FMDV2, whereas competition with a small molecule RGD-mimetic (SC-68448) or unlabelled A20FMDV2 (Figure 3.2.4B) only caused a partial dissociation of radioligand (~30-32 %) over the 24 h time course defined in the study.

Previously published data suggested that A20FMDV2 forms an EDTA-resistant complex with αvβ6, but only if the peptide-integrin complex is pre-formed (DiCara *et al.*, 2008). It was shown that after 30 min in the presence of an excess of non-biotinylinated A20FMDV2, binding could not be reversed from the pre-formed biotinylated A20FMDV2-αvβ6 complex. For comparison in this study, full dissociation profiles over a 24 h time course were generated for [^{3}H]A20FMDV2, investigating a number of methods to initiate radioligand dissociation. These included the sequestering of divalent metal cations with EDTA and competition with excess unlabelled ligands (both an RGD small molecule RGD-mimetic (SC-68448) and unlabelled A20FMDV2). Over this extended timeframe EDTA was able to reverse the binding of [^{3}H]A20FMDV2 fully. At 30 min no reversal of A20FMDV2 binding to αvβ6 was observed by DiCara and co-workers (DiCara *et al.*, 2008) whereas in this study ~50 % of [^{3}H]A20FMDV2 is unbound at this time point. These previously published experiments were completed at 4°C. However, in contrast all binding experiments in this study were completed at 37°C and therefore an explanation for this could be that the slower kinetics at the low temperature conditions resulted in A20FMDV2 dissociation not being detected at the 30 min time

point. When dissociation of [^{3}H]A20FMDV2 from αvβ6 was initiated by either a small molecule RGD-mimetic (SC-68448) or unlabelled A20FMDV2 in this study, only a partial reversal of radioligand binding could be achieved up to 24 h. This may provide further evidence for the so-called "synergy site" that has been proposed for the interaction of RGD-containing peptides with a number of integrins (Mardon and Grant, 1994; Kumar *et al.*, 1997), including αvβ6 (DiCara *et al.*, 2007), whereby an interface between the secondary structure of the peptide stabilises the RGD site binding. This is supported by direct competition at the RGD binding site with SC-68448 not being sufficient to fully reverse binding of A20FMDV2 to the αvβ6 integrin. Interestingly, the unlabelled A20FMDV2 was also unable to compete with the second site that may suggest it is not structurally in the correct conformation to achieve this unless first bound to the RGD binding site. The full reversal of [^{3}H]A20FMDV2 binding observed with EDTA suggests the binding of the peptide to both the RGD site and synergy site requires the presence of divalent metal cations. However, it is not clear whether this observation is a result of EDTA having a more efficient inhibition of [^{3}H]A20FMDV2 RGD ligand binding compared with direct competition with a cold RGD-ligand or whether binding to the synergy site itself requires the presence of divalent metal cations. This dissociation profile was completely different to that observed with [^{3}H]compound **1** where a full and faster dissociation was observed under the same conditions. In contrast to the [^{3}H]A20FMDV2 dissociation studies, the association, saturation and competition binding data generated with this radioligand showed that if the peptide competes with unlabelled αvβ6 ligands at the same time i.e. is not allowed to form a complex with αvβ6, all [^{3}H]A20FMDV2 can be competed off to NSB levels.

Binding of [^{3}H]A20FMDV2 to αvβ6 also required the presence of divalent cations with Ca^{2+}, Mg^{2+} and Mn^{2+} able to support binding. All of these divalent cations were able to support maximal binding of the radiolabelled peptide with αvβ6 although Mn^{2+} was able to achieve this at ~26- and 35-fold lower concentrations compared with Mg^{2+} and Ca^{2+} respectively. Again a difference was evident with [^{3}H]compound **1** where Ca^{2+} was able to support full binding of [^{3}H]A20FMDV2 compared to partial binding with the former radioligand. This suggests that different αvβ6 ligands are able to demonstrate different binding profiles when in the presence of the same type and concentration of divalent cation. It also highlights that each ligand needs to be assessed on an individual basis and this may be important when investigating more physiological relevant divalent cation conditions. For example, SLF contains 0.5 mM Mg^2 and 2.5 mM Ca^{2+} (Marques *et al.*, 2011) and the binding profile of different ligands may differ under these conditions. For example, it could be predicted that the binding of [^{3}H]compound **1** to αvβ6 would be reduced (in terms of affinity and B_{max}) in the presence of such an inhibitory concentration of Ca^{2+} present in SLF. It is also worth considering that the profiles may also differ between αv integrin subtypes in relation to divalent cation type and concentration.

Radioligand binding assays provide increased accuracy in determining affinity within and comparisons between the αvβ1, αvβ3, αvβ5, αvβ6 and αvβ8 integrins

The use of radioligand binding assays to determine affinity with soluble protein preparations for the integrins αvβ1, αvβ3, αvβ5, αvβ6 and αvβ8 has allowed accurate K_I values to be calculated by incorporating the K_D and the concentration of radioligand ([^{3}H]compound **1**) present in each competition binding assay, allowing the use of the Cheng-Prusoff equation (see 2.11 Data analysis section). The

comparison of a radioligand binding assay with a cell adhesion assay format for αvβ3, αvβ5, αvβ6 and αvβ8 integrins has not only allowed a direct ligand-integrin affinity to be measured in a simple system redundant of the full cell architecture, but more importantly has allowed a direct comparison between integrins to estimate accurate selectivity profiles of ligands. The shifts observed to higher affinity measurements from cell adhesion to radioligand binding assay is unlikely to be solely due to the Cheng-Prusoff correction, as the radioligand format uses a soluble integrin receptor compared with a whole cell in cell adhesion studies. Consequently, the more complex cell system could result in a lower empirical measure of competitor potency as a result of increased non-specific binding of unlabelled ligands to cellular proteins or loss of ligand due to cellular uptake mechanisms. As the background cell line (K562) used as the expression system for the integrins is kept constant, it could be hypothesised that these mechanisms would be comparable and affect each individual integrin cell adhesion assay to the same degree in terms of reducing the pIC_{50} value observed. As the fold shifts between cell adhesion and radioligand binding (Figure 3.2.8) are different between integrins, this suggests that the difference is likely to be due to the type of endogenous ligand used and/or its affinity for the individual integrins. If αvβ3, αvβ5, αvβ6 and αvβ8 all had the same affinity for an endogenous ligand that could be used in all cell adhesion assays at the same concentration, comparisons between integrins from cell adhesion assays could be used to determine an accurate selectivity profile for a ligand. However, this is not the case in the panel of cell adhesion assays shown here where either the affinity of endogenous ligand varies (αvβ3, αvβ6 and αvβ8 use $tLAP_1$ and differences in affinity can be observed in Figure 3.2.9 and Table 3.2.7) or a different endogenous ligand is

used (vitronectin has to be used for αvβ5 due the low affinity this integrin has for $tLAP_1$). In addition, the n_H values observed in the cell adhesion assay were significantly greater than unity (one-sample *t*-test completed on $\log_{10} n_H$ vs. 0, $p < 0.05$) except for SC-68448, $tLAP_1$ and $tLAP_3$. This potentially indicates equilibrium had not been achieved during the 30 min incubation between ligand and integrin (Motulsky and Christopoulos, 2004). This is further supported by the n_H data for SC-68448, $tLAP_1$ and $tLAP_3$ not being significantly greater than unity as these display the lowest IC_{50} (as a crude measure of affinity) and would equilibrate faster than ligands with a higher IC_{50}. Unfortunately no cell adhesion assay exists for αvβ1 due to the lack of a suitable cell line and the selective tools required to validate this. However, the radioligand binding assay developed with [^{3}H]compound **1** and αvβ1 serves not only to compare selectivity of ligands at this integrin versus the other αv integrins, but also as a platform to aid in the identification of selective tools for this integrin, either from novel or literature tool small molecule RGD-mimetics and peptides.

In conclusion, as the radioligand binding assays used for αvβ1, αvβ3, αvβ5, αvβ6 and αvβ8 utilises the same radioligand ([^{3}H]compound **1**), whose affinity and concentration present in the system is accurately known and only measures binding directly to the integrin, these offer the most accurate method for determining an affinity measurement for integrin ligands at a specific integrin as well as providing the most accurate selectivity profile. Although the radioligand format is not amenable to the high throughput required for SAR screening, this radioligand binding work has enabled the relative fold shifts between pIC_{50} values generated in cell adhesion (as an empirical measure of competitor potency) with pK_I values

(affinity measure) to be determined. As such, in future SAR analysis using the high throughput cell adhesion assays these fold shifts can be incorporated to predict an estimated affinity and also selectivity profiles for larger sets of novel small molecule RGD-mimetics with smaller focused sets then confirmed when required in the low throughput binding assay format.

Identification of high affinity and selective αvβ6 small molecule RGD-mimetics with slow receptor dissociation kinetics

As part of a medicinal chemistry lead optimisation campaign to identify novel, high affinity and selective αvβ6 small molecule RGD-mimetics, compounds **2** and **3** were selected as being two of the optimal chemical entities identified. In radioligand binding assays both demonstrated a high affinity (low pM - Table 3.2.4) and selectivity for the αvβ6 integrin (minimum profile > 93-fold selective over αvβ1, αvβ3, αvβ5 and αvβ8 - Table 3.2.7) as well as a slow dissociation profile (Figure 3.2.10 and Table 3.2.8). In order to generate these data, a number of different experimental designs were investigated to enable optimal profiling of the characteristics of compound **2** and **3**.

From the correlation of cell adhesion pIC_{50} and radioligand binding pK_I values (Figure 3.2.8C) there appeared to be an upper limit of detection in both assays (~8.5 pIC_{50} and ~10.5 pK_I) at which compound **2** and **3** were either close to or at in both formats. In enzymology, a tight binding limit can be observed when the concentration of an enzyme inhibitor required to cause inhibition is close to the concentration of the enzyme in the system (Williams and Morrison, 1979). To investigate if a similar tight binding limit was being observed with the αvβ6 integrin

in radioligand competition binding experiments, the concentration of integrin was lowered to observe if a shift in affinity occurred. To control this experiment a low affinity control (SC-68448) was included and when the concentration of soluble αvβ6 protein was lowered from 0.3 to 0.075 nM (4-fold lower) no change in the affinity was observed. This would be expected for a low affinity compound that was not at the tight binding limit. However, for compound **2** and **3** a shift was observed that was shown to be significant for compound **3**. Within the high protein (0.3 nM αvβ6) competition binding assay the difference between the affinities of compound **2** and **3** was minimal (Figure 3.2.6 and Table 3.2.4). However, the fold difference between the compounds pK_I values was almost doubled when compared in the low protein (0.075 nM αvβ6) competition binding assay. When the incubation time was extended to 24 h in the low protein format no further shift in the pK_I values was observed, however the n_H value for compound **3** was no longer significantly different from unity. This suggested that the system was not at equilibrium at 6 h (Motulsky and Christopoulos, 2004) but that this was not resulting in an underestimation of affinity. The range of concentrations used to construct a competition binding curve will all reach equilibrium at different times with higher concentrations equilibrating faster than lower (as can be seen in association studies with [^{3}H]compound **1** and [^{3}H]A20FMDV2 where equilibrium is achieved quicker at higher concentrations of radioligand (Figure 3.2.3)). If the lower concentrations of compound **3** are not at equilibrium at 6 h then an underestimation of binding would occur at those concentrations compared to the higher concentrations that would result in a steep n_H when the non-linear four-parameter fit is applied to the data. If the system was not at a tight binding limit it would be predicted that this would also have resulted in a

further increase in affinity. The slow dissociation profile observed for compound **3** in subsequent studies confirmed that equilibrium would not have been achieved at 6 h in competition binding studies. Taking all the data in the low format and dissociation studies into consideration it is still possible that the affinity of compound **3** is being underestimated under these experimental conditions.

When the law of mass action is applied to an interaction between a ligand and its protein/receptor binding partner it has been shown that the ligands affinity (K_D or K_I) is a combination of the ligands kinetic constants (k_{off} and k_{on}) (Hulme and Trevethick, 2010). At steady state the K_D (or K_I in an unlabelled ligands case) is defined by the ratio of the k_{off} and k_{on} and is a measure of the likelihood of the ligand-receptor complex to dissociate. Therefore, a high affinity ligand would be predicted to have a lower k_{off} value and a slower dissociation from the protein/receptor. To test this and also endeavor to obtain an early estimate of unlabelled ligand dissociation kinetics, a novel radioligand binding assay format was developed. Unlabelled ligands were allowed to form a complex with the αvβ6 integrin for 1 h prior to being competed off the integrin with an excess (50 x K_D) of radioligand ([^{3}H]compound **1**), using the association of the radioligand to measure the dissociation of the unlabelled ligand. Using this method low affinity ligands for αvβ6 were shown to dissociate quickly (SC-68448, fLAP$_1$, compound **1**) and high affinity ligands slowly (compound **2** and **3**) (Figure 3.2.10). This assay format was validated by having compound **1** and A20FMDV2 characterized as controls. Identical dissociation profiles were observed via this method for compound **1** and A20FMDV2 when compared with the classical methods used for the radiolabelled forms of these ligands (Figure 3.2.4 vs. Figure 3.2.10A). The highest affinity ligand compound **3** was shown to have the slowest

dissociation profile from the αvβ6 integrin and full dissociation was not observed up to 48 h. As such a one-phase dissociation model could not be fitted with a high degree of accuracy. In addition, from the dissociation data generated in this system there was a suggestion that the dissociation of compound **3** from αvβ6 was bi-phasic with a fast initial phase (~30 % of the total) occurring over the first hour and a slow second phase that was not completely resolved at 48 h. However, a bi-phasic dissociation model was poorly fitted to this data. Therefore, it is likely that it would be more optimal to further investigate this via the classical route of radiolabelling compound **3** with [^{3}H] that would enable a full characterisation of its binding with the αvβ6 integrin, including an increased number of time points of dissociation for improved curve definition.

Summary

The data generated in this chapter provides evidence for a complex interaction between A20FMDV2 and the αvβ6 that differs from that observed with [^{3}H]compound **1**, a small molecule RGD-mimetic that binds exclusively to the RGD binding site on the integrin. Consequently, this study has aided in the understanding of how the peptide and small molecule could be used in future studies as pharmacological tools. Although there is evidence for differences beyond the RGD binding components of [^{3}H]A20FMDV2 and [^{3}H]compound **1**, there has been good agreement in affinity measurements and profiling of unlabelled integrin ligands at the αvβ6 RGD binding site with both these radioligands. In addition, when data from αvβ6 competition binding, selectivity and unlabelled ligand dissociation binding studies is taken into consideration for compound **2** and **3**, it is compound **3** that has been shown to have the most desirable profile. It displays high affinity and selectivity for αvβ6 combined with

a slow dissociation profile from the integrin and therefore was chosen as a potential small molecule RGD-mimetic drug candidate to be taken forward for further characterisation in low throughput physiological *in vitro* test systems.

CHAPTER 4: CHARACTERISATION OF THE BINDING OF [^{3}H]COMPOUND 3 TO THE αVβ6 INTEGRIN

4.1. Introduction

The first point of contact for a therapeutic agent targeting the αvβ6 integrin would be to bind to a site on the protein that would result in inhibition of the LAP_1 component of the TGFβ1 large latent complex. This is predicted to result in inhibition of the release of the active form of TGFβ1 (Munger *et al.*, 1999) that has been hypothesised to be a key contributor in the fibrogenesis of IPF (Khalil *et al.*, 1996; Koli *et al.*, 2008; Fernandez and Eickelberg, 2012). This binding event with the αvβ6 integrin, and hence subsequent blockade of TGFβ1 activation, could take place via a number of different mechanisms. The first, and most likely, is by binding directly to the RGD binding site on the integrin (or what could be termed the orthosteric site) that would result in a direct competitive interaction between therapeutic ligand (whether it be a small molecule, a peptide or antibody) and LAP_1. Alternatively, binding to the integrin could be at a site distinct from the orthosteric site, defined as an allosteric site, that would cause inhibition of LAP_1 binding by either occluding, but not binding to, the orthosteric site or by causing a conformational change in the protein structure of the integrin that caused a decrease in the affinity of the orthosteric site for LAP_1. The existence on the αvβ6 integrin of an allosteric site that modulates the RGD binding site via conformational changes, other than the cation binding site conserved in all integrins (Lee *et al.*, 1995), is yet to be shown to exist. However, therapeutic antibodies have been developed that either bind to the αvβ6 RGD binding site directly or to an allosteric site that precludes the binding to the orthosteric RGD binding site (Weinreb *et al.*, 2004; Horan *et al.*, 2008). In order to achieve the latter, the ligand binding to the integrin would be required to be of sufficient size to prevent the binding to the RGD binding site and realistically this could only be achieved by

an antibody or large peptide. For a small molecule approach to targeting αvβ6 a direct competition with the RGD binding site would be the most feasible approach and is the predicted method for the engagement of compound **3** with the integrin. It can be predicted that there would be both advantages and disadvantages not only for orthosteric compared with allosteric interactions but also for a small molecule compared with an antibody therapy. Targeting αvβ6 with an allosteric antibody would give the greatest chance of a truly αvβ6 selective therapy. However, the potential downside of an antibody compared with a small molecule RGD-mimetic would be the cost of goods (in terms of manufacturing the amounts required for a therapies launch), less convenient and more costly administration (antibodies require trained healthcare workers to administer by injection only) and poor tissue penetration (Chames *et al.*, 2009; Flego *et al.*, 2013).

The characterisation of the αvβ6 binding profile of compound **3** in its unlabelled form has been completed (see Chapter 3) and provided evidence of a desirable engagement with the integrin to be selected and progressed as a potential clinical drug candidate. Further investigation of its functional properties and mechanism of action of αvβ6 inhibition and subsequent reduction in TGFβ activation are investigated in Chapter 5. However, to allow a broader and in-depth characterisation of the engagement of compound **3** with the αvβ6 integrin in multiple systems, a radiolabelled form of the molecule was generated ([^{3}H]compound **3**). The incorporation and replacement of hydrogen atoms in the molecule with [^{3}H] negated any structural changes that could alter the pharmacology of compound **3**. There is a limitation to the extent of characterisation of binding interactions that can be completed on unlabelled compounds beyond affinity estimates in competition

binding studies with a tool radioligand. Even though a method for ranking the dissociation profiles of unlabelled compounds from αvβ6 was validated and used for compound progression in this study, it was still important to verify these observations and confirm affinity and kinetic measurements completed on the unlabelled form with a radiolabelled version. This would not only enable accurate K_D, k_{on}, k_{off} and B_{max} parameters to be determined against the integrin in multiple systems (human soluble protein and human lung tissue) but also the profiling of compound **3** binding at the RGD binding site under a greater range of conditions, such as different divalent metal cations/concentrations and pH.

To aid in further target validation of αvβ6 in IPF and to provide a pharmacological evaluation of the ability of compound **3** to interact with the integrin in human diseased tissue, studies using membrane fragments generated from human IPF lung tissue were completed with [^{3}H]compound **3** and compared with normal human lung tissue. This would build on published observations of the increased expression of the αvβ6 integrin in IPF compared with normal lung tissue (Horan *et al.*, 2008) by quantifying αvβ6 levels in tissue from these patient cohorts as well as providing key data to assist in the analysis for determining appropriate human clinical doses.

4.2. Results

4.2.1. General radioligand binding assay optimisation

In order to develop accurate and robust radioligand binding assays for [^{3}H]compound **3** against αvβ6 in soluble recombinant protein preparations and human lung tissue homogenates a number of conditions were optimised that included protein

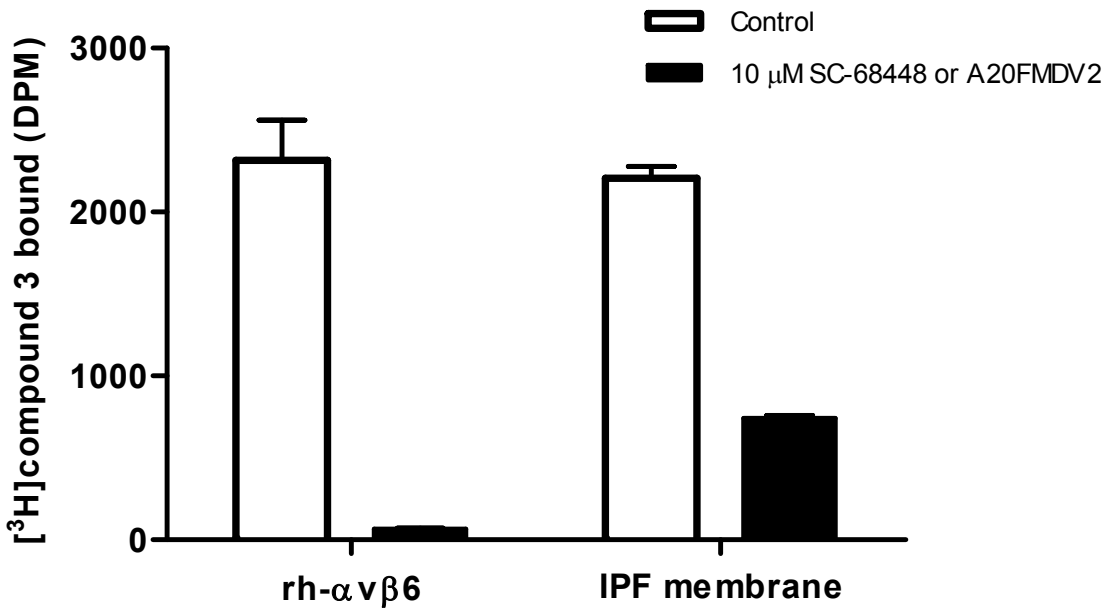

Figure 4.2.1 [^{3}H]compound 3 demonstrates a robust binding window with αvβ6 in recombinant soluble human protein preparations and human IPF lung parenchyma membranes. Total and non-specific binding of radioligands were measured by incubation of [^{3}H]compound **3** with recombinant soluble human αvβ6 integrin protein (rh-αvβ6) or membranes generated from human IPF lung parenchyma in the presence of either vehicle (1 % DMSO), 10 μM SC-68448 (soluble recombinant αvβ6) or 10 μM A20FMDV2 (IPF membranes). Plates were then filtered after a 24 h (soluble recombinant αvβ6) or 72 h (IPF membranes) incubation and the amount of radioligand bound to integrin measured by liquid scintillation spectroscopy. Experiments were carried out using ~0.01 nM concentrations of radioligand with 25 pM soluble recombinant αvβ6 or 50 μg/well IPF membranes. Data shown are the mean ± SD of duplicate points and are representative of at least four individual experiments with similar results.

concentrations and stability over time. The concentration of soluble integrin or membrane preparation used in each radioligand binding assay was optimised to ensure <30 % of radioligand was bound under all conditions. In addition, saturation studies completed with human lung parenchyma membranes used a high volume format with a total volume of 1.5 ml. This would negate the issues associated with ligand depletion and deviation from the law of mass action (Hulme and Birdsall, 1992) that could result in the underestimation of affinity values within an assay.

Figure 4.2.1 demonstrates representative total binding and NSB DPM values for [^{3}H]compound **3** binding with either soluble recombinant αvβ6 integrin protein or human IPF lung parenchyma membranes (Figure 4.2.1). The NSB values observed with soluble recombinant αvβ6 integrin protein (defined by 10 μM SC-68448) were much lower than those in human IPF lung parenchyma membranes (defined by 10 μM A20FMDV2).

To test if saturation experiments were being completed at equilibrium i.e. that binding was at steady state in the system (Hulme and Trevethick, 2010), extended incubation times were required. As all experiments were undertaken at physiological temperature (37ºC) a robust and stable specific binding window was required, in some cases, up to 72 h. A stable specific binding window was observed between [^{3}H]compound **3** and either soluble recombinant αvβ6 integrin protein or human lung membranes for up to 72 h.

4.2.2. [^{3}H]compound 3 αvβ6 integrin binding divalent cation dependency

The regulation of ligand binding to integrins has been shown to be dependent on divalent cations due to the presence of allosteric cation binding sites within their

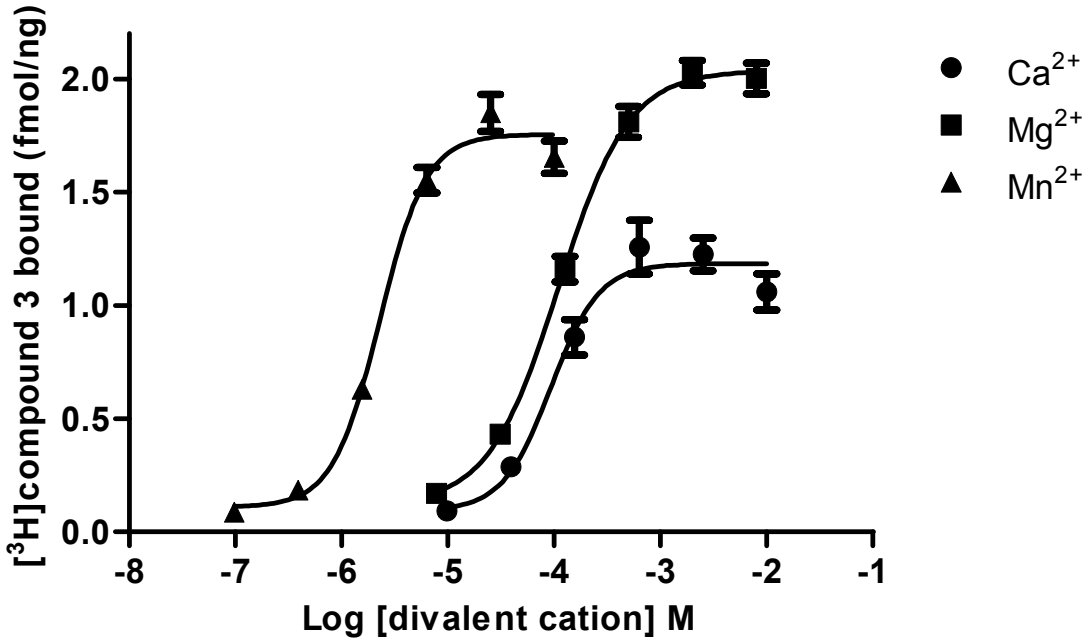

Figure 4.2.2 [^{3}H]compound 3 binds in a divalent metal cation-dependent manner to αvβ6 with different profiles observed between Ca^{2+}, Mg^{2+} and Mn^{2+}. Specific binding was measured by incubation of [^{3}H]compound **3** with soluble αvβ6 integrin protein (25 pM) in the presence of either vehicle (1 % DMSO) or 10 μM SC-68448 in the presence of increasing concentrations of Ca^{2+}, Mg^{2+} or Mn^{2+}. Plates were then filtered after a 6 h incubation and the amount of radioligand bound to αvβ6 measured by liquid scintillation spectroscopy. Specific binding was measured by subtracting the non-specific binding (10 μM SC-68448) from the total radioligand binding in the presence of vehicle (1 % DMSO) with disintegration per minute values converted to fmol/ng (as detailed in 2.11 Data analysis section). Specific binding data were fitted using non-linear regression analysis (four-parameter logistic equation with variable slope (Hill, 1909)) (see 2.11 Data analysis section). Experiments were carried out using 5 x K_D concentrations of radioligand. Data shown are the mean ± SEM of four individual experiments carried out in quadruplicate.

protein structure (Plow *et al.*, 2000; Hynes, 2002) as well as in this study (see Chapter 3). Binding of [^{3}H]compound **3** to αvβ6 required the presence of divalent cations with Ca^{2+}, Mg^{2+} and Mn^{2+} able to support the binding of this radioligand (Figure 4.2.2). However, the concentration required to enable binding of [^{3}H]compound **3** with αvβ6 was different between divalent cations with Mn^{2+} (EC_{50} 2.3 ± 0.3 μM) able to support binding at much lower concentrations compared with Mg^{2+} (EC_{50} 95.0 ± 2.7 μM) and Ca^{2+} (EC_{50} 94.7 ± 9.6 μM) (mean ± SEM, n=4). In addition, Ca^{2+} was unable to produce maximal binding of the small molecule RGD-mimetic radioligand (up to a concentration of 10 mM) compared with Mn^{2+} and Mg^{2+}. In terms of EC_{50} values, the divalent cation binding profile of [^{3}H]compound **3** was more comparable to that observed with [^{3}H]A20FMDV2 (see section 3.2.2. [^{3}H]compound **1** and [^{3}H]A20FMDV2 αvβ6 integrin binding divalent cation dependency). However, the partial ability to support binding in the presence of Ca^{2+} was more comparable to [^{3}H]compound **1**, although the level to which binding was enabled was greater for [^{3}H]compound **3** (see section 3.2.2. [^{3}H]compound **1** and [^{3}H]A20FMDV2 αvβ6 integrin binding divalent cation dependency).

4.2.3. Radioligand binding characterisation of [^{3}H]compound 3 in human soluble αvβ6 integrin protein

For comparison with previous binding studies using compound **3** against the human form of αvβ6, [^{3}H]compound **3** association, dissociation and saturation binding studies were completed with human soluble recombinant αvβ6 integrin protein in the presence of 2 mM Mg^{2+}. The association of [^{3}H]compound **3** with αvβ6 was observed to follow a single phase (Figure 4.2.3A) with the k_{on} determined to be 3.56 ± 0.22 x 10^8 $M^{-1}.min^{-1}$ (mean ± SEM, n=4, Table 4.2.1). The pooled data generated

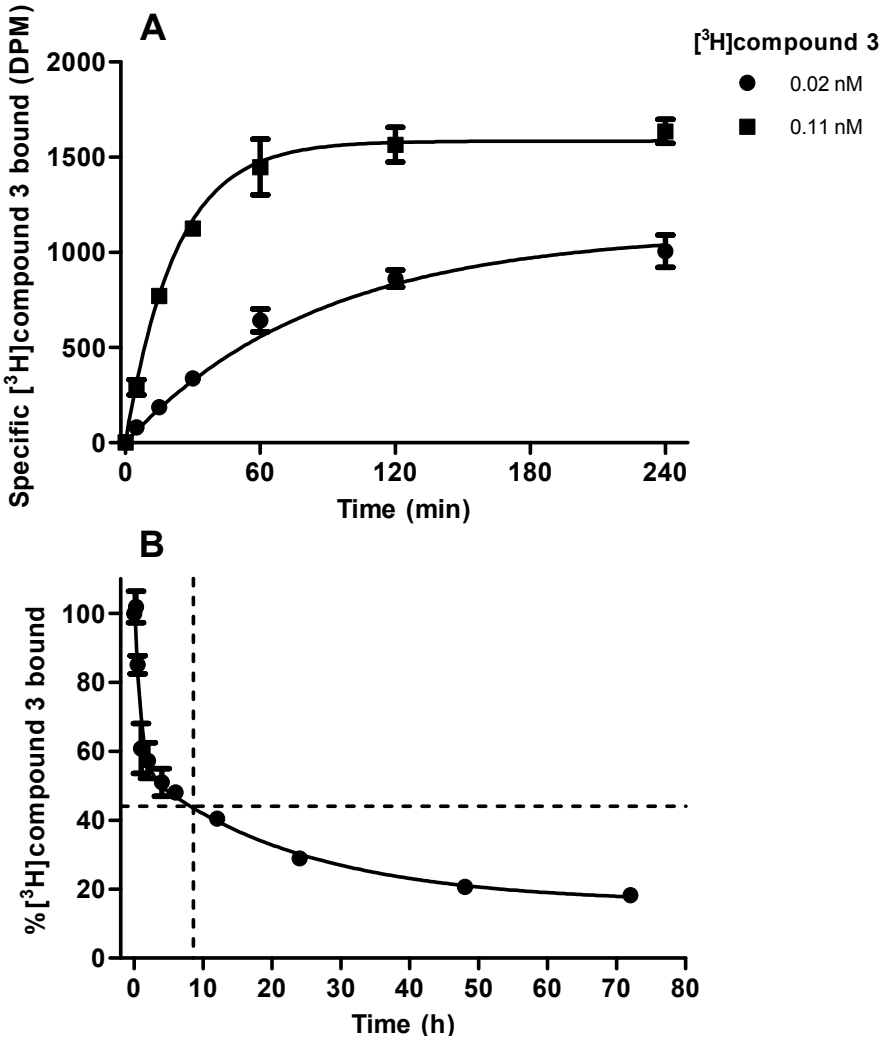

Figure 4.2.3 Association (A) and bi-phasic dissociation (B) binding kinetics of [^{3}H]compound 3 to and from αvβ6. In association studies specific binding was measured by incubation of [^{3}H]compound **3** with 25 pM soluble αvβ6 integrin protein in the presence of either vehicle (1 % DMSO) or 10 μM SC-68448. Association binding data were generated at the radioligand concentrations indicated (~ K_D and 5 x K_D) and globally fitted to the association kinetic model (see 2.11 Data analysis section). Plates were then filtered after the time indicated and the amount of radioligand bound was measured by liquid scintillation spectroscopy. Specific binding was measured by subtracting the non-specific binding (10 μM SC-68448) from the total radioligand binding in the presence of vehicle (1 % DMSO). Association data shown are the mean ± SD of duplicate points and are representative of four individual experiments with similar results. For dissociation studies soluble αvβ6 integrin protein (0.25 pM) was pre-incubated for 1 h with a fixed concentration of radioligand (~0.1 nM) before dissociation was initiated by addition of 10 μM SC-68448. Plates were then filtered after the time indicated and the amount of radioligand bound was measured by liquid scintillation spectroscopy. Total and non-specific binding values were measured at each time point in the presence of vehicle (1 % DMSO) and 10 μM SC-68448 respectively, and were used to calculate the % inhibition of radioligand bound. Dissociation binding data were best fitted to a two-phase dissociation model (extra-sum-of-square F test, $p < 0.05$) (see 2.11 Data analysis section) to generate fast and slow k_{off} values. The dashed line on the y-axis depicts the % fast phase (56 %) and the dashed line on the x-axis depicts the corresponding duration of the fast phase (8.2 h). Dissociation data shown are the mean ± SEM of four individual experiments carried out in duplicate.

during dissociation studies with [^{3}H]compound **3** and αvβ6 were best fitted to a two-phase dissociation model (extra-sum-of-square F test, $p < 0.05$) with a fast k_{off} 1.22 ± 0.28 h^{-1} ($t_{1/2}$ 0.70 ± 0.20 h, fast phase = 56 % of total dissociation) and slow k_{off} 0.04 ± 0.01 h^{-1} ($t_{1/2}$ 19.9 ± 4.42 h, slow phase = 44 % of total dissociation) (mean ± SEM, n=4)) observed (Table 4.2.1). Using the association rate constant calculated above, at 1 nM [^{3}H]compound **3** (αvβ6 integrin saturating concentration) the $t_{1/2}$ for association with the αvβ6 integrin was calculated to be 1.9 min.

The affinity of [^{3}H]compound **3** at αvβ6 was confirmed to be high with a pK_D value of 10.8 ± 0.08 with a n_H value of 1.06 (0.87, 1.25) (mean ± SEM or 95 % confidence limits in parentheses, n=4, Table 4.2.1) that was not significantly different (Student's unpaired *t*-test, $p > 0.05$) to the pK_I value (10.7 ± 0.08 (mean ± SEM, n=4)) determined for [^{3}H]compound **3** in competition binding studies against [^{3}H]compound **1** at the αvβ6 integrin (low protein version of this assay with a 24 h incubation time detailed in section 3.2.8. Effect of αvβ6 protein concentration and incubation time on affinity estimates). Overall, the binding profile observed with [^{3}H]compound **3** and αvβ6 was extremely comparable to that generated for the unlabelled compound **3** (see Chapter 3).

In addition, to ensure equilibrium in the saturation binding studies between [^{3}H]compound **3** and αvβ6 had been achieved at 24 h, pK_D values were also determined following a 48 h incubation. At 48 h the pK_D value was determined to be 10.9 ± 0.07 (mean ± SEM, n=3) that was not significantly different to that observed at 24 h (Student's unpaired *t*-test, $p > 0.05$) suggesting equilibrium had been achieved. To investigate more physiological and disease relevant conditions the saturation binding of [^{3}H]compound **3** with αvβ6 was also measured in SLF at pH

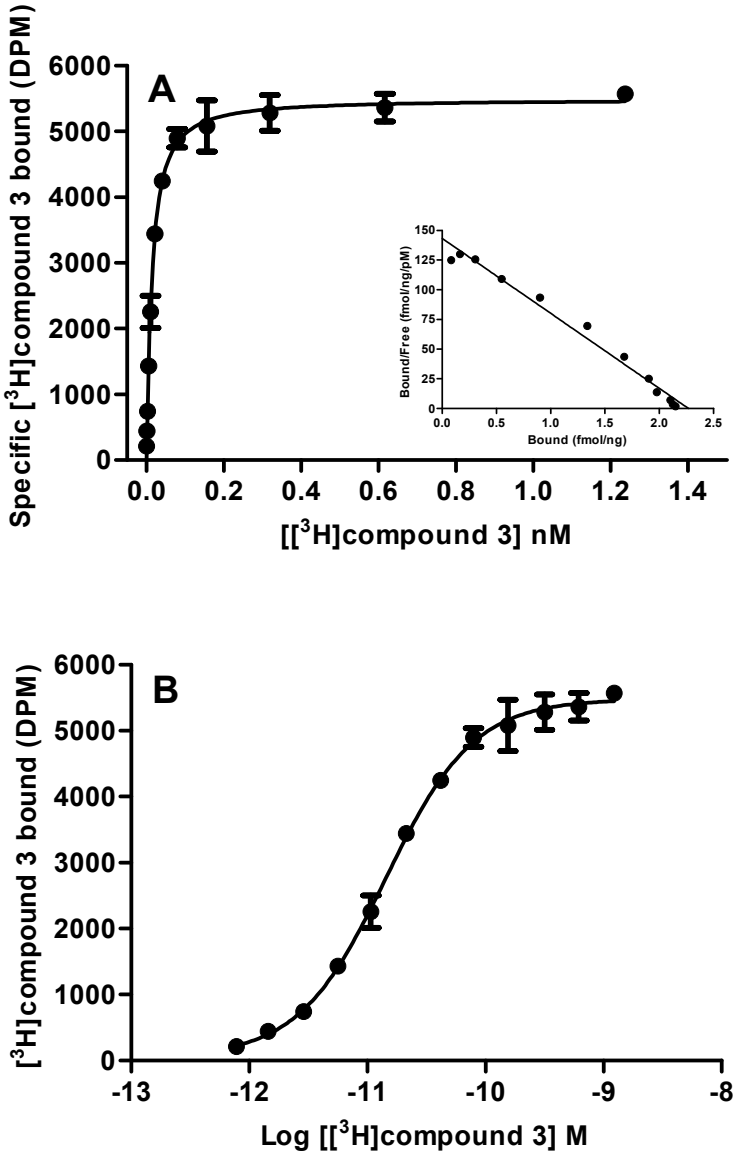

Figure 4.2.4 **[^{3}H]compound 3 binds to a single, saturable site on αvβ6.** For saturation studies specific binding of [^{3}H]compound **3** was measured by incubation of increasing concentrations of radioligand with soluble αvβ6 integrin protein (25 pM) in the presence of either vehicle (1 % DMSO) or 10 μM SC-68448. Plates were then filtered after a 24 h incubation and the amount of radioligand bound to αvβ6 was measured by liquid scintillation spectroscopy. Specific binding was measured by subtracting the non-specific binding (10 μM SC-68448) from the total radioligand binding in the presence of vehicle (1 % DMSO). Saturation binding over a linear (A) and logarithmic (B) scale are shown. Specific saturation binding data were fitted to a one affinity site model with Hill slope (A) or using non-linear regression analysis (four-parameter logistic equation with variable slope (Hill, 1909)) (B) (see 2.11 Data analysis section). Data shown are the mean ± SD of duplicate points and are representative of four individual experiments with similar results. Inset A: Scatchard transformation of specific binding with the straight line fit constrained to the mean B_{max} and K_D values (from Table 4.2.1) from non-linear regression using the one affinity site model with Hill slope (where x = 0, y = B_{max}/K_D and y = 0, x = K_D).

[^{3}H]compound 3 Binding Parameter	*Human αvβ6 Protein*
k_{on} ($M^{-1}.min^{-1}$)	3.56 ± 0.22 x 10^8
Two-phase dissociation fast k_{off} (h^{-1})	1.22 ± 0.28
Two-phase dissociation fast $t_{1/2}$ (h)	0.70 ± 0.20
Two-phase dissociation slow k_{off} (h^{-1})	0.04 ± 0.01
Two-phase dissociation slow $t_{1/2}$ (h)	19.9 ± 4.42
K_D (pM)	15.7 ± 2.24
pK_D	10.8 ± 0.06
Hill slope (n_H)	1.06 (0.87, 1.25)
B_{max} (fmol/ng)	2.27 ± 0.10

Table 4.2.1 Kinetic and saturation binding parameters for [^{3}H]compound 3 with soluble human αvβ6 integrin protein. Specific association binding data were globally fitted to the association kinetic model (see 2.11 Data analysis section) to determine k_{on} values. Dissociation binding data were fitted to a two-phase dissociation model (see 2.11 Data analysis section) to generate fast and slow k_{off} values. k_{off} values were subsequently used to calculate dissociation half-life ($t_{1/2}$) values using the equation $t_{1/2} = 0.693/k_{off}$. Specific saturation binding data were fitted to a one affinity site model with Hill slope (see 2.11 Data analysis section). Data shown are mean values ± SEM or 95 % confidence limits (shown in parentheses) for at least four individual determinations. pK_D, negative $\log_{10}$ of K_D.

6.2. An ~3-fold reduction in affinity of [^{3}H]compound **3** for the human αvβ6 integrin was observed when saturation binding was completed in SLF at pH 6.2 (binding

buffer pK_D 10.8 ± 0.08 vs. SLF at pH 6.2 pK_D 10.4 ± 0.04 (mean ± SEM, n=4)) that was shown to be significantly different (Student's unpaired *t*-test, $p < 0.05$). No significant difference in B_{max} values (binding buffer B_{max} 2.27 ± 0.14 vs. SLF at pH 6.2 B_{max} 2.09 ± 0.11 (mean ± SEM, n=4)) between these conditions was observed (Student's unpaired *t*-test, $p < 0.05$).

4.2.4. Quantifying levels and activation state of the αvβ6 integrin in human IPF lung tissue

Plasma membranes prepared from normal and IPF human lung tissues were used to investigate the αvβ6 integrin affinity and kinetics of [^{3}H]compound **3** in a disease relevant system. In addition, differences in the αvβ6 expression in normal vs. diseased lung were also determined. Although normal (non-fibrotic) human lungs were designated by medical history and IPF disease state defined by medical history and post-transplant pathology confirmed by a board-certified pathologist experienced in evaluating pulmonary fibrosis, tissue sections from all donor populations were IHC stained with H&E and αvβ6 for comparison. A representative example of the lower airways is shown in Figure 4.2.5 where the normal (delicate monolayers of AECs and endothelial cells (Figure 4.2.5A)) and fibrotic lung (excessive ECM deposition and severe scarring (Figure 4.2.5C)) architecture can be observed. The upregulation of αvβ6 from normal to IPF lung tissues can also be seen with a much more intense staining observed for the β6 subunit in AECs between normal (Figure 4.2.5B) and disease (Figure 4.2.5D) sections.

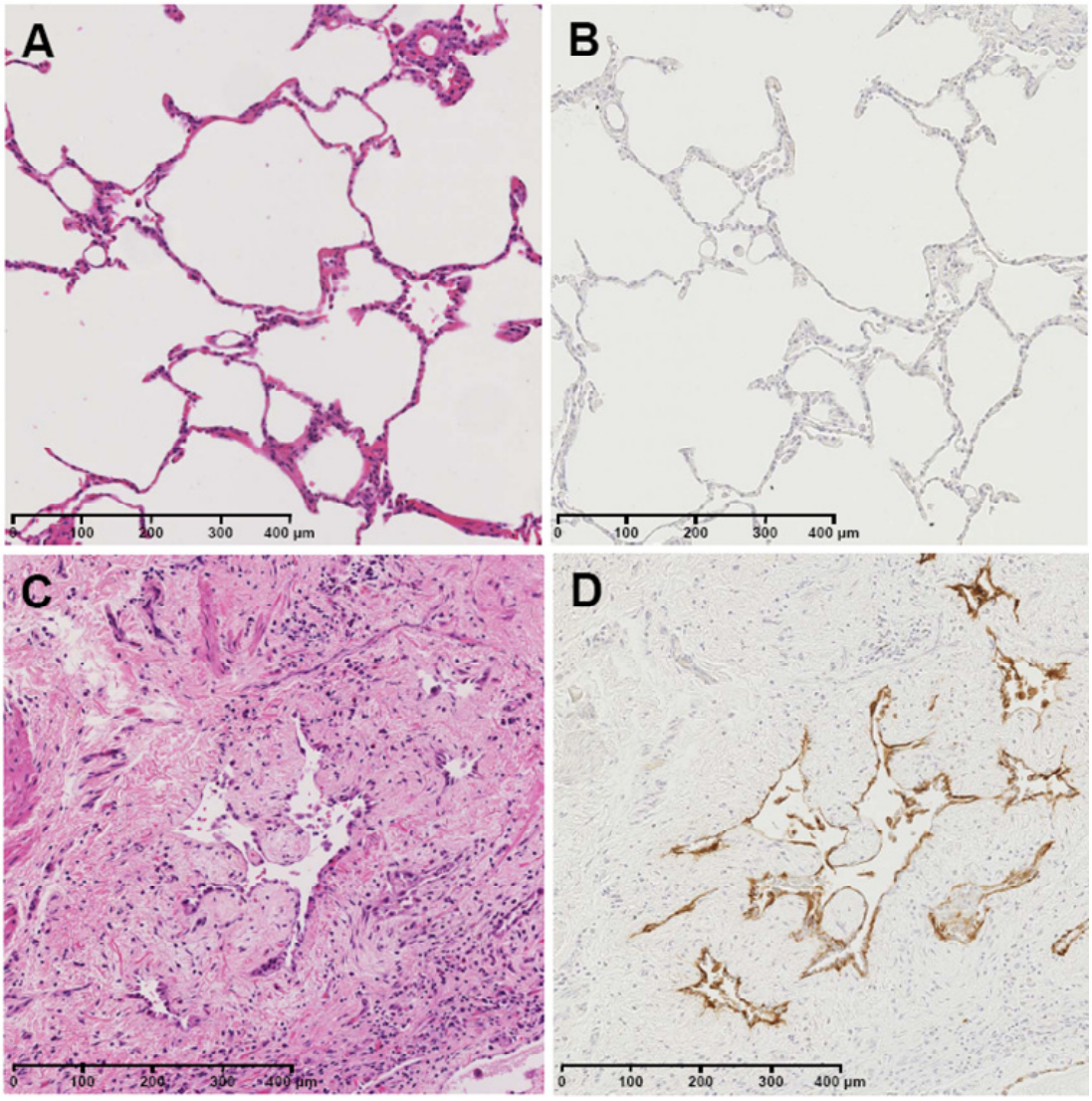

Figure 4.2.5 αvβ6 expression measured via immunohistochemical staining is increased from normal to IPF human lung tissue. Normal (panel A and B) and IPF (panel C and D) tissue sections were stained (brown) for the αvβ6 integrin (panel B and D) and a serial section from the same tissue block stained with haematoxylin and eosin (H&E) (panel A and C). For αvβ6 integrin staining, tissue sections were prepared as detailed in section 2. Materials and Methods (2.8 Immunocytochemistry (ICC) and immunohistochemistry (IHC) staining) prior to incubation with sheep polyclonal anti-human integrin β6 antibody followed by biotinylated rabbit anti-sheep IgG antibody, streptavidin-horseradish peroxidase and 3,3'-diaminobenzidine (in chromogen solution). For H&E staining, tissue sections were immersed in Harris's haematoxylin followed by 0.5 % acid (acetic) ethanol, 70 % ethanol, 1 % eosin, xylene, 3 x absolute ethanol then 4 x absolute ethanol and finally in 3 x xylene (as detailed in section 8.2 Additional methods (8.2.4 Haematoxylin and eosin (H&E) IHC staining)). Data shown are original magnification x10 and are representative of the normal and IPF donors used in radioligand binding studies.

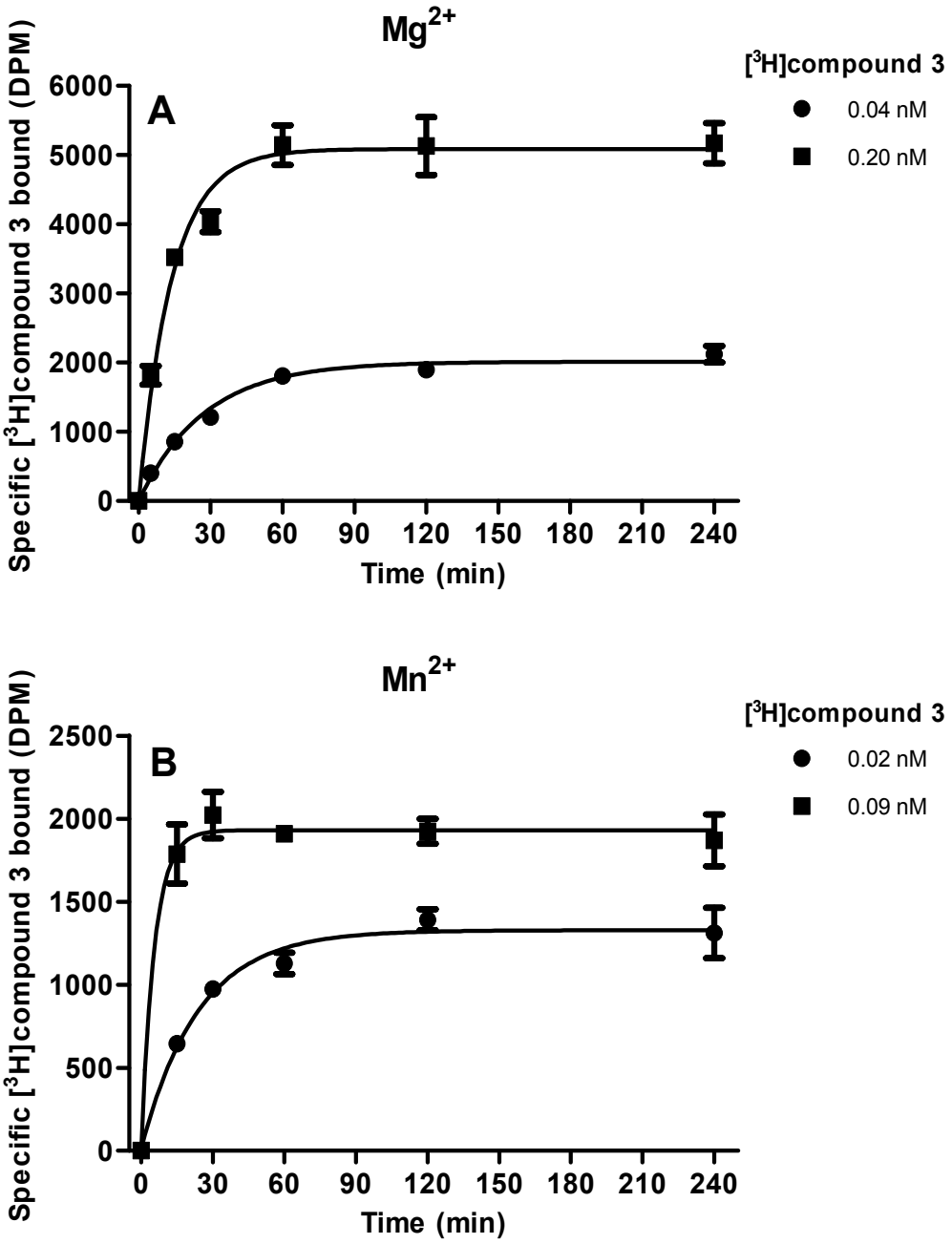

Figure 4.2.6 Association binding kinetics of [^{3}H]compound 3 to αvβ6 in human IPF lung parenchyma membranes. In association binding studies specific binding was measured by incubation of [^{3}H]compound **3** with human IPF lung parenchyma membranes in buffer containing (A) 2 mM Mg^{2+} or (B) 2 mM Mn^{2+} in the presence of either vehicle (1 % DMSO) or 10 µM A20FMDV2. Association binding data were generated at the radioligand concentrations indicated (~ K_D and 5 x K_D) and globally fitted to the association kinetic model (see 2.11 Data analysis section). Plates were then filtered after the time indicated and the amount of radioligand bound was measured by liquid scintillation spectroscopy. Specific binding was measured by subtracting the non-specific binding (10 µM A20FMDV2) from the total radioligand binding in the presence of vehicle (1 % DMSO). Association data shown are the mean ± SD of duplicate points and are representative of 6 donors (n=1 per donor).

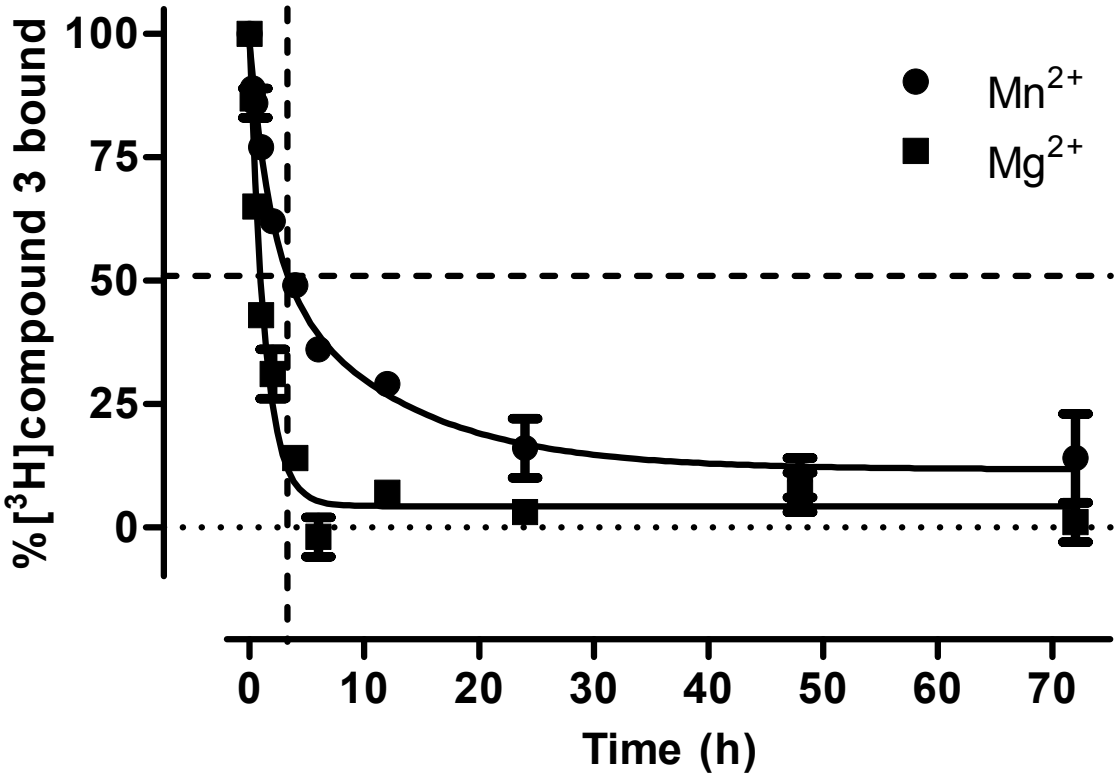

Figure 4.2.7 Dissociation binding kinetics of [^{3}H]compound 3 from αvβ6 in human IPF lung parenchyma membranes is slower and bi-phasic in the presence of Mn^{2+} compared with Mg^{2+}. For dissociation binding studies human IPF lung parenchyma membranes were pre-incubated with [^{3}H]compound **3** for 1 h with a fixed concentration of radioligand (~0.1 pM) before dissociation was initiated by addition of 10 μM A20FMDV2 in the presence of either 2 mM Mg^{2+} or 2 mM Mn^{2+}. Plates were then filtered after the time indicated and the amount of radioligand bound was measured by liquid scintillation spectroscopy. Total and non-specific binding values were measured at each time point in the presence of vehicle (1 % DMSO) and 10 μM A20FMDV2 respectively, and were used to calculate the % inhibition of radioligand bound. Dissociation binding data generated in the presence of Mg^{2+} were best fitted to a one-phase dissociation model whilst data generated in the presence of Mn^{2+} were best fitted to a two-phase dissociation model (extra-sum-of-square F test, $p < 0.05$) (see 2.11 Data analysis section) to generate fast and slow k_{off} values. The dashed line on the y-axis depicts the % fast phase (49 %) and the dashed line on the x-axis depicts the corresponding duration of the fast phase (3.3 h). Dissociation data shown are the mean ± SEM of 6 donors (single experiment per donor) carried out in duplicate.

[^{3}H]compound 3 Binding Parameter	*IPF Lung (Mg^{2+})*	*IPF Lung (Mn^{2+})*
k_{on} ($M^{-1}.min^{-1}$)	$0.17 \pm 0.02 \times 10^9$	$1.20 \pm 0.09 \times 10^9$
One phase dissociation k_{off} (h^{-1})	0.75 ± 0.09	0.22 ± 0.04
One phase dissociation $t_{1/2}$ (h)	1.0 ± 0.1	3.5 ± 0.4
Two phase dissociation fast k_{off} (h^{-1})	N.F.	0.57 ± 0.20
Two phase dissociation fast $t_{1/2}$ (h)	N.F.	1.2
Proportion fast phase (%)	N.F.	49 ± 14
Two phase dissociation slow k_{off} (h^{-1})	N.F.	0.09 ± 0.03
Two phase dissociation slow $t_{1/2}$ (h)	N.F.	7.7
Proportion slow phase (%)	N.F.	51 ± 14

Table 4.2.2 Association and dissociation binding kinetic parameters of [^{3}H]compound 3 to and from αvβ6 in human IPF lung parenchyma membranes. Specific association binding data were globally fitted to the association kinetic model (see 2.11 Data analysis section) to determine k_{on} values. Dissociation binding data were fitted to either a one-phase or two-phase dissociation model (see 2.11 Data analysis section) to generate fast k_{off} and slow k_{off} values. k_{off} values were subsequently used to calculate dissociation half-life ($t_{1/2}$) values using the equation $t_{1/2} = 0.693/k_{off}$. For data analysed with the two-phase dissociation model the % proportion of the fast and slow phase was also calculated. Data shown are mean values ± SEM of 6 donors (single experiment per donor). N.F. not fitted as dissociation data best fitted to a one-phase dissociation model (extra-sum-of-square F test, $p < 0.05$).

The αvβ6 integrin association rate constants for [^{3}H]compound **3** in IPF membranes were 0.17 ± 0.02 x 10^9 and 1.20 ± 0.09 x 10^9 $M^{-1}.min^{-1}$ (Table 4.2.2) in the presence of 2 mM Mg^{2+} (Figure 4.2.6A) and 2 mM Mn^{2+} (Figure 4.2.6B) respectively (mean ± SEM of 6 donors (n=1 per donor)). Using these association rate constants at 1 nM [^{3}H]compound **3** (αvβ6 integrin saturating concentration) the $t_{1/2}$ for association with the αvβ6 integrin was calculated to be 0.6 and 3.8 min in the presence of 2 mM $Mn^{2+}$and 2 mM Mg^{2+} respectively (when using k_{off} calculated from a one-phase dissociation model).

Dissociation binding data generated in the presence of Mg^{2+} were best fitted to a one-phase dissociation model whilst data generated in the presence of Mn^{2+} were best fitted to a two-phase dissociation model (extra-sum-of-square F test, $p < 0.05$) (Figure 4.2.7). The k_{off} value for [^{3}H]compound **3** in IPF membranes from the αvβ6 integrin in the presence 2 mM Mg^{2+} was 0.75 ± 0.09 h^{-1} ($t_{1/2}$ 1.0 ± 0.1 h) (mean ± SEM of 6 donors (n=1 per donor)) (Table 4.2.2). The fast and slow k_{off} values for [^{3}H]compound **3** in IPF membranes from the αvβ6 integrin in the presence of 2 mM Mn^{2+} was 0.57 ± 0.20 h^{-1} ($t_{1/2}$ 1.2 h) and 0.09 ± 0.03 h^{-1} ($t_{1/2}$ 7.7 h) respectively (mean ± SEM of 6 donors (n=1 per donor)) with 49 % making up the fast phase and 51 % making up the slow phase (Figure 4.2.7C, Table 4.2.2). The fast phase of dissociation observed in the presence of 2 mM Mn^{2+} was complete at 3.3 h with full dissociation almost complete at this time in the presence of 2 mM Mg^{2+}. The slow phase of dissociation observed in the presence of 2 mM Mn^{2+} was resolved between 24 and 48 h.

Saturation binding parameters for [^{3}H]compound **3** with the αvβ6 integrin in normal and IPF human lung parenchyma membranes were determined in the presence of 2

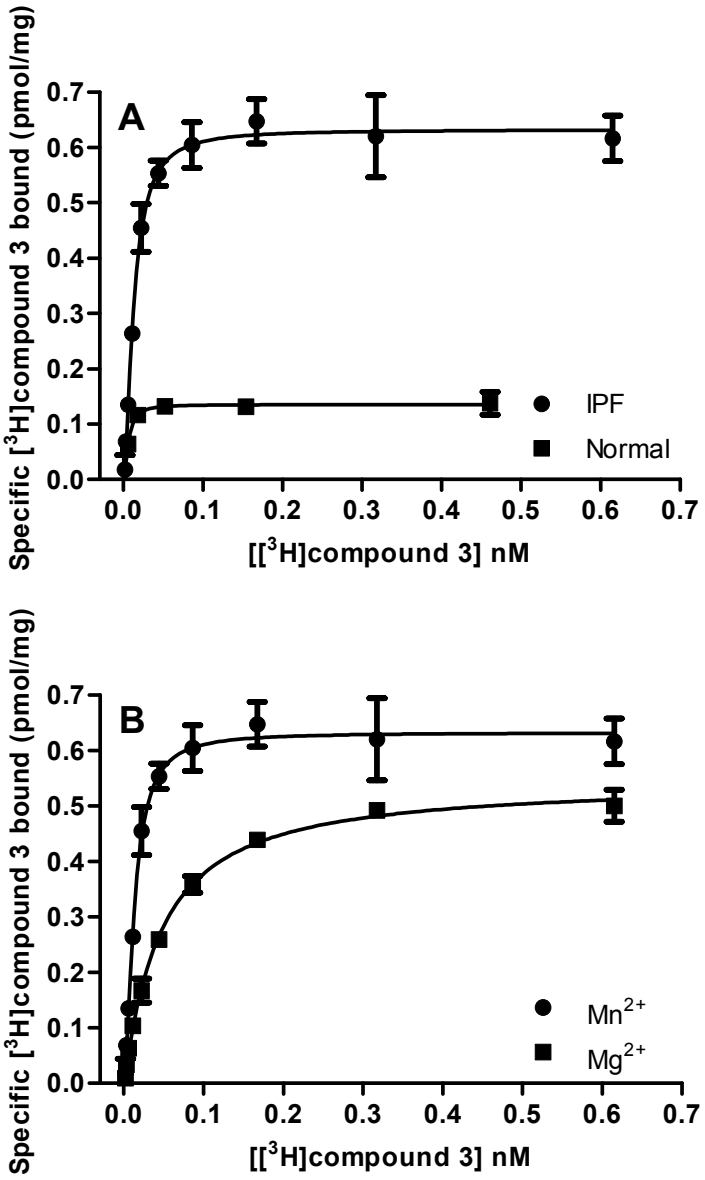

Figure 4.2.8 αvβ6 expression measured via [^{3}H]compound 3 saturation binding is increased from normal to IPF human lung tissue (A) and in the presence of Mn^{2+} in IPF human lung tissue (B). For saturation studies specific binding of [^{3}H]compound **3** was measured by incubation of increasing concentrations of radioligand with normal (non-fibrotic) or IPF human lung parenchyma membranes in the presence of either vehicle (1 % DMSO) or 10 μM A20FMDV2. Panel A shows a representative saturation plot comparing normal with IPF human lung parenchyma membranes (membrane concentration standardised) completed in the presence of 2 mM Mn^{2+}. Panel B shows representative saturation plots for IPF human lung parenchyma membranes (membrane concentration standardised) completed in the presence of either 2 mM Mg^{2+} or 2 mM Mn^{2+}. For all saturation binding studies plates were filtered after a 72 h incubation and the amount of radioligand bound to αvβ6 was measured by liquid scintillation spectroscopy. Specific binding was measured by subtracting the non-specific binding (10 μM A20FMDV2) from the total radioligand binding in the presence of vehicle (1 % DMSO). Specific saturation binding data were fitted to a one affinity site model with Hill slope to determine K_D and B_{max} values (see 2.11 Data analysis section). Data shown are mean ± SD of duplicate points and are of representative 6 donors (at least three individual experiments per donor).

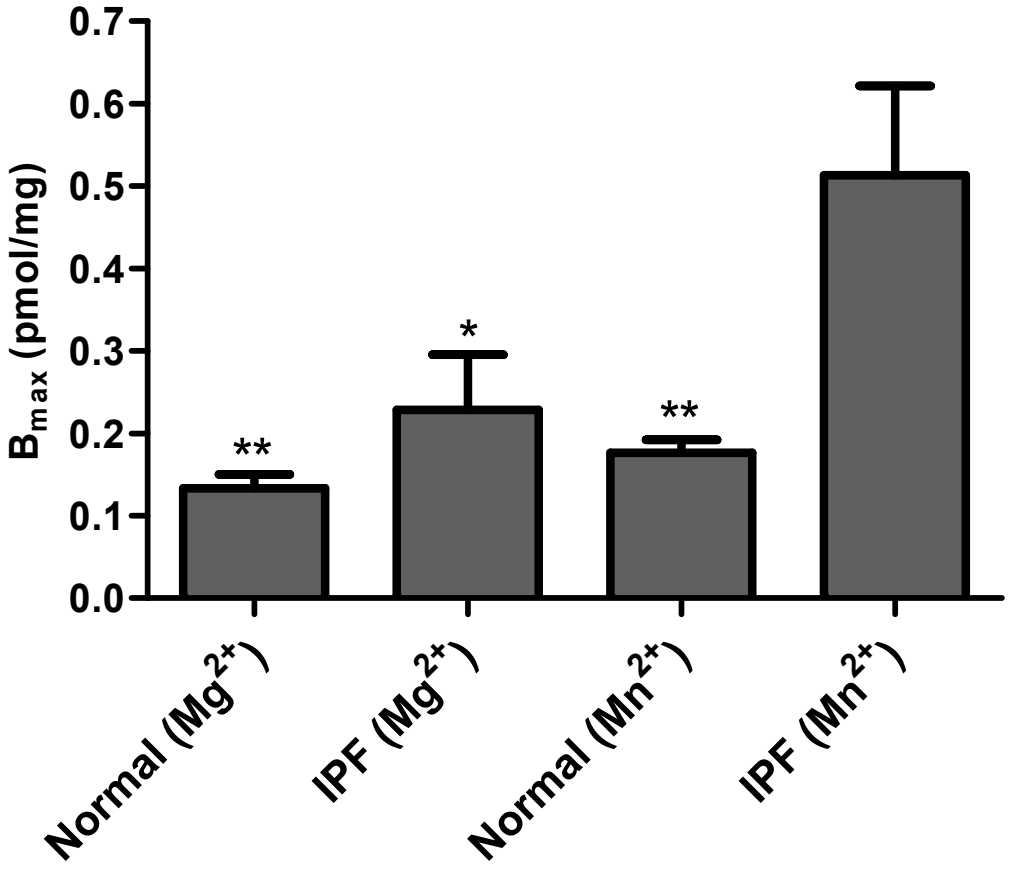

Figure 4.2.9 αvβ6 B_{max} is increased from normal to IPF human lung tissue and in the presence of Mn^{2+} in IPF human lung tissue. For saturation studies specific binding of [^{3}H]compound **3** was measured by incubation of increasing concentrations of radioligand with normal (non-fibrotic) or IPF human lung parenchyma membranes in the presence of either vehicle (1 % DMSO) or 10 μM A20FMDV2. B_{max} values generated from all saturation binding studies using healthy and IPF human lung parenchyma membranes are shown in the presence of either 2 mM Mg^{2+} or 2 mM $Mn^{2+}$with significant differences with IPF (Mn^{2+}) denoted by * $p < 0.05$ or ** $p < 0.01$ with no significant differences ($p > 0.05$) shown between any other conditions (ANOVA, Bonferonni post-test). For all saturation binding studies plates were filtered after a 72 h incubation and the amount of radioligand bound to αvβ6 was measured by liquid scintillation spectroscopy. Specific binding was measured by subtracting the non-specific binding (10 μM A20FMDV2) from the total radioligand binding in the presence of vehicle (1 % DMSO). Specific saturation binding data were fitted to a one affinity site model with Hill slope to determine K_D and B_{max} values (see 2.11 Data analysis section). Data shown are mean ± SEM of 6 normal and 6 IPF donors with at least three individual experiments completed per donor.

Condition	pK_D	Hill slope (n_H)	B_{max} *(pmol/mg)*
Normal Lung (Mg^{2+})	10.3 ± 0.04	1.01 (0.85, 1.18)	0.13 (0.09, 0.18)
IPF Lung (Mg^{2+})	10.7 ± 0.05	*1.55 (1.28, 1.83)	0.23 (0.06, 0.40)
Normal Lung (Mn^{2+})	11.0 ± 0.06	*1.27 (1.02, 1.52)	0.18 (0.14, 0.22)
IPF Lung (Mn^{2+})	11.3 ± 0.07	*1.86 (1.62, 2.10)	0.51 (0.23, 0.79)

Table 4.2.3 Saturation binding parameters for [^{3}H]compound 3 with the αvβ6 integrin in normal and IPF human lung parenchyma membranes. Specific saturation binding data were fitted to a one affinity site model with Hill slope to determine K_D, n_H and B_{max} values (see 2.11 Data analysis section). Data shown are mean values ± SEM or 95 % confidence limits (shown in parentheses) for 6 normal (non-fibrotic) or 6 IPF donors with at least three individual experiments completed per donor. *denotes n_H significantly greater than unity (one-sample *t*-test completed on $\log_{10}$ n_H vs. 0, $p < 0.05$). pK_D, negative $\log_{10}$ of K_D.

mM Mn^{2+} or 2 mM Mg^{2+} (Figure 4.2.8 and Table 4.2.3). A significant increase in B_{max} was observed in IPF membranes in the presence of Mn^{2+} compared with normal membranes in the presence of 2 mM Mg^{2+} and 2 mM Mn^{2+} and IPF membranes in the presence of 2 mM Mg^{2+} (ANOVA, Bonferroni post-test $p < 0.05$) (Figure 4.2.9 and Table 4.2.3). No other significant differences in B_{max} values between conditions were observed (ANOVA, Bonferroni post-test $p > 0.05$) although there was a trend for an increased B_{max} in IPF membranes in the presence of 2 mM Mg^{2+} compared with normal membranes in the presence of 2 mM Mg^{2+}. An average 2.9-fold increase was observed for αvβ6 between normal to IPF lungs (in the presence of 2 mM Mn^{2+}). A significant difference in pK_D was observed in IPF membranes in the presence of 2 mM Mn^{2+} compared with IPF membranes in the presence of 2 mM Mg^{2+}, normal membranes in the presence of 2 mM Mg^{2+} and 2 mM Mn^{2+} (ANOVA, Bonferroni post-test $p < 0.05$) (Figure 4.2.9 and Table 4.2.3). n_H values generated during saturation binding studies between [^{3}H]compound **3** and lung membranes were significantly greater than unity (one-sample *t*-test completed on $\log_{10} n_H$ vs. 0, $p < 0.05$), except for normal membranes completed in the presence of 2 mM Mg^{2+}.

4.3. Discussion

[^{3}H]compound 3 displays a binding profile with the human αvβ6 integrin comparable with its unlabelled form

In order to confirm the binding profile observed for the unlabelled form of compound **3** in previous studies using tool radioligands, compound **3** was radiolabelled with [^{3}H]. This would allow the scope of the binding characterisation with the αvβ6 integrin to be broadened to confirm affinity and determine accurate kinetic

measurements. Using [^{3}H]compound **1** to determine the affinity for compound **3** resulted in a pK_I value of 10.7 ± 0.08 (mean ± SEM, n=4) when run in a low αvβ6 protein assay format at 24 h to negate a tight binding limit that had been observed with the higher αvβ6 protein format (see Chapter 3). There was still the potential that this pK_I value for compound **3** was also being underestimated due to a tight binding limit (observed when the concentration of ligand required to cause inhibition is close to the concentration of the receptor (in this case the αvβ6 integrin) in the system). However, the pK_D determined from saturation binding studies for [^{3}H]compound **3** was comparable (pK_D 10.8 ± 0.08 measured at a low concentration of αvβ6 protein (25 pM) (mean ± SEM, n=4)) showing that the previous low αvβ6 protein competition binding assay was accurately determining the affinity of compound **3**. The mode of binding of [^{3}H]compound **3** with the αvβ6 RGD binding site has been shown to be a simple, competitive and reversible interaction (Figures 4.2.3 and 4.2.4, Table 4.2.1).

Previously the dissociation profile for compound **3** had been determined in a novel assay format where an excess of [^{3}H]compound **1** was used to compete off unlabelled αvβ6 ligands. In this novel system a slow dissociation profile had been observed with the high affinity compound **3** compared with fast dissociation profiles with low affinity compounds like compound **1**. There was also a suggestion that the dissociation profile of compound **3** was bi-phasic with a fast initial phase followed by a slow lag phase. This trend was also observed when dissociation studies with [^{3}H]compound **3** from the human αvβ6 were completed. However, direct measurements with [^{3}H]compound **3** allowed for a bi-phasic dissociation model to be fitted due to a greater level of accuracy and extended time course achievable. This

analysis showed that each phase contributed ~50 % of the total dissociation profile with a fast $t_{1/2}$ of 0.7 h and a slow $t_{1/2}$ of 19.9 h. These data further validated the use of the previous assay format used in the early lead optimisation for selection of compound **3** as a potential drug candidate for targeting αvβ6-mediated TGFβ release in IPF.

One aspect of the binding interaction of compound **3** with αvβ6 integrin not investigated directly before was its association kinetics. With [^{3}H]compound **3** it was shown that the association kinetics with αvβ6 was fast compared with previous radioligands (~4-fold faster than [^{3}H]compound **1** and ~6-fold faster than [^{3}H]A20FMDV2). This desirable characteristic aids for a rapid engagement of the integrin in the lung post-delivery of drug via nebulisation. Confirmation of the mode of [^{3}H]compound **3** binding to the αvβ6 integrin via the RGD-binding site was shown by the necessity for the presence of divalent metal cations. Mn^{2+} was the most potent activator of binding followed by Mg^{2+} and Ca^{2+}, with Ca^{2+} only able to partially activate the integrin with partial binding of [^{3}H]compound **3** observed. The latter observation prompted the testing of binding under more physiological divalent metal cation conditions using SLF that contains a combination of Mg^{2+} and Ca^{2+}, but no Mn^{2+}. In addition, the IPF lung environment is predicted to be of a lower pH than a normal lung as a result of increased lactic acid production (Kottmann *et al.*, 2012), therefore SLF at pH 6.2 was investigated to determine a relevant affinity of [^{3}H]compound **3** in the predicted conditions it would encounter in a diseased IPF lung. The affinity of [^{3}H]compound **3** under these conditions was only marginally decreased by ~3-fold suggesting that even in a diseased IPF lung compound **3** would be predicted to retain its high affinity for the αvβ6 integrin.

The αvβ6 integrin is significantly upregulated and potentially exists in a highly activated state in IPF compared with normal human lung tissue

In an effort to characterise the binding of compound **3** with the αvβ6 integrin in human tissue, [^{3}H]compound **3** was used in radioligand binding experiments with membranes generated from normal and IPF human lung tissue. This would confirm and quantify the upregulation of αvβ6 from normal to IPF human lung tissue, as well as determine the affinity and binding kinetics of compound **3** for αvβ6 in IPF human lung tissue, and investigate these parameters under different divalent cation conditions. As the membrane preparations generated from human lung tissue will contain plasma membranes from all lung parenchyma cell types e.g. containing alveoli, blood vessels and small airways; combined with the moderate affinity compound **3** has for non-αvβ6 integrins (see Chapter 3), the selective αvβ6 peptide A20FMDV2 was used to define the specific αvβ6 binding window. There was potential evidence of this as a higher NSB was observed in human lung membranes compared with soluble αvβ6 protein (Figure 4.2.1). This may be indicative of the increased protein in the lung membrane preparations that could contribute to high NSB or potentially binding of [^{3}H]compound **3** to other RGD integrins present.

It is well established from published findings (Bazzoni and Hemler, 1998; Plow *et al.*, 2000; Luo *et al.*, 2007), and supported by data generated with a number of radioligands (including [^{3}H]compound **3**) in binding assays with soluble αvβ6 integrin protein in this study, that the binding of integrin ligands is dependent on the presence of divalent metal cations (see Chapter 3). This is due to the presence of allosteric divalent metal cation binding sites on both α and β integrin subunits and it is hypothesised that it is the interactions with these sites on the β subunit that

influence ligand binding by induction of conformational changes (Mould, 1996). These conformational changes result in an activation of integrin from a low affinity state to a high affinity state increasing ligand affinity for the RGD binding site, in the case of αvβ6. Different types and concentrations of divalent metal cation have different effects with activation observed to be greater in the presence of Mn^{2+} vs. Mg^{2+} vs. Ca^{2+} at the same concentration. Or put another way the EC_{50} for activation of αvβ6 is lower for Mn^{2+} vs. Mg^{2+} vs. Ca^{2+} at a fixed concentration of [^{3}H]compound **3**. These effects are more than likely integrin and ligand specific though general trends between ligands at the same integrin have been shown to be consistent. In addition to RGD ligands and divalent metal cations, the activation of αvβ6 can also occur from inside the cell (inside-out signalling) via activation of the β subunit (anchored to actin filaments) during cell cytoskeleton reorganisation mediated via the GPCRs LPA receptor 2 (LPAR2) and protease-activated receptor 1 (PAR1) (Xu *et al.*, 2009), whose endogenous ligands have both been implicated in IPF (Howell *et al.*, 2005; Tager *et al.*, 2008).

Determining the expression levels of αvβ6 in normal compared with IPF lungs provides two important pieces of information. Firstly to confirm its upregulation in IPF and secondly to quantify the amount of integrin present in disease tissue to enable a dose prediction model to be generated for potential therapeutic small molecules. Due to the processing method for generation of cell plasma membranes from human lung tissue, the intracellular connection, and therefore inside-out activation, is disrupted and more than likely either partially or fully lost. This could result in activated αvβ6 in the high affinity state in the intact tissue shifting back to the low affinity state in the final membrane preparation. In addition, the preparation

method was completed in the presence of EDTA that would sequester the cations and inactivate the integrin. Therefore, to investigate this, saturation and dissociation binding were completed in the presence of either 2 mM Mg^{2+} or Mn^{2+}, with Mg^{2+} tested as a baseline (also allowed direct comparison to previous *in vitro* work) and Mn^{2+} tested to cause maximal activation.

As expected the affinity and dissociation $t_{1/2}$ increased for [^{3}H]compound **3** from Mg^{2+} to Mn^{2+} in IPF lung membranes (Figures 4.2.7, 4.2.8 and 4.2.9, Tables 4.2.2 and 4.2.3). More interestingly, the number of αvβ6 binding sites also increased significantly from Mg^{2+} to Mn^{2+} (Figure 4.2.9 and Table 4.2.3). When repeated in normal lung membranes no significant increase was observed between cations. In addition, there was a significant increase in the number of αvβ6 binding sites between normal and IPF lung membranes in the presence of Mn^{2+} with a trend also observed in the presence of Mg^{2+} (Figure 4.2.9 and Table 4.2.3). This suggested that a population of αvβ6 integrin was not detectable or present in the low affinity/inactive state in the presence of Mg^{2+} in IPF lung membranes that then were measurable upon activation (or when shifted to the high affinity state) via the addition of Mn^{2+}. In radioligand binding experiments completed with soluble αvβ6 protein, a shift in affinity has been observed when comparing Mg^{2+} with Mn^{2+}. However, no change in the maximum number of binding sites labelled in the soluble αvβ6 protein preparation was observed. This observation, combined with no significant difference observed in normal membranes between Mg^{2+} and Mn^{2+}, suggests that this is not an artefact of the switch in cations. To put the level of αvβ6 integrin measured in the human lungs of IPF donors (in the presence of Mn^{2+}) into context, it was of a comparable level to that determined for the β_2-adrenoceptor in

normal human lungs (Slack, 2014), that is deemed to be moderately high (Motulsky and Christopoulos, 2004). The trend to an increased affinity between normal and IPF lung membranes (Table 4.2.3) may also provide further evidence of a more activated αvβ6 integrin present in IPF. For example, it has been shown that as a result of LPA and thrombin activation of LPAR2 and PAR1, respectively, succeeded by Gαq, RhoA and Rho kinase signalling and cytoskeleton changes transmitted to αvβ6 via its cytoplasmic domains (Xu *et al.*, 2009) cause activation of the integrin.

n_H values generated during saturation binding studies between [^{3}H]compound **3** and lung membranes were significantly greater than unity (one-sample *t*-test completed on $\log_{10} n_H$ vs. 0, $p < 0.05$), except for normal membranes completed in the presence of 2 mM Mg^{2+}. The trend observed for steepening curves correlated with the increase in B_{max} of αvβ6 integrin observed. There are a number of potential explanations for observing a steep Hill slope value when completing saturation or competition binding studies. It could be that equilibrium in the system has not been achieved within the timeframe of the assay (Motulsky and Christopoulos, 2004; Hulme and Trevethick, 2010). As these studies were completed with an incubation time of 72 h, and based on the kinetics studies in the same membrane preparations with this radioligand, it is unlikely that this is the cause as equilibrium would be predicted to be achieved at this time point. Another potential explanation could be ligand depletion where a large fraction of the radioligand binds to a receptor (Hulme and Trevethick, 2010). As an increased amount of receptor is available for radioligand binding in IPF membranes and also in the presence of Mn^{2+} vs. Mg^{2+} within each lung state (normal and IPF) this could be having an effect. However, as conditions were optimised to reduce the amount of radioligand bound in these experiments, by

reducing membrane concentration to achieve <30 % radioligand bound (by lowering the amount added per well and increasing the volume of the assay from 0.5 ml to 1.5 ml) whilst maintaining a workable specific binding window, this has been controlled as much as possible. If ligand depletion was having an impact on affinity it would be predicted that it would cause an underestimation of pK_D (Carter *et al.*, 2007). Therefore, the total binding saturation data generated in IPF membranes in the presence of Mn^{2+} (steepest n_H) were also fitted to a model that corrected for ligand depletion ('One site – Total, accounting for ligand depletion' using Prism 5.0 (Motulsky and Christopoulos, 2004)). The pK_D value generated via this analysis was shown to be lower (pK_D 11.0 ± 0.04; mean ± SEM for 6 IPF donors with at least three individual experiments completed per donor) than that determined via the standard one affinity site model with Hill slope. This suggested ligand depletion was not having an impact on the affinity estimates in these studies.

The other interesting observation from this work is that a detectable level of αvβ6 in the normal human lung that is very consistent between donors. It is clear there is an upregulation in IPF, however this population is much more variable between donors. This could be a result of a number of factors that may influence these types of experiment. The starting human tissue sample for both normal and IPF donors are approximately the same and equates to ~2 % of the whole lung. Normal lung samples were randomly selected whilst for IPF lung samples fibrotic areas were selected via a visual inspection of tissue (selected from the site of disease in the lower interstitial lung) by experienced pulmonary fibrosis research scientists and pathologists. As the fibrosis in IPF is not homogenously distributed throughout the lung, and due to the inability to confirm its presence in the tissue sample processed via IHC, the increased

variability observed in the IPF human lung samples could well be as a result of tissue sampling error i.e. some samples selected from a more fibrotic region.

Comparing the profile of [^{3}H]compound **3** in IPF membranes with the soluble αvβ6 integrin protein overall, the latter predicts the characteristics observed in the former in terms of affinity. However, there is the suggestion that the integrin exists in a more activated state in the soluble protein preparation as the profile between the two systems are most comparable between different divalent metal cation conditions i.e. Mg^{2+} in soluble protein and Mn^{2+} in IPF membranes. This could be a consequence of the different methods used for generation of the different biological reagents, whereby the absence or presence of divalent metal cations during this process could influence the baseline conformation of the integrin. In addition, structurally there will be differences that could also influence the sensitivity to divalent metal cation i.e. solubilised free αvβ6 protein in solution compared with αvβ6 held in the plasma membrane from tissue preparations.

Summary

In summary, the mode of binding of [^{3}H]compound **3** with the human αvβ6 RGD binding site (soluble integrin protein systems) was shown to be a simple, competitive and a reversible interaction that was divalent metal cation dependent. Under all conditions, it exhibits an extremely high affinity for the αvβ6 integrin. The quantification of the upregulation of αvβ6 from healthy to IPF human lung tissue has been determined for the first time and αvβ6 has the potential to exist in a more highly activated state within diseased tissue.

CHAPTER 5: INHIBITION OF αVβ6-MEDIATED TGFβ ACTIVATION AND RGD LIGAND-INDUCED αVβ6 INTERNALISATION

5.1. Introduction

Following the identification of compound **3**, a high affinity, selective αvβ6 small molecule RGD-mimetic with a slow dissociation profile from the integrin, it was important to further characterise its functional effects in more physiologically relevant *in vitro* test systems. This is vital for a number of reasons. Firstly, it is imperative to confirm that compound **3** is able to inhibit the activation of TGFβ via blockade of αvβ6 with a sustained duration of action. This would not only be required for progression into *in vivo* studies but also provide further target validation for the integrin and test the slow binding dissociation hypothesis. Secondly, binding of a small molecule RGD-mimetic to the RGD binding site on αvβ6 could potentially result in ligand-induced internalisation as demonstrated for peptides (Hausner *et al.*, 2009). This phenomenon could be critical if ligand-induced internalisation resulted in the slow binding dissociation profile of compound **3** becoming irrelevant if αvβ6 were quickly recycled back to the surface post-internalisation, as the duration of action of compound **3** would rely on factors other than its slow dissociation kinetics.

Historically, the functional consequences of engaging αvβ6 in lung epithelial cells, in terms of TGFβ activation in primary cell *in vitro* systems, have been investigated in NHBE cells (Araya *et al.*, 2007; Xu *et al.*, 2009). Although it has been shown by immunohistochemistry that there are low levels of αvβ6 in the lower airways of normal human lung (Horan *et al.*, 2007), in primary epithelial cells isolated from bronchial regions of normal lung a measurable level of the integrin is observed that increases over culturing passage (Araya *et al.*, 2007). The initial level of αvβ6 may be an artefact of the enzymatic isolation process and a response to this stimulus that is then further exacerbated via *in vitro* culture, comparable to the up regulation of the

integrin in response to inflammation in man (Breuss *et al.*, 1995). However, from radioligand binding studies completed as part of this study the data generated suggests there is a detectable level of αvβ6 in normal human lung. Nevertheless, the NHBE cells offer an approach to probe the biology of αvβ6, albeit in a system with some caveats. These cells are normal, bronchial epithelial cells rather than the desired diseased IPF alveolar type II epithelial cells, where the observed up regulation of αvβ6 occurs. However, as the isolation and culturing of alveolar type II cells from healthy lung is a challenge (Jenkins *et al.*, 2011), and IPF tissue is scarcely available, the NHBE cells currently offer the closest surrogate. Therefore, experimental studies described in this chapter were aimed at the characterisation of compound **3** in primary NHBE cells, with functional end points that allowed the examination of potency and duration of direct inhibition of TGFβ activation. This utilised a co-culture of NHBE cells and a TMLC line (epithelial cell line) expressing firefly luciferase under the control of a TGFβ-sensitive portion of the PAI-1 promoter, allowing the measurement of TGFβ activation (Abe *et al.*, 1994). To complement these studies and provide a higher throughput assay, a co-culture system previously used for determining inhibition of αvβ6-mediated TGFβ activation (Weinreb *et al.*, 2004) was established and further characterised. This also utilised the TMLC line but with a co-culture of a colon cancer cell line recombinantly expressing αvβ6 (SW480-αvβ6) rather than NHBE cells.

In addition, the turnover of αvβ6 would also be investigated in the NHBE system post-binding of RGD-peptides ($tLAP_1$ and A20FMDV2) and small molecule RGD-mimetics (SC-68448 and compound **3**). This would provide informative data on the similarities and differences between small molecule RGD-mimetics and RGD

peptides in relation to ligand-induced αvβ6 internalisation and subsequent recycling. This would also further aid in testing the slow binding dissociation hypothesis for compound **3**. This data would be critical for progression of compound **3** as a potential drug candidate for the treatment of IPF as well as potentially aiding in dose prediction in subsequent *in vivo* and clinical studies as it would provide potency and kinetic data in a relevant primary cell system.

5.2. Results

5.2.1. Surface expression of RGD integrins and TGFβRII on SW480-αvβ6 cells

To determine the surface expression of the RGD integrin subunits α5, α8, αv, β1, β6, β8, integrin heterodimers αvβ3 and αvβ5 and the TGFβRII on SW480-αvβ6 cells, flow cytometric assays were completed. There was a clear differentiation between populations of SW480-αvβ6 cells labelled with selective flow cytometry antibodies compared with isotype controls for αv, β1, β6 and αvβ5 but no differentiation was observed for α5, α8, β8, αvβ3 and TGFβRII (Figure 5.2.1). All flow cytometry antibodies were selected based on data showing validation, i.e. clear differentiation between populations of control cells known to contain that protein being labelled with selective flow cytometry antibody, compared with isotype controls that had been completed by the manufacturer. However, where no differentiation was observed between a selective flow cytometry antibody and its matched isotype control, either in SW480-αvβ6 or NHBE cell flow cytometry studies (i.e. α5, α8, β8, αvβ3), control cells were used to confirm manufacturers validation (see Appendix section 8.3.2, Figure 8.3.2).

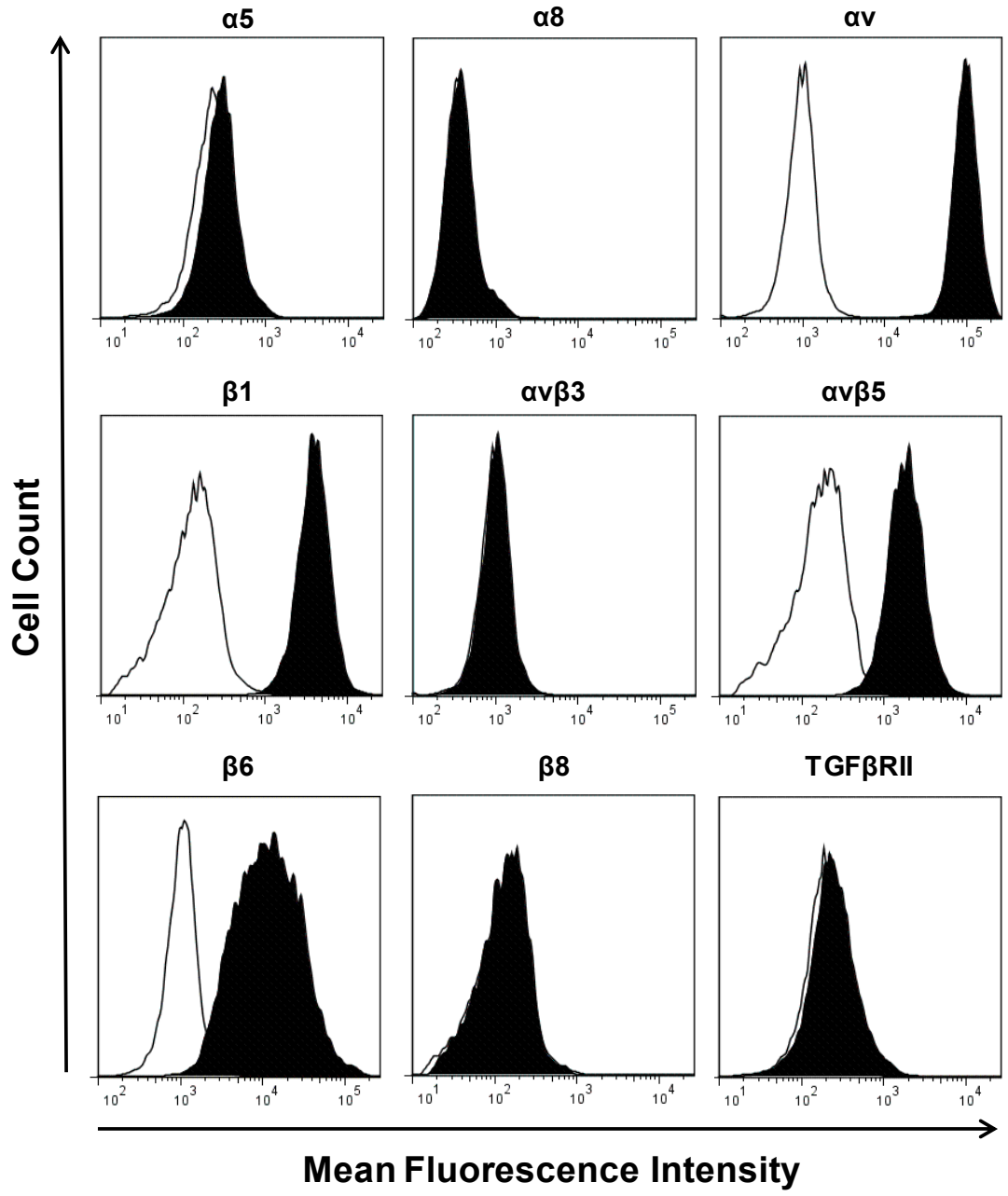

Figure 5.2.1 Expression of RGD integrin subunits or heterodimers and the TGFβRII on the surface of SW480-αvβ6 cells. SW480-αvβ6 cells were recovered from culture and surface staining of the human α5, α8, αv, β1, αvβ3, αvβ5, β6 and β8 integrin subunits or heterodimers and the TGFβRII were determined by flow cytometry. SW480-αvβ6 cells were washed and stained with flow cytometry antibodies (see section 2.1 Materials) that were either specific for the protein of interest (black peaks) or the relevant isotype control (white peaks). Fluorescence-activated cell analyses histograms shown are plotted with normalised cell count against mean cell fluorescence intensity and are representative of expression levels in SW480-αvβ6 cells in continuous culture.

5.2.2. Inhibition of TGFβ activation in SW480-αvβ6 cells

In order to measure the functional inhibition of TGFβ release via αvβ6 blockade a co-culture system was investigated using SW480-αvβ6 cells and TMLCs. To ensure that compound **3** did not cause direct blockade at TGFβRI or II on the TMLCs it was shown that no inhibition of luciferase activity by compound **3** was observed in the presence of TGFβ (10 ng/ml) stimulated TMLCs in the absence of SW480-αvβ6 cells (Figure 5.2.2A). The ALK5 (TGFβRI) inhibitor SB-525334 was shown in the same experiments to attenuate the luciferase activity (Figure 5.2.2A). In the co-culture system a measureable level of TGFβ was produced on the linear phase of the TGFβ standard curve (Figure 5.2.2B). In single shot studies using selective RGD integrin subunit or heterodimer blocking antibodies or RGD-mimetic small molecules/peptides, complete inhibition of TGFβ activation from SW480-αvβ6 was observed with the anti-αv antibody 17E6, the anti-TGFβ1, 2 and 3 antibody 1D11 and compound **3** (Figure 5.2.3A). Partial inhibition of TGFβ release was observed with the anti-β1 antibody 4B4, the anti-αvβ6 antibody 10D5, the αvβ1, αvβ3 and αvβ5 cyclic-peptide cilengitide, αvβ6 selective peptide A20FMDV2 and $fLAP_1$ (Figure 5.2.3A). No inhibition of TGFβ release was observed with the anti-αvβ5 antibody 5H9 and the IgG1 and IgG2a isotype controls (Figure 5.2.3A). Cilengitide was shown in radioligand binding studies to cause greater than 80 % inhibition of radioligand binding at αvβ1 and αvβ5 at the maximum concentration used in the SW480-αvβ6/TMLC co-culture (1 μM) but less than 20 % inhibition of radioligand binding at αvβ6 (Chapter 3, Figure 3.2.9C). Cilengitide demonstrated a pIC_{50} value for TGFβ release inhibition that was comparable to its pK_I value (7.10 ± 0.16, mean

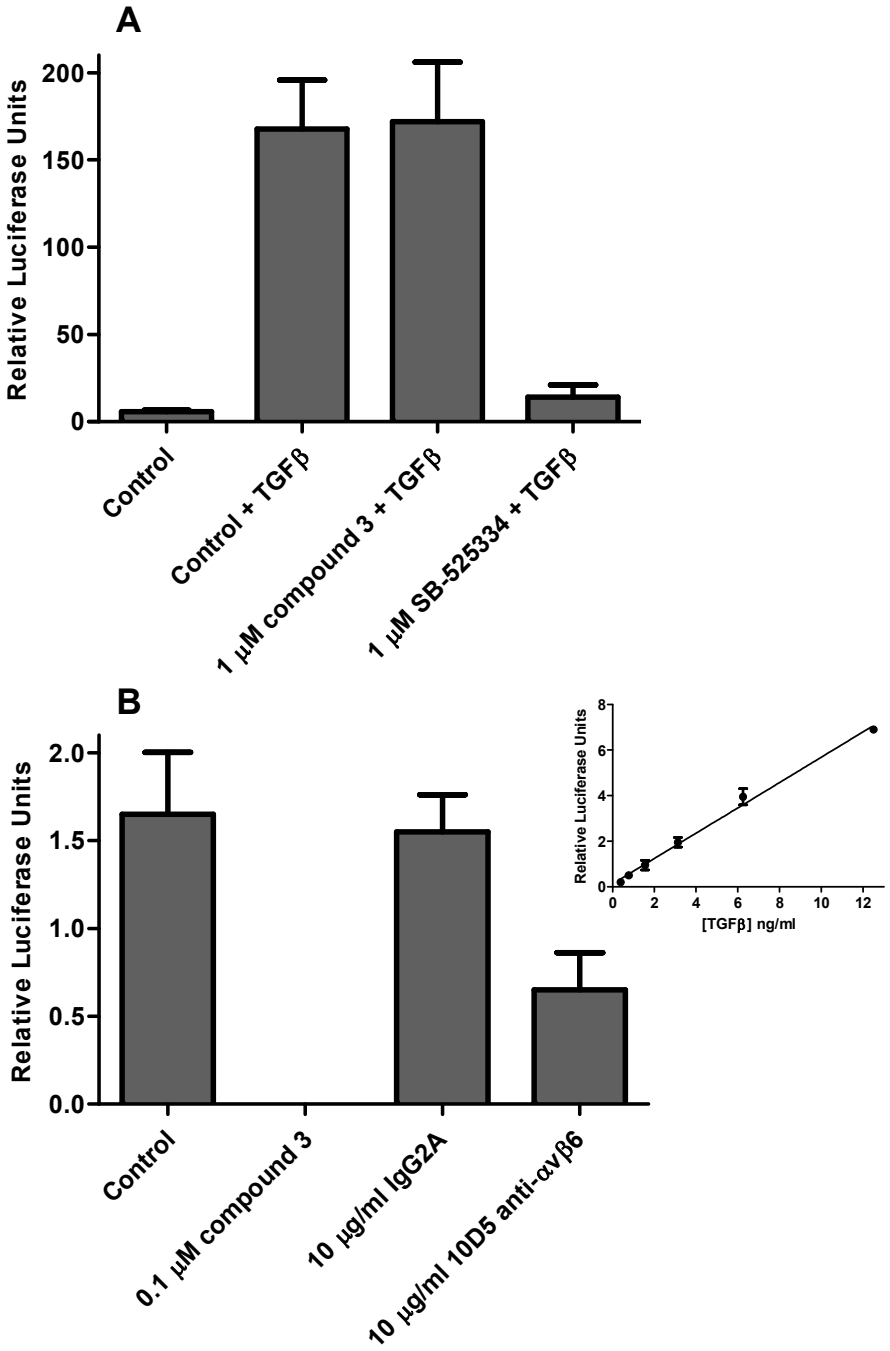

Figure 5.2.2 Compound 3 does not inhibit the TGFβRI/II complex directly (A) but inhibits both αvβ6- and non-αvβ6-mediated TGFβ release from SW480-αvβ6 cells (B). TGFβ activation and release from SW480-αvβ6 cells was determined by co-culturing with TMLCs expressing the firefly luciferase under the control of a TGFβ-sensitive portion of the PAI-1 promoter following a 20 h incubation. The effect of TGFβ in the absence and presence of the small molecule RGD-mimetic compound **3** and ALK5 (TGFβRII) inhibitor SB-525334 was measured on TMLCs in a single cell culture system (A). Inhibition of TGFβ release from SW480-αvβ6 cells in co-culture with TMLCs was determined for control (0.1 % DMSO), isotype control (IgG2A), the small molecule αvβ6 RGD-mimetic compound **3** and a selective anti-αvβ6 antibody (10D5) (B). Data shown in panel A are the mean ± SEM of four individual experiments carried out in duplicate. Data shown in panel B are the mean ± SD of duplicate points and are representative of at least four individual experiments with similar results. Inset B: TGFβ standard curve to allow comparison of relative luciferase units generated in test wells.

± SEM, n=4) at the αvβ1 integrin (Table 5.2.1 and Chapter 3, Table 3.2.7). In addition, full CRCs were completed with compound **3** in the absence and presence of either 1 μM cilengitide or 10 μg/ml 10D5 (Figure 5.2.3B). When CRCs for compound **3** were completed alone, full inhibition of TGFβ release with a high pIC_{50} value was observed (Table 5.2.1). In the presence of 1 μM cilengitide, compound **3** caused partial inhibition of TGFβ release with a comparatively very high pIC_{50} value observed (Figure 5.2.3B, Table 5.2.1) comparable to its pK_I value (11.0 ± 0.09, mean ± SEM, n=6 determined in 'low protein assay') at the αvβ6 integrin (Chapter 3). In the presence of 10 μg/ml 10D5, compound **3** caused partial inhibition of TGFβ release with a comparatively low pIC_{50} value observed (Figure 5.2.3B, Table 5.2.1) comparable to its pK_I value (8.68 ± 0.17, mean ± SEM, n=4) at the αvβ1 integrin (Table 5.2.1 and Chapter 3, Table 3.2.7).

5.2.3. Surface expression of RGD integrins and TGFβRII on NHBE cells

To determine the baseline surface expression of the RGD integrin subunits α5, α8, αv, β1, β6, β8, integrin heterodimers αvβ3 and αvβ5 and the TGFβRII on NHBE cells, flow cytometric assays were completed at P1. To monitor the change in surface expression of these proteins on NHBE cells through their lifetime in culture, assays were then repeated at P2, P3 and P4 (for P2, P3 and P4 data see Appendix section 8.3.1, Figure 8.3.1). At P1 there was a clear differentiation between populations of NHBE cells labelled with selective flow cytometry antibodies compared with isotype controls for αv, β1, β6, αvβ5 and TGFβRII (Figure 5.2.4). No differentiation was observed for α5, α8, β8 and αvβ3 (Figure 5.2.4) and this trend continued for P2, P3 and P4 (data not shown). Very high levels of the αv and β1 integrin subunit were

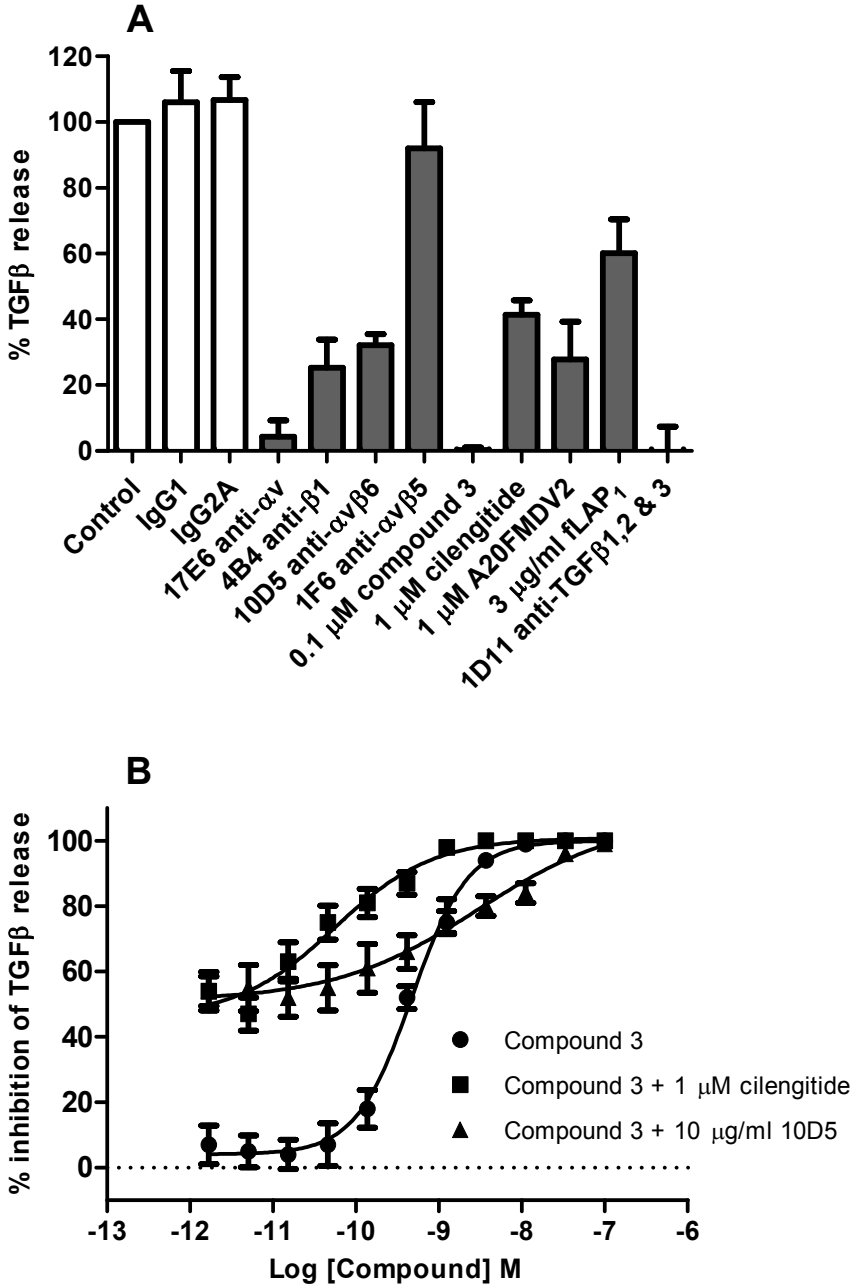

Figure 5.2.3 TGFβ release from SW480-αvβ6 cells is mediated via αvβ1 and αvβ6 (A) and compound 3 is able to inhibit both mechanisms (B). TGFβ activation and release from SW480-αvβ6 cells was determined by co-culturing with TMLCs expressing the firefly luciferase under the control of a TGFβ-sensitive portion of the PAI-1 promoter following a 20 h incubation. Inhibition of TGFβ release from SW480-αvβ6 cells was determined in single shot for a range of blocking antibodies (all tested at 10 μg/ml including isotype controls), small molecule RGD-mimetics and RGD peptides (A). Control (0.1 % DMSO) and 0.1 μM compound **3** were used to calculate the % release of TGFβ within each experiment (as detailed in 2.11 Data analysis section). CRCs were generated for compound **3** (B) by incubation at a range of concentrations with SW480-αvβ6 cells in the absence and presence of either 1 μM cilengitide or 10 μg/ml 10D5 (αvβ6 blocking antibody). Control (0.1 % DMSO) and 0.1 μM compound **3** were used to calculate % inhibition of TGFβ release (as detailed in 2.11 Data analysis section). Data shown are the mean ± SEM of at least four individual experiments carried out in quadruplicate.

Test Compound/Combination	*TGFβ Inhibition* pIC_{50}/IC_{50}	n_H
10D5 anti-αvβ6	145 ± 52 ng/ml	0.91 (0.22, 1.61)
Cilengitide	7.00 ± 0.51	0.86 (0.53, 1.19)
Compound 3	9.44 ± 0.06	1.09 (0.77, 1.41)
Compound 3 + 1 µM cilengitide	10.4 ± 0.24	1.38 (-0.34, 3.11)
Compound 3 + 10 µg/ml 10D5 anti-αvβ6	8.48 ± 0.29	0.93 (0.17, 1.69)

Table 5.2.1 pIC_{50}/IC_{50} values for inhibition of TGFβ release by RGD ligands determined in a SW480-αvβ6/TMLC co-culture assay. TGFβ activation and release from SW480-αvβ6 cells was determined by co-culturing with TMLCs expressing the firefly luciferase under the control of a TGFβ-sensitive portion of the PAI-1 promoter following a 20 h incubation. CRCs were fitted using non-linear regression analysis (four-parameter logistic equation with variable slope (Hill, 1909)) (as detailed in 2.11 Data analysis section). IC_{50} values in ng/ml have been shown for the 10D5 anti-β6 antibody. Data shown are mean values ± SEM for at least four individual determinations. n_H, Hill slope; pIC_{50}, negative $\log_{10}$ of IC_{50}.

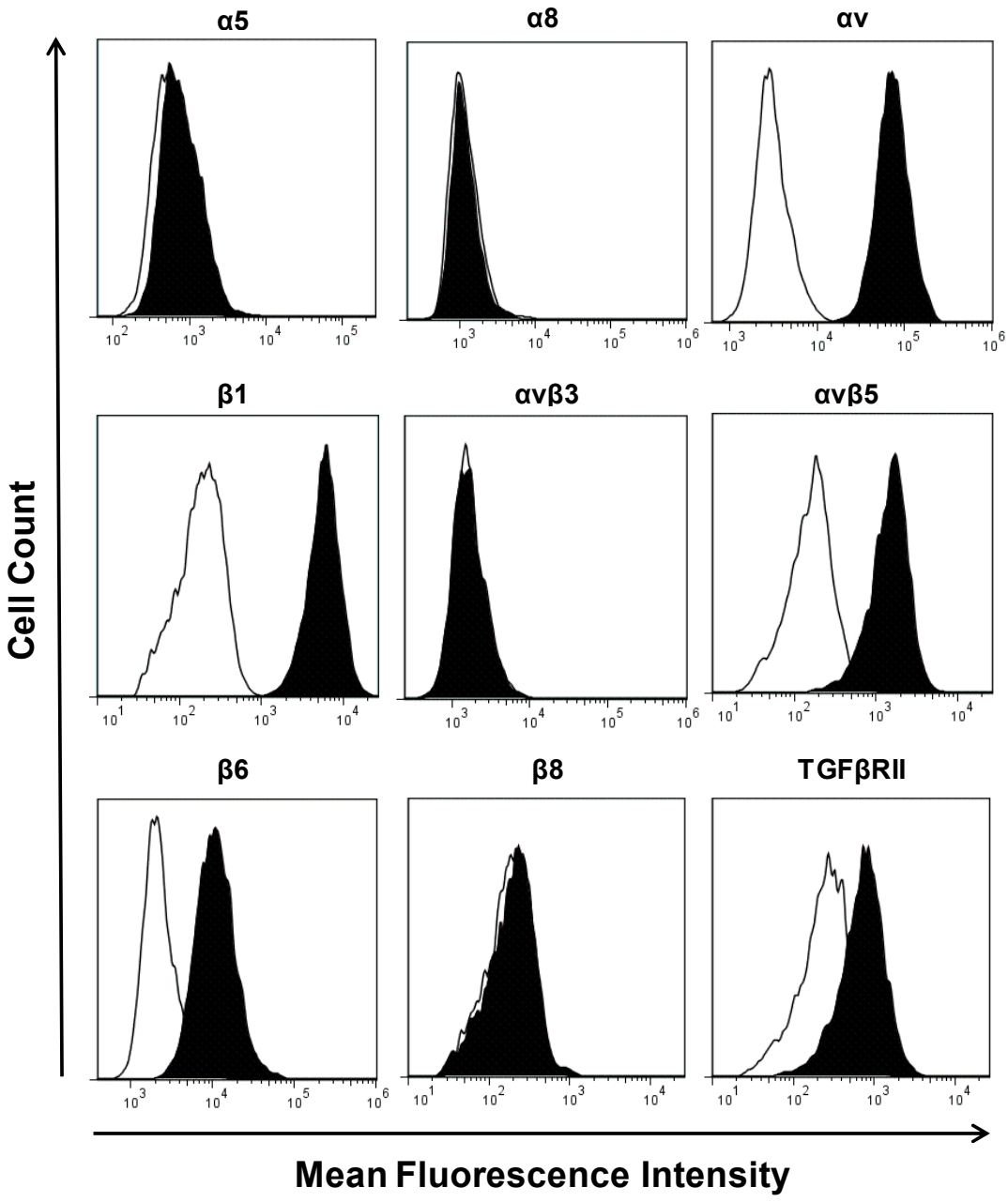

Figure 5.2.4 Expression of RGD integrin subunits or heterodimers and the TGFβRII on the surface of NHBE cells. NHBE cells were recovered from culture and surface staining of the human α5, α8, αv, β1, αvβ3, αvβ5, β6 and β8 integrin subunits or heterodimers and the TGFβRII were determined by flow cytometry. NHBE cells were washed and stained with flow cytometry antibodies described in section '2.1 Materials' that were either specific for the protein of interest (black peaks) or the relevant isotype control (white peaks). Fluorescence-activated cell analyses histograms shown are plotted with normalised cell count against mean cell fluorescence intensity and are representative of expression levels in NHBE cells at passage 1 (P1).

observed on the surface of NHBE cells at P1 that both increased to P2, peaked at P3 and decreased to P4. At P4 the levels of the αv and β1 integrin subunits were still greater than that observed at P1. High levels of the β6 integrin subunit were observed on the surface of NHBE cells at P1 that increased to P2, decreased to P3 and further decreased to P4. At P4 the levels of β6 integrin subunit were still greater than that observed at P1 (see Appendix section 8.3.2, Figure 8.3.2).

Moderate levels of the TGFβRII were observed on the surface of NHBE cells at P1 that increased to P2, peaked at P3 and decreased to P4. At P4 the levels of TGFβRII were still greater than that observed at P1. The moderate expression of αvβ5 at P1 were observed to be stable over the culture lifecycle up to and including P4. All flow cytometry antibodies were selected based on data showing validation, i.e. clear differentiation between populations of control cells known to contain that protein being labelled with selective flow cytometry antibody compared with isotype controls that had been completed by the manufacturer. However, where no differentiation was observed between a selective flow cytometry antibody and its matched isotype control (i.e. α5, α8, β8, αvβ3), control cells were used to confirm manufacturers validation (see Appendix section 8.3.2, Figure 8.3.2).

5.2.4. Inhibition of TGFβ activation in NHBE cells

To demonstrate the functional activity of compound **3**, an assay using a physiologically relevant cell line (NHBE cells) was developed to measure inhibition of TGFβ activation. This used a co-culture system with TMLCs and a measurement of TGFβ activation via firefly luciferase under the control of a TGFβ-sensitive portion of the PAI-1 promoter. In the co-culture system a measureable level of

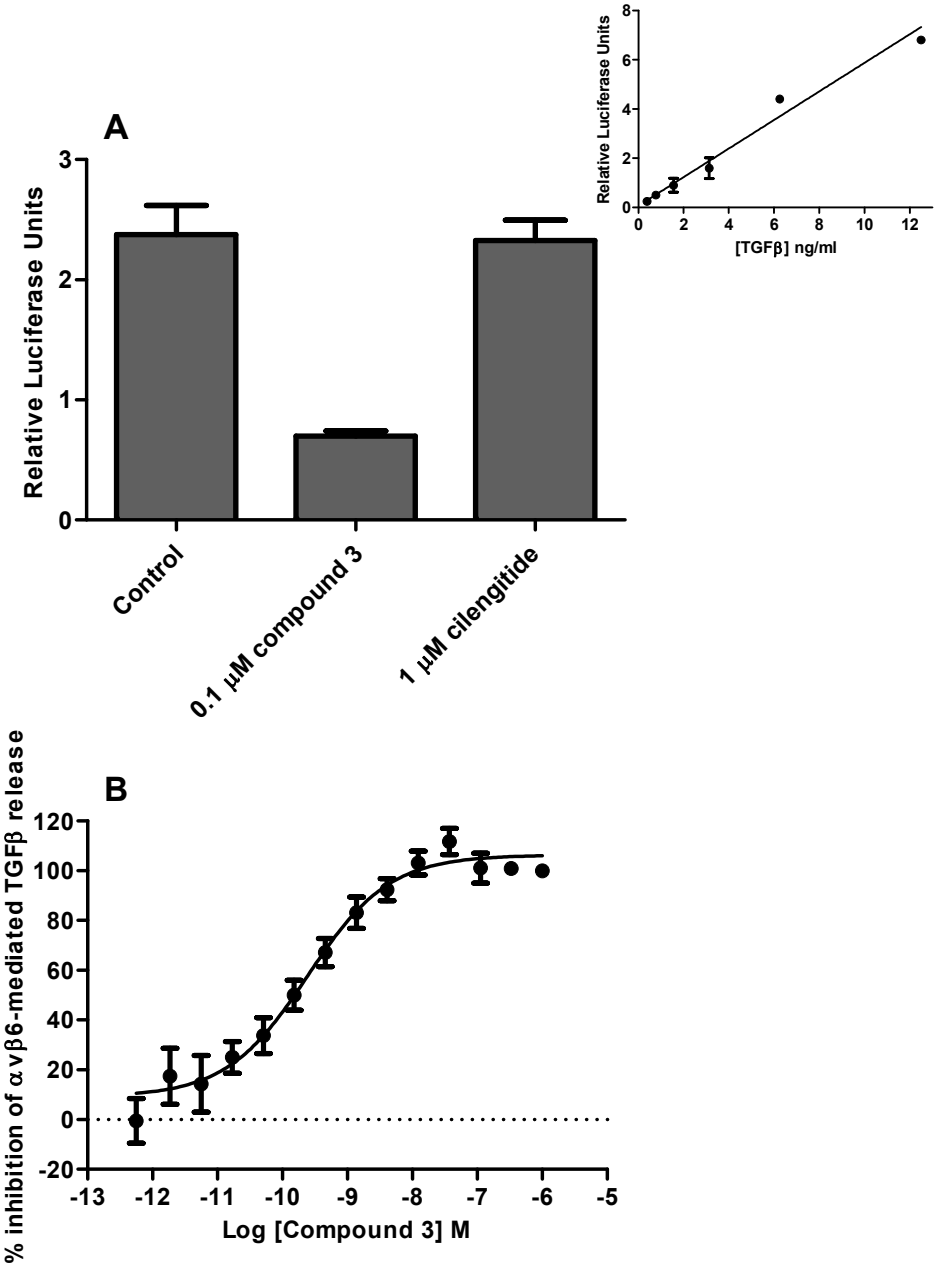

Figure 5.2.5 TGFβ release from NHBE cells is mediated via αvβ6 (A) and compound 3 is able to inhibit in a concentration-dependent manner (B). TGFβ activation and release from NHBE cells was determined by co-culturing with TMLCs expressing the firefly luciferase under the control of a TGFβ-sensitive portion of the PAI-1 promoter following a 20 h incubation. Inhibition of TGFβ release from NHBE cells in co-culture with TMLCs was determined for control (0.1 % DMSO), the small molecule αvβ6 RGD-mimetic compound **3** and the αvβ1, 3 and 5 selective RGD cyclic peptide cilengitide (A). A full CRC was generated (B) for compound **3** by incubation at a range of concentrations with NHBE cells. CRC for compound **3** was fitted using non-linear regression analysis (four-parameter logistic equation with variable slope (Hill, 1909)) (as detailed 2.11 Data analysis section). Data shown in panel A are the mean ± SEM of quadruplicate points and are representative of at least four individual experiments with similar results. Data shown in panels B are the mean ± SEM of seven individual experiments carried out in quadruplicate. Inset A: TGFβ standard curve to allow comparison of relative luciferase units generated in test wells.

TGFβ was produced on the linear phase of the TGFβ standard curve (Figure 5.2.5A). Compound **3** was shown to inhibit TGFβ activation in this system whilst cilengitide did not cause any inhibition of TGFβ activation compared with control (0.1 % DMSO) when tested at 1 μM (Figure 5.2.5A). A pIC_{50} of 9.41 ± 0.11 and n_H of 0.74 (0.51, 1.01) (mean ± SEM or 95 % confidence intervals shown in parentheses, n=7) (Figure 5.2.5B) for inhibition of TGFβ activation was demonstrated in this system. The n_H was not significantly different from unity (one-sample *t*-test completed on $\log_{10}$ n_H vs. 0, $p > 0.05$). This data was comparable to the affinity estimate (pK_D value of 9.91 ± 0.12 and n_H of 0.95 (0.67, 1.24) (mean ± SEM or 95 % confidence limits in parentheses, n=4)) determined by saturation binding of [^{3}H]compound **3** in NHBE cells (using 10 μM A20FMDV2 to define NSB and a 6 h incubation period). In washout studies over 24 h it was shown that a significant level of inhibition (66 ± 8 %, mean ± SEM, n=4) was still evident for compound **3** compared with control (ANOVA, Dunnett post-test, $p < 0.001$) (Figure 5.2.6).

5.2.5. Internalisation and recycling of the αvβ6 integrin in NHBE cells

To quantitatively measure the surface (membrane) and total (membrane and intracellular pools) NHBE cell expression of αvβ6, flow cytometric assays were completed. The β6 integrin subunit was measured as a surrogate for the αvβ6 heterodimer to reduce the likelihood of competition between an αvβ6 ligand and the staining antibody (antibodies raised to the heterodimer could potentially bind at the RGD-site therefore having an increased likelihood of direct competition), therefore allowing the measurement of ligand-induced internalisation. However, to ensure that the hβ6-PE antibody did not bind to the αvβ6 RGD-site, the unlabelled form of the antibody was tested in an αvβ6 cell adhesion assay (K562 cells recombinantly

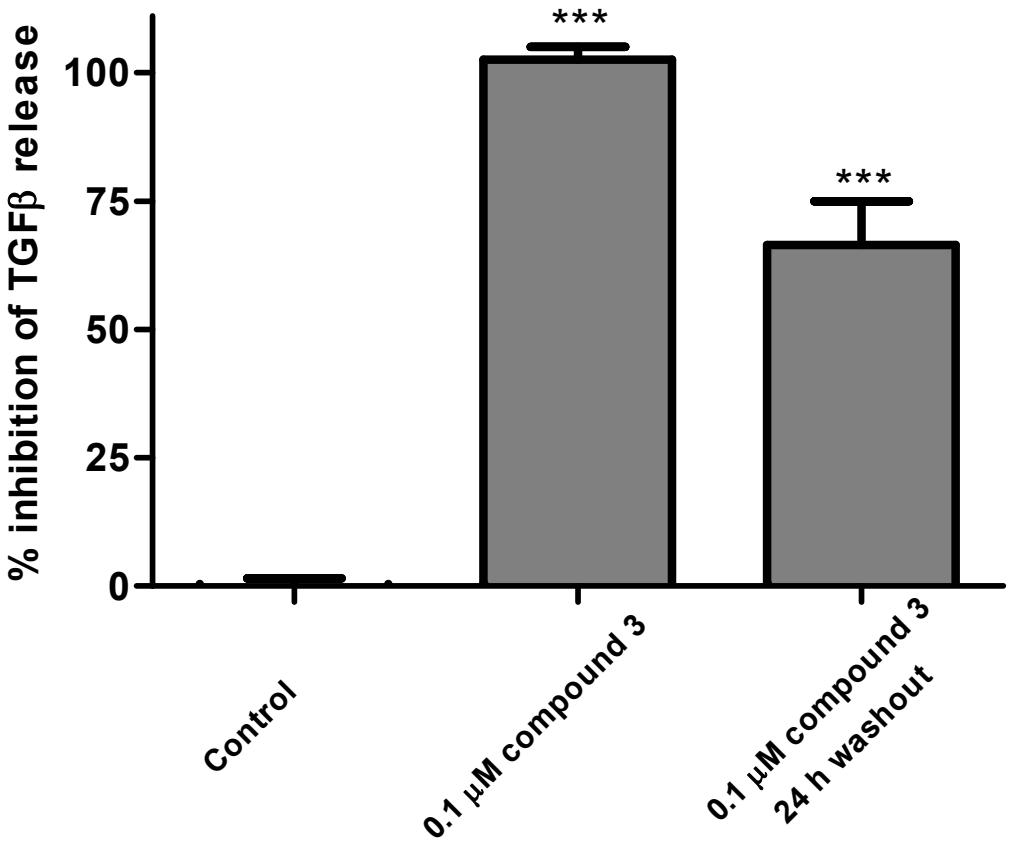

Figure 5.2.6 Compound 3 causes a sustained inhibition of TGFβ release from NHBE cells. TGFβ activation and release from NHBE cells was determined by co-culturing with TMLCs expressing the firefly luciferase under the control of a TGFβ-sensitive portion of the PAI-1 promoter following a 20 h incubation. Duration of inhibition of TGFβ release from NHBE cells was determined following a 1 h compound incubation followed by removal (washout) and a further 24 h incubation with control (0.1 % DMSO). Significant difference compared to control (0.1 % DMSO) denoted by *** (ANOVA, Dunnett post-test, $p < 0.001$). Control (0.1 % DMSO) and 0.1 μM compound **3** were used to calculate % inhibition of TGFβ release (as detailed in 2.11 Data analysis section). Data shown are the mean ± SEM of at least four individual experiments carried out in quadruplicate.

expressing the αvβ6 integrin adhering to GST- LAP_1). The unconjugated form of the antibody used in flow cytometric assays displayed no inhibition of αvβ6-mediated cell adhesion (Figure 5.2.7A). In addition, 0.2 % w/v saponin (concentration used to permeabilise NHBE cells) did not reduce the affinity of $tLAP_1$ or compound **3** for the αvβ6 integrin in a radioligand competition binding assay (Figure 5.2.7B).

$fLAP_1$ and compound **3** both caused a significant reduction in surface expression of αvβ6 (ANOVA, Bonferroni post-test, $p < 0.05$) (Figure 5.2.8A). Although $fLAP_1$ and compound **3** did not reduce MFI to the same level as the IgG2B-PE isotype control, no significant difference was observed between these groups (ANOVA, Bonferroni post-test, $p > 0.05$). In addition, there was no significant difference between the loss of surface αvβ6 observed with $fLAP_1$ and compound **3** (ANOVA, Bonferroni post-test, $p > 0.05$). When cells were permeabilised to allow antibodies intracellular access, there was no significant difference observed between hβ6-PE with and without either $fLAP_1$ or compound **3** (ANOVA, Bonferroni post-test, $p > 0.05$), providing further evidence the perceived internalisation was not a result of the αvβ6 ligand preventing antibody binding (Figure 5.2.8A). Based on the mean MFI values for hβ6-PE in permeabilised (total cell staining) and unpermeabilised (membrane staining) NHBE cells, ~36 % of αvβ6 integrin was present intracellularly and ~64 % at the cell surface. The internalisation observed in the presence of $fLAP_1$ and compound **3** was inhibited when NHBE cells were pre-incubated with the clathrin-coated pit inhibitor chlorpromazine, whilst the lipid raft inhibitor filipin had no effect (Figure 5.2.8B). The internalisation of cell surface αvβ6 was confirmed using confocal microscopy by immunofluorescence staining of the β6 subunit (Figure

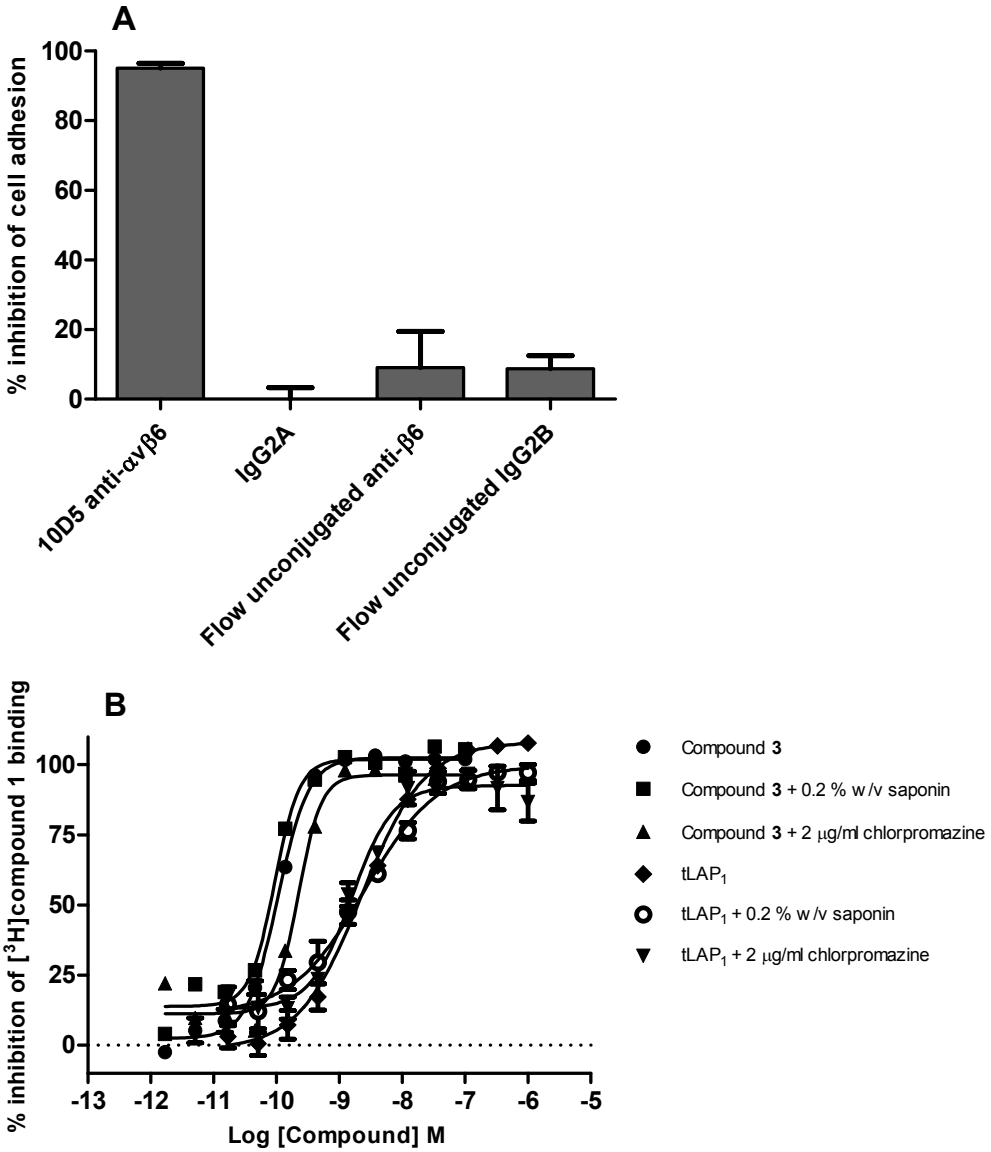

Figure 5.2.7 β6 flow cytometry antibodies do not inhibit αvβ6 cell adhesion (A) and saponin/chlorpromazine do not inhibit compound 3 and fLAP$_1$ binding to αvβ6 (B). The effect of blocking and unconjugated flow cytometry β6 antibodies (including isotype controls) on αvβ6 cell adhesion was measured by incubating antibodies at 100 μg/ml with K562 cells recombinantly expressing the αvβ6 integrin in plates coated with GST-LAP$_1$ (A). Plates were incubated for 30 min prior to removal of non-adhering cell populations and the remaining adhered cells were then quantified by fluorescence using BCECF-AM. Total and non-specific binding values were measured in the presence of vehicle (1 % DMSO) and 10 mM EDTA respectively, and were used to calculate the % inhibition of cell adhesion (as detailed in 2.11 Data analysis section). Full competition binding curves were generated by incubating unlabelled integrin ligand at a range of concentrations with αvβ6 integrin (0.3 nM) and [^{3}H]compound **1** (~1 nM) in absence and presence of 0.2 % w/v saponin or 2 μg/ml chlorpromazine (B). Plates were then filtered after a 6 h incubation and the amount of radioligand bound to αvβ6 was measured by liquid scintillation spectroscopy. Total and non-specific binding values were measured in the presence of vehicle (1 % DMSO) and 10 μM SC-68448 respectively, and were used to calculate the % inhibition of radioligand bound to the αvβ6 integrin (as detailed in 2.11 Data analysis section). Competition binding data were fitted using non-linear regression analysis (four-parameter logistic equation with variable slope (Hill, 1909)) (as detailed in 2.11 Data analysis section). Data shown are the mean ± SEM of at least four individual experiments carried out in singlicate.

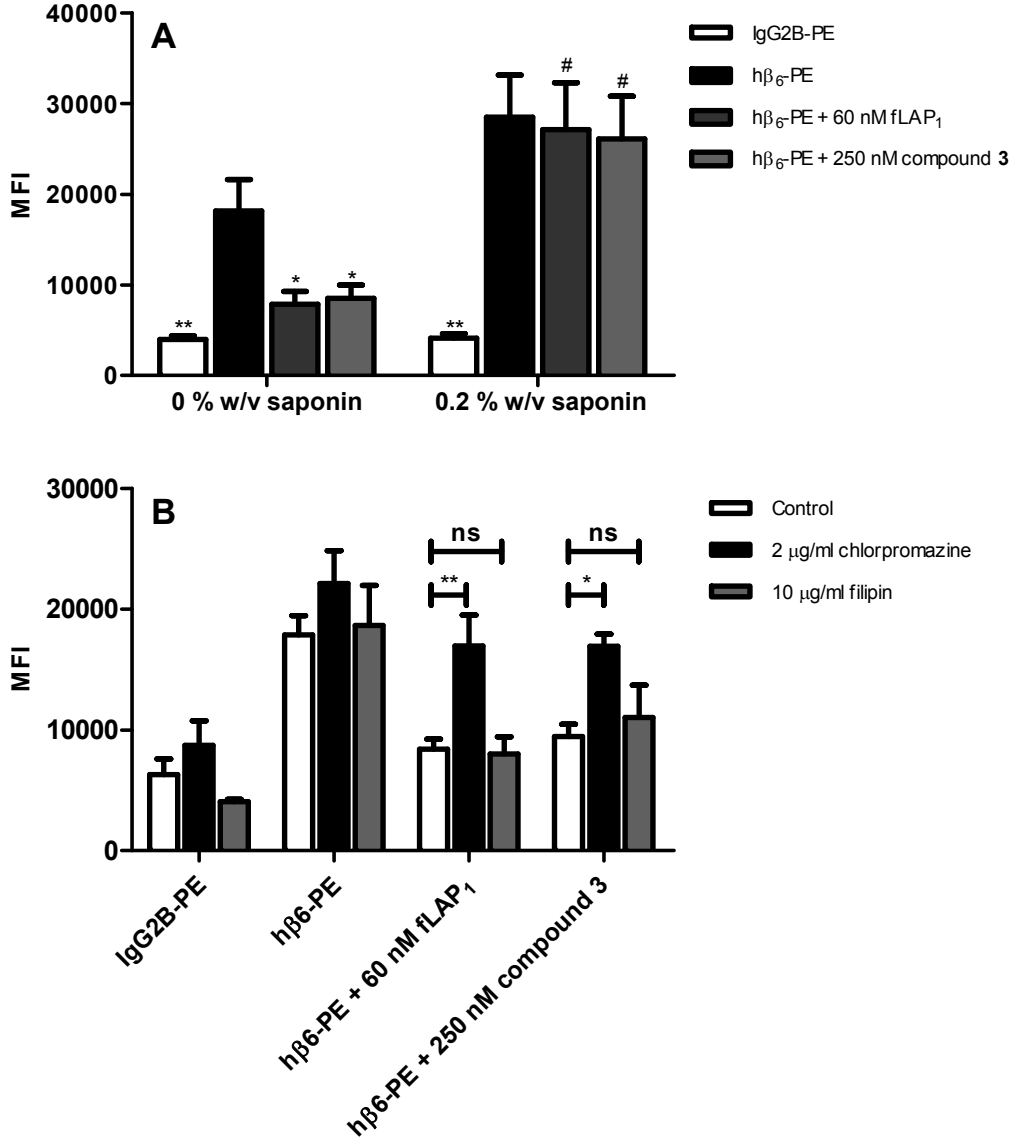

Figure 5.2.8 Flow cytometry MFI plots showing ligand-induced αvβ6 internalisation triggered by $fLAP_1$ and compound 3 (A) that is inhibited by chlorpromazine (B). NHBE cells were incubated for 2 h in the presence of either vehicle (0.1 % DMSO), 60 nM $fLAP_1$ or 250 nM compound **3**. β6 integrin staining was then determined by flow cytometry where NHBE cells were washed and stained with a PE-conjugated mouse monoclonal anti-human integrin β6 (hβ6-PE), either with or without permeabilisation (i.e. with or without 0.2 % w/v saponin) (A) or in the absence or presence of chlorpromazine (2 μg/ml) or filipin (10 μg/ml) (B). Control NHBE cell groups were also stained with a PE-conjugated mouse IgG2B isotype control (IgG2B-PE). In panel A significant difference compared to hβ6-PE denoted by *$p < 0.05$ or **$p < 0.01$ and to IgG2B-PE denoted by #$p < 0.05$ (ANOVA, Bonferoni post-test). In panel B significant difference denoted by *$p < 0.05$ or **$p < 0.01$ (ANOVA, Bonferoni post-test). Data shown are the mean ± SEM of four individual experiments carried out in duplicate. MFI, mean fluorescence intensity; ns, not significant.

5.2.9A and B). Blocking internalisation at 4°C revealed abundant cell surface αvβ6 expression on the plasma membrane (Figure 5.2.9A1 and A2) and intracellular staining when cells were permeabilised prior to staining with anti-hβ6 antibody (Figure 5.2.9A5 and A6). However, incubation of cells with compound **3** at 37°C for 1 h confirmed that almost no αvβ6 remains on the cell surface and all the integrin appears intracellularly with juxtanuclear localisation (Figure 5.2.9A4 and A8), but with a visibly lower level of staining. No effect of compound **3** was observed when tested at 4°C confirming internalisation had been blocked (Figure 5.2.9A2) and no internalisation was observed in control conditions (0.1 % DMSO) at 37°C (Figure 5.2.9A3). Additional control slides were processed by omitting the primary anti-hβ6 antibody or by addition of an isotype control (sheep IgG). No staining was observed in the absence of primary anti-hβ6 antibody and only a very low level staining in the presence of an isotype control (see Appendix section 8.3.3, Figure 8.3.3). To quantify the loss of αvβ6 membrane staining induced by compound **3** in confocal microscopy studies, the mean staining intensity in chamber slide wells for anti-hβ6 antibody in the four optical sections captured for each condition were calculated (Figure 5.2.9B). The trends observed in flow cytometric experiments were confirmed, but in the cell adhered system a greater loss of β6 staining was observed in the permeabilised cells in the presence of compound **3** compared to control (Figure 5.2.9B).

In flow cytometric assays all αvβ6 ligands tested caused concentration-dependent ligand-induced αvβ6 internalisation following a 2 h incubation with NHBE cells (Figure 5.2.10 and Table 5.2.2). The rank order of potency values (pEC_{50}s) for internalisation of αvβ6 for RGD-ligands tested was the same as the affinity values

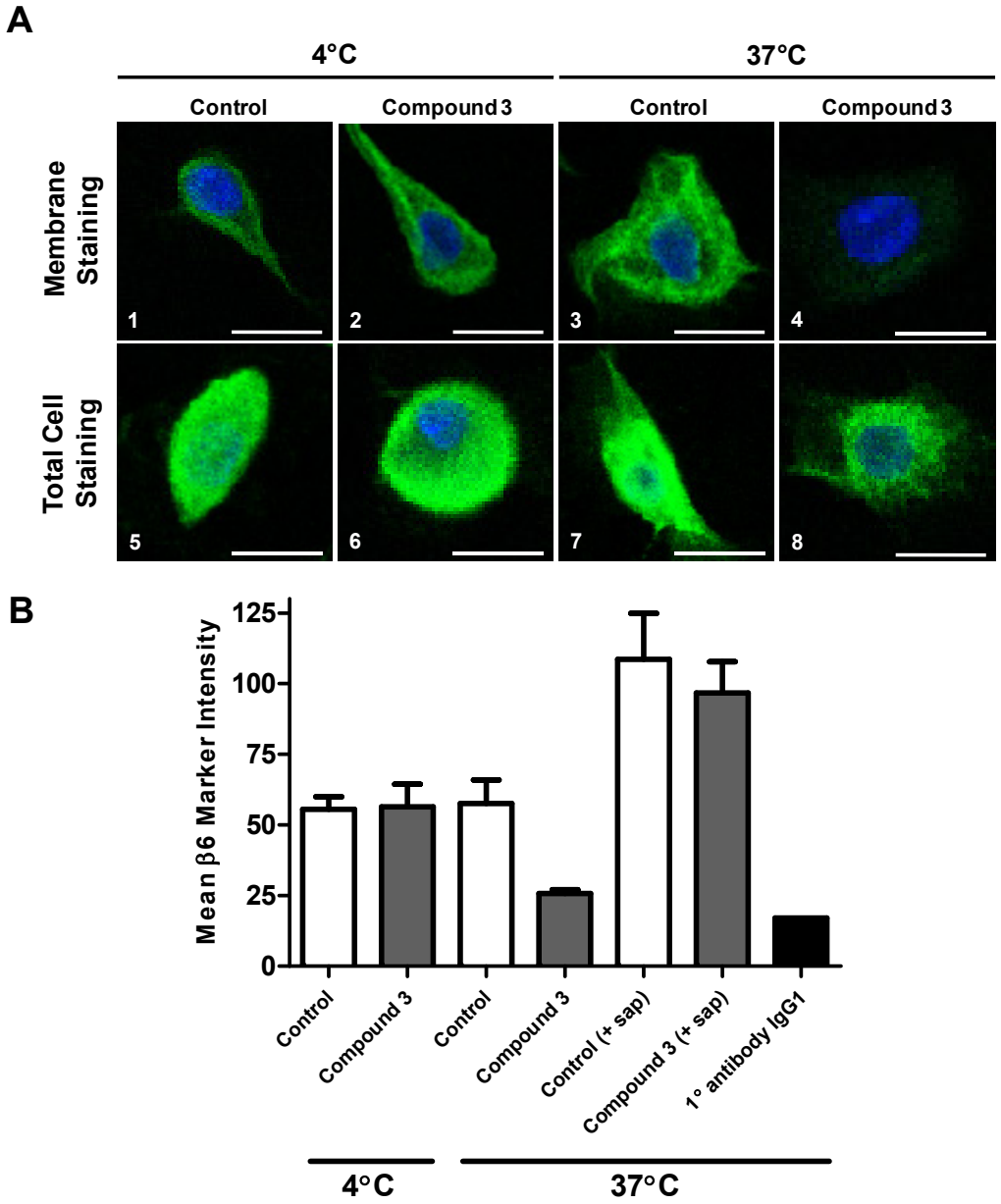

Figure 5.2.9 Localisation of αvβ6 integrin in NHBE cells post-compound 3 addition measured by confocal microscopy. NHBE cells were treated with 0.1 % DMSO vehicle (panel A, sections 1, 3, 5 and 7) or 250 nM compound **3** (panel A, sections 2, 4, 6 and 8) for 1 h at either 4ºC (panel A, sections 1, 2, 5 and 6) or 37ºC (panel A, sections 3, 4, 7 and 8). Following fixation, cells were left unpermeabilised (membrane staining, panel A, sections 1-4) or permeabilised with 0.2 % w/v saponin (total cell staining (membrane and intracellular), panel A, sections 5-8). β6 integrin was stained with sheep polyclonal anti-human integrin β6 antibody followed by donkey anti-sheep IgG Alexa Fluor® 488 antibody (green stain) and imaged by confocal microscopy to produce a 3D cell z-stack. Nuclear staining with Hoechst 33342 dye was also completed (blue stain). Single cells shown (50x magnification) are representative of the optical sections captured (four per condition with similar staining patterns observed). Panel B shows the mean β6 marker intensity (as detailed in Chapter 2: Materials and Methods) for all cells captured from the four optical sections exemplified in panel A sections 1-4, 7 and 8 (control (0.1 % DMSO) vs. compound **3** (250 nM) membrane staining at 4 ºC vs. 37ºC ± 0.2 % w/v saponin) including a single primary (1°) antibody isotype control image (for example isotype images see Appendix section 8.3.3). Data shown from a single replicate. sap, saponin. Scale bar = 25 μm.

(pK_I) observed in radioligand binding (Table 5.2.2 and Chapter 3, Table 3.2.7). The maximal amount of αvβ6 internalised was comparable for all αvβ6 ligands tested and no ligand-induced αvβ6 internalisation was observed with SB-525334 (Figure 5.2.10). To determine the rates of ligand-induced internalisation the surface expression of αvβ6 was measured over time following the addition of a maximal concentration of compound **3** or test ligand, as determined in CRC studies. All RGD-ligands caused a rapid internalisation of αvβ6 again with comparable maximal loss of cell surface integrin observed over the 1 h time course studied (Figure 5.2.11).

To measure the return of αvβ6 to the surface membrane post-internalisation, washout studies were completed where a maximal concentration of test ligand was incubated with NHBE cells for 1 h followed by the removal of αvβ6 ligand and washing of cells in PBS twice (washout). Cells were then incubated for increasing time periods up to 48 h and surface expression of αvβ6 measured at different intervals by flow cytometry. The return of αvβ6 to the surface membrane following washout was ~3-fold slower for the RGD-small molecule compound **3** compared with the RGD peptides $fLAP_1$ and A20FMDV2, and the low affinity αvβ6 RGD-small molecule compound SC-68448 (Figure 5.2.11 and Table 5.2.2). For all αvβ6 ligands tested a full recovery of 100 % integrin to the cell surface was not observed over 48 h. The maximal αvβ6 returned to the cell surface for A20FMDV2, $fLAP_1$, compound **3** and SC-68448 were 58 ± 5 %, 62 ± 6 %, 82 ± 8 % and 84 ± 7 % (mean ± SEM, n=3-4), respectively, over the 48 h time course studied (Figure 5.2.11) with no significant difference observed between groups (ANOVA, Bonferroni post-test, $p < 0.05$).

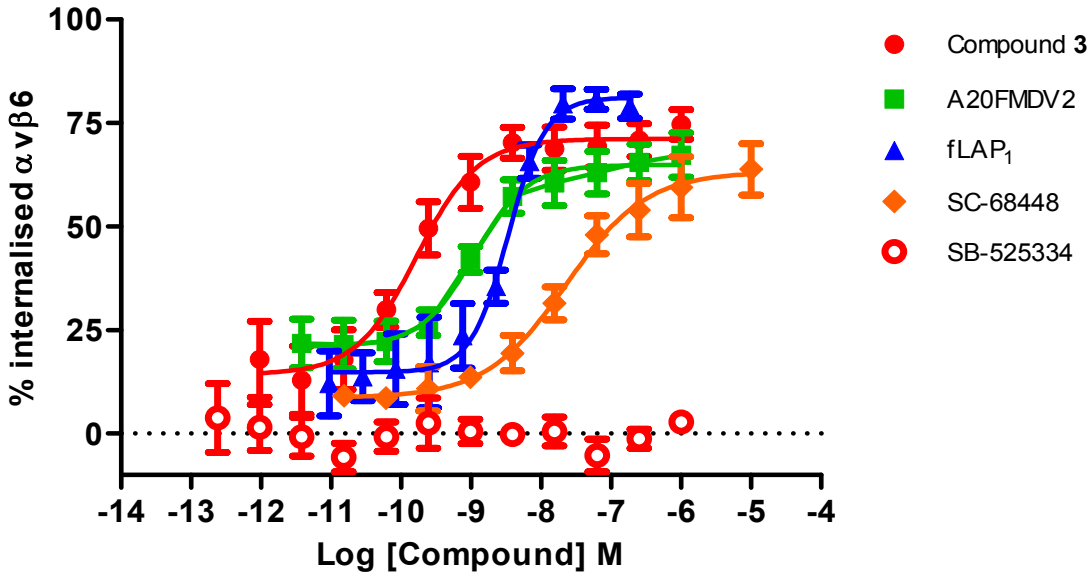

Figure 5.2.10 Compound 3 demonstrates a concentration-dependent ligand-induced internalisation of the αvβ6 integrin in NHBE cells with increased potency compared with other RGD ligands. Full concentration response curves (CRC) were generated by incubating compounds at a range of concentrations with NHBE cells for 2 h prior to the measurement of the β6 integrin subunit at the cell surface in a flow cytometric assay (used as a surrogate for the αvβ6 heterodimer). NHBE cells were washed and stained with either a PE-conjugated mouse monoclonal anti-human integrin β6 (hβ6-PE) or PE-conjugated mouse IgG2B isotype control (IgG2B-PE). Ligand-induced internalisation CRCs data were normalised using the MFI values for IgG2B-PE and hβ6-PE in the presence of 0.1 % DMSO and expressed as % internalised αvβ6 (as detailed in 2.11 Data analysis section). Data shown are the mean ± SEM of four individual experiments carried out in duplicate.

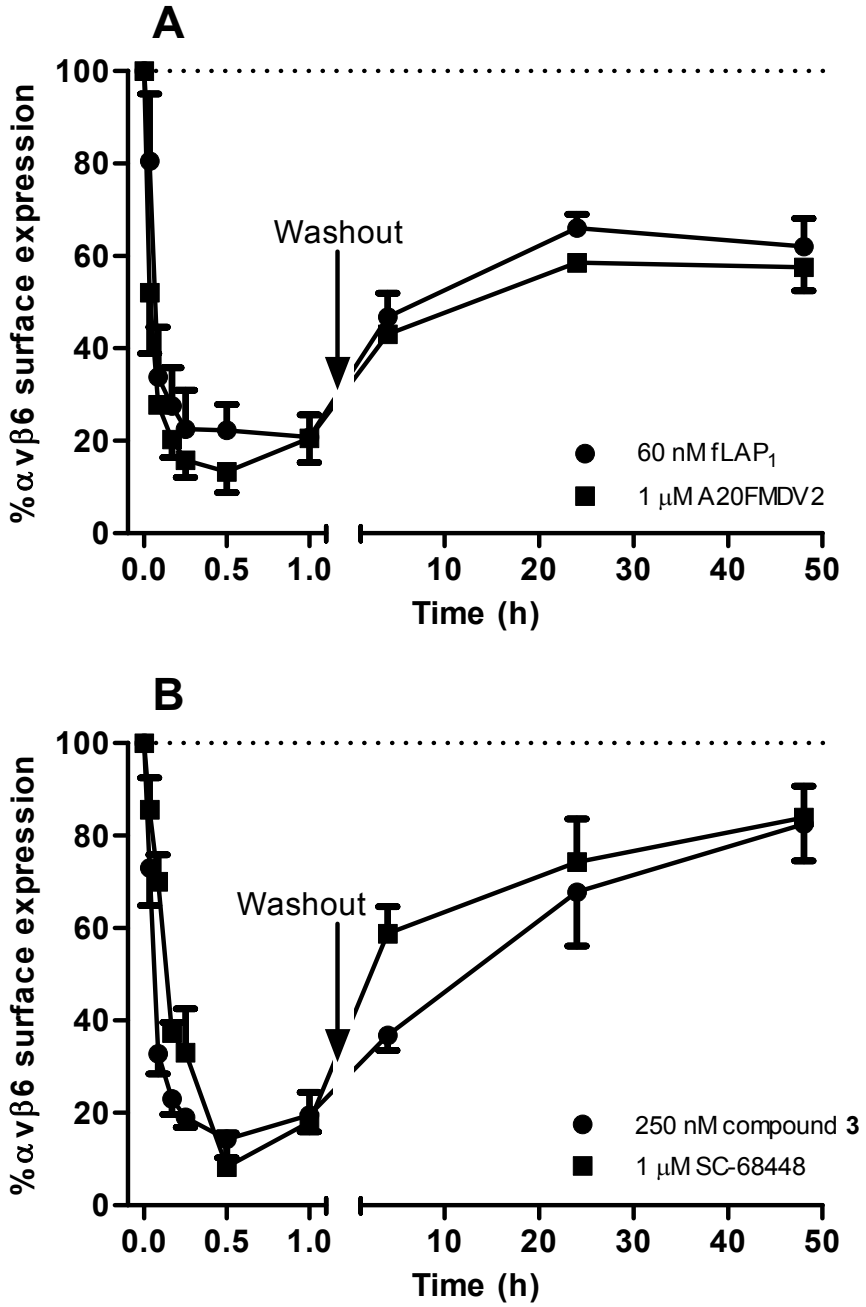

Figure 5.2.11 Compound 3 induces fast αvβ6 ligand-induced internalisation and slow subsequent recycling in NHBE cells. Single concentrations of small molecule RGD-mimetics (250 nM compound **3** and 1 μM SC-68448) or RGD-peptides (60 nM $fLAP_1$ and 1 μM A20FMDV2) were used to induce αvβ6 internalisation at 37ºC. To investigate the kinetics of internalisation plates were transferred on to ice at different time points post-compound addition and the β6 integrin subunit at the cell surface measured in a flow cytometric assay (used as a surrogate for the αvβ6 heterodimer). To measure the return of the αvβ6 integrin to the surface post-ligand-induced internalisation, NHBE cells were exposed to compound for 1 h and then washed twice with PBS and additionally incubated at 37ºC for various time points up to 48 h. NHBE cells were washed and stained with either a PE-conjugated mouse monoclonal anti-human integrin β6 (hβ6-PE) or PE-conjugated mouse IgG2B isotype control (IgG2B-PE) at the time points indicated. Data were normalised using the MFI values for IgG2B-PE and hβ6-PE in the presence of 0.1 % DMSO at each time point and expressed as % αvβ6 surface expression (as detailed in 2.11 Data analysis section). Data shown are the mean + or - SEM of at least three individual experiments carried out in duplicate.

Test Compound	*Internalisation* pEC_{50}	*Internalisation* n_H	*Internalisation* $t_{1/2}$ *(min)*	*Recycling* $t_{1/2}$ *(h)*
SC-68448	7.66 ± 0.03	0.78 (0.33, 1.23)	6.6 ± 1.6	3.0
Compound 3	9.76 ± 0.25	1.39 (0.87, 1.90)	2.6 ± 0.5	9.5
$fLAP_1$	8.45 ± 0.07	*2.21 (1.54, 2.88)	3.1 ± 0.8	2.9
A20FMDV2	9.01 ± 0.13	1.22 (0.66, 1.78)	1.5 ± 0.6	3.4
SB-525334	<6.00	N.A.	N.D.	N.D.

Table 5.2.2 Small molecule RGD-mimetics and RGD-peptides internalisation pEC_{50} values and turnover kinetics for αvβ6 ligand-induced internalisation in NHBE cells. Internalisation CRC from flow cytometric assays measuring β6 integrin subunit at the cell surface (used as a surrogate for the αvβ6 heterodimer) were fitted using non-linear regression analysis (four-parameter logistic equation with variable slope (Hill, 1909)) (as detailed in 2.11 Data analysis section) to generate EC_{50} values. Single concentrations of small molecule RGD-mimetics (1 μM SC-68448 and 250 nM compound **3**) or RGD-peptides (60 nM $fLAP_1$ and 1 μM A20FMDV2) were used to induce αvβ6 internalisation at 37ºC and the β6 integrin subunit at the cell surface measured in a flow cytometric assay over time. Return of the αvβ6 integrin to the surface post-ligand-induced internalisation was measured in washout experiments where cells were then additionally incubated at 37ºC for various time points up to 72 h. Internalisation and recycling kinetics data (% αvβ6 surface expression) were fitted to a one-phase decay or one-phase association model respectively (as detailed in 2.11 Data analysis section) to generate internalisation (k_{in}) or recycling (k_{out}) rate constants. Due to the lack of time points for recycling experiments data was pooled for analysis. k_{in}/k_{out} values were subsequently used to calculate internalisation or recycling half-life ($t_{1/2}$) values using the equation $t_{1/2} = 0.693/k_{in}$ or k_{out}. *denotes n_H significantly greater than unity (one-sample *t*-test completed on $\log_{10} n_H$ vs. 0, $p < 0.05$). Data shown are mean values ± SEM for at least three individual determinations. pEC_{50}, negative $\log_{10}$ of EC_{50}. N.A., not applicable; N.D., not determined.

5.2.6. Duration of NHBE-LAPβ$_1$ cell adhesion inhibition

To allow confirmation that the observations in the flow cytometry system measuring β6 subunit loss from the surface was indeed a surrogate for the αvβ6 heterodimer, NHBE-LAP$_1$ cell adhesion washout studies were completed. A time dependent return in the ability of NHBE cells to adhere to GST-LAP$_1$ was observed post-washout of compound **3** (Figure 5.2.12A) with the trend observed comparable to that in the flow cytometry washout experiments (Figure 5.2.11B).

5.2.7. β6 and PAI-1 mRNA expression in NHBE cells

To further demonstrate the inhibition of αvβ6-mediated TGFβ activation as well as determine effects on the level of β6 integrin subunit in NHBE cells post-compound addition, mRNA expression of PAI-1 (pro-fibrotic mediator downstream of TGFβRI/II pathway activation) and the β6 integrin subunit were investigated. To measure effects on the β6 integrin subunit and PAI-1 mRNA expression either by direct inhibition of TGFβRI or inhibition of αvβ6-mediated TGFβ activation, NHBE cells were incubated for 24 h with test compounds prior to determining mRNA levels via qPCR. Both the ALK5 (TGFβRI) inhibitor SB-525334 and compound **3** caused a significant downregulation of β6 and PAI-1 mRNA (ANOVA, Dunnett post-test, with $p < 0.01$ for β6 and $p < 0.05$ for PAI-1) over the 24 h incubation period compared to control (0.3 % DMSO) (Figure 5.2.12B). This demonstrated that attenuation of the TGFβ pathway via direct (ALK5 (TGFβRI) inhibitor) or indirect (compound **3** αvβ6 inhibitor) inhibition caused a decrease in the expression of PAI-1 and the β6 integrin subunit. The latter observation suggesting that αvβ6 expression is

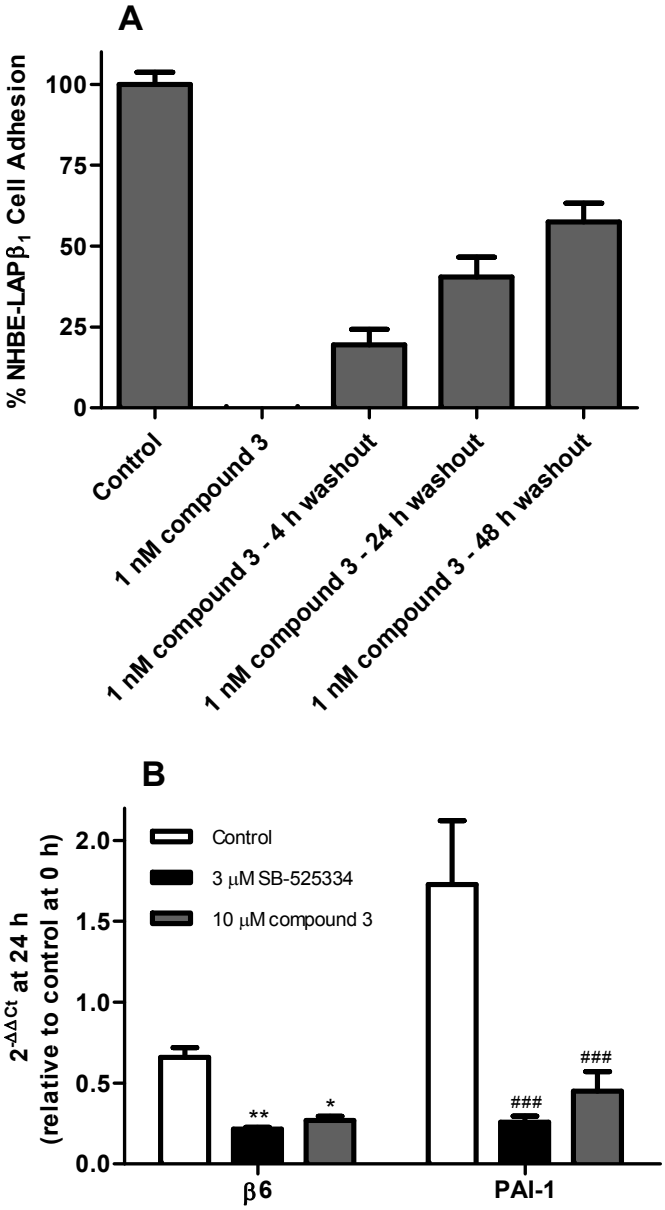

Figure 5.2.12 Compound 3 causes sustained duration of NHBE-LAPβ$_1$ cell adhesion inhibition (A) and reduces β6 and PAI-1 mRNA expression in NHBE cells (B). Duration of inhibition of NHBE cell adhesion to GST-LAPβ$_1$ coated plates (A) determined following a 1 h compound pre-incubation followed by removal (washout) and a further 4, 24 or 48 h incubation with vehicle (0.1 % DMSO). NHBE cells were then recovered and added to GST-LAPβ$_1$ coated plates that were then incubated for 30 min prior to removal of non-adherent cell populations and the remaining adhered cells quantified by fluorescence using BCECF-AM. Control (0.1 % DMSO) and 1 nM compound **3** were used to calculate % cell adhesion (as detailed in 2.11 Data analysis section) at each time point and data for these groups were pooled for comparison with all washout time points. The effect of the ALK5 (TGFβRII) inhibitor SB-525334 and compound **3** on mRNA levels of β6 and PAI-1 (B) was determined by incubating NHBE cells for 24 h in the presence of control (0.3 % DMSO) or compound prior to recovery, preparation and profiling of mRNA expression, with $2^{-\Delta\Delta Ct}$ normalised to a GAPDH housekeeping gene (see Appendix section 8.2.6). Significant differences in β6 mRNA levels compared to control (0.3 % DMSO) denoted by *$p < 0.05$ and **$p < 0.01$ (ANOVA, Dunnett post-test). Significant differences in PAI-1 mRNA levels compared to control (0.3 % DMSO) denoted by ### (ANOVA, Dunnett post-test, $p < 0.001$). Data shown are the mean ± SEM of at least three individual experiments carried out in quadruplicate (A) or duplicate (B). $2^{-\Delta\Delta Ct}$, fold increase in gene expression relative to comparator; Ct, cycle threshold.

under the control of the TGFβ pathway in this system and that direct inhibition via compound **3** at the integrin does not downregulate the mRNA expression.

5.2.8. The effect of chloroquine on the inhibition of αvβ6-mediated TGFβ activation from NHBE cells by compound 3

To investigate the mechanism by which compound **3** causes a prolonged inhibition of αvβ6-mediated TGFβ release from NHBE cells, washout studies were completed in the absence and presence of the lysosomal degradation inhibitor chloroquine. To also allow comparison with the truncated form of an endogenous ligand and a low affinity αvβ6 RGD-mimetic small molecule, these studies also included $tLAP_1$ and SC-68448. Firstly, it was shown that 10 μM chloroquine did not reduce the affinity of $tLAP_1$ or compound **3** for the αvβ6 integrin in a radioligand competition binding assay (Figure 5.2.13A). Compound **3**, $tLAP_1$ and SC-68448 all caused inhibition of TGFβ activation in the presence and absence of chloroquine (Figure 5.2.13B). In the absence of chloroquine the inhibitory effect observed for compound **3** was partially reversed with washout whilst for $tLAP_1$ and SC-68448 the reversal was almost full compared to control (Figure 5.2.13B). In the presence of chloroquine there was no statistical difference for levels of TGFβ activation inhibited by $tLAP_1$ and SC-68448 following washout compared with washout conditions for these ligands in the absence of chloroquine (ANOVA, Bonferroni post-test, $p > 0.05$) (Figure 5.2.13B). This was not the case for compound **3** where the partial reversal of inhibition caused by washout in the absence of chloroquine was significantly further reversed in the presence of chloroquine (ANOVA, Bonferroni post-test, $p < 0.01$) (Figure 5.2.13B). This demonstrated a difference in the duration of action observed between compound **3** and other protein and small molecule RGD ligands. In addition, this data also

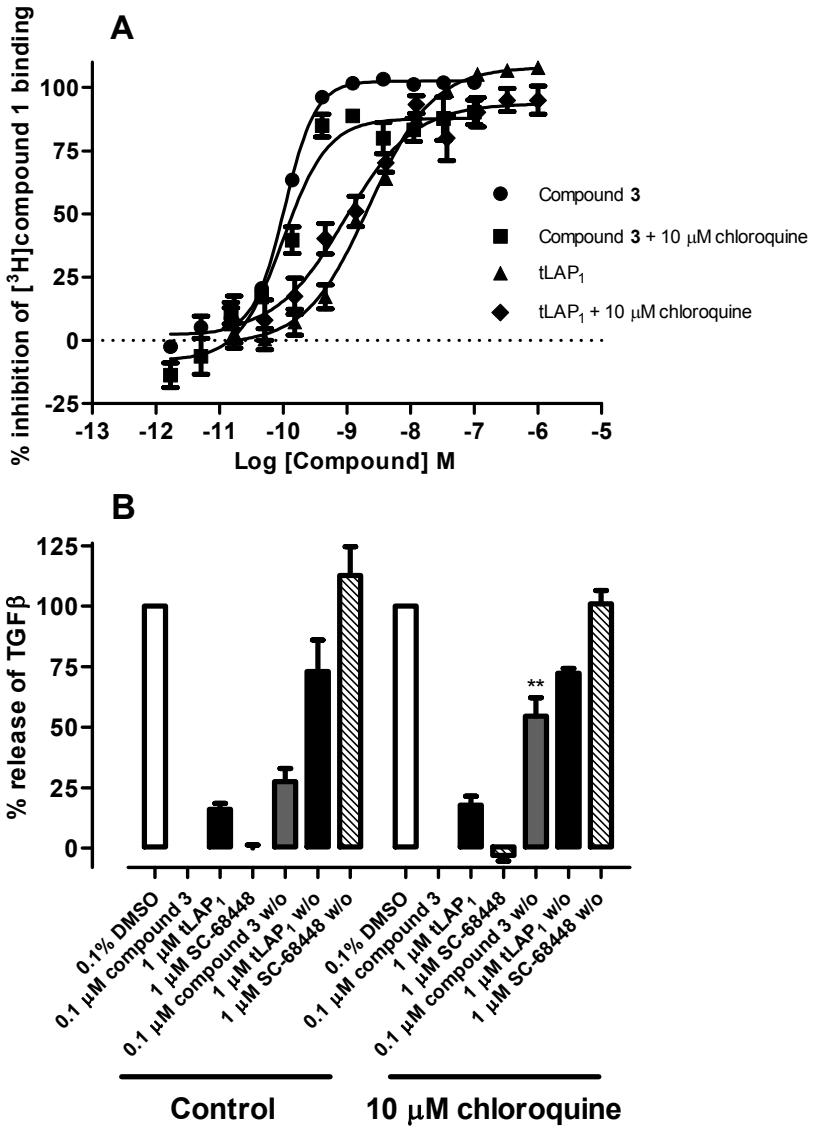

Figure 5.2.13 The lysosomal inhibitor chloroquine does not inhibit compound 3 binding to αvβ6 (A) but does inhibit the sustained duration of inhibition of TGFβ release from NHBE cells observed with compound 3 (B). Full competition binding curves were generated by incubating unlabelled integrin ligand at a range of concentrations with αvβ6 integrin (0.3 nM) and [^{3}H]compound **1** (~1 nM) in absence and presence of 10 μM chloroquine (A). Plates were then filtered after a 6 h incubation and the amount of radioligand bound to αvβ6 was measured by liquid scintillation spectroscopy. Total and non-specific binding values were measured in the presence of vehicle (1 % DMSO) and 10 μM SC-68448 respectively, and were used to calculate the % inhibition of radioligand bound to the αvβ6 integrin (as detailed in 2.11 Data analysis section). Competition binding data were fitted using non-linear regression analysis (four-parameter logistic equation with variable slope (Hill, 1909)) (as detailed in 2.11 Data analysis section). TGFβ activation and release from NHBE cells was determined by co-culturing with TMLCs expressing the firefly luciferase under the control of a TGFβ-sensitive portion of the PAI-1 promoter following a 20 h incubation. Duration of inhibition of TGFβ release from NHBE cells was determined following a 1 h compound incubation followed by removal (washout) and a further 24 h incubation with control (0.1 % DMSO). Significant difference between washout conditions in the absence and presence of 10 μM chloroquine denoted by ** (ANOVA, Bonferroni post-test, $p < 0.01$). Control (0.1 % DMSO) and 0.1 μM compound **3** were used to calculate % inhibition of TGFβ release (as detailed in 2.11 Data analysis section). Data shown are the mean ± SEM of at least four individual experiments carried out in singlicate (A) or quadruplicate (B). w/o, washout.

suggested that the extended duration of action observed for compound **3** is a result of lysosomal degradation of αvβ6 initiated post-ligand binding and internalisation.

5.2.9. The effect of chloroquine on αvβ6 integrin levels in NHBE cells post-compound 3 addition

Confocal microscopy studies were completed to measure β6 subunit levels by immunofluorescence staining, as a surrogate for the αvβ6 integrin, in the absence and presence of the lysosomal degradation inhibitor chloroquine. These studies were completed in the presence of 0.2 % w/v saponin to allow measurement of total αvβ6. Following a 24 h incubation with compound **3** the levels of staining for αvβ6 was significantly reduced compared to control (0.1 % DMSO) (Figure 5.2.14A and B) (ANOVA, Bonferroni post-test, $p < 0.05$). The effect of compound **3** was reversed in the presence 10 μM chloroquine with no significant change in the levels in control conditions observed between the absence or presence of the lysosomal inhibitor (Figure 5.2.14A and B) (ANOVA, Bonferroni post-test, $p > 0.05$). This data provided further evidence that the extended duration of action observed for compound **3** is a result of lysosomal degradation of αvβ6.

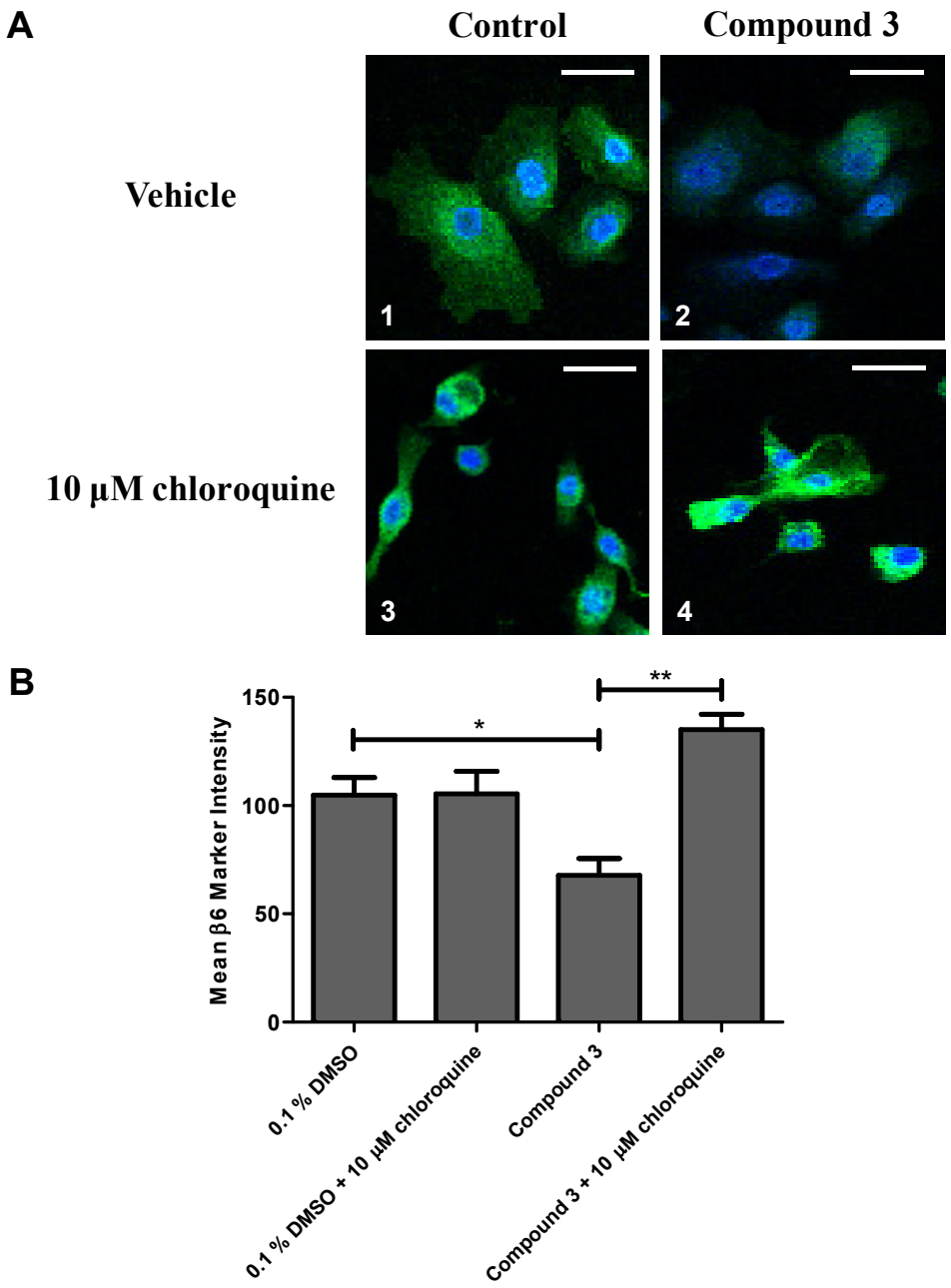

Figure 5.2.14 Compound 3 reduces total levels of αvβ6 integrin in NHBE cells that is reversed by the lysosomal inhibitor chloroquine. NHBE cells were treated with 0.1 % DMSO vehicle (panel A, sections 1 and 3) or 250 nM compound **3** (panel A, sections 2 and 4) for 24 h in the absence (panel A, sections 1 and 2) or presence (panel A, sections 3 and 4) of 10 µM chloroquine. Following fixation, cells were permeabilised with 0.2 % w/v saponin (total cell staining (membrane and intracellular). β6 integrin was stained with sheep polyclonal anti-human integrin β6 antibody followed by donkey anti-sheep IgG Alexa Fluor® 488 antibody (green stain) and imaged by confocal microscopy to produce a 3D cell z-stack. Nuclear staining with Hoechst 33342 dye was also completed (blue stain). Cells shown (20x magnification) are representative of the optical sections captured (four per condition with similar staining patterns observed). Panel B shows the mean β6 marker intensity (as detailed in Chapter 2: Materials and Methods) ± SEM for all cells captured from the four optical sections exemplified in panel A sections 1-4 (control (0.1 % DMSO) vs. compound **3** (250 nM) total staining ± 10 µM chloroquine). Significant differences between conditions denoted by *$p < 0.05$ and **$p < 0.01$ (ANOVA, Bonferroni post-test). Data shown are representative of four individual experiments with similar results. Scale bar = 50 µm.

5.3. Discussion

SW480-αvβ6 cells activate TGFβ via the αvβ1 and αvβ6 integrins providing a high throughput system for measuring integrin-mediated inhibition of TGFβ release

In order to investigate a sensitive and high throughput assay to measure the functional inhibition of TGFβ with αvβ6 inhibitors, a co-culture system was set-up using SW480-αvβ6 cells (a stable cell line established from a primary adenocarcinoma of the colon recombinantly expressing αvβ6) and TMLCs expressing firefly luciferase under the control of a TGFβ-sensitive portion of the PAI-1 promoter. This assay system has been used by Weinreb and co-workers (Weinreb *et al.*, 2004) to investigate the selective αvβ6 blocking antibodies 3G9 and 8G6. Firstly, it was shown that this system was producing a measurable and robust level of TGFβ on the linear region of the TGFβ standard curve. In addition, to ensure that any observations with compound **3** were not a result of direct TGFβRI/RII competition it was also shown that this small molecule RGD-mimetic did not inhibit the TGFβ stimulated luciferase signal. It is worth noting that the increased signal generated in these experiments (Figure 5.2.2A) was due to a different method where increased TMLCs were used in a single cell culture, plated in the absence of SW480-αvβ6 cells. Although it was suggested from previous literature (Weinreb *et al.*, 2004) that the TGFβ activation in this co-culture system was driven by αvβ6, flow cytometry was used to profile the expression of the RGD-integrins potentially able to activate TGFβ in SW480-αvβ6 cells. From these studies the SW480-αvβ6 cells were shown to express high levels of αv, β1, β5 and β6 integrin subunits but no β3 or β8 integrin subunits. αvβ1 and αvβ5 (in addition to αvβ6) have the potential to activate

TGFβ, therefore all these integrins could contribute to TGFβ activation in this system. Therefore, to confirm αvβ6 was the key TGFβ activating integrin in this system a number of selective blocking monoclonal antibodies and small molecules were tested. The αvβ5 blocking antibody (1F6) did not inhibit TGFβ activation whilst a β1 (4B4 tested as no selective αvβ1 antibodies are available commercially), an αvβ6 blocking antibody (10D5), a selective αvβ6 peptide (A20FMDV2), $fLAP_1$ and the small molecule cilengitide (that binds αvβ3, αvβ5 and αvβ1 (in that order of affinity from high to low)) partially blocked. In addition, compound **3** (that binds αvβ6, αvβ1 and αvβ5 (in that order of affinity from high to low)) completely blocked TGFβ activation to a comparable level as an αv blocking antibody and a TGFβ1, 2 and 3 binding antibody. The pIC_{50} value determined for cilengitide was most comparable with its binding affinity for the αvβ1 integrin.

These observations combined suggested the integrins activating TGFβ in this system were αvβ1 and αvβ6. Therefore, to further dissect the effect observed with compound **3**, that is proposed to be engaging both these integrins to inhibit TGFβ activation in this system, full CRCs were performed in the absence or presence of either cilengitide (to block αvβ1 and therefore reveal the αvβ6 IC_{50} for compound **3**) or 10D5 (to block αvβ6 and therefore reveal the αvβ1 IC_{50} for compound **3**). In the absence of either cilengitide or 10D5, full inhibition of TGFβ activation was observed. In the presence of cilengitide a pIC_{50} value for inhibition of TGFβ activation was comparable to the affinity of compound **3** for the αvβ6 integrin. In the presence of 10D5 a pIC_{50} value for inhibition of TGFβ activation was comparable to the affinity of compound **3** for the αvβ1 integrin. This provided further evidence that the αvβ1 and αvβ6 integrins were the key TGFβ activating mechanisms in this

SW480-αvβ6/TMLC co-culture system. This also provided evidence that the binding selectivity determined in Chapter 3 of this study was able to predict the functional selectivity also. This is important when relating the selectivity profiles of potential small molecule RGD-mimetic drugs to either additional beneficial anti-fibrotic effects or safety liabilities at non-αvβ6 RGD integrins.

NHBE cells contain the components required for investigation of functional engagement and inhibition of the αvβ6 integrin

To further investigate the ability of compound **3** to inhibit the activation of TGFβ via αvβ6 in a more physiologically relevant system, and to determine if it was able to initiate ligand-induced αvβ6 internalisation, a primary lung epithelial cell (NHBE cells) test system was developed. It has already been shown that these cells provide the most robust and relevant system for probing αvβ6 biology (Araya *et al.*, 2007; Xu *et al.*, 2009) and have the added benefit of being a human primary lung epithelial cell making them more relevant to investigating the biology of αvβ6 in the lung. It would be more of an advantage to have diseased IPF alveolar type II epithelial cells, where αvβ6 has been shown to be upregulated in IPF (Horan *et al.*, 2008). However, with the acquisition of IPF lung tissue a challenge, combined with the difficulties associated with the recovery of these cell types from even healthy explants (Jenkins *et al.*, 2011), the NHBE cells represent the best surrogate that can be readily obtained from commercial sources.

Prior to the measurement of TGFβ activation and release as a measure for αvβ6 inhibition, the presence of the components necessary for this type of investigation were confirmed. The αv and β6 integrin subunits were shown to be present at high levels on the surface of NHBE cells throughout their culture lifecycle (division was

observed up to P4). As the β6 subunit only forms a heterodimer with the αv subunit (Hynes, 2002) and with such a high level of αv observed on NHBE cells, this suggests that the majority, if not all, of the β6 would be associated with αv. Therefore, a population of αvβ6 integrin was shown to be present on NHBE cells that could be targeted with αvβ6 ligands.

Previously published studies have shown that the αvβ8 integrin is present on NHBE cells at a low level but that it does not contribute to the activation and release of TGFβ in the system (Araya *et al.*, 2007). However, the presence and contribution of the other TGFβ activating integrins αvβ1, αvβ3 and αvβ5 (Margadant and Sonnenberg, 2010) on NHBE cells has not been demonstrated. It was important to investigate the expression of these integrins in this system due to the potential of low affinity binding to αvβ1, αvβ3 and αvβ5 with compound **3**. αvβ3 was shown to be expressed at very low levels, αvβ5 expressed at low levels and αvβ1 expressed at high levels during all stages of the NHBE cell culture lifecycle. Therefore, based on this data a role for any of these integrins in TGFβ activation could not be ruled out completely and would require further investigation by measuring the effect of cilengitide (a selective αvβ1, αvβ3 and αvβ5 cyclic-RGD peptide) on TGFβ activation.

Compound 3 is a potent inhibitor of TGFβ activation via αvβ6 blockade and demonstrates a sustained duration of action in NHBE cells

Following the confirmation that NHBE cells expressed the αvβ6 integrin via flow cytometry, an assay was developed to measure inhibition of TGFβ release. This used a co-culture system with TMLCs and a measurement of TGFβ release via firefly

luciferase under the control of a TGFβ-sensitive portion of the PAI-1 promoter. In addition to the αvβ6 integrin, the other RGD integrins αvβ1 and αvβ5 were also shown to be present on the surface of the NHBE cells tested in this study. Therefore, to confirm the contribution from these integrins in terms of TGFβ activation, cilengitide was tested in this test system at a concentration that had been shown to completely inhibit radioligand binding to the αvβ1 and αvβ5 integrins as well as inhibit αvβ1-mediated TGFβ activation in a SW480-αvβ6/TMLC co-culture test system. Cilengitide did not inhibit TGFβ activation from NHBE cells when tested at 1 μM showing no involvement of these integrins. However, compound **3** was shown to inhibit TGFβ activation and release in this system with a pIC_{50} comparable to the pK_D value observed with radioligand binding studies, suggesting the activation of TGFβ from the NHBE cells was a result of αvβ6 blockade.

To further investigate the hypothesis that slow dissociation kinetics from the αvβ6 integrin would result in an extended duration of inhibition of TGFβ activation, washout experiments were completed in this assay with compound **3**. This involved the exposure of compound to cells for 1 h prior to removal and washing of cells with buffer not containing compound. TGFβ levels were then determined 24 h post-washout and compared with control wells to estimate recovery. Post-washout of compound **3** there was minimal recovery of TGFβ production (<35 %) and this confirmed that duration of functional inhibition, and the potential anti-fibrotic activity, was being achieved with compound **3** via blockade of αvβ6.

Compound 3 induces fast internalisation of αvβ6 followed by slow return to the cell surface

It has been demonstrated following the binding of selective peptides (derived from the human foot-and-mouth virus) to αvβ6 that internalisation of the integrin occurs (Hausner *et al.*, 2009; Saha *et al.*, 2010). It has also been demonstrated with other members of the RGD-integrin family that ligand-induced internalisation can also take place (Temming *et al.*, 2005). Therefore, to investigate if a RGD-mimetic small molecule could also induce internalisation a number of techniques were investigated. One of these included flow cytometry to measure the surface expression of αvβ6 and its subsequent loss post-addition of ligand. Although this technique has not been used routinely for measuring ligand-induced internalisation, over the last 10 years a number of groups have applied the technique successfully in the G-protein coupled receptor field investigating agonist and antagonist-induced internalisation and recycling of the CCR4 receptor (Mariani *et al.*, 2004; Sato *et al.*, 2013; Ajram *et al.*, 2014). To confirm observations in flow cytometric assays, confocal microscopy was also employed and in unison these techniques showed that the RGD-mimetic small molecule compound **3** caused concentration-dependent ligand-induced internalisation of the αvβ6 integrin in NHBE cells. In order to successfully demonstrate this, a number of suitable controls were completed to validate the assay. Firstly, human anti-β6 flow and confocal microscopy antibodies were used to measure via fluorescence the spatial location of the β6 integrin subunit as a surrogate for αvβ6. This was to negate the risk of using anti-αvβ6 antibodies as these could bind either orthosterically (at the RGD-site) or allosterically (site distinct from RGD-site) and both would have the potential to compete with αvβ6 ligands. Orthosteric antibodies

would also have the potential to induce internalisation (Weinreb *et al.*, 2004) thus making the measurement of ligand-induced internalisation with these antibodies not possible. Even though the antibody used for flow cytometry in this study was anti-β6, it was still confirmed not to bind and compete with the αvβ6 integrin in cell adhesion studies.

The inferred ligand-induced internalisation observed for $fLAP_1$ and compound **3** in flow cytometry was almost completely abolished in the presence of saponin although there was a trend for a small difference in the presence of RGD-ligand compared with control. Saponin permeabilises the plasma cell membrane by forming complexes with cholesterol to generate pores (Francis *et al.*, 2002) that would allow the flow antibody to access the intracellular pool of αvβ6. This not only acted as an additional control to confirm $fLAP_1$ and compound **3** were not competing with the anti-β6 antibody, but also data from control wells showed the total cell αvβ6 levels relative to the surface level allowing a measurement of intracellular αvβ6. To control that the presence of saponin was not having a direct effect on the affinity of $fLAP_1$ and compound **3** it was shown this condition did not alter the binding affinity of these ligands for the integrin. In addition, it was shown that the αvβ6 internalisation in the NHBE system was being driven by a clathrin-dependent mechanism due to the inhibition observed with chlorpromazine (this was also shown not to alter the binding affinity of ligands for αvβ6), which agrees with published data where this endocytic mechanism was linked to the αvβ6 integrin (Ramsay *et al.*, 2007).

It is well established that endocytic pathways are inhibited at 4°C due to the inhibition of all energy-dependent pathways (dos Santos *et al.*, 2011) and therefore the data from confocal microscopy investigating this condition was further evidence

of a real internalisation event being measured in this cell system. Once the NHBE flow cytometric assay had been shown to be suitably controlled to measure ligand-induced αvβ6 internalisation, RGD-peptides and small molecule RGD-mimetics were compared in different experimental set-ups to measure their αvβ6 internalisation potency, rate of internalisation, and rate of the return of αvβ6 to the cell surface post-washout. Compound **3** was shown to induce internalisation with high potency compared with the other ligands tested (Table 5.2.2) with the rank order of internalisation pEC_{50} correlating with the ligand affinities. The endogenous non-ligand-induced internalisation and recycling of the αvβ6 integrin has been shown to occur very quickly with both mechanisms plateauing after ~30 minutes (Ramsay *et al.*, 2007; Wang *et al.*, 2011). Although there has been extensive research completed on endogenous turnover of the integrin, there is less known regarding ligand-induced αvβ6 internalisation and its subsequent recycling back to the cell surface. Although RGD-peptide induced internalisation has been investigated, the fate of the integrin post-internalisation was not determined (Hausner *et al.*, 2009; Saha *et al.*, 2010). In this study the rate of internalisation was determined for αvβ6 ligands. All were observed to internalise αvβ6 very quickly and with comparable $t_{1/2}$ values that were measured within minutes of ligand addition. In addition, they all caused a comparable level of αvβ6 internalisation (~80 % when normalised to isotype control). This suggested that there was potentially a population of non-functional αvβ6 that could not be engaged and internalised (non-functional αvβ6 heterodimer). Alternatively, there was also the potential that as the β6 integrin subunit was being used as a surrogate for αvβ6, that the ~20 % at the surface were β6 integrin subunit unable to associate with αv. These could either be non-functional β6 subunits or

other αvβ integrin interactions had depleted total αv subunit available for partnering thus not allowing all β6 to be associated in a heterodimer. The more interesting observations in this study were the rates of recycling or return of αvβ6 to the cell surface post-washout of ligand. Post-washout of compound **3** αvβ6 returned to the cell surface ~3-fold slower compared with all other ligands tested. As the flow cytometry system utilised NHBE cells incubated in suspension over long periods, it was key to investigate cell surface αvβ6 over time post-washout of compound **3** in studies where cells were adhered, better representing the physiological environment where cell-cell interaction may influence the integrins behaviour. These were completed using αvβ6 cell adhesion as the endpoint and a comparable trend was observed post-washout of compound **3** with slow return of αvβ6 to the cell surface. This also suggested that if the αvβ6 returned to the cell surface was from the same population that had been internalised i.e. integrin recycled from endosome, that it did not have compound **3** bound.

Over the time course of these studies (up to 48 h post-washout) 100 % return of αvβ6 was not observed under any test condition, with a maximum of 76 % of the internalised integrin returning to the membrane. This could be a result of down regulation of αvβ6 mRNA via inhibition of the TGFβ activation pathway that has been shown to upregulate αvβ6 and other integrins upon stimulation (Wang *et al.*, 1996). Over 24 h a decrease in β6 and PAI-1 mRNA was observed in the presence of either compound **3** or the ALK5 (TGFβRI) inhibitor SB-525334 suggesting this mechanism may influence the levels of αvβ6 if inhibition of TGFβ is sustained. The rate of return of αvβ6 to the cell surface observed in these studies post-washout of compound **3** compared with that of endogenous turnover of αvβ6 is considerably

slower suggesting that the internalised ligand-αvβ6 complex is potentially degraded and returning αvβ6 is newly synthesised. To further develop this hypothesis the lysosomal inhibitor chloroquine was tested in a number of test systems to observe its effect on compound **3**. Chloroquine in its unprotonated form can freely diffuse across cell and organelle membranes, however it becomes trapped in lysosomes once protonated, due to the low pH of this environment (Solomon and Lee, 2009). In this form it has been shown to inhibit proteolytic processes and therefore has been used as a tool for determining mechanisms of receptor turnover (Dunmore *et al.*, 2013). Firstly, and again to control subsequent experiments, chloroquine was shown not to affect the ability of compound **3** to bind to the αvβ6 integrin. In washout experiments using NHBE cells investigating αvβ6-mediated inhibition of TGFβ activation, the sustained duration of inhibition observed with compound **3** was reversed in the presence of chloroquine. In addition, over a 24 h period a reduction in total αvβ6 (cell surface and intracellular) was observed in the presence of compound **3** that was reversed in the presence of chloroquine. These observations combined suggest that post-internalisation of αvβ6 by compound **3**, the integrin is sorted for degradation in lysosomes. Interestingly for lower affinity αvβ6 ligands with fast dissociation profiles ($tLAP_1$/$fLAP_1$ and SC-68448) the sustained duration of inhibition of TGFβ activation is not observed.

Therefore, compound **3** causes a more prolonged down regulation of αvβ6 in this system compared with other lower affinity ligands. The slower return of integrin to the cell surface post-washout observed with the small molecule RGD-mimetic compound **3** compared to the endogenous $fLAP_1$ and A20FMDV2 could be a result of their physico-chemical properties e.g. a protein/peptide will be more susceptible to

degradation within intracellular compartments. However, this assumes that a continual engagement with αvβ6 post-internalisation is required to achieve sustained down regulation. If this is the case then again perhaps the ligand dissociation kinetics is also playing a role and the longer dissociation $t_{1/2}$ from the αvβ6 integrin observed for compound **3** vs. SC-68448/fLAP$_1$/A20FMDV2 may account for the differences observed between these RGD-ligands. It is also worth noting that it could well be the result of a combination of both the physico-chemical properties and the dissociation $t_{1/2}$, although the small molecule SC-68448 does demonstrate it is not just a protein/peptide vs. small molecule difference. The high affinity of compound **3** for the αvβ6 integrin combined with its slow dissociation profile would likely result in a prolonged activation of the integrin in intracellular vesicles. Even at the low pH encountered it has already be shown in Chapter 4 that this will not have an impact on the prolonged engagement of compound **3** with αvβ6. It could be hypothesised that the longer the integrin is engaged at the RGD-site post-internalisation, as a result of slow dissociation kinetics, the more likely it is to be intracellularly designated for degradation, as has been observed with other small molecule/protein interactions (Long *et al.*, 2012; Harling *et al.*, 2013). The prolonged activation of the RGD-integrin α5β1 has been shown to delay its recycling back to the cell surface of A2780 cells post-internalisation, as a result of sorting into lysosomes prior to transportation back to the plasma membrane (Dozynkiewicz *et al.*, 2012). A similar mechanism is hypothesised for degradation of αvβ6, where compound **3** binds with high affinity, activates and internalises the integrin, remains bound intracellularly causing sustained activation and sorting of the integrin for lysosomal degradation rather than

recycling. This then ultimately results in prolonged duration of inhibition of αvβ6-mediated TGFβ activation.

Summary

Test systems to investigate the functional consequences of αvβ6 inhibition in SW480-αvβ6 cells and NHBE cells measuring direct TGFβ activation have been developed and used to provide proof of mechanism for the RGD-mimetic small molecule compound **3**. Furthermore, it has been shown that inhibition of TGFβ activation by compound **3** is prolonged. The ligand-induced αvβ6 internalisation data generated in this study suggest this could be a result of fast ligand-induced internalisation (minutes) followed by a slow return of the integrin to the cell surface (hours). It has also been shown the integrin is degraded post-internalisation in lysosomes by compound **3** potentially as a result of its prolonged engagement and activation of αvβ6 that suggests the slow return to the surface is a consequence of the requirement for synthesis of new integrin.

CHAPTER 6: GENERAL DISCUSSION

6.1. Overview

Fibrosis is the formation of scar tissue due to injury or long-term inflammation and is a leading cause of morbidity and mortality (Wynn, 2007) in disorders that include IPF, hepatic fibrosis and renal fibrosis. Within these indications there are currently limited therapeutic options for patients and over recent years there has been an increased focus on identifying targets and subsequent development of drugs for these diseases. The αvβ6 integrin has been identified as playing a key role in the activation of TGFβ from the constitutively expressed latent TGFβ. TGFβ has been hypothesised to be pivotal in the development of IPF (Goodwin and Jenkins, 2009) thus αvβ6 is an attractive therapeutic target for this debilitating disease. There is also the added potential that αvβ6 may also be relevant in other fibrotic disease states in the liver and kidneys (Popov *et al.*, 2008; Sheppard, 2004) as well as cancer (Bandyopadhyay and Raghavan, 2009). Although the αv integrins distinguish their endogenous target ligands competently, their recognition sequence contains a core RGD amino acid sequence (Ruoslahti, 1996). This makes it a challenge to develop selective small molecule RGD-mimetics for αvβ6 over the other αv integrins that could be crucial to negate any potential negative effects of engaging integrins not relevant in treating fibrotic disease.

Data presented in this thesis is aimed at the pharmacological characterisation of small molecule αvβ6 RGD-mimetics to aid in the selection of a novel lead chemical entity as a potential clinical candidate for the treatment of IPF. The proposal was to identify a small molecule RGD-mimetic with high affinity and selectivity for the αvβ6 integrin with suitable properties for inhaled delivery via nebulisation. Highly accurate radioligand binding assays for all the αv integrins have been generated that

have allowed for the first time true affinity selectivity profiles for both novel and tool ligands to be determined. In addition, the relationships between these assays and early stage high throughput SAR assays have been established to aid in the screening of large numbers of potential chemical series. In parallel, the physico-chemical and pharmacokinetic properties of compounds were assessed to track suitability for inhaled delivery. These parameters included solubility (impact on formulation, lung distribution and safety profile), passive permeability (tissue penetration and rate of pulmonary absorption), bioavailability (contribution to systemic exposure of the swallowed fraction), lung tissue binding (free drug in the lung) and lung residence time (one of the enablers of duration of action). In addition, the efficiency and location of pulmonary deposition is key for inhaled delivery and via the nebulisation administration route this is primarily dictated by the nebuliser type (Rau, 2005) as well as the disease specific lung function i.e. how the disease has altered the lung architecture and airflow (Heijerman *et al.*, 2009). However, in terms of physico-chemical and pharmacokinetic properties the desired profile of an inhaled drug would be high solubility and permeability suitable to deliver the agent to site of action. In addition, a compound with low bioavailability and tissue binding with a long retention in the lung, if this is the mechanism supporting the duration of action (Tayah and Hochhaus, 2005), would also be preferable. The majority of these properties were evident in the lead series discovered as part of this drug discovery programme (see section 8.3.5. Physico-chemical and pharmacokinetic properties of the small molecule RGD-mimetics compound **2** and **3**). However, during the SAR process it was identified that there was a balance between selectivity and lung retention whereby the more selective compounds like compound **2** and **3** exhibited

poor lung retention. Therefore, to achieve a long duration of action and enable a maximum of twice daily dosing into the lung, the strategic decision was made to drive duration of action of the lead chemical series based on high affinity and therefore hypothesised slow dissociation kinetics. Consequently, the primary aim of this study was to design, develop and implement key assays and experiments to aid in the selection of an optimal candidate with this desired profile, and validate the hypothesis in the most physiologically relevant pre-clinical *in vitro* systems.

6.2. Identification of high affinity and selective αvβ6 small molecule RGD-mimetics with slow receptor dissociation kinetics

The characterisation of small molecule RGD-mimetics and peptides binding to the RGD binding site of αvβ6 has not been completed to any significant degree using radioligand binding studies to fully elucidate affinity, selectivity and kinetic profiles. It has been demonstrated in this study that a radiolabelled novel small molecule RGD-mimetic (compound **1**) exhibits a simple, competitive and reversible interaction with the RGD binding site on the αvβ6 integrin as well as αvβ1, αvβ3, αvβ5 and αvβ8. This provided a powerful tool for the characterisation of unlabelled ligands at all of these integrins. More interestingly, a radiolabelled selective αvβ6 peptide derived from the foot-and-mouth virus, A20FMDV2, demonstrated a much more complex interaction with αvβ6. The foot-and-mouth virus has been shown to use integrins to initiate the infection of cattle (Neff *et al.*, 1998; Monaghan *et al.*, 2005) via high affinity interactions. With A20FMDV2 demonstrating such a high affinity and selectivity for αvβ6 it has been used to great effect as a tool in the cancer field, especially as a radiotracer for *in vivo* positron emission tomography studies investigating αvβ6 expression in tumours (Hausner *et al.*, 2009; Hausner *et al.*,

2007). In this study it has provided a tool compound for comparison not only with novel small molecule RGD-mimetics but also endogenous ligands (LAP_1 and LAP_3). A number of characteristics of A20FMDV2 demonstrated in previous studies have been confirmed with the use of a [^{3}H] labelled form of the peptide. Firstly, the high affinity and selectivity of A20FMDV2 for the αvβ6 integrin has been confirmed (DiCara *et al.*, 2007; DiCara *et al.*, 2008; Hausner *et al.*, 2009). In fact in this study the affinity of A20FMDV2 for αvβ6 has been shown to be much higher than previously demonstrated, more than likely due to the more sensitive methodology used i.e. radioligand binding.

Where this study has added to the data already published on A20FMDV2 is the demonstration of its kinetics at the αvβ6 integrin. Although reversibility of A20FMDV2 from αvβ6 has been investigated using a biotinylated form of the peptide (DiCara *et al.*, 2008) in both a solid-phase binding assay (using recombinant αvβ6 protein) and a flow cytometry assay (using cell lines recombinantly expressing αvβ6), only a single time point (30 min) was investigated with either 20 mM EDTA or 1,000-fold excess of unbiotinylinated peptide used to dissociate the biotinylated A20FMDV2. The literature data suggested that A20FMDV2 forms an EDTA-resistant complex with αvβ6, but only if the peptide-integrin complex is pre-formed (DiCara *et al.*, 2008). It was also shown that after 30 min in the presence of an excess of unbiotinylinated A20FMDV, binding could not be reversed from the pre-formed biotinylated A20FMDV2-αvβ6 complex. For comparison, full dissociation profiles over a 24 h time course were generated for [^{3}H]A20FMDV2 in this study, investigating a range of methods to initiate radioligand dissociation, that included the sequestering of cations with 10 mM EDTA and competition with excess unlabelled

ligands (both a RGD small molecule binder (SC-68448) and unlabelled A20FMDV2). Over this extended timeframe EDTA was able to reverse the binding of [^{3}H]A20FMDV2 fully. At 30 min no reversal of A20FMDV2 binding to αvβ6 was observed by DiCara and co-workers (DiCara *et al.*, 2008) whereas ~50% of [^{3}H]A20FMDV2 is unbound at this time point in this study (Chapter 3). However, the literature experiments were completed at 4°C (in the flow cytometry assay although it is unclear the temperature used for solid-phase binding studies), more than likely to combat ligand-mediated endocytosis of αvβ6 observed with A20FMDV2 (Hausner *et al.*, 2009). In contrast all binding experiments in this study were completed at 37°C. Therefore, it could be that the slower kinetics at the low temperature conditions resulted in A20FMDV2 dissociation not being detected at the 30 min time point. To test this further, dissociation binding experiments with [^{3}H]A20FMDV2 at 4°C vs. 37°C could be completed, although conditions recreating the physiological temperature is always advisable. Alternatively, radioligand binding in a suitable αvβ6 cell line could be completed, but again the complexity of endocytosis may also hinder these types of experiment in a whole cell system.

When dissociation of [^{3}H]A20FMDV2 from αvβ6 was initiated by either an RGD small molecule RGD-mimetic (SC-68448) or unlabelled A20FMDV2 only a partial reversal of radioligand binding could be achieved up to 24 h. The hypothesis behind testing these conditions was to observe if the unlabelled A20FMDV2 resulted in a different dissociation profile compared with a small molecule RGD-mimetic. As a second non-RGD binding site for [^{3}H]A20FMDV2 has been hypothesised by DiCara and co-workers (DiCara *et al.*, 2008), these different conditions may have revealed if there was interaction between the high affinity (RGD site) and the predicted

"synergy site" i.e. an allosteric mechanism. However, a comparable profile was observed for all conditions tested and this was the case when these conditions were used to initiate dissociation of [^{3}H]compound **1**, although full reversal of binding was observed in contrast to the partial effect with [^{3}H]A20FMDV2. This profile of partial dissociation was confirmed for unlabelled A20FMDV2 when competition over 48 h with [^{3}H]compound **1** was investigated. This data may provide further evidence for a second binding site on the integrin. Interestingly, the unlabelled A20FMDV2 is unable to compete with the second site that may suggest it is not structurally in the correct conformation to achieve this unless first bound to the RGD binding site, again adding weight to the "synergy site" hypothesis. In contrast to the dissociation studies, the association, saturation and competition binding data for [^{3}H]A20FMDV2 shows that if the peptide competes with unlabelled αvβ6 ligands at the same time i.e. isn't allowed to form a complex with αvβ6, all the radioligand can be competed off to NSB levels. A final observation worth highlighting from [^{3}H]A20FMDV2 dissociation experiments is that $fLAP_1$ does not share the same dissociation profile as A20FMDV2, as determined in the [^{3}H]compound **1** studies. This suggests that the synergy site hypothesised for A20FMDV2 is not applicable in the case of LAP_1 binding to αvβ6.

In these studies $tLAP_1$, containing the RGD binding motif and flanking amino acids, has been shown to have a comparable affinity for the αvβ6 integrin as the $fLAP_1$. Due to the constraint on the highest concentration achievable with $fLAP_1$ (due to the high cost of small amounts of peptide), only concentrations up to 10 nM could be studied. As such, when tested against αvβ1, αvβ3, αvβ5 and αvβ8 no inhibition of binding was observed up to 10 nM (data not shown). This alone only showed a

minimum of 10-fold selectivity of LAP_1 for the αvβ6 integrin as there was the inability to determine exact K_I values at the other integrins. As the $tLAP_1$ could be used at higher concentrations and its affinity for αvβ6 was comparable to $fLAP_1$, this was used to obtain a more accurate selectivity profile for LAP_1. This data showed that $tLAP_1$ has a minimum of 3,000-fold selectivity over the other integrins tested (~3,000-fold over αvβ3, ~3,500-fold over αvβ1, ~5,000-fold over αvβ8 and ~11,000-fold over αvβ5) under the cation conditions tested (standardised to 2 mM Mg^{2+} in all assays). The high level of selectivity exhibited by $tLAP_1$ for αvβ6 is important when considering the importance of each integrin in activating TGFβ1 in disease settings. There is evidence that αvβ5 expressed in myofibroblasts may be important in activating TGFβ1 via the same mechanical stretch mechanism as αvβ6 (Wipff and Hinz, 2008), but with such a low affinity for LAP_1 it is difficult to know if this would be a significant contributor. It is also worth noting that due to the divalent metal cation dependency of integrin binding (Plow *et al.*, 2000), the type and concentration of divalent metal cation used should also be carefully considered. The effects observed in relation to affinity and potency will differ, potentially to varying degrees for a ligand at a specific integrin that will be further complicated when comparing analyses between integrins.

As has been observed in this study, the divalent metal cation used to support the binding of ligands to an integrin will affect the level of binding observed and hence more than likely the affinity of that ligand. In these studies, it has been shown that binding with the αvβ6 integrin in the presence of different cations or varying concentrations of cation alters the profile of a small molecule RGD-mimetics ([^{3}H]compound **1**) compared with a peptide ([^{3}H]A20FMDV2). All integrins have

three to five low affinity (μM to mM) divalent metal cation binding sites that can act as both inhibitors or promoters of ligand binding as well as having the ability to change ligand binding specificity (Plow *et al.*, 2000). However, little is still known on the physiological role of the integrin ion binding sites. Therefore, in the case of αvβ6 it is not clear what divalent metal cation plays the key role in a physiological setting. As such, it is important to consider this variable when setting up systems to probe ligand-integrin interactions and endeavouring to standardise divalent metal cation type and concentration where possible. This becomes even more critical for ligands proposed to be developed as therapeutics when the key endogenous divalent metal cations and their abilities to alter ligand binding are not known. It is therefore prudent to ensure ligand affinity is measured in a full spectrum of divalent metal cations and concentrations to provide best and worst case binding profiles, with plasma/tissue levels of these divalent metal cations used as starting points. Depending on the target organ and the divalent metal cation concentrations present in the fluid the target and drug are exposed to, the binding profile is likely to differ but can be begun to be investigated using simulated body fluids (Marques *et al.*, 2011). This area has been further investigated and discussed below (section 6.3. Characterising the binding of compound **3** with the αvβ6 integrin).

Following the identification of a series of small molecule αvβ6 RGD-mimetics using cell adhesion SAR assays, that included compound **3**, a number of lead compounds were fully characterised against a panel of integrin radioligand competition binding assays. During this process various control small molecule RGD-mimetics and peptides were also profiled for comparison, and to aid validation of different systems to answer specific questions in a variety of radioligand binding studies. The original

hit molecule (Figure 6.2.1A1) identified in GSK that ultimately led to the lead optimisation of compounds **2** and **3**, was made via cross screening of αvβ6 with libraries of known αvβ3 small molecule RGD-mimetics. During the medicinal chemistry SAR development of this compound series it had been suggested that the tetrahydronaphthyridine fragment was fully optimised for engagement with the αv integrin subunit and that binding to the divalent metal cation in the active site required a carboxylic acid group (Anderson, 2014). It was then shown that the substituted aryl fragment could optimise interactions with the β6 subunit and that the core of the molecule was key to affinity, selectivity and its physico-chemical properties rather than just a spacer group between the integrin subunits (Anderson, 2014). In addition, the chiral centre contained within these molecules had been shown to result in affinity differences between the separated enantiomers (Anderson, 2014). As such, the substituted aryl group, alternative saturated cores and chiral centre had been the main areas of focus for medicinal chemistry during the lead optimisation process that led to the discovery of compound **3** (Figure 6.2.1A4).

One of the key data required for the lead optimisation of these small molecule RGD-mimetics was the definition of a true selectivity against a range of αv integrins, with the aim to define the fold selectivity for αvβ6. Historical data for these molecules from cell adhesion assays hinted at the selectivity but the potency values in these systems are only an empirical measure of competitor potency. The studies completed in radioligand binding assays allowed the determination of true affinity measurements (K_I). To aid these studies a number of positive and negative controls were used. SC-68448 is a small molecule RGD-mimetic that was developed to interact with the αvβ3 integrin as a potential inhibitor of tumour angiogenesis and

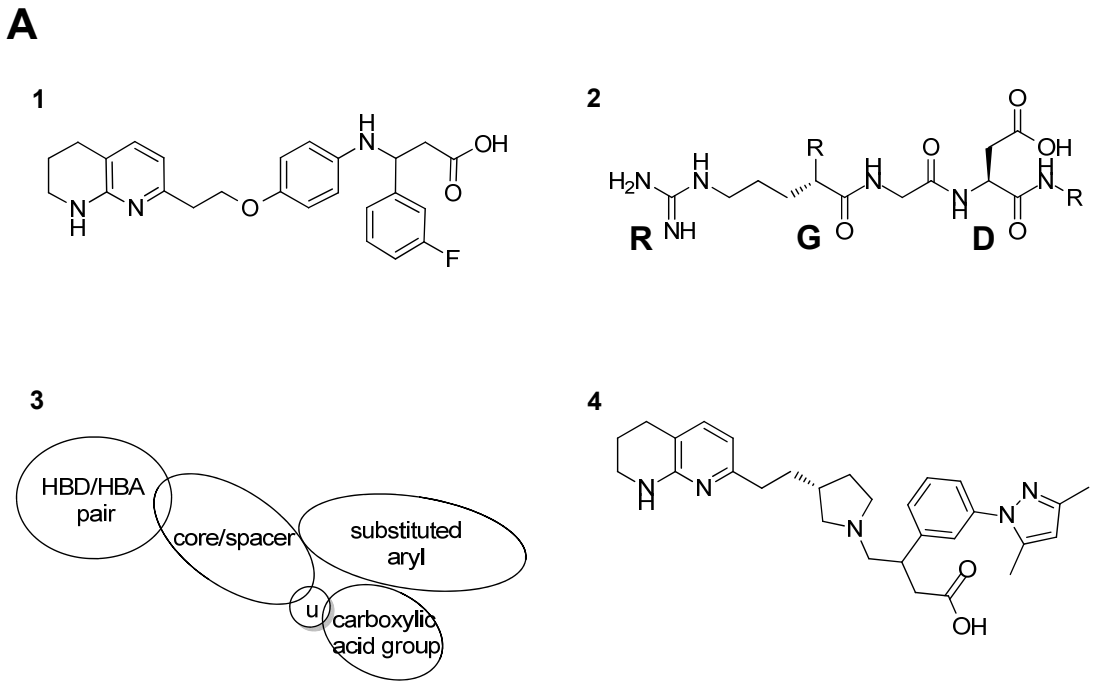

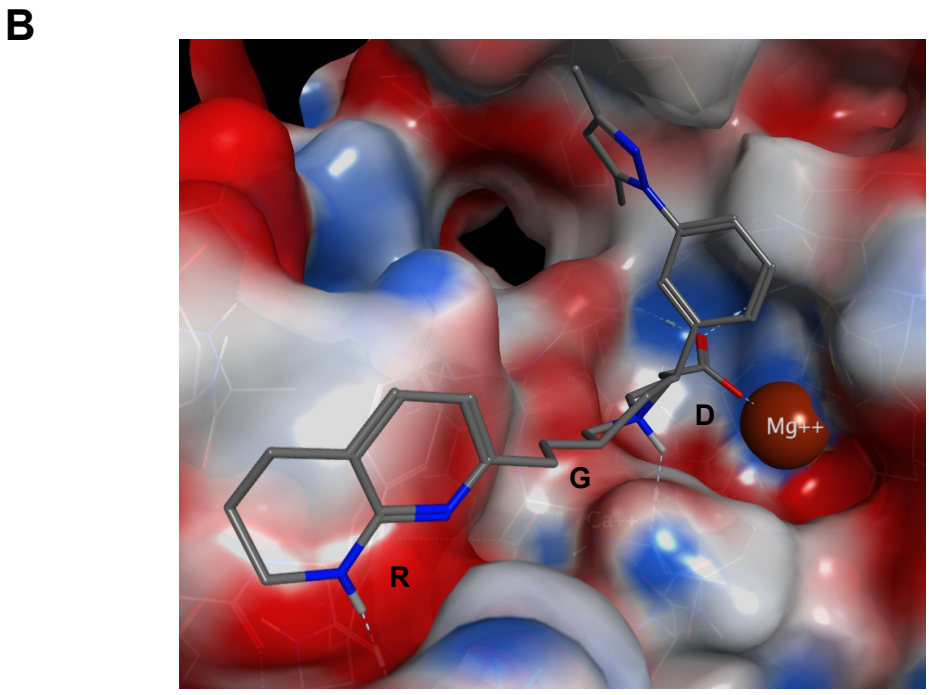

Figure 6.2.1 The key chemical structures and pharmacophore model generated in the lead optimisation of compound 3. (A) The original hit molecule identified by cross screening of αvβ6 with libraries of known αvβ3 small molecule RGD-mimetics (1) with the RGD (Arg-Gly-Asp) sequence shown for comparison (2). The general pharmacophore model (3) used by medicinal chemists during lead optimisation that resulted in the drug candidate compound **3** (4). HBA, hydrogen bond acceptor; HBD, hydrogen bond donor; u, unresolved stereocentre. (B) The binding of compound **3** in the αvβ6 RGD binding pocket with the integrin protein surface coloured by charge (red = positive; blue = negative; white = neutral) (GSK computational model based on the crystal structure described in Dong *et al.*, 2014). Hydrogen bond contacts between compound **3** and αvβ6 are shown by the dotted line as well as the MIDAS Mg^{2+} interaction. Carbon (grey), nitrogen (blue) and oxygen (red) atoms are highlighted in the compound **3** structure.

growth (Carron *et al.*, 1998). The only data available for this molecule shows it profiled against the αvβ3 and alpha-IIb beta-3 (αIIbβ3) RGD integrins, where the chemistry efforts were focussed on enhancing potency at αvβ3 and selectivity over αIIbβ3 alone (Carron *et al.*, 1998). However, in these studies SC-68448 has been shown to have pan-activity across αvβ1, αvβ3, αvβ5, αvβ6 and αvβ8, and as far as the author is aware this is the first time this has been demonstrated for this molecule. As such it was utilised as one of the positive controls in all integrin binding assays completed to measure variability in affinity estimates between individual experiments and also to define NSB. In addition, the αvβ6 selective peptide A20FMDV2 acted as a positive control in the αvβ6 assays and a negative control in αvβ1, αvβ3, αvβ5 and αvβ8, whereas the cyclic peptide cilengitide acted as a positive control in the αvβ3 and αvβ5 assays and a negative control in αvβ6 and αvβ8. Interestingly, cilengitide was also shown to bind with moderate affinity to αvβ1 that is another novel observation that may provide further insight to its biological activities in historical studies. Comparisons with cilengitide affinity for αvβ3 and αvβ5 were important as one of the aims of this study was to define the selectivity of compound **2** and **3** for αvβ6 over αvβ3 and αvβ5, as there is evidence that engaging these integrins may result in negative effects on angiogenesis (Eliceiri and Cheresh, 1998). In addition, cilengitide has also been shown to exacerbate fibrosis in liver fibrosis models (Patsenker *et al.*, 2009) providing further evidence to obtain selectivity over these integrins. Although it is fair to say that the clinical data generated for cilengitide (Gilbert *et al.*, 2011) and the pan-αv antibody intetumumab (Heidenreich *et al.*, 2013) to date is yet to suggest any negative side effects of interacting with αvβ3 and αvβ5, as well as any of the other αv integrins in man.

However, historically the true selectivity profile and affinities of these potential therapeutic agents is not well characterised across the whole of the αv integrins that makes a definitive conclusion on safety liabilities difficult. Conversely, it has also been suggested that inhibiting αvβ1, αvβ5 and αvβ8 may offer added benefit to a therapeutic agent in the treatment of fibrotic disease (Margadant and Sonnenberg, 2010; Henderson *et al.*, 2013; Henderson and Sheppard, 2013; Reed *et al.*, 2015) in combination with αvβ6 activity, again due to their roles in TGFβ activation. However, in contrast to αvβ6 the literature validation for αvβ1, αvβ5 and αvβ8 is still building (the lack of selective tools and/or protein preparations for αvβ1 and αvβ8 has stunted the research in this area) and evidence exists for caution around these integrins due to safety liabilities (as detailed above for the role of αvβ5 in angiogenesis, the loss of αvβ8 on dendritic cells of mice resulting in autoimmunity and a colitis phenotype (Travis *et al.*, 2007) and the general lack of information on αvβ1, in part due to the inability to generate a β1 knockout mouse phenotype (Henderson *et al.*, 2013)).

Historically, due to the conserved RGD binding site exhibited for αvβ1, αvβ3, αvβ5, αvβ6 and αvβ8, designing small molecules with true selectivity for one or a combination of these integrins has been challenging (Goodman *et al.*, 2002). As such, with a small molecule approach to targeting the αvβ6 integrin, a true αvβ6 selective molecule, such as that achieved with an antibody, is unlikely to be achieved. Therefore the comparison between these integrins in terms of selectivity becomes important when taking into consideration the potential advantages and disadvantages of activity at αvβ1, αvβ3, αvβ5 and αvβ8. Although, the selectivity profile defined for $tLAP_1$ in this study also brings into question what the benefit of

targeting αvβ1, αvβ5 and αvβ8 (in addition to αvβ6) would be in a therapeutic agent designed to treat IPF (and potentially other fibrotic diseases) by inhibiting the activation of TGFβ. However, these observations would need to be confirmed in functional *in vitro* and *in vivo* systems measuring inhibition of these other RGD integrins to put the $tLAP_1$ binding selectivity data into context. Nevertheless, a conservative approach was taken with the GSK αvβ6 drug discovery programme, with the aim to identify an as selective as possible αvβ6 small molecule RGD-mimetic, with compound **3** being shown to be the most desirable candidate.

As the physico-chemical properties of compound **3** are comparable to that of compound **2** (see Appendix 8.3), the selection of compound **3** as the lead small molecule RGD-mimetic was as a result of its characterisation in a range of radioligand binding studies. Firstly, it was shown to demonstrate a high affinity for αvβ6, so much so that in the original binding format it was shown to be at the upper limit of detection when 0.3 nM of αvβ6 integrin protein was used. The affinity for compound **3** in this assay was ~40 pM (K_I) that equated to being ~7-fold lower than the concentration of αvβ6 protein. When the αvβ6 integrin was lowered by 4-fold to 0.075 nM a shift of ~4-fold was also observed for the affinity of compound **3** (~10 pM K_I). Further reduction of the αvβ6 integrin concentration could not be achieved without losing a robust specific binding window. Using this affinity value as a minimum for comparison between αvβ6 and the other integrins a highly selective profile is observed for compound **3** compared with compound **2**, with ~180-fold selectivity over αvβ8, ~190-fold selectivity over αvβ1, ~1,000-fold selectivity over αvβ5 and ~3,400-fold selectivity over αvβ3.

The key piece of data showing compound **3** to be superior to compound **2** was the dissociation data showing it to have a slow dissociation from the αvβ6 integrin. At ~10 h post-initiation of dissociation using an excess of [^{3}H]compound **1**, ~50% of compound **3** remained bound to the αvβ6. This was is in comparison to ~30% of compound **2** at the 10 h time point. It is worth highlighting that these studies were all completed at 37°C and that the dissociation profile exhibited for compound **3** at a physiological temperature is unprecedented for an integrin ligand and would still be categorised as long in other target classes e.g. for drugs targeting GPCRs (Vaquelin and Charlton, 2010) where it is more routine to investigate drug-receptor kinetics. If these characteristics of high affinity and slow dissociation from αvβ6 displayed by compound **3** were to translate into a long duration of action in an *in vivo* and clinical setting, then this would make the dosing regimen more convenient with less drug required to be dosed less frequently.

6.3. Characterising the binding of compound 3 with the αvβ6 integrin

To build upon the binding profile at the αvβ6 integrin characterised using the unlabelled form of the RGD-mimetic compound **3**, the radiolabelled version ([^{3}H]compound **3**) was synthesised that offered a more optimal version for full pharmacological characterisation of the properties of compound **3**. It also allowed further characterisation of αvβ6 in a number of different biological systems. The binding parameters determined between the labelled and unlabelled form of compound **3** using soluble αvβ6 protein preparations were highly comparable. The high affinity pM interaction displayed in competition binding studies with the tool integrin radioligand [^{3}H]compound **1** was confirmed in saturation studies with [^{3}H]compound **3**. In addition, the slow dissociation profile was also confirmed and

acted as a further validation of the technique used for determining the dissociation profile of unlabelled ligands in Chapter 3. This early indicator of dissociation kinetics not only had a significant impact on the selection of compound **3**, but also provides a good rationale for investigating the kinetic properties of molecules much earlier in the lead optimisation process. Although similar techniques have been used to gather kinetics data early (Dowling and Charlton, 2006), it is generally not until a drug candidate has been selected to be taken forward for clinical studies that a full binding characterisation is completed on a radiolabelled form. Furthermore, in the majority of cases it is GPCRs drug candidates that have been fully profiled historically (Vaquelin and Charlton, 2010), but this study has shown that the integrins as a target class are amenable to the same studies as well as highlighting the ability to identify high affinity and slow dissociating integrin small molecules suitable for clinical investigation. However, the analysis of the dissociation of compound **3** using the unlabelled form was only able to differentiate and rank the profile of this molecule compared with other RGD-mimetics. The unlabelled compound **3** dissociation data suggested a bi-phasic dissociation from αvβ6, however an accurate fit could not be applied to this set of data to allow a statistical comparison of one vs. two-phase models of exponential decay. However, with [^{3}H]compound **3** binding studies the increased level of accuracy provided by using the directly labelled molecule enabled this comparison and confirmed the dissociation was bi-phasic, with a fast phase of dissociation completed at just over 2 h that remained unresolved at the 72 h time point. It could be hypothesised that the initial fast phase is dissociation from a low affinity state of the integrin i.e. low activation state, and the slow late phase is dissociation from a high affinity state of

the integrin i.e. high activation state. The activation of integrins can be achieved via three mechanisms that include extracellular ligand binding (referred to as 'outside-in' signalling), intracellular β-integrin tail activation (referred to as 'inside-out' signalling) and divalent metal cation occupancy of the ligand-binding pocket (Luo *et al.*, 2007; Tiwari *et al.*, 2011). It would have been predicted that due to the pre-incubation [^{3}H]compound **3** has with αvβ6 (1 h) and the equilibrium observed at the same concentration when tested in association studies, that the majority of the integrin would have been converted into the high affinity state, though this bi-phasic dissociation suggests otherwise. In addition, a single phase of association was observed with [^{3}H]compound **3** at the time points tested. This potentially suggests that either the rates of association for the low and high affinity states were the same and undetectable or the time points were too far apart to accurately define. Although if the affinity state (and therefore K_D) was shifted and this is manifested by changes in dissociation rates, it could be predicted that the association rates would remain overall constant in terms of the law of mass action. For example, if the law of mass action is applied to an interaction between a ligand and its receptor it has been demonstrated that the K_D is a combination of the kinetic constants (k_{off} and k_{on}) (Hulme and Trevethick, 2010) where $K_D = k_{off}/k_{on}$. Following on from this it may have also been expected that if there were two αvβ6 affinity states achievable that they could have been observed in [^{3}H]compound **3** saturation binding studies. This would have been revealed if the saturation binding curve demonstrated a shallow Hill slope (Hill slope (n_H) < 1) and/or a bi-phasic curve when the data is plotted using the $\log_{10}$ transformed concentration values. Neither of these was observed suggesting

that at the 24 h time point tested, the majority of the αvβ6 integrins had been shifted into the high affinity state by engagement with [^{3}H]compound **3**.

One area of αvβ6 biology where there is limited research is the role of different types and concentrations of divalent metal cations on the ability of ligands to bind this integrin. For some of the other RGD integrins the interplay between different metal ions and the MIDAS has been investigated (Plow *et al.*, 2000; Xia and Springer, 2014), however for αvβ6 there is more limited information. Even when studies in this area of integrin biology have been completed they tend to focus on single ligands at limited concentrations of divalent metal cation. Therefore, in order to gather further information regarding the relationship between ligands, divalent metal cations and concentrations thereof, in this study saturating concentrations of radioligands were tested at increasing concentrations of either Ca^{2+}, Mg^{2+} or Mn^{2+}. It was demonstrated for the binding of [^{3}H]compound **3** to αvβ6 that the concentration required to enable binding was different between divalent metal cations with Mn^{2+} able to support binding at much lower concentrations compared with Mg^{2+} and Ca^{2+}. In addition, Ca^{2+} was unable to produce maximal binding of the small molecule RGD-mimetic radioligand compared with Mn^{2+} and Mg^{2+}. This profile was more comparable to that observed with [^{3}H]A20FMDV2 in terms of EC_{50} values however the partial ability to support binding in the presence of Ca^{2+} was more comparable to [^{3}H]compound **1** (although the level to which binding was enabled was greater for [^{3}H]compound **3**). This suggests that different αvβ6 ligands are able to demonstrate different binding profiles when in the presence of the same type and concentration of divalent metal cation. This is not only the case between different types of ligand i.e. peptide vs. small molecule, but also within i.e. small molecule vs. small molecule. This

highlighted that each αvβ6 ligand needs to be assessed on an individual basis and that this may be important when investigating more physiologically relevant divalent metal cation conditions. As such, in the context of delivering a drug into the lung to target a protein on the baso-lateral surface of the airway epithelial layer, SLF was investigated that contains 0.5 mM Mg^2 and 2.5 mM Ca^{2+} (Marques *et al.*, 2011). To further endeavour to re-create physiological conditions, not only of the lung but an IPF lung, SLF fluid with a pH of 6.2 was investigated. This lower pH was tested due to literature evidence suggesting in the diseased IPF lung that lactic acid production creates a more acidic environment (Kottmann *et al.*, 2012). Only a minimal effect of these conditions were observed on the binding of [^{3}H]compound **3** to the αvβ6 integrin with a an ~3-fold shift to a lower affinity observed. This suggested the predicted lung conditions that compound **3** will encounter upon nebulised delivery into an IPF lung will not reduce its ability to engage with αvβ6. The miminal effect on affinity observed by lowering the pH from 7.4 to 6.2 for compound **3** is interesting when compared to recent data that showed that the drop in afiinity is much more significant (~10-fold) for endogenous ligands (Dong *et al.*, 2014) over a similar range. This highlights a potential advantage for compound **3** in disease settings when competing with endogenous ligands, specifically the LLC for TGFβ1.

As all the studies described thus far were completed using a soluble form of the αvβ6 integrin protein, it was important to confirm these observation in a more physiologically relevant and, if possible, diseased system. Although the use of soluble protein preparations is more convenient, the integrin is not present in the cell plasma membrane where it will be influenced by a range of structural and biochemical forces. Therefore, the use of whole cells or plasma membrane

preparations from whole cells or human tissue are systems that offer a closer set of conditions to that *in vivo*. The use of membrane preparations generated from human IPF lung tissue in this study has allowed the characterisation of ligand binding with αvβ6 in its natural conformation, held in a plasma membrane. In addition, it has also allowed the quantification of the levels of αvβ6 in both normal and fibrotic lung tissue. Optimisation of the radioligand binding assay using [^{3}H]compound **3** and IPF human lung membranes revealed a much higher level of NSB compared with that observed in studies with the recombinant soluble protein preparation of αvβ6. This could be anticipated for a number of reasons. Firstly, there is a much higher level of background protein in the IPF membrane preparations providing a much greater opportunity for non-specific protein binding i.e. [^{3}H]compound **3**/non-αvβ6 background binding. Secondly, the soluble αvβ6 protein preparations contain a single population of integrin receptors whilst the human lung membranes contain plasma membranes from all cell types in the diseased IPF lung i.e. alveoli, blood vessels, small airways myofibroblasts, and therefore potentially multiple RGD integrins. To overcome this and only measure αvβ6 binding of [^{3}H]compound **3** the selective αvβ6 peptide A20FMDV2 was used to define NSB and therefore the specific αvβ6 binding window. Although compound **3** demonstrates a high affinity and selectivity for αvβ6 it has been shown to bind to other RGD integrins that would likely be present in these membrane preparations. Therefore, even though the affinity of [^{3}H]compound **3** for the non-αvβ6 RGD integrins is low there is the potential that the high NSB observed is a combination of non-specific protein binding and binding to single/multiple non-αvβ6 RGD integrins.

The characterisation of the binding of [^{3}H]compound **3** with the αvβ6 in normal and IPF human lung membranes resulted in a number of novel and interesting observations. Firstly, a much greater level of αvβ6 was observed in normal lung tissue than had been expected based upon the literature findings where IHC staining had been completed (Horan *et al.*, 2008) and showed no evidence of the integrin present. In addition, the IHC staining for αvβ6 in this study in normal lung tissue yielded the same observations and conclusion. This highlights the sensitivity of the two methods and perhaps a common pitfall when using IHC staining to validate drug targets. The conditions and affinity of the IHC antibody probe used in studies comparing normal with diseased tissue will influence the results. For example, this has been demonstrated for αvβ6 expression in other organs where one group claimed the absence of the integrin in the gastric mucosa (Zhuang *et al.*, 2013) and another group the presence (Sipos *et al.*, 2004), with both conclusions arrived at using the same technique but different conditions and antibodies. This shows that the use of radioligand binding is a more sensitive and accurate technique for not only assessing affinity for potential drug targets in diseased tissue but also to quantify the levels of targets, and therefore the upregulation, in normal compared with diseased tissue. Secondly, the significant increase observed in αvβ6 B_{max} between different divalent metal cations in IPF human lung membranes (increasing from Mg^{2+} to Mn^{2+}), that was not observed in normal membranes, not only confirmed the upregulation in disease for this integrin but also a potential difference in activation/affinity state. It is highly likely that due to the conditions used to generate the membrane preparations from human lung tissue e.g. buffers containing high concentrations of EDTA chelating the divalent metal cations in the preparations, that αvβ6 would be shifted

into an inactive state. It is hypothesised in IPF that αvβ6 exists in an activated, high affinity state as a result of "inside-out" signalling via LPAR2 and PAR1 (Xu *et al.*, 2009) (that are both upregulated in IPF). There is also the potential for "outside-in" signalling via constant engagement of the integrin with the LAP component of the TGFβ LLC, as it drives the over activation of TGFβ hypothesised to be responsible for the fibrotic state in IPF. Therefore, the use of Mn^{2+} to activate and shift αvβ6 to a high affinity state potentially recovers the disease state of the integrin. Although it is difficult to fully conclude that all αvβ6 activated *in vitro* were in this state *in vivo* prior to removal and processing of the tissue, the controls completed with normal membranes generated using the same protocol and assayed under the same conditions, the trend for a higher affinity in IPF vs. normal human lung membranes (regardless of divalent metal cation condition) and different receptor kinetics in IPF human lung membranes between divalent metal cations, all go some way to add weight to this hypothesis.

The final observations made in this part of the study allowed the comparison of radioligand studies completed in human diseased IPF tissue with those in basic preparations of the αvβ6 integrin (recombinant soluble protein preparations). The affinity estimates agreed well between systems as did the association studies when comparing data obtained in the presence of Mg^{2+}. However, the dissociation profile observed was faster in IPF human lung membranes even when comparing different divalent metal cations i.e. 2 mM Mg^{2+} in soluble protein preparations vs. 2 mM Mn^{2+} in IPF human lung membranes. This suggested a difference between the two systems potentially again as a result of differing affinity states and that using the simpler and more accessible soluble protein preparation of the integrin was over estimating the

dissociation profile observed from αvβ6 compared with the more relevant physiological and disease setting of IPF human lung membranes. Finally it is also worth highlighting that now this link between the soluble protein preparations and IPF human lung membranes has been made, the simpler system can be used to predict the disease setting parameters more effectively for any future drug discovery initiatives focussing on αvβ6 and potentially other integrins. This data suggests that an even higher affinity engagement (<10 pM) with αvβ6 would be required to drive duration of action in the IPF lung via slow receptor dissociation kinetics.

In order to test the hypothesis in a clinical setting that αvβ6-mediated TGFβ activation is fundamental in driving fibrosis in IPF, a preferred first study would be designed to maximally inhibit αvβ6 for the duration of the dosing regimen. For inhibitors/antagonists it is recommended that high levels of target occupancy is achieved (Grimwood and Hartig, 2009). In the case of TGFβ activation in fibrosis there is the potential that other mechanisms contribute to the increased levels in disease, for example other TGFβ-activating integrins (Margadant and Sonnenberg, 2010; Henderson *et al.*, 2013; Henderson and Sheppard, 2013; Reed *et al.*, 2015) and the low pH in the IPF lung (Kottmann *et al.*, 2012). Therefore, to determine if αvβ6-mediated TGFβ release is the primary contributor it could be hypothesised that >90 % occupancy would be required. The dissociation of [^{3}H]compound **3** from the αvβ6 integrin observed in IPF human lung membranes was still relatively slow but potentially not slow enough to provide the duration of action required to overcome the low lung retention observed with compound **3** and meet the criteria of twice daily dosing. Therefore, in order to achieve >90 % occupancy of αvβ6 over the entire dosing period it is likely a high loading dose would be required that would be

dependent on the limits set by pre-clinical toxicological studies in rats and dogs. Once the highest predicted safe dose in humans is calculated this can be used in combination with the binding kinetics of [^{3}H]compound **3** and the pharmacokinetic profile to model the αvβ6 blockade over time and allow the estimation of dosing levels and regimen i.e. once, twice or three times a day. This assumes that the relationship between inhibition of αvβ6 and TGFβ activation is stoichiometric in terms of one αvβ6 integrin activates one TGFβ molecule that activates one TGFβRI/RII complex to initiate downstream signalling and generation of pro-fibrotic mediators. However, binding studies investigating αvβ6 alone are unable to elucidate this and therefore functional studies to determine the mechanism of action of compound **3**, in addition to understanding the relationship between compound **3**/αvβ6/TGFβ activation in more physiological systems, are a necessity to build into the final dose prediction model.

6.4. Inhibition of αvβ1- and αvβ6-mediated TGFβ activation by compound 3

Following the full characterisation of the binding of compound **3** with the αvβ6 integrin in a range of test systems, it was essential to establish the ability of the molecule to inhibit the activation of TGFβ. In addition, investigating systems that could link functional potency to binding affinity not only for αvβ6 but potentially beyond for other RGD integrins would help understand the selectivity profiles established in radioligand binding assays and the assumptions made in terms of the avoidance of undesired engagement with RGD integrins perceived to have a safety liability e.g. αvβ3.

In terms of the competitor landscape for compound **3**, developed as a high affinity and selective αvβ6 inhibitor proposed as a therapeutic for fibrotic diseases, the main opposition is from STX-100 (also known as 3G9 pre-clinically) the selective αvβ6 monoclonal allosteric antibody (Horan *et al.*, 2008) currently in phase II clinical trials for IPF. Although there was the inability to directly compare compound **3** with 3G9 in the same test system due to antibody availability, assays could be set-up that had been used historically to measure the efficacy of 3G9 and suitable control agents compared alongside compound **3** that would allow an indirect comparison between the small molecule RGD-mimetic and the monoclonal antibody to be made. One of the systems that enabled this comparison was the SW480-αvβ6/TMLC co-culture bioassay that measured the activation and release of TGFβ. In previous studies this system had been used to show that 3G9 was a potent inhibitor of TGFβ activation with an IC_{50} of ~4 pM (Weinreb *et al.*, 2004). Within those studies a commercially available control anti-αvβ6 antibody 10D5 was tested and this offered the opportunity to rank compound **3** in this test system indirectly with 3G9. 10D5 in these studies was shown to inhibit αvβ6-mediated TGFβ activation in the SW480-αvβ6/TMLC co-culture bioassay with an IC_{50} of 145 ng/ml. This was very comparable to that generated by Weinreb and co-workers where 10D5 exhibited an IC_{50} of ~100 ng/ml. Consequently, compound **3** was shown to inhibit αvβ6-mediated TGFβ in this system with an IC_{50} of ~40 pM that was 10-fold lower than 3G9. This is an interesting comparison of a small molecule RGD-mimetic with a high degree of affinity and selectivity for αvβ6 generated via a medicinal chemistry lead optimisation process compared with a truly selective, allosteric (non-RGD-mimetic), anti-αvβ6 monoclonal antibody raised to the integrin by immunisation of mice with

the protein. Although the high levels of affinity, selectivity and extended pharmacokinetic profile generally achievable with a therapeutic antibody is almost impossible to deliver with a small molecule drug, the generation of a profile like that observed with compound **3** in relation to integrin affinity, selectivity and functional efficacy can be viewed as an impressive medicinal chemistry effort. The SW480-αvβ6/TMLC co-culture system used in this study has also been shown to not only be driven by αvβ6 but also partially by the other RGD integrin αvβ1, a finding that had previously not been observed or reported in the literature. In this study this observation was concluded from the positive effects observed for selective blocking antibodies of the individual αv and β1 integrin subunits but also the small molecule cilengitide, which has also been shown for the first time to bind and inhibit TGFβ via αvβ1. Historically, the role of αvβ1 in activation of TGFβ was questioned (Munger *et al.*, 1999) although more recently it has been shown that it not only activates TGFβ but has also been implicated in a number of pre-clinical models of organ fibroses (Reed *et al.*, 2015). As a potential anti-fibrotic target in the lung, in terms of pre-clinical validation, the evidence is now beginning to build that inhibition of αvβ1 in addition to αvβ6 could provide an added therapeutic benefit. The hypothesis from the αvβ1 and αvβ6 studies completed by Sheppard and co-workers (Huang *et al.*, 1996; Munger *et al.*, 1999; Horan *et al.*, 2008; Henderson *et al.*, 2013; Henderson and Sheppard, 2013; Reed *et al.*, 2015) is that αvβ6 is the epithelial RGD integrin responsible for driving TGFβ activation at the leading edge of fibrotic lesions, and that αvβ1 is the myofibroblast RGD integrin responsible for driving TGFβ activation within the fibrotic foci. Though it is fair to say that there still remains an unclear picture of the key integrin/s and cell type/s in lung fibrogenesis as even from the

same groups there are conflicting reports. For example, there is data that has recently emerged from Sheppard and co-workers that the fibrotic myofibroblast phenotype may not be the only offender in the fibrotic milieu (Sun and Sheppard, 2015). While it is anticipated that as more studies are completed and the literature builds around a relatively new disease like IPF (in terms of characterisation and being the target of therapeutics), this highlights the difficulty in drug discovery for such disorders on the back drop of an ever evolving landscape when it can take several years to develop clinical candidates before even beginning to test in human trials and seek approval from global drug approval agencies. With question marks surrounding the pre-clinical models used for lung fibrosis (Scotton and Chambers, 2010) it suggests that further development of *ex vivo* diseased tissue models are required, that are currently lacking in this area, followed by well designed and focussed clinical trials using clearly characterised target–specific pharmacodynamic biomarkers and more importantly disease biomarkers (Jenkins *et al.*, 2015).

Although a rather insensitive fibrotic endpoint the measurement of collagen production via hydroxyproline in the bleomycin-induced mouse lung fibrosis model, where these RGD integrin hypotheseses have been tested, suggests inhibition is partial either with a selective αvβ6 antibody (Horan *et al.*, 2008) or a selective small molecule αvβ1 RGD-mimetic (Reed *et al.*, 2015). It would be interesting to complete such a study in this model where these two agents are tested individually and in combination to observe if full inhibition of collagen production could be achieved down to control levels when administered together. Whilst the αvβ1 integrin is a promising pre-clinical target for fibrosis, there remains some significant gaps in validation that would be required to build evidence for its role in disease. One of

these is the expression of this integrin in normal and diseased tissues that is a challenge to measure. This is due to a lack of selective αvβ1 antibodies to measure via IHC and that measures of mRNA for β1 provides limited information as this subunit can partner with a further 11 α-subunits beyond αv (Hynes, 2002). Furthermore, the lack of global expression information combined with the lack of a knockout mouse phenotype (Reed *et al.*, 2015) place a significant question mark over the potential safety liability of inhibiting this RGD integrin. Compound **3** has been shown to be able to inhibit not only αvβ6 but also αvβ1-mediated TGFβ in the SW480-αvβ6/TMLC system with a comparable rank order of potency as the affinity observed in binding studies at these integrins. This shows the selectivity profile observed for these integrins in binding assays correlates with the functional potency differences. This is an extremely useful observation as it allows the tracking of the functional potency, in terms of TGFβ activation, very early in the drug discovery process as the radioligand binding affinity can be linked to the early high throughput SAR cell adhesion assays. Therefore, if back-up templates for compound **3** were required, a new RGD integrin selectivity profile or even a selective tool/drug candidate at another predicted TGFβ activating RGD integrin with a role in fibrosis or other diseases e.g. αvβ1, these high throughput SAR assays could be used as part of hit identification. However, compound **3** would not be predicted to engage αvβ1 for a sustained duration of time due to the low affinity it demonstrates at this integrin. Therefore, it is unlikely that it would inhibit TGFβ activation via αvβ1 and would not have an impact on a fibrotic disease if this integrin was a key driver. This could be viewed as a disadvantage based on more recent data (Reed *et al.*, 2015), but as discussed above the target validation for αvβ1 is still in its infancy and the

unknown safety liabilities of inhibiting this integrin would suggest the predicted lack of αvβ1 inhibition by compound **3** is an advantage and the more conservative approach based on the current literature in this area.

6.5. Novel mechanism of action for prolonged inhibition of αvβ6-mediated TGFβ activation by compound 3

Following the characterisation of the functional inhibition of TGFβ activation achieved with compound **3** in the SW480-αvβ6/TMLC system via αvβ1 and αvβ6, it was then important to build upon these observations in more physiologically relevant cellular system using a primary lung epithelial cell line. In addition, a critical component of this work was to link the slow receptor kinetics observed in previous binding experiments to a sustained duration of functional inhibition to further aid in clinical dose prediction and design of clinical experiments.

A similar TGFβ bioassay co-culture system to that generated with the SW480-αvβ6/TMLC assay was optimised with NHBE cells to allow measurement of TGFβ activation in a primary lung epithelial cell system. Historically, this primary cell line had only demonstrated the ability to activate TGFβ via αvβ6 alone (Xu *et al.*, 2009). Nevertheless, due to the novel observations made in the SW480-αvβ6/TMLC systems compared with published literature, where a combination of αvβ1 and αvβ6-mediated TGFβ activation was demonstrated, cilengitide was tested and shown to be inactive compared with compound **3** in the NHBE/TMLC co-culture assay. This set of experiments showed that this system was only driven by the αvβ6 integrin. It is worth noting however that a high background level of TGFβ was observed in this system that suggested other mechanisms of TGFβ activation, beyond the RGD

integrins, were evident e.g. proteases, that were not observed in the SW480-αvβ6/TMLC assay. The high potency for the inhibition of TGFβ activation observed with compound **3** linked to the high affinity shown in binding studies with the radiolabelled version of this molecule. In addition, following washout of compound **3** a sustained duration of inhibition of TGFβ activation was observed that suggested that the slow dissociation kinetics also shown with [^{3}H]compound **3** binding studies were manifested in the cellular system. It is worth highlighting that even though a high level of inhibition of TGFβ activation was apparent at 24 h in this co-culture system, the measurement of this effect in the NHBE cells is indirectly measured using the TMLC TGFβ bioassay. Therefore, there is likely a lag in measuring the loss of αvβ6 inhibition in the NHBE cells through to re-activation and release of TGFβ via this mechanism, the generation and activation of the TGFβRI/II complex that would then subsequent re-initiate PAI-1 transcription and luciferase production in the TMLCs. This system confirmed a duration effect but it is fair to conclude it doesn't quantify the timings but is sufficient to compare between RGD ligands as was shown later in studies with chloroquine. To aid in the determination of a more accurate and physiologically relevant estimation of the duration of effect for compound **3**, the use of an *in vivo* model would be required to combine a pharmacodynamic measurement of this molecules activity e.g. TGFβ release or pSMAD2 signalling, with the pharmacokinetic profile over time.

However, in parallel with these TGFβ activation studies an interesting set of findings were made upon completion of αvβ6 internalisation studies in NHBE cells (and then subsequently recycling/surface repopulation studies), that were initially designed to ensure the slow dissociation hypothesis was valid. For example, if compound **3**

internalised αvβ6 and a scenario existed where an expedited loss and recycling of αvβ6 to the cell surface occurred, with αvβ6 returning unbound to compound **3**, then TGFβ activation could reinitiate and no sustained duration of action would be achieved. Subsequently, a fast clathrin-coated pit dependent-internalisation of the αvβ6 via compound **3** engagement was observed that prompted concerns that the compound **3**/αvβ6 complex could be quickly uncoupled in the endosome and free αvβ6 recycled to the cell surface.

Interestingly the predicted fast return of αvβ6 post-internalisation by compound **3** did not occur and was much slower than that demonstrated by other RGD ligands, both peptide and small molecule RGD-mimetics alike. Comparing the RGD ligands tested in terms of pre-clinical profiling it was clear that the high affinity/slow receptor dissociation kinetics of compound **3** set it apart. Therefore, it was now predicted, that even though it was still the same characteristic of a slow dissociation from αvβ6 that provided duration of action, the mechanism was not due to prolonged engagement at the cell surface but rather intracellularly and that either slowed recycling or an effect on the levels of the integrin e.g. protein degradation, were responsible. To begin to probe the mechanism by which compound **3** demonstrated a sustained duration of action, the effect of the lysosomal inhibitor chloroquine on αvβ6 levels and TGFβ activation post-addition of compound **3** was investigated.

Chloroquine is an anti-malaria drug that in its unprotonated form can freely diffuse across cell and organelle membranes but becomes trapped in lysosomes once protonated, due to the low pH of this environment (Solomon and Lee, 2009). In this form it has been shown to inhibit proteolytic processes and therefore has been used as a tool for determining mechanisms of receptor turnover (Dunmore *et al.*, 2013).

The ability of compound **3** to cause prolonged inhibition of TGFβ activation following washout was reversed in the presence of chloroquine providing evidence that proteolytic processes were involved in the mechanism of duration of action of this αvβ6 inhibitor. Furthermore, using confocal microscopy to quantify the total levels of αvβ6 (surface and intracellular by completing experiments in the presence of saponin) it was demonstrated that not only did compound **3** reduce the amount of αvβ6 in NHBE cells following a 24 h treatment but that this could also be reversed when chloroquine was added. All these observations combined are consistent with the αvβ6 integrin being degraded post-internalisation by compound **3**. They suggested that the high affinity and slow dissociation kinetics were responsible for a sustained engagement and activation, intracellularly sorting αvβ6 for degradation in lysosomes rather than recycling it to the cell surface from the endosome. The pH of the conditions that the compound **3**/αvβ6 complex would encounter from the extracellular environment (pH 7.0-7.5) would drop from pH 6.0-6.5 in early endosomes through to pH 4.5-5.5 in late lysosomes (Sorkin and von Zastrow, 2002). This drop to a more acidic pH could potentially be predicted to reduce the affinity of RGD ligands and weaken/dissociate the ligand/αvβ6 complex. However, it has already been shown in this study that reduced pH only resulted in a marginal drop in the affinity of compound **3** for αvβ6 suggesting that the compound **3**/αvβ6 complex would be maintained for long periods, as it passed from the plasma membrane to early/late endosomes and finally early/late lysosomes. There is evidence for another RGD integrin, α5β1, that a prolonged activation delays recycling back to the cell surface post-internalisation (Dozynkiewicz *et al.*, 2012) as a result of sorting into lysosomes prior to transportation back to the plasma membrane. However, rather

than the same αvβ6 being slowly recycled post-engagement with compound **3**, it is suggested from data generated in this study that it is new synthesis of the integrin that returns to the cell surface to re-initiate TGFβ activation over a prolonged time period.

6.6. Summary

The primary aim of this study was to pharmacologically characterise tool RGD ligands and small molecule αvβ6 RGD-mimetics generated from a GSK drug discovery initiative targeting IPF by developing, designing and implementing key assays and experiments to aid in the development of a lead chemical series and subsequent identification of a clinical drug candidate. Following this the focus was on the pharmacological characterisation of a novel αvβ6 small molecule RGD-mimetic drug candidate proposed as a potential therapeutic agent for IPF by targeting the inhibition of the TGFβ pathway.

The data generated in this thesis has provided further insight into the mechanism of action of not only αvβ6 ligands e.g. A20FMDV2 and endogenous LAP_1, but also other RGD ligands and their engagement with the other αv integrins beyond αvβ6. As a result, compound **3** has been selected as a drug candidate using radioligand binding systems developed and validated using these tool RGD ligands, to be taken forward for further pre-clinical and clinical investigational studies. It has been shown to bind with a high affinity and selectivity for αvβ6 as well as demonstrating slow receptor dissociation kinetics. The radiolabelled form [^{3}H]compound **3** has also been used to confirm these observations and further demonstrate the mode of binding to be simple, competitive and a reversible interaction with the αvβ6 RGD binding site that

was divalent metal cation dependent. These observations have also been confirmed with the integrin in diseased human lung tissue and in addition [^{3}H]compound **3** acted as a tool radioligand to quantify the upregulation of αvβ6 from normal to IPF human lung tissue.

More complex and physiological test systems have been developed that investigated the functional consequences of compound **3** αvβ6 inhibition in NHBE cells measuring direct TGFβ activation. Furthermore, it has been shown that inhibition of TGFβ activation by compound **3** is prolonged. The ligand-induced αvβ6 internalisation data generated in this study suggests that this is a result of fast ligand-induced internalisation (minutes) followed by a slow return of the integrin to the cell surface (hours). It has also been suggested that the integrin is degraded post-internalisation in lysosomes by compound **3** potentially as a result of its prolonged engagement and activation of αvβ6 that suggests the slow return to the surface is a consequence of the requirement for synthesis of new integrin. To aid in the visualisation of the proposed mechanism of action of compound **3** and to incorporate all the data, observations and conclusions generated as part of this study, Figure 6.6.1 shows the hypothesised passage and the subsequent chain of events post-administration of compound **3** into an IPF patient's lung. It maps the passage of compound **3**, an αvβ6 selective RGD-mimetic, from inhalation via nebulisation through to target engagement in an IPF patient's lung, followed by αvβ6 internalisation, degradation and slow return due to new synthesis, that is proposed to provide extended duration of the inhibition of TGFβ activation and therefore halt the progression of fibrosis.

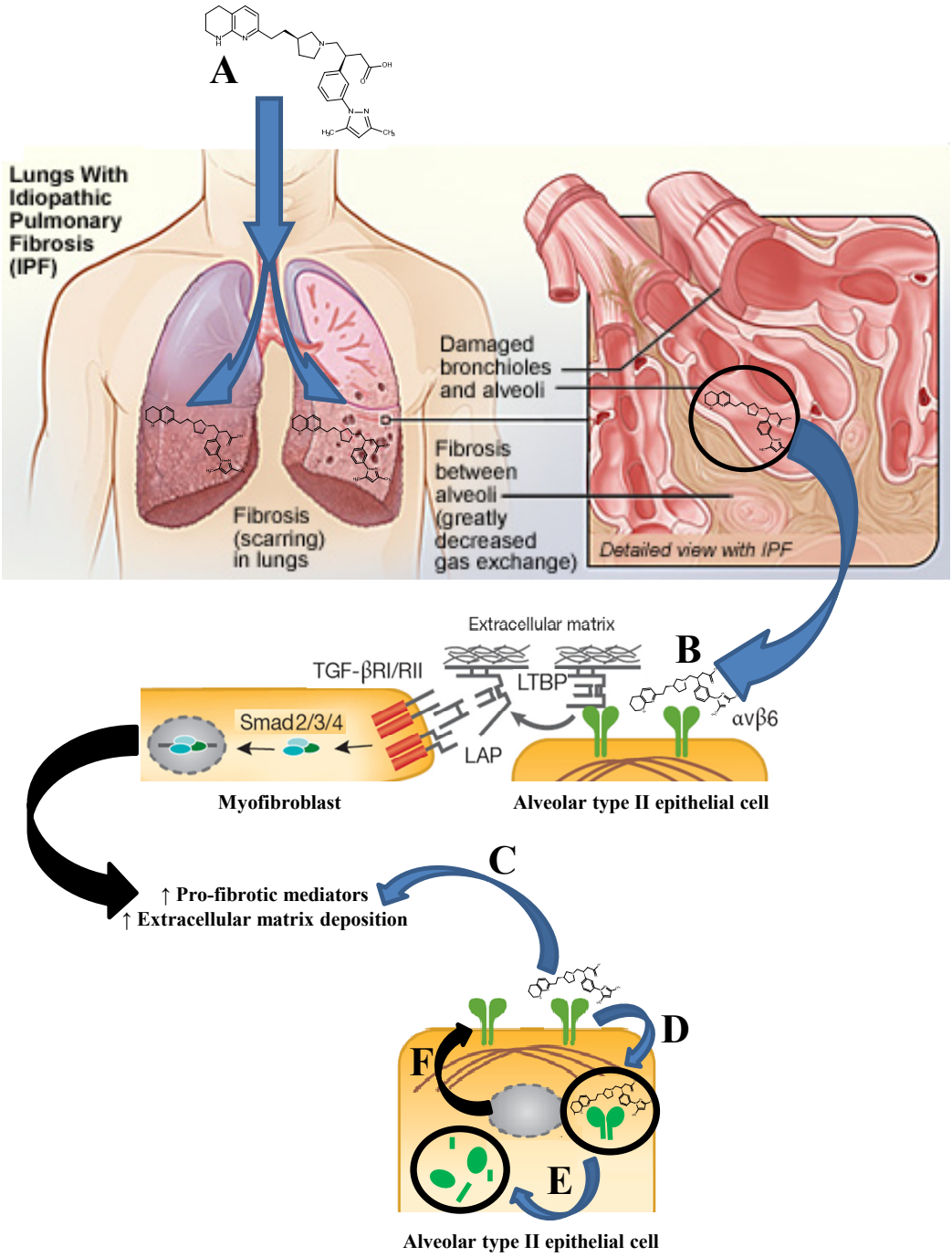

Figure 6.6.1 The hypothesised mechanism of action of compound 3 post-administration into an IPF patient's lung. Nebulised compound **3** enters the lung (A) and binds to αvβ6 with high affinity and fast association kinetics (B). The αvβ6-mediated TGFβ activation in the IPF lung is inhibited reducing pro-fibrotic mediators and extracellular matrix deposition (C). The compound **3**/αvβ6 complex is then rapidly internalised (D) in minutes and the integrin degraded in lysosomes (E). This is hypothesised to result in an extended duration of the inhibition of TGFβ activation thus halting disease progression due to slow synthesis of new αvβ6 (F) over 24 h. IPF, idiopathic pulmonary fibrosis; LAP, Latency associated peptide; LTBP, Latent TGFβ binding protein; SMAD, Sma and Mad protein; TGFβ, Transforming growth factor β; TGFβRI/II, TGFβ receptor I/II complex (images adapted from Margadant and Sonnenberg, 2010 and National Heart Lung and Blood Institute (NIH) web site (http://www.nhlbi.nih.gov/health/health-topics/topics/ipf/lungworks)).

6.7. Future directions

There are a number of avenues to explore from the work completed in this study. They can be split into work that would either provide further insight into compound **3** as a potential drug candidate in IPF or expand the novel findings observed with the αvβ6 integrin to the other RGD integrins for comparison.

In terms of the development of compound **3** as a therapeutic, future work would predominantly focus on *in vivo* studies in both safety/toxicology and pharmacology models, with the latter investigating the bleomycin-induced lung fibrosis model to measure and validate both disease and potential pharmacodynamic markers, upon dosing of compound **3**. These markers could then potentially be used in the clinic to test the pharmacology of this αvβ6 RGD-mimetic in IPF patient cohorts. These studies would also enable the duration hypothesis for compound **3** to be tested *in vivo*, as well as linking occupancy/internalisation of the integrin and pharmacokinetics to the functional effects in a whole body system. This would also enable the best pre-clinical *in vitro* systems that predict the *in vivo* scenario to be identified.

For further work in the area of the RGD integrins, it would be insightful to apply the same binding and internalisation experiments completed here with αvβ6 against the other αv integrins and potentially beyond to the other RGD integrins α5β1, α8β1 and αIIbβ3, where the availability of selective tool antibodies and inhibitors allowed. Although some work has been completed looking at α5β1 and αvβ3 internalisation, there is little known about the other RGD integrins and this may provide a method for identifying more selective molecules. For example, if only αvβ6 displayed fast

internalisation and slow return it would add to the selectivity of inhibitors targeting this integrin via an RGD-mimetic interaction. And so on and so forth if only αvβ6 and other specific RGD integrins, e.g. αvβ1, displayed this mechanism then a higher degree of selectivity over the other integrins may potentially be achievable for RGD-mimetic inhibitors targeting multiple TGFβ-activating integrins.

The role of different divalent metal cations in ligand binding beyond αvβ6 and between RGD integrins is also an area for further investigation as again this could provide a method for improving selectivity. The binding work completed in human lung tissue to characterise the αvβ6 integrin could also be expanded into other organs and disease states including and beyond fibrosis e.g. cancer. As more suitable selective tool molecules become available the other RGD integrins could also be started to be investigated in human tissue, and these studies could not only focus on binding interactions but functional inhibition to stand alongside the αvβ6 binding data already generated.

CHAPTER 7: REFERENCES

Abe M, Harpel JG, Metz CN, Nunes I, Loskutoff DJ and Rifkin DB (1994) An assay for transforming growth factor-β using cells transfected with a plasminogen activator inhibitor-1 promotor-luciferase construct *Anal Biochem* **216**: 276-284.

Adcock IM and Lane SJ (2003) Corticosteroid-insensitive asthma: molecular mechanisms *J Endocrinol* **178**: 347-355.

Agrez MV, Bates RC, Mitchell D, Wilson N, Ferguson N, Anseline and Sheppard D (1996) Multiplicity of fibronectin-binding αv integrin receptors in colorectal cancer *Br J Cancer* **73**: 887-892.

Ajram L, Begg M, Slack R, Cryan J, Hall D, Hodgson S, Ford A, Barnes A, Swieboda D, Mousnier A and Solari R (2014) Internalization of the chemokine receptor CCR4 can be evoked by orthosteric and allosteric receptor antagonists *Eur J Pharmacol* **729**: 75-85.

Akhurst RJ and Hata A (2012) Targeting the TGFβ signalling pathway in disease *Nat Rev Drug Discov* **11**: 790-811.

Allen JT, Knight RA, Bloor CA and Spiteri MA (1999) Enhanced insulin-like growth factor binding protein-related protein 2 (connective tissue growth factor) expression in patients with idiopathic pulmonary fibrosis and pulmonary sarcoidosis *Am J Respir Cell Mol Biol* **21**: 693-700.

Anderson, NA (2014) The design, synthesis and optimisation of αvβ6 antagonists as potential idiopathic pulmonary fibrosis agents. *PhD thesis* University of Sthrathclyde, Glasgow.

Anderton MJ, Mellor HR, Bell A, Sadler C, Pass M, Powell S, Steele SJ, Roberts RR and Heier A (2011) Induction of heart valve lesions by small-molecule ALK5 inhibitors *Toxicol Pathol* **39**: 916-924.

Araya J, Cambier S, Markovics JA, Wolters P, Jablons D, Hill A, Finbeiner W, Jones K, Courtney Broaddus V, Sheppard D, Barzcak A, Xiao Y, Erle DJ and Nishimura SL (2007) Squamous metaplasia amplifies pathologic epithelial-mesenchymal interactions in COPD patients *J Clin Invest* **117**: 3551-3562.

Ashburn TT and Thor KB (2004) Drug repositioning: Identifying and developing new uses for existing drugs *Nat Rev* **3**: 673-683.

Bandyopadhyay A and Raghavan S (2009) Defining the role of integrin αvβ6 in cancer *Curr Drug Targets* **10**: 654-652.

Barry ST, Ludbrook SB, Murrison E and Horgan CMT (2000) A regulated α5β1 integrin and osteopontin *Biochem Biophys Res Commun* **267**: 764-769.

Barry-Hamilton V, Spangler R, Marshall D, McCauley S, Rodriguez HM, Oyasu M, Mikels A, Vaysberg M, Ghermazien H, Wai C, Garcia CA, Velayo AC, Jorgensen B, Biermann D, Tsai D, Green J, Zaffryar-Eilot S, Holzer A, Ogg S, Thai D, Neufeld G, Van Vlasselaer P and Smith V (2010) Allosteric inhibition of lysyl oxidase-like-2 impedes the development of a pathologic microenvironment *Nat Med* **16**: 1009-1017.

Baumgartner KB, Samet JM, Stidley CA, Colby TV, Waldron JA and collaborating centers (2007) Cigarette smoking: A risk factor for idiopathic pulmonary fibrosis *Am J Respir Crit Care Med* **155**: 242-248.

Bazzoni G and Hemler ME (1998) Are changes in integrin affinity and conformation overemphasized? *Trends Biochem Sci* **23**: 30-34.

Ben-Chetrit E, Bergmann S and Sood R (2006) Mechanism of the anti-inflammatory effect of colchicine in rheumatic diseases: a possible new outlook through microarray analysis *Rheumatology* **45**: 274-282.

Bonnans C, Chou J and Werb Z (2014) Remodelling the extracellular matrix in development and disease *Nat Rev Mol Cell Biol* **15**: 786-801.

Bonniaud P, Margetts PJ, Kolb M, Schroeder JA, Kapoun AM, Damm D, Murphy A, Chakravarty S, Dugar S, Higgins L, Potter AA and Gauldie J (2005) Progressive transforming growth factor β1-induced lung fibrosis is blocked by an orally active ALK5 kinase inhibitor *Am J Respir Crit Care Med* **171**: 889-898.

Borowski A, Kuepper M, Horn U, Knupfer U, Zissel G, Hohne K, Luttmann W, Krause S, Virchow JC and Friedrich K (2008) Interleukin-13 acts as an apoptotic effector on lung epithelial cells and induces pro-fibrotic gene expression in lung fibroblasts *Clin Exp Allergy* **38**: 619-628.

Breuss JM, Gallo J, DeLisser HM, Klimamskaya IV, Folkesson HG, Pittet JF, Nishimura SL, Aldape K, Landers DV, Carpenter W, Gillett N, Sheppard D, Matthay MA, Albelda SM, Kramer RH and Pytela R (1995) Expression of the β6 subunit in development, neoplasia and tissue repair suggests a role in epithelial remodeling *J Cell Sci* **108**: 2241-2251.

Busk M, Pytela R and Sheppard D (1992) Characterization of the integrin αvβ6 as a Fibronectin-binding protein *J Biol Chem* **267**: 5790-5796.

Calderwood DA, Campbell ID and Critchley DR (2013) Talins and kindlins: partners in integrin-mediated adhesion *Nat Rev Mol Cell Biol* **14**: 503-517.

Cara CJ, Pena AS, Sans M, Rodrigo L, Guerrero-Esteo M, Hinojosa J, García-Paredes J and Guijarro LG (2004) Reviewing the mechanism of action of thiopurine drugs: towards a new paradigm in clinical practice *Med Sci Monit* **10**: RA247-254.

Caraci F, Gili E, Calafiore M, Failla M, La Rosa C, Crimi N, Sortino MA, Nicoletti F, Copani A and Vancheri C (2008) TGF-β1 targets the GSK-3β/βeta-catenin pathway via ERK activation in the transition of human lung fibroblasts into myofibroblasts *Pharmacol Res* **57**: 274-282.

Carron CP, Meyer DM, Pegg JA, Engleman VW, Nickols MA, Settle SL, Westlin WF, Ruminski PG and Nickols GA (1998) A peptidomimetic antagonist of the integrin αvβ3 inhibits leydig cell tumor growth and the development of hypercalcemia of malignancy *Cancer Res.* **58**: 1930-1935.

Carter CM, Leighton-Davies JR and Charlton SJ (2007) Miniaturized receptor binding assays: complications arising from ligand depletion *J Biomol Screen* **12**: 255-266.

Castelino FV and Varga J (2010) Interstitial lung disease in connective tissue diseases: evolving concepts of pathogenesis and management *Arthritis Res Ther* **12**: 213.

Chambers RC, Leoni P, Kaminski N, Laurent GJ and Heller RA (2003) Global expression profiling of fibroblast responses to transforming growth factor-β1

reveals the induction of inhibitor of differentiation-1 and provides evidence of smooth muscle cell phenotypic switching *Am J Pathol* **162**: 533-546.

Chames P, Van Regenmortel M, Weiss E and Baty D (2009) Therapeutic antibodies: successes, limitations and hopes for the future *Br J Pharmacol* **157**: 220-233.

Chaudhary NI, Roth GJ, Hilberg F, Müller-Quernheim J, Prasse A, Zissel G, Schnapp A and Park JE (2007) Inhibition of PDGF, VEGF and FGF signalling attenuates fibrosis *Eur Respir J* **29**: 976-985.

Cheifetz S, Weatherbee JA, Tsang ML, Anderson JK, Mole JE, Lucas R and Massagué J (1987) The transforming growth factor-β system, a complex pattern of cross-reactive ligands and receptors *Cell* **48**: 409-415.

Chen J, Salas A and Springer TA (2003) Bistable regulation of integrin adhesiveness by a bipolar metal ion cluster *Nat Struct Biol* **10**: 995-1001.

Cheng Y and Prusoff WH (1973) Relationship between the inhibition constant (K_I) and the concentration of inhibitor which causes 50 per cent inhibition (I_{50}) of an enzymatic reaction *Biochem Pharmacol* **22**: 3099-3108.

Christopoulos A and Kenakin T (2002) G protein-coupled receptor allosterism and complexing *Pharm Rev* **54**: 323-374.

ClinicalTrials.gov, STX-100 in Patients With Idiopathic Pulmonary Fibrosis (IPF) [Online] Available from https://clinicaltrial.gov/ct2/show/NCT01371305. [Accessed: 2nd June 2015].

Clozel M and Salloukh H (2005) Role of endothelin in fibrosis and anti-fibrotic potential of bosentan *Ann Med* **37**: 2-12.

Coker RK, Laurent GJ, Shahzeidi S, Lympany PA, du Bois RM, Jeffrey PK and McAnulty RJ (1997) Transforming growth factors-β1, -β2 and -β3 stimulate fibroblast procollagen production *in vitro* but are differentially expressed during bleomycin-induced lung fibrosis *Am J Pathol* **150**: 981-991.

Coon DR, Roberts DJ, Loscertales M and Kradin R (2006) Differential epithelial expression of *SHH* and *FOXF1* in usual and non-specific interstitial pneumonia *Exp Mol Pathol* **80**: 119-123.

Copeland RA, Pompliano DL and Meek TD (2006) Drug-target residence time and its implication for lead optimization *Nat Rev Drug Discov* **5**: 730-739.

Costabel U (2015) The changing treatment landscape in idiopathic pulmonary fibrosis *Eur Respir Rev* **24**: 65-68.

Cox D, Brennan M and Moran N (2010) Integrins as therapeutic targets: lessons and opportunities *Nat Rev Drug Discov* **9**: 804-820.

Crosby LM and Waters CM (2010) Epithelial repair mechanisms in the lung *Am J Physiol Lung Cell Mol Physiol* **298**: L715-L731.

Datta A, Scotton CJ and Chambers RC (2011) Novel therapeutic approaches for pulmonary fibrosis *Br J Pharmacol* **163**: 141-172.

Davis-Dusenbury BN and Hata A (2011) Smad-mediated miRNA processing: a critical role for a conserved RNA sequence *RNA Biol* **8**:71-76.

Derynck R, Akhurst RJ and Balmain A (2001) TGFβ signaling in tumor suppression and cancer progression *Nat Genet* **29**: 117-129.

DiCara D, Burman A, Clark S, Berryman S, Howard MJ, Hart IR, Marshall JF and Jackson T (2008) Foot-and-mouth disease virus forms a highly stable, EDTA-resistant complex with its principal receptor, integrin αvβ6: Implications for infectiousness *J Virol* **82**: 1537-1546.

DiCara D, Rapisarda C, Sutcliffe JL, Violette SM, Weinreb PH, Hart IR, Howard MJ and Marshall JF (2007) Structure-function analysis of Arg-Gly-Asp helix motifs in αvβ6 integrin ligands *J Biol Chem* **282**: 9657-9665.

Dong X, Hudson NE, Lu C and Springer TA (2014) Structural determinants of integrin β-subunit specificity for latent TGF-β *Nat Struct Mol Biol* **21**: 1091-1096.

Dong X, Mi LZ, Zhu J, Wang W, Hu P, Luo BH and Springer TA (2012) αvβ3 integrin crystal structures and their functional implications *Biochemistry* **51**: 8814-8828.

dos Santos T, Varela J, Lynch I, Salvati A and Dawson KA (2011) Effects of transport inhibitors on the cellular uptake of carboxylated polystyrene nanoparticles in different cell lines PLoS One **6**: e24438.

Dowling MR and Charlton SJ (2006) Quantifying the association and dissociation rates of unlabelled antagonists at the muscarinic M3 receptor *Br J Pharmacol* **148**: 927-937.

Dozynkiewicz MA, Jamieson NB, Macpherson I, Grindlay J, van den Berghe PV, von Thun A, Morton JP, Gourley C, Timpson P, Nixon C, McKay CJ, Carter R, Strachan D, Anderson K, Sansom OJ, Caswell PT and Norman JC (2012) Rab25 and CLIC3 collaborate to promote integrin recycling from late endosomes/lysosomes and drive cancer progression *Dev Cell*.**22**: 131-145.

Dunmore BJ, Drake KM, Upton PD, Toshner MR, Aldred MA and Morrell NW (2013) The lysosomal inhibitor, chloroquine, increases cell surface BMPR-II levels and restores BMP9 signalling in endothelial cells harbouring BMPR-II mutations *Hum Mol Genet* **22**: 3667-3679.

Eberlein C, Kendrew J, McDaid K, Alfred A, Kang JS, Jacobs VN, Ross SJ, Rooney C, Smith NR, Rinkenberger J, Cao A, Churchman A, Marshall JF, Weir HM, Bedian V, Blakey DC, Foltz IN and Barry ST (2012) A human monoclonal antibody 264RAD targeting αvβ6 integrin reduces tumour growth and metastasis, and modulates key biomarkers *in vivo Oncogene* **32**: 4406-4416.

Egger LA, Cao J, McCallum C, Kidambi U, Van Riper G, McCauley E, Mumford RA, Lanza TJ, Lin LS, de Laszlo SE, Young DN, Yang G, Dean DC, Raab CE, Wallace MA, Jones AN, Hagmann WK, Schmidt JA, Pepinsky RB, Scott DM, Lee WC, Cornebise MA and Detmers PA (2003) A small molecule α4β1/α4β7 antagonist differentiates between the low-affinity states of α4β1 and α4β7: characterization of divalent cation dependence *J Pharmacol Exp Ther* **306**: 903-913.

Eliceiri BP and Cheresh DA (1998) The role of αv integrins during angiogenesis *Mol Med* **4**: 741-750.

Faull RJ and Ginsberg MK (1996) Inside-out signaling through integrins *J Am Soc Nephrol* **7**: 1091-1097.

Fermini B and Fossa AA (2003) The impact of drug-induced QT interval prolongation on drug discovery and development *Nat Rev Drug Discov* **2**: 439-447.

Fernandez IE and Eickelberg O (2012) The impact of TGFβ on lung fibrosis: From targeting to biomarkers *Proc Am Thorac Soc* **9**: 111-116.

Flego M, Ascione A, Cianfriglia M and Vella S (2013) Clinical development of monoclonal antibody-based drugs in HIV and HCV diseases *BMC Med* **11**: 4.

Fontana L, Chen Y, Prijatelj P, Sakai T, Fässler R, Sakai LY and Rifkin DB (2005) Fibronectin is required for integrin αvβ6-mediated activation of latent TGFβ complexes containing LTBP-1 *FASEB J* **19**:1798-1808.

Francis G, Kerem Z, Makkar HP and Becker K (2002) The biological action of saponins in animal systems: a review *Br J Nutr* **88**: 587-605.

Friedlander M, Brooks PC, Shaffer RW, Kincaid CM, Varner JA and Cheresh DA (1995) Definition of two angiogenic pathways by distinct αv integrins *Science* **270**: 1500-1502.

Gan Y, Herzog EL and Gomer RH (2011) Pirfenidone treatment of idiopathic pulmonary fibrosis *Ther Clin Risk Manag* **7**: 39-47.

Gilbert MR, Kuhn J, Lamborn KR, Lieberman F, Wen PY, Mehta M, Cloughesy T, Lassman AB, Deangelis LM, Chang S and Prados M (2012) Cilengitide in

patients with recurrent glioblastoma: the results of NABTC 03-02, a phase II trial with measures of treatment delivery *J Neurooncol* **106**: 147-153.

Goffe B and Cather JC (2003) Etanercept: An overview *J Am Acad Dermatol* **49**: S105-11.

Goodman SL and Picard M (2012) Integrins as therapeutic targets *Trends Pharmacol Sci* **33**: 405-412.

Goodman SL, Hölzemann G, Sulyok GAG and Kessler H (2002) Nanomolar small molecule inhibitors for αvβ6, αvβ5, and αvβ3 integrins *J Med Chem* **45**: 1045-1051.

Goodwin A and Jenkins G (2009) Role of integrin-mediated TGFβ activation in the pathogenesis of pulmonary fibrosis *Biochem Soc Trans* **37**: 849-854.

Gossard AA and Lindor KD (2011) Current therapies for non-alcoholic fatty liver disease *Drugs of Today* **47**: 915-922.

Grimwood S and Hartig PR (2009) Target site occupancy: emerging generalizations from clinical and preclinical studies *Pharmacol Ther* **122**: 281-301.

Grygielko ET, Martin WM, Tweed C, Thornton P, Harling J, Brooks DP and Laping NJ (2005) Inhibition of gene markers of fibrosis with a novel inhibitor of transforming growth factor-β type I receptor kinase in puromycin-induced nephritis *J Pharmacol Exp Ther* **313**: 943-51.

Guo XG and Wang X (2009) Signaling cross-talk between TGFβ/BMP and other pathways *Cell Res* **19**: 71-88.

Hagimoto N, Kuwano K, Inoshima I, Yoshimi M, Nakamura N, Fujita M, Maeyama T and Hara N (2002) TGFβ1 as an enhancer of Fas-mediated apoptosis of lung epithelial cells *J Immunol* **168**: 6470-6478.

Hancock A, Armstrong L, Gama R and Millar R (1998) Production of interleukin 13 by alveolar macrophages from normal and fibrotic lung *Am J Respir Cell Mol Biol* **18**: 60-65.

Harling JD, Deakin AM, Campos S, Grimley R, Chaudry L, Nye C, Polyakova O, Bessant CM, Barton N, Somers D, Barrett J, Graves RH, Hanns L, Kerr WJ and Solari R (2013) Discovery of novel irreversible inhibitors of interleukin (IL)-2-inducible tyrosine kinase (Itk) by targeting cysteine 442 in the ATP pocket *J Biol Chem* **288**: 28195-28206.

Hausner SH, Abbey CK, Bold RJ, Gagnon MK, Marik J, Marshall JF, Stanecki CE and Sutcliffe JL (2009) Targeted *in vivo* imaging of integrin αvβ6 with an improved radiotracer and its relevance in a pancreatic tumor model *Cancer Res* **69**: 5843-5850.

Hausner SH, DiCara D, Marik J, Marshall JF and Sutcliffe JL (2007) Use of a peptide derived from foot-and-mouth disease virus for the noninvasive imaging of human cancer: generation and evaluation of 4-[^{18}F]Fluorobenzoyl A20FMDV2 for *in vivo* imaging of αvβ6 integrin expression with positron emission tomography *Cancer Res* **67**: 7833-7840.

Heidenreich A, Rawal SK, Szkarlat K, Bogdanova N, Dirix L, Stenzl A, Welslau M, Wang G, Dawkins F, de Boer CJ and Schrijvers D (2013) A randomized, double-blind, multicenter, phase 2 study of a human monoclonal antibody to human αv integrins (intetumumab) in combination with docetaxel and prednisone for the first-line treatment of patients with metastatic castration-resistant prostate cancer *Ann Oncol* **24**: 329-336.

Heijerman H, Westerman E, Conway S, Touw D and Döring G (2009) Inhaled medication and inhalation devices for lung disease in patients with cystic fibrosis: A European consensus *J Cyst Fibros* **8**: 295-315.

Henderson NC and Sheppard D (2013) Integrin-mediated regulation of TGFβ in fibrosis *Biochim Biophys Acta* **1832**: 891-896.

Henderson NC, Arnold TD, Katamura Y, Giacomini MM, Rodriguez JD, McCarty JH, Pellicoro A, Raschperger E, Betsholtz C, Ruminski PG, Griggs DW, Prinsen MJ, Maher JJ, Iredale JP, Lacy-Hulbert A, Adams RH and Sheppard D (2013) Targeting of αv integrin identifies a core molecular pathway that regulates fibrosis in several organs *Nat Med* **19**: 1617-1624.

Higashiyama H, Yoshimoto D, Kaise T, Matsubara S, Fujiwara M, Kikkawa H, Asano S and Kinoshita M (2007) Inhibition of activin receptor-like kinase 5 attenuates Bleomycin-induced pulmonary fibrosis *Exp Mol Pathol* **83**: 39-46.

Hill AV (1909) The mode of action of nicotine and curari, determined by the form of the contraction curve and the method of temperature coefficients *J Physiol* **39**: 361-373.

Ho S, Clipstone N, Timmermann L, Northrop J, Graef I, Fiorentino D, Nourse J and Crabtree GR (1996) The mechanism of action of cyclosporin A and FK506 *Clin Immunol Immunopathol* **80**: S40-5.

Horan GS, Wood S, Ona V, Jun Li D, Lukashev ME, Weinreb PH, Simon KJ, Hahm K, Allaire NE, Rinaldi NJ, Goyal J, Feghali-Bostwick CA, Matteson EL, O'Hara C, Lafyatis R, Davis GS, Huang X, Sheppard D and Violette S (2008) Partial inhibition of integrin prevents pulmonary fibrosis without exacerbating inflammation *Am J Respir Crit Care Med* **177**: 56-65.

Horowitz JC, Lee DY, Waghray M, Keshamouni VG, Thomas PE, Zhang H, Cui Z and Thannickal VJ (2004) Activation of the pro-survival phosphatidylinositol 3-kinase/AKT pathway by transforming growth factor-β1 in mesenchymal cells is mediated by p38 MAPK-dependent induction of an autocrine growth factor *J Biol Chem* **279**: 1359-1367.

Howell DC, Johns RH, Lasky JA, Shan B, Scotton CJ, Laurent GJ and Chambers RC (2005) Absence of proteinase-activated receptor-1 signaling affords protection from bleomycin-induced lung inflammation and fibrosis *Am J Pathol* **166**: 1353-1365.

Hoyt DG and Lazo JS (1988) Alterations in pulmonary mRNA encoding procollagens, fibronectin and transforming growth factor-β precede bleomycin-induced pulmonary fibrosis in mice *J Pharmacol Exp Ther* **246**: 765-771.

Hu Y, Peng J, Feng D, Chu L, Li X, Jin Z, Lin Z and Zeng Q (2006) Role of extracellular signal-regulated kinase, p38 kinase, and activator protein-1 in

transforming growth factor-β1-induced alpha smooth muscle actin expression in human fetal lung fibroblasts *in vitro Lung* **184**: 33-42.

Huang XW, Wu JF, Cass D, Erle DJ, Corry D, Young SG, Farese RV and Sheppard D (1996) Inactivation of the integrin β6 subunit gene reveals a role of epithelial integrins in regulating inflammation in the lungs and skin *J Cell Biol* **133**: 921-928.

Huang XW, Wang JY, Li F, Song ZJ, Xie C and Lu WY (2010) Biochemical characterization of the binding of cyclic RGDyK to hepatic stellate cells *Biochem Pharmacol* **80**:136-143.

Hulme EC and Birdsall NJM (1992) Strategy and tactics in receptor-binding studies, in *Receptor-Ligand Interactions. A Practical Approach* (Hulme EC ed) pp 63-176, Oxford University Press, Oxford.

Hulme EC and Trevethick MA (2010) Ligand binding assays at equilibrium: validation and interpretation *Br J Pharmacol* **161**: 1219-1237.

Hynes RO (1987) Intergins: A family of cell surface receptors *Cell* **48**: 549-554.

Hynes RO (2002) Integrins: Bidirectional, allosteric signaling machines *Cell* **110**: 673-687.

Inagaki Y, Truter S, Bou-Gharios G, Garrett LA, de Crombrugghe B, Nemoto T and Greenwel P (1998) Activation of Proα2(I) collagen promoter during hepatic fibrogenesis in transgenic mice *Biochem Biophys Res Commun* **250**: 606-611.

Ivanov AI (2008) Pharmacological inhibition of endocytic pathways: is it specific enough to be useful? *Methods Mol Biol* **440**: 15-33.

Jenkins G, Blanchard A, Borok Z, Bradding P, Ehrhardt C, Fisher A, Hirani N, Johnson S, Königshoff M, Maher TM, Millar A, Parfrey H, Scotton C, Tetley T, Thickett D and Wolters P (2011) In search of the fibrotic epithelial cell: opportunities for a collaborative network *Thorax* **67**: 179-182.

Jenkins RG, Simpson JK, Saini G, Bentley JH, Russell AM, Braybrooke R, Molyneaux PL, McKeever TM, Wells AU, Flynn A, Hubbard RB, Leeming DJ, Marshall RP, Karsdal MA, Lukey PT and Maher TM (2015) Longitudinal change in collagen degradation biomarkers in idiopathic pulmonary fibrosis: an analysis from the prospective, multicentre PROFILE study *Lancet Respir Med* **3**: 462-472.

Jiang C, Huang H, Liu J, Wang Y, Lu Z and Xu Z (2012) Adverse events of pirfenidone for the treatment of pulmonary fibrosis: a meta-analysis of randomized controlled trials *PLoS One* **7**: e47024.

Kaartinen V, Voncken JW, Shuler C, Warburton D, Bu D, Heisterkamp N and Groffen J (1995) Abnormal lung development and cleft palate in mice lacking TGFβ3 indicates defects of epithelial-mesenchymal interaction *Nat Genet* **11**: 415-421.

Khalil N, O'Connor RN, Flanders KC and Unruh H (1996) TGFβ1, but not TGFβ2 or TGFβ3, is differentially present in epithelial cells in advanced

pulmonary fibrosis: An immunohistochemical study *Am J Respir Cell Mol Biol* **14**: 131-138.

Kim KK, Kugler MC, Wolters PJ, Robillard L, Galvez MG, Brumwell AN, Sheppard D and Chapman HA (2006) Alveolar epithelial cell mesenchymal transition develops *in vivo* during pulmonary fibrosis and is regulated by the extracellular matrix *Prot Natl Acad Sci* **103**: 13180-13185.

King TE Jr, Bradford WZ, Castro-Bernardini S, Fagan EA, Glaspole I, Glassberg MK, Gorina E, Hopkins PM, Kardatzke D, Lancaster L, Lederer DJ, Nathan SD, Pereira CA, Sahn SA, Sussman R, Swigris JJ and Noble PW (2014) A phase 3 trial of pirfenidone in patients with idiopathic pulmonary fibrosis *N Engl J Med* **370**: 2083-2092.

King TE, Pardo A and Selman M (2011) Idiopathic pulmonary fibrosis *Lancet* **378**: 1949-1961.

Kliment CR, Englert JM, Crum LP and Oury TD (2011) A novel method for accurate collagen and biochemical assessment of pulmonary tissue utilizing one animal *Int J Clin Exp Pathol* **4**: 349-355.

Koli K, Myllarniemi M, Keski-Oja J and Kinnula VL (2008) Transforming growth factor-β activation in the lung: Focus on fibrosis and reactive oxygen species *Antioxid Redox Signal* **10**: 333-342.

Königshoff M, Balsara N, Pfaff E. Kramer M, Chrobak I, Seeger W and Eickelberg O (2009) Functional Wnt signaling is increased in idiopathic pulmonary fibrosis *PLoS ONE* **3**: E2142.

Kottmann RM, Kulkarni AA, Smolnycki KA, Lyda E, Dahanayake T, Salibi R, Honnons S, Jones C, Isern NG, Hu JZ, Nathan SD, Grant G, Phipps RP and Sime PJ (2012) Lactic acid is elevated in idiopathic pulmonary fibrosis and induces myofibroblast differentiation via pH-dependent activation of transforming growth factor-β *Am J Respir Crit Care Med* **186**: 740-751.

Kubiczkova L, Sedlarikova L, Hajek R and Sevcikova S (2012) TGF-β - an excellent servant but a bad master *J Transl Med* **3**: 183.

Kumar CC, Nie H, Rogers CP, Malkowski M, Maxwell E, Catino JJ and Armstrong L (1997) Biochemical characterization of the binding of echistatin to integrin αvβ3 receptor *J Pharmacol Exp Ther* **283**: 843-853.

Lau TL, Kim C, Ginsberg MH and Ulmer TS (2009) The structure of the integrin αIIbβ3 transmembrane complex explains integrin transmembrane signalling *EMBO J* **28**: 1351-1361.

Lee JO, Bankston LA, Arnaout MA and Liddington RC (1995) Two conformations of the integrin A-domain (I-domain): a pathway for activation? *Structure* **3**: 1333-1340.

Livak KJ and Schmittgen TD (2001) Analysis of relative gene expression data using real-time quantitative PCR and the $2^{-\Delta\Delta C}{}_T$ method *Methods* **25**: 402-408.

Logan D, Abu-Ghazaleh R, Blakemore W, Curry S, Jackson T, King A, Lea S, Lewis R, Newman J, Parry N, Rowlands D, Stuart D and Fry E (1993) Structure of a major immunogenic site on foot-and-mouth disease virus *Nature* **362**: 566-568.

Long MJ, Gollapalli DR and Hedstrom L (2012) Inhibitor mediated protein degradation *Chem Biol* **19**: 629-37.

Lozzio CB and Lozzio BB (1975) Human chronic myelogenous leukemia cell-line with positive Philadelphia chromosome *Blood* **45**: 321-334.

Ludbrook SB, Barry ST, Delves CJ and Horgan CM (2003) The integrin αvβ3 is a receptor for the latency-associated peptides of transforming growth factors β1 and β3 *Biochem J* **369**: 311-318.

Luo BH, Carman CV and Springer TA (2007) Structural basis of integrin regulation and signaling *Annu Rev Immunol* **25**: 619-647.

Lyons RM, Keski-Oja J and Moses HL (1988) Proteolytic activation of latent transforming growth factor-β from fibroblast-conditioned medium *J Cell Biol* **106**: 1659-1665.

Mardon HJ and Grant KE (1994) The role of the ninth and tenth type III domains of human fibronectin in cell adhesion *FEBS Lett* **340**: 197-201.

Margadant C and Sonnenberg A (2010) Integrin-TGFβ crosstalk in fibrosis, cancer and wound healing *EMBO Rep* **11**: 97-105.

Mariani M, Lang R, Binda E, Panina-Bordignon P and D'Ambrosio D (2004) Dominance of CCL22 over CCL17 in induction of chemokine receptor CCR4 desensitization and internalization on human Th2 cells *Eur J Immunol* **34**: 231-240.

Marques MRC, Loebenberg R and Almukainzi M (2011) Simulated biological fluids with possible application in dissolution testing *Dissolution Technologies* **18**: 15-29.

Meltzer EB and Noble PW (2008) Idiopathic pulmonary fibrosis *Orphanet J Rare Dis* **3**: 8.

Millan FA, Denhez F, Kondaiah P and Akhurst RJ (1991) Embryonic gene expression patterns of TGF β1, β2 and β3 suggest different developmental functions *in vivo Development* **111**: 131-143.

Minagawa S, Lou J, Seed RI, Cormier A, Wu S, Cheng Y, Murray L, Tsui P, Connor J, Herbst R, Govaerts C, Barker T, Cambier S, Yanagisawa H, Goodsell A, Hashimoto M, Brand OJ, Cheng R, Ma R, McKnelly KJ, Wen W, Hill A, Jablons D, Wolters P, Kitamura H, Araya J, Barczak AJ, Erle DJ, Reichardt LF, Marks JD, Baron JL and Nishimura SL (2014) Selective targeting of TGF-β activation to treat fibroinflammatory airway disease *Sci Transl Med* **6**: 1-14.

Mittl PR, Priestle JP, Cox DA, McMaster G, Cerletti N and Grütter MG (1996) The crystal structure of TGF-β3 and comparison to TGF-β2: implications for receptor binding *Protein Sci* **5**: 1261-1271.

Mobley AK, Tchaicha JH, Shin J, Hossain MG and McCarty JH (2009) β8 integrin regulates neurogenesis and neurovascular homeostasis in the adult brain *J Cell Sci* **122**: 1842-1851.

Molina-Molina M, Vicens V and Estany S (2010) New aspects of idiopathic pulmonary fibrosis *Clin Pulm Med* **17**: 170-176.

Molina-Molina M, Xaubet A, Li X, Abdul-Hafez A, Friderici K, Jernigan K, Fu W, Ding Q, Pereda J, Serrano-Mollar A, Casanova A, Rodriguez-Becerra E, Morell F, Anchochea J, Picado C and Uhal BD (2008) Angiotensinogen gene G-6A polymorphism influences idiopathic pulmonary fibrosis disease progression *Eur Respir J* **32**: 1004-1008.

Monaghan P, Gold S, Simpson J, Zhang Z, Weinreb PH, Violette SM, Alexandersen S and Jackson T (2005) The αvβ6 integrin receptor for Foot-and-mouth disease virus is expressed constitutively on the epithelial cells targeted in cattle *J Gen Virol* **86**: 2769-80.

Morris DG, Huang X, Kaminski N, Wang Y, Shapiro SD, Dolganov G, Glick A and Sheppard D (2003) Loss of integrin αvβ6-mediated TGFβ activation causes Mmp12-dependent emphysema *Nature* **422**: 169-173.

Motulsky H and Christopoulos A (2004) "Fitting Models to Biological Data using Linear and Nonlinear Regression: A Practical Guide to Curve Fitting" Oxford University Press, New York, ISBN: 0195171802.

Mould AP (1996) Getting integrins into shape: recent insights into how integrin activity is regulated by conformational changes *J Cell Sci* **109**: 2613-2618.

Munger JS, Harpel JG, Gleizes P, Mazzieri R, Nunes I and Rifkin DB (1997) Latent transforming growth factor-β: Structural features and mechanisms of activation *Kidney Int* **51**: 1376-1382.

Munger JS, Huang X, Kawakatsu H, Griffiths MJD, Dalton SL, Wu J, Pittet J, Kaminski N, Garat C, Matthay MA, Rifkin DB and Sheppard D (1999) The

integrin αvβ6 and activates latent TGFβ1: a mechanism for regulating pulmonary inflammation and fibrosis *Cell* **96**: 319-328.

National Heart Lung and Blood Institute (NIH), How the Lung Works [Online] Available from http://www.nhlbi.nih.gov/health/health-topics/topics/ipf/lungworks [Accessed: 2nd June 2015].

Navaratnam V, Fleming KM, West J, Smith CJP, Jenkins RG, Fogarty A and Hubbard RB (2011) The rising incidence of idiopathic pulmonary fibrosis in the UK *Thorax* **66**: 462-467.

Neff S, Sá-Carvalho D, Rieder E, Mason PW, Blystone SD, Brown EJ and Baxt B (1998) Foot-and-mouth disease virus virulent for cattle utilizes the integrin αvβ3 as its receptor *J Virol* **72**: 3587-94.

Noth I and Martinez FJ (2007) Recent advances in idiopathic pulmonary fibrosis *Chest* **132**: 637-650.

O'Connell OJ, Kennedy MP and Henry MT (2011) Idiopathic pulmonary fibrosis: Treatment update *Adv Ther* **28**: 986-999.

Patsenker E, Popov Y, Stickel F, Schneider V, Ledermann M, Sägesser H, Niedobitek G, Goodman SL and Schuppan D (2009) Pharmacological inhibition of integrin αvβ3 aggravates experimental liver fibrosis and suppresses hepatic angiogenesis *Hepatology* **50**: 1501-1511.

Plow EF, Haas TA, Zhang L, Loftus J and Smith JW (2000) Ligand binding to integrins *J Biol Chem* **275**: 21785-8.

Popov Y, Patsenker E, Stickel F, Zaks J, Ramakrishnan Bhaskar K, Niedobitek G, Kolb A, Friess H and Schuppan D (2008) Integrin αvβ6 is a marker of the progression of biliary and portal liver fibrosis and a novel target for antifibrotic therapies *J Hepatol* **48**: 453-464.

Raghow R, Postlethwaite AE, Keski-Oja J, Moses HL and Kang AH (1987) Transforming growth factor-β increases steady state levels of type 1 procollagen and fibronectin messanger RNAs posttranscriptionally in cultured human dermal fibroblasts *J Clin Invest* **79**: 1285-1288.

Raghu G, Collard HR, Egan JJ, Martinez FJ, Behr J, Brown KK, Colby TV, Cordier J, Flaherty KR, Lasky JA, Lynch DA, Ryu JH, Swigris JJ, Wells AU, Ancochea J, Bouros D, Carvalho C, Costabel U, Ebina M, Hansell DM, Johkoh T, Kim DS, King TE, Kondoh Y, Myers J, Muller NL, Nicholson AG, Richeldi L, Selman M, Duffen RF, Griss BS, Protzko SL and Schunemann HJ (2011) An official ATS/ERS/JRS/ALAT statement: Idiopathic pulmonary fibrosis: Evidence-based guidelines for diagnosis and management *Am J Respir Crit Care Med* **183**: 778-824.

Ramos C, Montaño M, García-Alvarez J, Ruiz J, Uhal BD, Selman M and Pardo A (2001) Fibroblasts from idiopathic pulmonary fibrosis and normal lungs differ in growth rate, apoptosis, and tissue inhibitor of metalloproteinases expression *Am J Respir Cell Mol Biol* **24**: 591-598.

Ramsay AG, Keppler MD, Jazayeri M, Thomas GJ, Parsons M, Violette S, Weinreb P, Hart IR and Marshall JF (2007) HS1-associated protein X-1 regulates

carcinoma cell migration and invasion via clathrin-mediated endocytosis of integrin αvβ6 *Cancer Res* **67**: 5275-5284.

Rau JL (2005) The inhalation of drugs: advantages and problems *Respir Care* **50**: 367-382.

Reed NI, Jo H, Chen C, Tsujino K, Arnold TD, DeGrado WF and Sheppard D (2015) The αvβ1 integrin plays a critical *in vivo* role in tissue fibrosis *Sci Transl Med* **7**: 1-8.

Richeldi L, Costabel U, Selman M, Kim DS, Hansell DM, Nicholson AG, Brown KK, Flaherty KR, Noble PW, Raghu G, Brun M, Gupta A, Juhel N, Klüglich M and du Bois RM (2011) Efficacy of a tyrosine kinase inhibitor in idiopathic pulmonary fibrosis *N Engl J Med* **365**: 1079-1087.

Richeldi L, du Bois RM, Raghu G, Azuma A, Brown KK, Costabel U, Cottin V, Flaherty KR, Hansell DM, Inoue Y, Kim DS, Kolb M, Nicholson AG, Noble PW, Selman M, Taniguchi H, Brun M, Le Maulf F, Girard M, Stowasser S, Schlenker-Herceg R, Disse B and Collard HR (2014) Efficacy and safety of nintedanib in idiopathic pulmonary fibrosis *N Engl J Med* **370**: 2071-2082.

Roth GJ, Binder R, Colbatzky F, Dallinger C, Schlenker-Herceg R, Hilberg F, Wollin SL and Kaiser R (2015) Nintedanib: from discovery to the clinic *J Med Chem* **58**: 1053-1063.

Ruoslahti E (1996) RGD and other recognition sequences for integrins *Annu Rev Cell Dev Biol* **12**: 697-715.

Saha A, Ellison D, Thomas GJ, Vallath S, Mather SJ, Hart IR and Marshall JF (2010) High-resolution *in vivo* imaging of breast cancer by targeting the pro-invasive integrin αvβ6 *J Pathol* **222**: 52-63.

Saini G, Porte J, Weinreb PH, Violette SM, Wallace WA, McKeever TM and Jenkins G (2015) αvβ6 integrin may be a potential prognostic biomarker in interstitial lung disease *Eur Respir J* **46**: 486–494.

Sanford LP, Ormsby I, Gittenberger-de Groot AC, Sariola H, Friedman R, Boivin GP, Cardell EL and Doetschman T (1997) TGFβ2 knockout mice have multiple developmental defects that are non-overlapping with other TGFβ knockout phenotypes *Development* **124**: 2659-2670.

Sarrazy V, Koehler A, Chow ML, Zimina E, Li CX, Kato H, Caldarone CA and Hinz B (2014) Integrins αvβ5 and αvβ3 promote latent TGF-β1 activation by human cardiac fibroblast contraction *Cardiovasc Res* **102**:407-417.

Sato T, Iwase M, Miyama M, Komai M, Ohshima E, Asai A, Yano H and Miki I (2013) Internalization of CCR4 and inhibition of chemotaxis by K777, a potent and selective CCR4 antagonist *Pharmacology* **91**: 305-313.

Scatchard G (1949) The attractions of proteins for small molecules and ions *Ann N Y Acad Sci* **51**: 660-672.

Schaefer CJ, Ruhrmund DW, Pan L, Seiwert SD and Kossen K (2011) Antifibrotic activities of pirfenidone in animal models *Eur Respir Rev* **20**: 85-97.

Schroder K, Hertzog PJ, Ravasi T and Hume DA (2004) Interferon-γ: an overview of signals, mechanisms and functions *J Leukoc Biol* **75**: 163-89.

Schultz-Cherry S, Ribeiro S, Gentry L and Murphy-Ullrich JE (1994) Thrombospondin binds and activates the small and large forms of latent transforming growth factor-β in a chemically defined system *J Biol Chem* **269**: 26775-26782.

Scotton CJ and Chambers RC (2010) Bleomycin revisited: towards a more representative model of IPF? *Am J Physiol Lung Cell Mol Physiol* **299**: L439-L441.

Scotton CJ, Krupiczojc MA, Königshoff M, Mercer PF, Lee YC, Kaminski N, Morser J, Post JM, Maher TM, Nicholson AG, Moffatt JD, Laurent GJ, Derian CK, Eickelberg O and Chambers RC (2009) Increased local expression of coagulation factor X contributes to the fibrotic response in human and murine lung injury *J Clin Invest* **119**: 2550-2563.

Selman M, King TE and Pardo A (2001) Idiopathic pulmonary fibrosis: Prevailing and evolving hypotheses its pathogenesis and implications for therapy *Ann Intern Med* **134**: 136-151.

Senoo T, Hattori N, Tanimoto T, Furonaka M, Ishikawa N, Fujitaka K, Haruta Y, Murai H, Yokoyama A and Kohno N (2010) Suppression of plasminogen activator inhibitor-1 by RNA interference attenuates pulmonary fibrosis *Thorax* **65**: 334-340.

Shattil SJ, Kim C and Ginsberg MH (2010) The final steps of integrin activation: the end game *Nat Rev Mol Cell Biol* **11**: 288-300.

Sheppard D (2004) Roles of αv integrins in vascular biology and pulmonary pathology *Curr Opin Cell Biol* **16**: 552-557.

Sheppard D (2008) The role of integrins in pulmonary fibrosis *Eur Respir Rev* **17**: 157-162.

Shi Y and Massagué J (2003) Mechanisms of TGFβ signalling from cell membrane to the nucleus *Cell* **113**: 685-700.

Shull MM, Ormsbury I, Kier AB, Pawlowski S, Diebold RJ, Yin M, Allen R, Sidman C, Proetzel G, Calvin D, Annunziata N and Doetschman T (1992) Targeted disruption of the mouse transforming growth factor-β1 gene results in multifocal inflammatory disease *Nature* **359**: 693-699.

Sipos B, Hahn D, Carceller A, Piulats J, Hedderich J, Kalthoff H, Goodman SL, Kosmahl M and Klöppel G (2004) Immunohistochemical screening for β6-integrin subunit expression in adenocarcinomas using a novel monoclonal antibody reveals strong up-regulation in pancreatic ductal adenocarcinomas *in vivo* and *in vitro Histopathology* **45**: 226-236.

Slack RJ (2014) Evidence for a non-β2-adrenoceptor binding site in human lung tissue for a subset of β2-adrenoceptor agonists *Pharmacology and Pharmacy* **5**: 30-36

Smith PK, Krohn RI, Hermanson GT, Mallia AK, Gartner FH, Provenzano MD, Fujimoto EK, Goeke NM, Olson BJ and Klenk DC (1985) Measurement of protein using bicinchoninic acid *Anal Biochem* **150:** 76-85.

Solomon VR and Lee H (2009) Chloroquine and its analogs: a new promise of an old drug for effective and safe cancer therapies *Eur J Pharmacol* **625**: 220-233.

Sonnylal S, Shi-Wen X, Leoni P, Naff K, Van Pelt CS, Nakamura H, Leask A, Abraham D, Bou-Gharios G and de Crombrugghe B (2010) Selective expression of connective tissue growth factor in fibroblasts *in vivo* promotes systemic tissue fibrosis *Arthritis Rheum* **62**: 1523-1532.

Sorkin A and Von Zastrow M (2002) Signal transduction and endocytosis: close encounters of many kinds *Nat Rev Mol Cell Biol* **3**: 600-614.

Stephens LE, Sutherland AE, Klimanskaya IV, Andrieux A, Meneses J, Pederson RA and Damsky CH (1995) Deletion of integrin β1 integrins in mice results in inner cell mass failure and peri-implantation lethality *Genes Dev* **9**: 1883-1895.

Su G, Atakilit A, Li JT, Wu N, Bhattacharya M, Zhu J, Shieh JE, Li E, Chen R, Sun S, Su CP and Sheppard D (2012) Absence of integrin αvβ3 enhances vascular leak in mice by inhibiting endothelial cortical actin formation *Am J Respir Crit Care Med* **185**: 58-66.

Sun K and Sheppard D (2015) Myofibroblasts are not the major fibroblasts responsible for integrin-dependent TGFβ activation during lung fibrogenesis *in vivo Am J Respir Crit Care Med* **191**: A5331.

Tager AM, LaCamera P, Shea BS, Campanella GS, Selman M, Zhao Z, Polosukhin V, Wain J, Karimi-Shah BA, Kim ND, Hart WK, Pardo A, Blackwell TS, Xu Y, Chun J and Luster AD (2008) The lysophosphatidic acid receptor LPA1 links pulmonary fibrosis to lung injury by mediating fibroblast recruitment and vascular leak *Nat Med* **14**: 45-54.

Taniguchi H, Ebina M, Kondoh Y, Ogura T, Azuma A, Suga M, Taguchi Y, Takahashi H, Nakata K, Sato A, Takeuchi M, Raghu G, Kudoh S and Nukiwa T (2010) Pirfenidone in idiopathic pulmonary fibrosis *Eur Respir J* **35**: 821-829.

Tatler AL and Jenkins G (2012) TGFβ activation and lung fibrosis *Proc Am Thorac Soc* **9**: 130-136.

Tayab ZR and Hochhaus G (2005) Pharmacokinetic/pharmacodynamic evaluation of inhalation drugs: application to targeted pulmonary delivery systems *Expert Opin Drug Deliv* **2**: 519-532.

Tcherakian C, Cottin V, Brillet P, Freynet O, Naggara N, Carton Z, Cordier J, Brauner M, Valeyre D and Nunes H (2011) Progression of idiopathic pulmonary fibrosis: Lessons from asymmetrical disease *Thorax* **66**: 226-231.

Temming K, Schiffelers RM, Molema G and Kok RJ (2005) RGD-based strategies for selective delivery of therapeutics and imaging agents to the tumour vasculature *Drug Resist Updat* **8**: 381-402.

ten Dijke P and Arthur HM (2007) Extracellular control of TGFβ signalling in vascular development and disease *Nat Rev Mol Cell Biol* **8**: 857-869.

Tiwari S, Askari JA, Humphries MJ and Bulleid NJ (2011) Divalent cations regulate the folding and activation status of integrins during their intracellular trafficking *J Cell Sci* **124**: 1672-1680.

Travis MA, Reizis B, Melton AC, Masteller E, Tang Q, Proctor JM, Wang Y, Bernstein X, Huang X, Reichardt LF, Bluestone JA and Sheppard D (2007) Loss of integrin αvβ8 on dendritic cells causes autoimmunity and colitis in mice *Nature* **449**: 361-365.

Vauquelin G and Charlton SJ (2010) Long-lasting target binding and rebinding as mechanisms to prolong *in vivo* drug action *Br J Pharmacol* **161**: 488-508.

Wahidi MM, Ravenel J, Palmer SM and McAdams HP (2002) Progression of idiopathic pulmonary fibrosis in native lungs after single lung transplantation *Chest* **121**: 2072-2076.

Walters WP (2012) Going further than Lipinski's rule in drug design *Expert Opin Drug Discov* **7**: 99-107.

Wang A, Yokosaki Y, Ferrando R, Balmes J and Sheppard D (1996) Differential regulation of airway epithelial integrins by growth factors *Am J Respir Cell Mol Biol* **15**: 664-72.

Wang J, Wu J, Hong J, Chen R, Xu K, Niu W, Peng C, Liu E, Wang J, Liu S, Agrez M and Niu J (2011) PKC promotes the migration of colon cancer cells by regulating the internalization and recycling of integrin αvβ6 *Cancer Lett* **311**: 38-47.

Wang M, Zhao D, Spinetti G, Zhang J, Jiang L, Pintus G, Monticone R and Lakatta EG (2006) Matrix metalloproteinase 2 activation of transforming growth factor-β1 (TGFβ1) and TGFβ1-type II receptor signalling within the aged arterial wall *Arterioscler Thromb Vasc Biol* **26**: 1503-1509.

Weinreb PH, Simon KJ, Rayhorn P, Yang WJ, Leone DR, Dolinski BM, Pearse BR, Yokota Y, Kawakatsu H, Atakilit A, Sheppard D and Violette SM (2004) Function-blocking integrin αvβ6 monoclonal antibodies: distinct ligand-mimetic and nonligand-mimetic classes *J Biol Chem* **23**: 17875-17887.

Williams JW and Morrison JF (1979) The kinetics of reversible tight-binding inhibition *Methods Enzymol* **63**: 437-467.

Wipff PJ and Hinz B (2008) Integrins and the activation of latent transforming growth factor β1 - an intimate relationship *Eur J Cell Biol* **87**: 601-615.

Wong A, Hwang SM, McDevitt P, McNulty D, Stadel JM and Johanson K (1996) Studies on αvβ3/ligand interactions using a [^{3}H]SK&F-107260 binding assay *Mol Pharmacol* **50**: 529-537.

Wynn TA (2007) Common and unique mechanisms regulate fibrosis in various fibroproliferative diseases *J Clin Invest* **117**: 524-529.

Xia W and Springer TA (2014) Metal ion and ligand binding of integrin α5β1 *Proc Natl Acad Sci USA* **111**: 17863-17868.

Xu MY, Porte J, Knox AJ, Weinreb PH, Maher TM, Violette SM, McAnulty RJ, Sheppard D and Jenkins G (2009) Lysophosphatidic acid induces αvβ6 integrin-

mediated TGF-β activation via the LPA2 receptor and the small G protein G alpha(q) *Am J Pathol* **174**: 1264-1279.

Yatohgo T, Izumi M, Kashiwagi H and Hayashi M (1988) Novel purification of vitronectin from human plasma by heparin affinity chromatography *Cell Struct Funct* **13**: 281-292.

Yu H, Königshoff M, Jayachandran A, Handley D, Seeger W, Kaminski N and Eickelberg O (2008) Transgelin is a direct target of TGFβ/Smad3-dependent epithelial cell migration in lung fibrosis *FASEB J* **22**: 1778-1789.

Yu Q and Stamenkovic I (2000) Cell surface-localized matrix metalloproteinase-9 proteolytically activates TGFβ and promotes tumor invasion and angiogenesis *Genes Dev* **14**: 163-176.

Zafarullah M, Li WQ, Sylvester J and Ahmad M (2003) Molecular mechanisms of N-acetylcysteine actions *Cell Mol Life Sci* **60**: 6-20.

Zambruno G, Marchisio PC, Marconi A, Vaschieri C, Melchiori A, Giannetti A and De Luca M (1995) Transforming growth factor-β1 modulates β1 and β5 integrin receptors and induces the de novo expression of the αvβ6 heterodimer in normal human keratinocytes: implications for wound healing *J Cell Biol* **129**: 853-865.

Zhao J, Shi W, Wang YL, Chen H, Bringas P Jr, Datto MB, Frederick JP, Wang XF and Warburton D (2002) Smad3 deficiency attenuates bleomycin-induced pulmonary fibrosis in mice *Am J Physiol Lung Cell Mol Physiol* **282**: L585-593.

Zhuang Z, Zhou R, Xu X, Tian T, Liu Y, Liu Y, Lian P, Wang J and Xu K (2013) Clinical significance of integrin αvβ6 expression effects on gastric carcinoma invasiveness and progression via cancer-associated fibroblasts *Med Oncol* **30**:580.

CHAPTER 8: APPENDIX

8.1. Inclusion of additional data

Where additional data has been generated by co-workers that was deemed to add value to the author's conclusions by being included, this has been highlighted in the relevant results section and any methodology from those experiments fully described in this appendix section (see below).

8.2. Additional methods

8.2.1. αvβ3, αvβ5, and αvβ8 cell adhesion assays

The pIC_{50} data presented in Figure 3.2.8 for αvβ3, αvβ5, αvβ6 and αvβ8 cell adhesion assays were generated in the Biological Sciences department at GSK Medicines Research Centre (Stevenage, UK) with full methods detailed below. The pIC_{50} and n_H data presented in Table 3.2.6 for the αvβ6 cell adhesion assay are combined data from the author's experiments and routine assay screening also generated in the Biological Sciences department at GSK Medicines Research Centre (Stevenage, UK).

8.2.2. K562 cell culture, freezing and recover

The myelogenous leukemia K562 cell line (Lozzio and Lozzio, 1975) stably expressing either the αvβ3, αvβ5 or αvβ8 integrin (K562-αvβ3, K562-αvβ5 and K562-αvβ8, respectively) were available within GSK and were generated as previously described (Ludbrook *et al.*, 2003). All cell types were cultured as a suspension in T175 tissue culture flasks using aseptic techniques in equal volumes of RPMI 1640 and DMEM containing 10 % heat inactivated FCS, 2 mM glutamine and 1 mg/ml geneticin in 95 %:5 % air:CO_2 at 37ºC. Cells were then frozen in 90 %

dialysed FCS:10 % DMSO in 5 ml aliquots (~1.5 x 10^8 cells/ml) and stored at –140ºC until required for use in cell adhesion assays. Cells (5 ml aliquots) were recovered by defrosting in a 37ºC water bath before transferring into 20 ml of HBSS (Ca^{2+} and Mg^{2+} free) containing 25 mM HEPES maintained at 37ºC. The cell suspension was then centrifuged at 300 *g* for 5 min, the supernatant removed and the cell pellet re-suspended in HBSS containing 25 mM HEPES to the required concentration for use in cell adhesion assays.

8.2.3. K562-αvβ3, K562-αvβ5 and K562-αvβ8 cell adhesion

GST-LAP_1 protein, corresponding to the RGD integrin-binding domain of LAP_1 (amino acids 242-252 – GRRGDLATIHG), or vitronectin (purified from pooled human plasma) was available within GSK (BRAD Department, GSK Stevenage, Hertfordshire, UK) and generated as previously described (GST-LAP_1 - Ludbrook *et al.*, 2003; vitronectin – Yatohgo *et al.*, 1988). GST-LAP_1 (αvβ3 and αvβ8) or vitronectin (αvβ5) were coated (100 µl/well) onto 96-well MaxiSorp® flat-bottom plates (Thermo Fisher Scientific, MA, USA) at a concentration of 100 µg/ml and 2.5 µg/ml respectively, and incubated for 2 h at 37ºC. Plates were then washed twice with 200 µl/well PBS and blocked with 3 % w/v BSA in PBS (100 µl/well) for 1 h. Plates were then washed twice with 200 µl/well PBS and 25 µl/well of cell adhesion assay buffer (HBSS containing 25 mM HEPES) containing 8 mM $MgCl_2$ added. Test compounds (small molecule RGD-mimetics or peptides) were made up in cell adhesion assay buffer (0.4 % DMSO to give a final DMSO concentration of 0.1 %) and added to plates (25 µl/well). K562-αvβ3, K562-αvβ5 or K562-αvβ8 cells were re-suspended to 3 x 10^6 cells/ml and BCECF-AM added to give a final concentration of 5 µM prior to a 10 min incubation at 37ºC. K562-αvβ3, K562-αvβ5 or K562-αvβ8

cells (0.15 x10^6 cells/well (50 µl/well)) were then added to plates (giving a final $MgCl_2$ concentration of 2 mM) prior to a 30 min incubation at 37ºC. Plates were then washed twice with 200 µl/well PBS and 50 µl/well 0.5 % Triton X-100 detection solution added. Following a 5 min incubation at ambient temperature (20-22ºC) fluorescence (relative light units) was measured (excitation wavelength 485 nm and emission wavelength 535 nm) using an EnVision® multilabel plate reader (PerkinElmer LAS UK Ltd., Beaconsfield, UK). Full CRCs were generated for test compounds to allow determination of IC_{50} values (as described under section 2.11 Data analysis). In order to average data between separate experimental determinations, data were normalised within experiments using a positive (10 mM EDTA) and negative control (0.1 % DMSO).

8.2.4. Haematoxylin and eosin (H&E) IHC staining

Haematoxylin and eosin (H&E) staining was completed by the Laboratory Animal Sciences department at GSK Medicines Research Centre (Stevenage, UK) using a standard protocol on the Leica ST5020 Multistainer (Leica Microsystems Inc., Milton Keynes, UK) with all reagents purchased from Pioneer Research Chemicals Ltd. (Colchester, Essex, UK). Tissue sections were immersed in Harris's haematoxylin for 5 min, followed by dH_2O for 3 min, then 0.5 % acetic acid in ethanol for 30 s before a further 3 min in dH_2O. Sections were then immersed in 70 % ethanol for 1 min, then 1 % eosin for 1.5 min, followed by xylene for 1 min, then 3 x absolute ethanol for 1 min before a further 3 min in dH_2O. The process was then completed by placing each section in 4 x absolute ethanol for 30 s and finally in 3 x xylene for 30 s.

8.2.5. Preparation and expression profiling of integrin β6 and plasminogen-activator inhibitor-1 (PAI-1) messenger ribonucleic acid (mRNA)

Total RNA was isolated from 24-well plates containing cultured NHBE cells using the RNeasy mini kit (Qiagen, West Sussex, UK) with on-column DNase digestion as per the manufacturer's instructions. Total RNA was reverse transcribed using the high-capacity complementary DNA (cDNA) reverse transcription kit (Life Technologies Ltd, Paisley, UK) as per the manufacturer's instructions. Integrin β6, PAI-1 and GAPDH (housekeeping gene) gene expression were determined using the respective TaqMan real-time PCR (RT-PCR) primers ITGB6 (Hs00168458_m1), PAI-1 (Hs01126604_m1) and GAPDH (Hs99999905_m1) (Life Technologies Ltd, Paisley, UK) on a LightCycler® 480 (Roche, Basil, Switzerland). This was completed using a LightCycler® 480 Probes Master kit as per the manufacturer's instructions with a pre-incubation at 95°C for 10 min, amplification at 95°C for 10 s followed by 60°C for 30 s (repeated for 45 cycles) and cooling at 4°C for 30 s. $2^{\wedge-\Delta\Delta C_t}$ (fold increase in gene expression relative to comparator (control (0.3 % DMSO) at t=0 h)) for integrin β6 and PAI-1 were calculated as described previously (Livak and Schmittgen, 2007) with gene expression normalised to the housekeeping gene (GAPDH).

8.3. Supplementary data

8.3.1. Surface expression of RGD integrins and TGFβRII on NHBE cells over passage

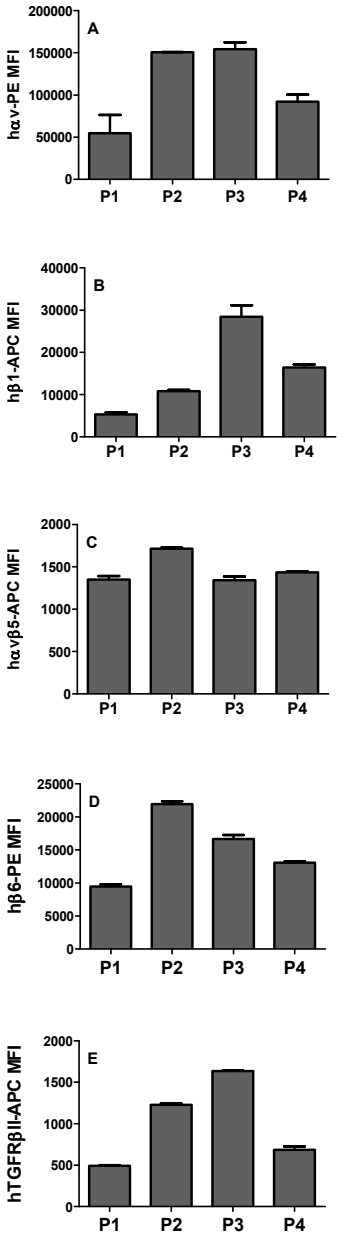

Figure 8.3.1 Surface expression of the human αv, β1, αvβ5, β6 and TGFβRII proteins over passage on NHBE cells. NHBE cells were recovered from culture at passage 1 (P1), 2 (P2), 3 (P3) and 4 (P4) and surface staining of the human αv (A), β1 (B), αvβ5 (C), β6 (D) and TGFβRII (E) proteins were determined by flow cytometry. NHBE cells were washed and stained with flow cytometry antibodies described in section '2.1 Materials' that were either specific for the protein of interest or a relevant isotype control. Specific mean fluorescence intensity (MFI) values shown were calculated by subtracting the MFI of isotype controls from the specific flow cytometry antibody. Data shown are mean ± SD of duplicate points from a single experiment carried out on the same batch of NHBE cells through a standard 4 passage culture lifecycle.

8.3.2. Positive cell controls for flow cytometry antibodies

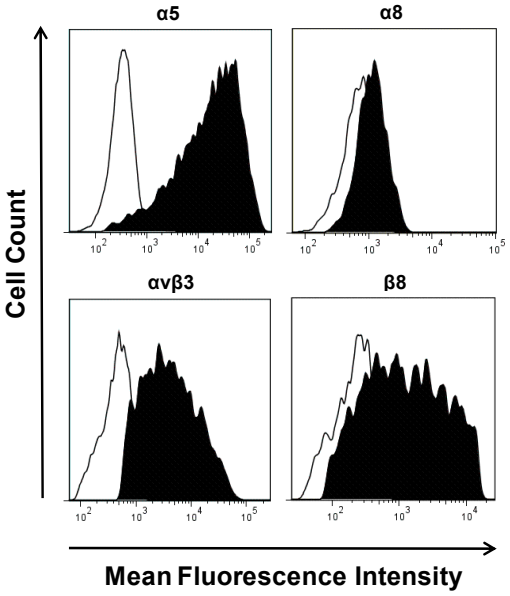

Figure 8.3.2 Positive cell controls for RGD integrin subunits or heterodimers with negative results in cell types tested in this study. Surface staining of the human α5, α8, αvβ3 and β8 integrin subunits or heterodimers were tested in K562-WT cells, IPF human lung derived fibroblast cells, K562-αvβ3 cells and K562-αvβ8 cells, respectively. Cells were washed and stained with flow cytometry antibodies described in section '2.1 Materials' that were either specific for the protein of interest (black peaks) or the relevant isotype control (white peaks). Fluorescence-activated cell analyses histograms shown are plotted with normalised cell count against mean cell fluorescence intensity and are representative of expression levels in the cell lines tested.

8.3.3. β6 integrin confocal microscopy isotype controls

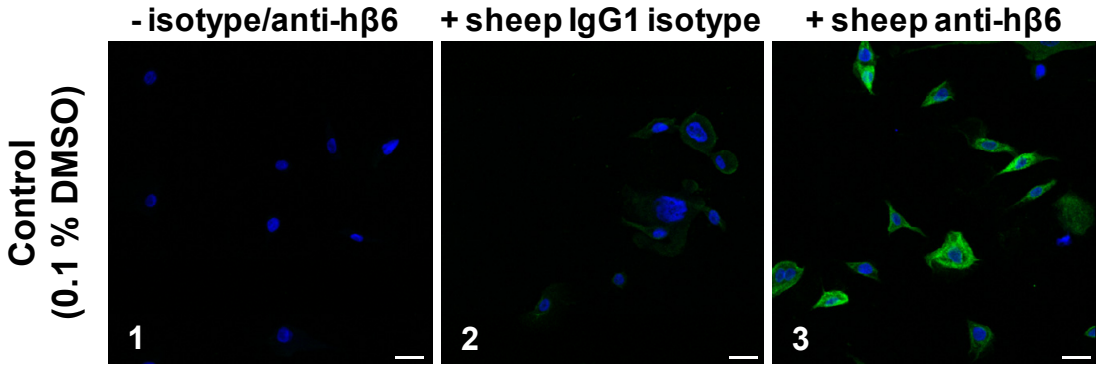

Figure 8.3.3 β6 integrin confocal microscopy isotype controls. NHBE cells were treated with 0.1 % DMSO vehicle control for 1 h at 37ºC. Following fixation, cells were left unpermeabilised and imaged by confocal microscopy. Panel 1 shows the background in the absence of either sheep IgG1 polyclonal anti-human integrin β6 antibody and sheep IgG1 isotype control, panel 2 shows the background staining in the presence of sheep IgG1 isotype control and panel 3 shows the β6 specific staining in the presence of sheep IgG1 polyclonal anti-human integrin β6 antibody (all conditions completed in the presence of anti-sheep IgG Alexa Fluor® 488 antibody (green stain) and nuclear staining with Hoechst 33342 dye (blue stain)). Single optical sections shown (50x magnification) representative of the four optical sections captured per condition with similar staining patterns observed. Scale bar = 50 μm.

8.3.4. Compound 1 integrin selectivity profile in cell adhesion assays

The selectivity profile determined in cell adhesion assays against αvβ3, αvβ5, αvβ6 and αvβ8 is shown in Table 8.3.1 (data generated in the Biological Sciences department at GSK Medicines Research Centre (Stevenage, UK)).

Integrin	*αvβ3 pIC_{50}*	*αvβ5 pIC_{50}*	*αvβ6 pIC_{50}*	*αvβ8 pIC_{50}*
Compound 1	7.2 ± 0.1	7.1 ± 0.2	7.5 ± 0.3	7.4 ± 0.2

Table 8.3.1 The IC_{50} values of compound 1 against the αvβ3, αvβ5, αvβ6 and αvβ8 integrins determined by cell adhesion assays. Cell adhesion concentration response curve data were fitted using non-linear regression analysis (four-parameter logistic equation with variable slope (Hill, 1909)) (see 2.11 Data analysis section) to generate IC_{50} values. Data shown are mean values ± SEM for at least three individual determinations. pIC_{50}, negative $\log_{10}$ of IC_{50}.

8.3.5. Physico-chemical and pharmacokinetic properties of the small molecule RGD-mimetics compound 2 and 3

The physico-chemical and pharmacokinetic properties of the novel small molecule RGD-mimetics characterised in this study are shown in Table 8.3.2 (data generated by Drug Metabolism and Pharmacokinetic Group (Respiratory Therapy Area Unit) or Platform, Technology and Sciences Group at GSK Medicines Research Centre (Stevenage or Ware, UK)). The methods are briefly described below:-

Solubility: Amount of compound (mg/ml) dissolved in saline (pH 4-7) at equilibrium detected by high performance liquid chromatography (HPLC).

Lung tissue binding (%): Amount of compound bound to human lung tissue homogenates following rapid equilibrium dialysis (RED) detected by HPLC-tandem mass spectrometry (MS). GSK criteria set as <85 % low, 85-95 % moderate, 95-99 % high and >99% very high.

MDCK passive permeability: The permeability of a molecule through a cell monolayer in the presence of an inhibitor of efflux transporters as measured in Madin-Darby canine kidney (MDCK) cells and detected by HPLC-tandem MS. GSK criteria set as <10 nm/s low, 10-100 nm/s moderate and >100 nm/s high.

Oral bioavailability: Fraction of orally dosed unchanged drug that reaches the systemic blood, as ratio of systemic exposures determined by HPLC-MS from oral and intravenous administration, normalised by the dose levels (determined in rat).

Lung retention: Expressed as percentage of the amount of drug administered intranasally still present in mouse lung tissue 30 min after dosing (tissue concentrations determined by HPLC-MS).

Property	Compound 2	Compound 3
Solubility in saline pH 4-7 (mg/ml)	N.D.	>55
Human lung tissue binding (%)	85.5 (moderate)	89.2 (moderate)
MDCK passive permeability (Pexact, nm/s)	3.2 (low)	20 (moderate)
Oral bioavailability (%F, rat)	*N.D.	<2%
Lung retention (% of intranasal dose retained in mouse lung 30 min after dosing)	<1%	<1%

Table 8.3.2 Physico-chemical and pharmacokinetic properties of the small molecule RGD-mimetics compound 2 and 3. Solubility (mg/ml), amount of compound dissolved in saline (pH 4-7) at equilibrium; Human lung tissue binding (%), amount of compound bound to human lung tissue homogenates; MDCK permeability, permeability of a molecule through a cell monolayer in the presence of an inhibitor of efflux transporters as measured in Madin-Darby canine kidney (MDCK) cells; Oral bioavailability (% F): fraction of orally dosed unchanged drug that reaches the systemic blood, as ratio of systemic exposures determined by HPLC-MS from oral and intravenous administration, normalised by the dose levels (determined in rat).; Lung retention, percentage of the amount of drug administered intranasally still present in mouse lung tissue 30 min after dosing. N.D., not determined with *N.D. as compound expected to be non-orally bioavailable based on very low passive permeability.

.